Spectroscopy and morphology study of polymer/ fullerene and non-fullerene organic photovoltaic blends

Junjun Guo

Supervised by Dr Tracey M. Clarke

University College London

Department of Chemistry

This thesis is submitted to University College London for the degree of Doctor of Philosophy

March 2023

Declaration

I, Junjun Guo, confirm that the work presented in this thesis is my own. Where information has been derived from other sources, I confirm that this has been indicated in the thesis.

Signature:

Abstract

Solution-processable organic solar cells (OSC) have attracted considerable attention in recent years with rapid increases in device efficiency. The improvement is primarily a consequence of newly designed non-fullerene acceptors (NFAs), providing a series of options to match with the donor and covering a broader spectral range than the fullerenes.

My thesis aims to study the charge and triplet photogeneration in fullerene and non-fullerene based OSCs. Triplet states are traditionally considered harmful to device stability and performance, but their recent discovery in high-performing non-fullerene OSCs brings their exact role in device performance into question. Furthermore, charge photogeneration mechanisms in non-fullerene acceptor OSC blends, particularly with minimal LUMO level offsets, still need to be fully understood. Millisecond and picosecond transient absorption spectroscopy mainly study the charge photogeneration and recombination process. Atomic force microscopy and grazing incident X-ray diffraction are used to study the morphology of films.

In the first results chapter, chapter 3, charge photogeneration is explored in temperature dependence aggregated polymer with fullerene blend films. Bimodal polarons are generated in polymer-dominated domains and mixed domains influenced by fullerene induced ordering. In addition, polymer triplet formation was identified for the first time in this high-performing PffBT4T-based polymer blend system via charge back recombination.

Chapter 4 studied charge photogeneration in the polymer PffBT4T-C9C13 blended with four different NFAs (ITIC, ITIC-Th, ITIC-2F and Y6). Triplet states are detected in three ITIC blend systems, and the ITIC-2F blend film shows the highest charge to triplet population ratio. Triplet extinction coefficient has been calculated in both NFA solutions and films, which is further used to quantify the triplet population in polymer:NFA blend films. The correlation between triplet and charge population is further investigated regarding film morphology.

In Chapter 5, Charge photogeneration and recombination are investigated in polymer PM6 with three novel PDFC NFA blend systems, two showing high fill factor and high device performance. An energy transfer process from the polymer singlet state to the NFA under the polymer dominant excitation was observed in all three blend systems.

Impact statement

Organic solar cells (OSCs), which are flexible, semi-transparent, low cost and easily processable, and have less environmental impact, can significantly expand the range of applications for solar technology. They could be wrapped around the exteriors of buildings. They can efficiently recycle the energy used for indoor lighting, neither of which is possible with conventional silicon panels. However, challenges for OSCs to be utilised commercially on a large scale have been highlighted by their relatively low power conversion efficiency (PCE) and the relatively short device lifetime compared to silicon photovoltaics. Previously, the highest PCE of 12% was found in a temperature dependence aggregated (TDA) polymer with fullerene acceptor solar cell, and this efficiency kept for a few years without further improving. Recent advances in OSCs demonstrate a 19% PCE in single junction devices with the emergence of non-fullerene acceptors. This is a big step for the improvement of OSCs. This could be rationalised by the new development of organic materials, including polymer and non-fullerene molecules, modification of the energy loss pathways, optimised film morphology, interfacial active layer, and device engineering.

With the emergence of new organic materials, the triplet state's high efficiency and high yield could coexist in the polymer:NFA blend systems. However, the triplet state is an intermediate excited state in OSCs, which is difficult to detect directly, like singlet exciton or free charge carriers. Therefore, this leads to triplet's poorly understood role in OSCs. The research presented in this thesis initially identified the energy loss pathways for the high-performing TDA polymer:fullerene blend systems, which could be attributed to the formation of triplet states via charge back recombination. Meanwhile, this thesis also describes a method to calculate the triplet molar extinction coefficient in both the solution and solid phases, which is further used to quantify the triplet yield in the polymer donor and NFA blend systems. With an understanding deeply about the role of triplet in OSCs, and the correlation between the charge photogeneration and the film morphology in both polymer with fullerene and non-fullerene acceptor blend systems, it is beneficial to guide the community to high device performance.

The high fill factor of such organic solar cells is attributed to the high mobility of charge carriers. The geminate recombination has also been identified as the main energy loss process

in highly performing (high PCE, high fill factor) polymers with highly crystalline PDI-based novel non-fullerene acceptors. The suppression of geminate recombination can be achieved by manipulating the molecules' energy levels inside the OSCs and controlling the polymer's blend morphology: non-fullerene acceptor active layers.

Research Paper Declaration Form

UCL Research Paper Declaration Form

referencing the doctoral candidate's own published work(s)

Please use this form to declare if parts of your thesis are already available in another format, e.g. if data, text, or figures:

- *have been uploaded to a preprint server*
- *are in submission to a peer-reviewed publication*
- *have been published in a peer-reviewed publication, e.g. journal, textbook.*

This form should be completed as many times as necessary. For instance, if you have seven thesis chapters, two of which containing material that has already been published, you would complete this form twice.

1. **For a research manuscript that has already been published** (if not yet published, please skip to section 2)

   a) **What is the title of the manuscript?**
   Bimodal polaron as a function of morphology in high efficiency polymer/acceptor blends for organic photovoltaics

   b) **Please include a link to or doi for the work**
   DOI:10.1088/2515-7639/ac0fbc

   c) **Where was the work published?**
   Journal of Physics: Material

   d) **Who published the work?** (e.g. OUP)

   IOP Publishing Ltd

   When was the work published?

   July 2021

   e) **List the manuscript's authors in the order they appear on the publication**
   Junjun Guo, Jose M Marin-Beloqui and Tracey M Clarke

   f) **Was the work peer reviewed?**

   Yes

   g) **Have you retained the copyright?**

   Yes, open access

   h) **Was an earlier form of the manuscript uploaded to a preprint server?** (e.g. medRxiv). If 'Yes', please give a link or doi) http://doi.org/10.1088/2515-7639/ac0fbc

   If 'No', please seek permission from the relevant publisher and check the box next to the below statement:

   ☐

   *I acknowledge permission of the publisher named under **1d** to include in this thesis portions of the publication named as included in **1c**.*

2. **For a research manuscript prepared for publication but that has not yet been published** (if already published, please skip to section 3)

   a) **What is the current title of the manuscript?**

Click or tap here to enter text.

b) **Has the manuscript been uploaded to a preprint server?** (e.g. medRxiv; if 'Yes', please give a link or doi)

Click or tap here to enter text.

c) **Where is the work intended to be published?** (e.g. journal names)

Click or tap here to enter text.

d) **List the manuscript's authors in the intended authorship order**

Click or tap here to enter text.

e) **Stage of publication** (e.g. in submission)

Click or tap here to enter text.

3. **For multi-authored work, please give a statement of contribution covering all authors** (if single-author, please skip to section 4)

Jose M Marine-Beloqui edit the final paper draft, and Tracey M Clarke edit the paper step by step

4. **In which chapter(s) of your thesis can this material be found?**

Chapter 3

5. **e-Signatures confirming that the information above is accurate** (this form should be co-signed by the supervisor/ senior author unless this is not appropriate, e.g. if the paper was a single-author work)

Candidate

Jnjun Guo

Date:

06/03/2023

Supervisor/ Senior Author (where appropriate)

Tracey M Clarke

Date

08/03/2023

UCL Research Paper Declaration Form

referencing the doctoral candidate's own published work(s)

Please use this form to declare if parts of your thesis are already available in another format, e.g. if data, text, or figures:

- *have been uploaded to a preprint server*
- *are in submission to a peer-reviewed publication*
- *have been published in a peer-reviewed publication, e.g. journal, textbook.*

This form should be completed as many times as necessary. For instance, if you have seven thesis chapters, two of which containing material that has already been published, you would complete this form twice.

6. For a research manuscript that has already been published (if not yet published, please skip to section 2)

i) **What is the title of the manuscript?**

Quantify triplet formation in conjugated polymer/non-fullerene acceptor blends.

j) **Please include a link to or doi for the work**
DOI.org/10.1039/D2TA05172A

k) **Where was the work published?**
Journal of material chemistry A

l) **Who published the work?** (e.g. OUP)
Royal Society Chemistry

When was the work published?

Sep 2022

m) **List the manuscript's authors in the order they appear on the publication**
Junjun Guo, Benjamin Moss, and Tracey M Clarke

n) **Was the work peer reviewed?**

Yes

o) **Have you retained the copyright?**

Yes, open access

p) **Was an earlier form of the manuscript uploaded to a preprint server?** (e.g. medRxiv). If 'Yes', please give a link or doi) http://doi.org/10.1039/d2ta05172a

If 'No', please seek permission from the relevant publisher and check the box next to the below statement:

☐

*I acknowledge permission of the publisher named under **1d** to include in this thesis portions of the publication named as included in **1c**.*

7. For a research manuscript prepared for publication but that has not yet been published (if already published, please skip to section 3)

f) **What is the current title of the manuscript?**

Click or tap here to enter text.

g) **Has the manuscript been uploaded to a preprint server?** (e.g. medRxiv; if 'Yes', please give a link or doi)

Click or tap here to enter text.

h) **Where is the work intended to be published?** (e.g. journal names)

Click or tap here to enter text.

i) **List the manuscript's authors in the intended authorship order**

Click or tap here to enter text.

j) **Stage of publication** (e.g. in submission)

Click or tap here to enter text.

8. **For multi-authored work, please give a statement of contribution covering all authors** (if single-author, please skip to section 4)

Benjamin Moss assist Junjun Guo in performing and analysing the SEC data and editing the final draft

9. **In which chapter(s) of your thesis can this material be found?**

Chapter 4

10. **e-Signatures confirming that the information above is accurate** (this form should be co-signed by the supervisor/ senior author unless this is not appropriate, e.g. if the paper was a single-author work)

Candidate

Jnjun Guo

Date:

06/03/2023

Supervisor/ Senior Author (where appropriate)

Tracey M Clarke

Date

08/03/2023

Acknowledgements

First of all, I would like to thank my supervisor Dr Tracey M Clarke, for her rigorous scientific research attitude and logical guidance for my scientific research methods and writing, Because of her, I have a better understanding of spectroscopist, which is not a simple analysis, but an attitude towards the essence of things. I would also thank my second supervisor, Prof Kathrine Holt, who introduced me to electrochemistry and for always encouraging my research and lifestyle.

Secondly, I would like to thank those experts who helped me train various instruments. Regarding spectroscopy, I would like to thank Dr Jose Beloqui for training me about the nanosecond-to-microsecond TAS and answering questions about the use of instruments during his postdoc period in our group. Thanks to Dr Michael Parkes for training me in the use of ground-state absorption spectroscopy. Thanks to Dr Helena Wong for using the water bath many times so that I could do some temperature dependence experiments. Thanks to Dr Cally Haynes for training me in using temperature-dependence photoluminescence spectroscopy at the right time. Regarding the training of morphology equipment, I would like to thank Dr Richard Thorogate for training me to use atomic force microscopy effectively and Dr Martin Vickers for training me about grazing incident X-ray Diffraction.

I would also like to thank former group members Dr Jose Beloqui, for his art of answering questions that 'do not know' made me think more independently, and Dr Jordan Shaik's attitude towards his data processing has taught me a lot. I would also thank my current group member Hristo who chats with me on career-picking topics.

I want to thank my collaborator Dr Moss Benjamin from Imperial College London, UK training me in using their spectroelectrochemistry (SEC) setup and teaching me how to deal with the SEC data. I also thank Dr Zhong from Shanghai Jiaotong University, China, for providing newly developed high-performance non-fullerene acceptor materials. This allowed me to study the photophysical mechanisms in such promising polymer: NFA blends systems. Importantly, I would also like to thank Dr James Shipp for the data acquisition on picosecond transient absorption spectroscopy measured during the pandemic. Meanwhile, I would like to thank Prof Julia Weinstein and Dr James Shipp for the initial discussion of the data.

I would also like to thank my boyfriend, Mr Junwen Gu, for his encouragement and support in my daily life and mental health, who will also be Dr Junwen Gu within the next few months.

The last and most important thing is that I want to thank my parents not only because they funded me for the scientific research direction I wanted to do during my PhD period but also because of their unconditional support and encouragement. I would also like to thank my brother Yu Guo for unconditionally supporting me and sharing his fun moments with me. During the last three and half years, when I had no chance to return to China, his severe and sensible attitude made me not need to be distracted to think about things other than my scientific research.

Table of Contents

Contents

List of equations

$$FF = \frac{I_{MP} \times V_{MP}}{I_{sc} \times V_{oc}} \quad (1.1)$$

$$PCE = \frac{I_{MP} \times V_{MP}}{P_{in}} = \frac{I_{sc} V_{oc} FF}{P_{in}} \quad (1.2)$$

$$\mathrm{V} = \frac{\mathrm{e}^2}{4\pi \mathrm{r} \varepsilon_0 \varepsilon_\mathrm{r}} \quad (1.3)$$

$$k_{FRET} = \frac{1}{\tau_D} \left(\frac{R_0}{r}\right)^6 \quad (1.4)$$

$$R_0^6 = \frac{9\Phi_{PL} K^2}{128\pi^5 n^4} J_F \quad (1.5)$$

$$k_D = K J_D e^{\left(\frac{-2r}{L}\right)} \quad (1.6)$$

$$\Delta G^{\ddagger} = \frac{\left(\lambda + \Delta G^0\right)^2}{4\lambda} \quad (1.7)$$

$$\ln[A]_t = \ln[A]_0 - kt \quad (1.8)$$

$$\mathrm{A} \propto \mathrm{t}^{-\alpha} \quad (1.9)$$

$$A_t = A_0 * \exp\left(-\frac{t}{\tau}\right)^{\beta} \quad (1.10)$$

$$A = -\log T = -\log \frac{I}{I_0} \quad (2.1)$$

$$A = \varepsilon \, c \, l \quad (2.2)$$

$$n\lambda = 2d \sin\theta \quad (2.3)$$

$$\mathrm{r} = \frac{\mathrm{K}\lambda}{\beta \cos\theta} \quad (2.4)$$

$$\Delta A_t = A_t - A_0 \quad (2.5)$$

$$\Delta OD_t = OD_t - OD_0 \quad (2.6)$$

$$\frac{V_{(t)} - V_{(0)}}{V_{(0)}} = \frac{10^{-OD_t} - 10^{-OD_0}}{10^{-OD_0}} = 10^{-OD_t + OD_0} - 1 \quad (2.7)$$

$$\frac{\Delta V_{(t)}}{V_{(0)}} = 1 - \Delta OD \ln 10 - 1 = \Delta OD \ln 10 \quad (2.8)$$

$$\Delta OD = \frac{1}{2.303} \frac{\Delta V_{(t)}}{V_{(0)}} \quad (2.9)$$

$$^3D \xrightarrow{k_1} D \quad (2.10)$$

$$^3D + A \xrightarrow{k_Q} D + {}^3A \quad (2.11)$$

$$^3A \xrightarrow{k_3} A \quad (2.12)$$

$$\frac{\varepsilon_T^D}{\varepsilon_T^A} = \frac{\Delta OD^D}{\Delta OD^A} \quad (2.13)$$

$$\Delta OD_{max}^A = \Delta OD^A \left(-\frac{ln k_2/k_3}{\frac{k_2}{k_3} - 1} \right) \quad (2.14)$$

$$\sigma_{GS\_soln} = \frac{\varepsilon_{GS\_soln} ln 10}{N_A} \quad (2.15)$$

$$\sigma_{GS\_solid} = A\sigma_{GS\_soln} \quad (2.16)$$

$$n_T = \frac{\Delta OD.A_v}{1000.\varepsilon_T.d} \quad (2.17)$$

List of Tables

List of Figures

Acronyms and Abbreviations

D: Donor

A: Acceptor

D/A: Donor/acceptor

BHJ: Bulk heterojunction

TDA: Temperature dependent aggregation

ISC: Intersystem crossing

PCE: Power conversion efficiency

OSC: Organic solar cell

BR: Bimolecular recombination

GR: Geminate recombination

ΔE_{ST}: Exchange energy of S_1-T_1

FRET: Förster resonant energy transfer

MD: molecular dynamics

PS: Polystyrene

ZnTpp: Zinc tetraphenyl-porphyrin

AFM: Atomic force microscopy

R_q: Root mean square

GIXRD: Grazing incident X-ray diffraction

SEC: Spectroelectrochemistry

ns-μs: Nanosecond to microsecond

TAS: Transient absorption spectroscopy

PffBT4T-2OD: poly[(5,6-difluoro-2,1, 3-benzothiadiazol-4,7-diyl)-*alt*-(3,3‴-di(2-octyldodecyl)-2,2′;5′,2″;5″,2‴-quaterthiophen-5,5‴-diyl)]);
PffBT4T-2DT:

PffBT4T-C9C13: poly[(5,6-difluoro-2,1,3-benzoth iadiazol-4,7-diyl)-alt-(3,3′′′-di (2-nonyltridecyl)-2,2′;5′,2″;5″,2‴ -quaterthiophen-5,5′′′-diyl)]

ITIC: 3,9-bis(2-methylene-(3-(1,1-dicyanomethylene)-indanone))-5,5,11,11-tetrakis(4-hexylphenyl)-dithieno[2,3-d:2’,3’-d’]-s-indaceno[1,2-b:5,6-b’]dithiophene

ITIC-M: 3,9-bis(2-methylene-(3-(1,1-dicyanomethylene)-6/7-methyl)-indanone))-5,5,11,11-tetrakis(4-hexylphenyl)-dithieno[2,3-d:2’,3’-d’]-s-indaceno[1,2-b:5,6-b’]dithiophene

ITIC-Th: 3,9-bis(2-methylene-(3-(1,1-dicyanomethylene)-indanone))-5,5,11,11-tetrakis(5-hexylthienyl)-dithieno[2,3-d:2’,3’-d’]-s-indaceno[1,2-b:5,6-b’]dithiophene

ITIC-2F: 3,9-bis(2-methylene-(3-(1,1-dicyanomethylene)-6,7-difluoro-indanone))-5,5,11,11-tetrakis(4-hexylthienyl)-dithieno[2,3-d:2’,3’-d’]-s-indaceno[1,2-b:5,6-b’]dithiophene

PTB7-Th: Poly[4,8-bis(5-(2-ethylhexyl)thiophen-2-yl)benzo[1,2-b;4,5-b’]dithiophene-2,6-diyl-alt- (4-(2-ethylhexyl)-3-fluorothieno[3,4-b]thiophene-)-2-carboxylate-2-6-diyl)]

PBDB-T: Poly[(2,6-(4,8-bis(5-(2-ethylhexyl)thiophen-2-yl)-benzo[1,2-b:4,5-b’]dithiophene))-alt-(5,5-(1’,3’-di-2-thienyl-5’,7’-bis(2-ethylhexyl)benzo[1’,2’-c:4’,5’-c’]dithiophene-4,8- dione)]

PBDB-T-SF (PM6): Poly[(2,6-(4,8-bis(5-(2-ethylhexyl-3-fleoro)thiophen-2-yl)-benzo[1,2-5:4,5-5’]dithiophene))-alt-(5,5-(1’,3’-di-2-thienyl-5’,7’-bis(2-ethylhexyl)benzo[1’,2’-c:4’,5’-c’]dithiophene-4,8-dione)]

Y6:2,2'-((2Z,2'Z)-((12,13-Bis(2-ethylhexyl)-3,9-diundecyl-12,13-dihydro-[1,2,5]thiadiazolo[3,4-e]thieno[2",3’':4’,5']thieno[2',3':4,5]pyrrolo[3,2-g]thieno[2',3':4,5]thieno[3,2-b]indole-2,10-diyl)bis(methanylylidene))bis(5,6-difluoro3-oxo-2,3-dihydro-1H-inde

List of Publications [1–5]

1 **J. Guo**, J. M. Marin-Beloqui and T. M. Clarke, Bimodal polarons as a function of morphology in high efficiency polymer/acceptor blends for organic photovoltaics, *JPhys Materials*, (***Chapter 3*** written based on this paper with more details)

2 **J. Guo**, B. Moss and T. M. Clarke, Quantifying triplet formation in conjugated polymer/non-fullerene acceptor blends, *J Mater Chem A*, 2022, **10**, 20874–20885. (***Chapter 4,*** written based on this paper with more details)

3 J. Marin-Beloqui, G. Zhang, **J. Guo**, J. Shaikh, T. Wohrer, S. M. Hosseini, B. Sun, J. Shipp, A. J. Auty, D. Chekulaev, J. Ye, Y. C. Chin, M. B. Sullivan, A. J. Mozer, J. S. Kim, S. Shoaee and T. M. Clarke, Insight into the Origin of Trapping in Polymer/Fullerene Blends with a Systematic Alteration of the Fullerene to Higher Adducts, *Journal of Physical Chemistry C*, 2022, **126**, 2708–2719.

4 J. M. Marin-Beloqui, D. G. Congrave, D. T. W. Toolan, S. Montanaro, **J. Guo**, I. A. Wright, T. M. Clarke, H. Bronstein and S. D. Dimitrov, Generating Long-Lived Triplet Excited States in Narrow Bandgap Conjugated Polymers, *J Am Chem Soc*, 2023, **145,** 3507-3514

5 W Lowrie, R.J E. Westbrook, **J Guo**, H Gonev, J M Beloqui, T M. Clarke, Organic Photovoltaics: The Current Challenges, J Chem. Phy. 2023, **158**, 110901

6 **J Guo**, J Shipp, K Ding, T Shan, H Zhong, J Weinstein, T M. Clarke, The influence of minimal energy offset for both hole and electron transfer in a polymer/non-fullerene blend (prepared) (This is partially the work from chapter 5)

Chapter 1 Introduction

1.1 Motivation and Overview

The rapid growth of demand for world energy has already raised concerns over supply difficulties, exhaustion of energy resources and heavy environmental impacts, such as ozone layer depletion, global warming, and climate change. This is considered to be the result of overusing fossil-based energy resources, which produces a significant increase in harmful greenhouse gases.[1] With increasing attention towards carbon-neutral energy production, solar energy, the most plentiful and clean energy source, is receiving heightened attention as a potentially widespread approach to sustainable energy production.[2] The emergence and development of solar cells have shown the ability to satisfy the world's energy demand. The solar future study explores pathways for solar energy to drive deep decarbonisation of the world electric grid and considers how to further electrification could decarbonise the broader energy system. It was suggested that solar could account for as much as 40% of the nation's electricity supply by 2035 and 45 % by 2050.[3] Figure 1.1 shows that decarbonised entire energy system could result in as much as 3000 GW of solar energy due to increased electricity demand, dramatically accelerating the decarbonisation of buildings, transportation, and industry. This study was made by the US Department of Energy (DOE) Solar Energy Technologies Office and the National Renewable Energy Laboratory (NREL).

Currently, crystalline silicon photovoltaics, as the most popular and commercialised solar cells, dominate 90% renewable energy market.[4] However, crystalline silicon PV modules are typically fragile, rigid, heavy, and have an energy payback time of about 4 years. The high cost of manufacturing and transportation has limited the further development of silicon solar cells in modern society.

In recent years, increasing attention has been given to solar cells based on organics semiconductors composed of π-conjugated polymers, the primary focus of this thesis. These polymers are flexible, lightweight, and versatile. They can be fabricated on plastic substrates via a solution-processable roll-to-roll process.[4] These promising properties indicate that organic solar cells (OSCs) are easier to transport at a relatively low cost and can be widely manufactured.

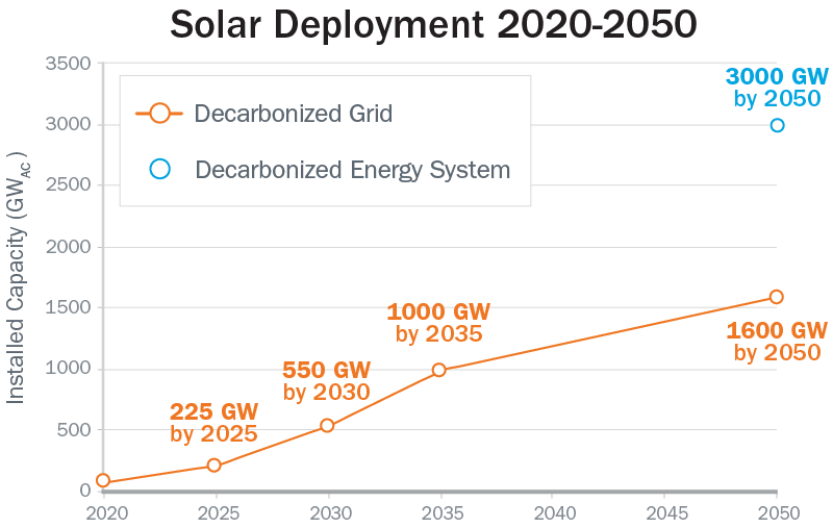

Figure 1.1 *The solar future study simulates the development of solar energy needed to decarbonise the electric grid. Preliminary models suggest that decarbonising the entire energy system could generate as much as 3000 GW of solar energy due to increased electrification of buildings, transportation, industrial power and production of clean fuels.*

1.2 Historical context

Solar cells are made of semiconducting materials that capture and convert sunlight directly into electricity. Edmond Becquerel first discovered the working principle of the solar cell known as the photovoltaic effect in 1839, he detected the electric current when he immersed an electrode in a conductive solution exposed to light.[5] Since the discovery of the photovoltaic effect, researchers have significantly developed this field. The first silicon solar cell was made by Bell Laboratory in 1954 by Chapin et al., with an efficiency of 6%. Since then, crystalline silicon solar cell efficiency can reach up to 27.6%.

One potential means to reduce the high cost of inorganic photovoltaics is to use organic materials. The photoconductivity of the organic compound anthracene was first reported in 1906 by the Italian physical chemist Alfredo Pochettino.[6] The first effort to fabricate an OSC using a small molecule to absorb light was in 1975, but the efficiency was as low as 0.001%.[7] The discovery of metallic conductivity of polymer was discovered by Alan Heeger, Alan MacDiarmid and Hideki Shirakawa based on the doped conjugated polyacetylene.[8] The application of the electrical property of the polymer was utilised in a wide range of semiconductor devices, such as organic photovoltaics. The three pioneers' unique conductivity finding of the polymer was later awarded the Nobel Prize in Chemistry 2000 for photovoltaics. Since then, there has been a revolution in the field of organic semiconductors.

The first relatively efficient OSC was reported by Tang's group in 1986; they came up with a new electron donor/acceptor (D/A) bilayer structure with a direct analogue to a conventional p-n inorganic semiconductor junction, as shown in Figure 1.2a. The efficiency of the bilayer device had a slightly increased efficiency of 1%.[9] The significant advantage of this bilayer device over the prevalent single material devices was that charge generation was no longer dependent on the electric field but rather the work function of the two-layer materials. This improvement in efficiency relied on the energy offset created by the differing electron affinity between D and A materials as a driving force to help exciton dissociation. An exciton is defined as a bound electron and hole pair that is initially generated after photoexcitation. However, this organic bilayer device's efficiency was reportedly low due to the short exciton diffusion length. The limited exciton diffusion length (around 10nm) indicates that only excitons reaching the interfacial area of D/A can dissociate to form free charge carriers and contribute to generating a photocurrent. Hence, the film thickness was required to be less than the optical absorption depth.

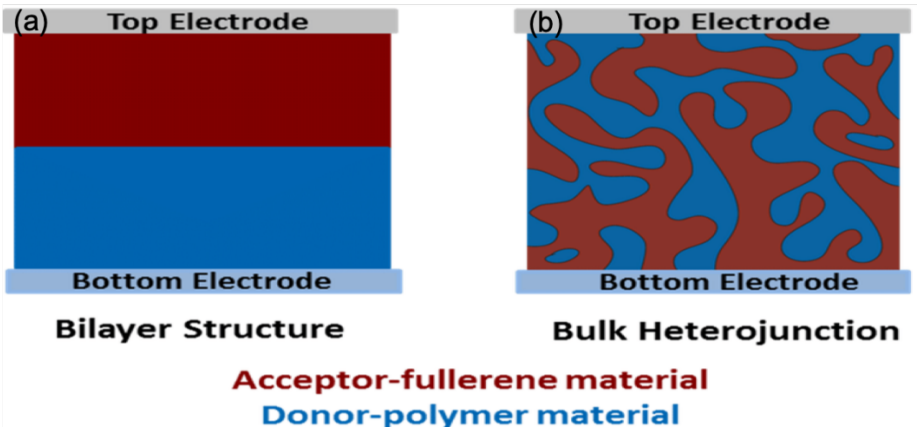

Figure 1.2 *(a)The bilayer structure of the organic solar cell. (b) bulk heterojunction structure of organic solar cell with two mixing blend solutions.*[8]

With the understanding of the limitation on bilayer sandwich structure and conductivity of polymer, Hiramoto et al. in 1991, first demonstrated that the efficiency of OSC could be enhanced via the incorporation of a mixing layer of molecules by low-temperature vacuum deposition.[15] The mixed solution for small molecules heterojunctions was defined by Yu's group as bulk heterojunction, as shown in Figure 1.2(b).[10,11] Heeger et al. [11] firstly studied bulk heterojunction solution of poly[2-methoxy-5-(2-ethylhexyloxy)-1,4-phenylenevinylene] (MEH-PPV) and phenyl-C61-butyric acid methyl ester ($PC_{60}BM$) that could be processed into

D/A mixed blend films, leading to improved efficiency to 1.7%. A surprising observation of the ultrafast photoinduced electron transfer from conjugated polymer to the $PC_{60}BM$ indicates good electron transfer process in OSC. The enhancement in charge photogeneration yield opened the potential to employ solution processable polymer in the next generation.

Historically, fullerene derivatives have been the most dominant acceptors in OSCs due to their excellent electron transporting properties and the favourable bulk heterojunction morphology from optimal combinations of polymer donors and fullerene acceptors. However, despite these promising characteristics, fullerene-based OSCs exhibit serious drawbacks, including poor light-absorption properties, limited energy level tunability, and morphological instability. Recently, the development of non-fullerene acceptors (NFAs) has overcome these limitations. The polymer blending with NFAs devices successfully achieves comparable or even higher efficiencies to the fullerene-based OSCs.

1.3 Solar cell performance

Figure 1.3 shows typical current to voltage (I-V) characteristics curves for photovoltaic device performance under the illumination conditions, with correlated defined parameters.[12] The operational regime of photovoltaics is between the short circuit (no voltage) and the open circuit (no current). For an operational photovoltaic device, the maximum power output (P_{max}) can be found when the current (I_{MP}) and voltage (V_{MP}) combinations result in the most significant power.

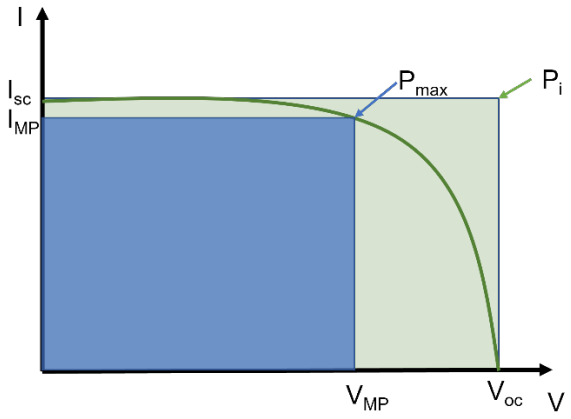

Figure 1.3 *Diagram for the fill factor of OSCs. I_{sc} is the short circuit current density, V_{oc} is the open circuit voltage, V_{MP} and I_{MP} are the voltage and current corresponding to the maximum power output (P_{max}).*

The fill factor is typically a measure of the efficiency of a solar photovoltaic, it can be measured by the ratio of the maximum combination of V_{MP} and I_{MP} to the product of the V_{oc} and I_{sc}, as displayed in equation 1.1.

$$FF = \frac{I_{MP} \times V_{MP}}{I_{sc} \times V_{oc}} \quad (1.1)$$

The fill factor of solar photovoltaic is usually about 80% for silicon cells,[13] and around 60-75% for OSCs.[14–17]

The power conversion efficiency (PCE) of photovoltaic is defined by the power density output at the operating condition against the incident power density, as shown in Equation 1.2.

$$PCE = \frac{I_{MP} \times V_{MP}}{P_{in}} = \frac{I_{sc} V_{oc} FF}{P_{in}} \quad (1.2)$$

With P_{in} the incident solar power, I_{sc} represents short circuit current, the current of a solar cell when voltage is zero. V_{oc} is open circuit voltage when current is zero. FF is the fill factor of solar cells. The current-voltage curve has shown all of the above parameters to show the device performance of solar cells, shown in Figure 1.3.

Organic solar cells fundamentally differ from conventional solar cells in the charge photogeneration process. π-conjugated polymers show a delocalized electron density along the conjugated chain length. As the chain lengths increase, the energy levels become closely spaced, resulting in a band structure of electron distribution.[18] As mentioned before, the initially photoexcitation generated excited state is named as Frenkel exciton state which shows as Columbic bound electron and hole, this is because of the relatively low dielectric constant of polymer (ε_r= 2 to 4). As shown in equation 1.3, the binding energy between the electron and hole is determined by the magnitude of dielectric constant: the smaller the dielectric constant, the higher Columbic binding force.

$$\mathrm{V} = \frac{\mathrm{e}^2}{4\pi \mathrm{r} \varepsilon_0 \varepsilon_\mathrm{r}} \quad (1.3)$$

Where V is the Columbic binding force between electron and hole, e is the charge of an electron, ε_r is the dielectric constant, ε_0 is the permittivity of vacuum, and r is the electron-hole separation distance. This binding energy in organic semiconductor are as large as 0.1 – 1 eV in comparison to the thermal energy k_BT at room temperature (0.025 eV). Thus, the strong binding energy stabilises the Frenkel excitons and results in a localised state. The localised

exciton formation is one of the reasons for the low PCE in organic solar cells in OSCs. In comparison to the conventional silicon solar cell, the dielectric constant of silicon is as large as $\varepsilon_r \sim 12$, resulting in weak binding energy between electron and hole.[19] Therefore, charge carriers in silicon based solar cells are immediately generated upon photoexcitation and easily transfer to the electrode contributing to electricity, resulting in a relatively high PCE.

For an ideal solar device, the Schockey-Queisser limit has shown the maximum efficiency for single junction solar device to be around 35% with only intrinsic energy loss.[20] They also expressed V_{oc} as a function of the energy bandgap (E_g) of the material, with $V_{oc}=E_g/q$ (q is the charge of electron). So far, the investigated organic solar cells are thus far away to reach the theoretical PCE of solar cells. As such, extensive research studies are aimed at overcoming the limitations of the current OSC systems.

1.4 Electronic structure of organic semiconductor

Organic semiconductors are commonly represented by the π conjugated small molecules and the π conjugated delocalised polymer composed of repeat units of oligomer. Homogenous organic semiconductors are made of carbon and hydrogen atoms, while heterogeneous types include nitrogen, sulphur and oxygen atoms.

1.4.1 MOs for organic materials

To understand the electronic structure of organic semiconductors, it is easier to get through the concept of molecular orbitals for small molecules. Molecular orbitals (MO) comprise the orbital overlap between the atomic orbitals (AO) of the adjacent atoms. A π conjugated system is based on an alternation between the single and double bonds, and the carbon AOs were under the sp^2 hybridisation showing with three sp^2 orbitals and one p_z orbital, as shown in Figure 1.4. The single bond is formed via two sp^2 orbital overlap in a head-to-head way, and the electron density is created along the axis named as the σ-bonding and the higher energy σ* anti-bonding. The double bond is created by the atomic p_z orbital, and the electron density is distributed above and below the axis of the adjacent carbon atoms. This type of orbital overlap is called the π-bonding and the higher energy π* anti-bonding. The heterogeneous atom, such as oxygen, also shows a pair of lone pairs that hardly interact with other orbitals, resulting in a non-bonding orbital (n).

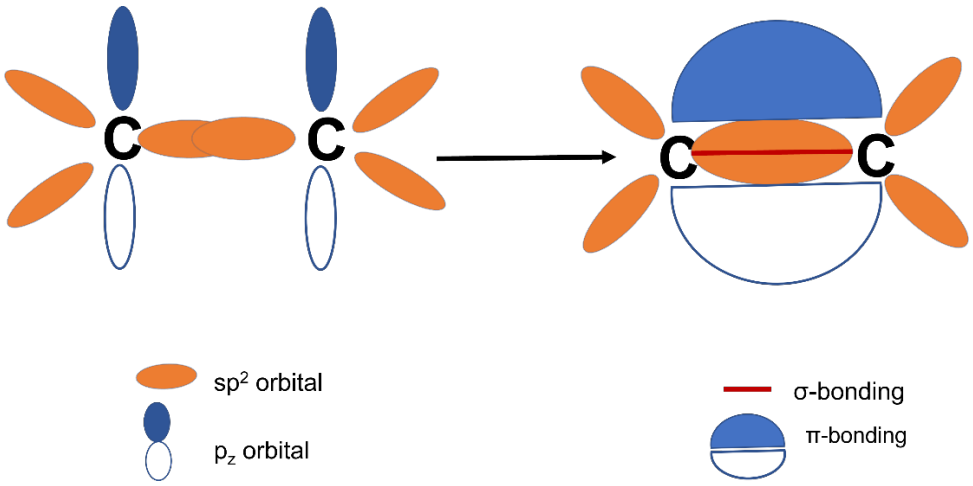

Figure 1.4 *Scheme for the AOs types in the π conjugated molecules, the formation of σ and π-bonding in adjacent carbon atoms.*

Conjugated polymer with a set of alternating single to double bonds, the backbone of it comprises a linear series of overlapping p_z orbitals and reduces the energy gap between adjacent MOs until it eventually become negligible and forms a cloud of delocalised electrons with a continuum energy. Therefore, the highest occupied molecular orbital (HOMO) and the lowest unoccupied molecular orbital (LUMO) can represent the MOs for large, conjugated molecules. The energy difference between the HOMO and LUMO is called the energy gap. Organic semiconductors generally show an energy gap of around 1.7 to 3 eV, corresponding to wavelengths between 400 nm to 700 nm.

Conjugated polymers are regarded as a semicrystalline material that shown with both crystalline and amorphous domains. The formation of the amorphous domain is due to high degree of branching or random linked polymer chains. Therefore, the delocalisation of electrons along the polymer chains can be divided into many segments by structural disorder. The interaction of the π electrons dictates the polymer's electronic structure and optical properties. In order to describe the state of electrons in conjugated polymer, a distribution of MOs can be represented as a state diagram, as shown in Figure 1.5.

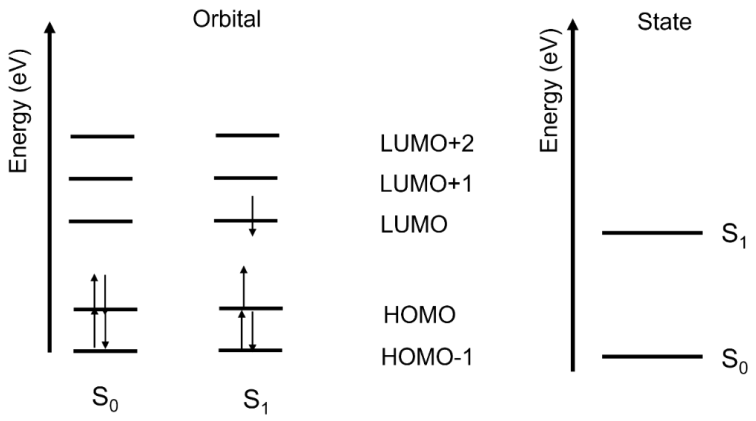

Figure 1.5 *Scheme shows the singlet ground state (S_0), and first (S_1) excited states in explanation with the electron configuration of their MOs. The HOMO and LUMO represented the highest occupied molecular orbital and lowest unoccupied orbital.*

1.4.2 Spin states in organic semiconductors

Organic semiconductors show conductivity because they have small spin-orbital coupling, allowing long-range spin coherence over time and distances longer than conventional metal semiconductors.[21] In quantum mechanics, spin is the inherent angular momentum of electrons. In the ground state, all spins are paired, thus termed as singlet ground state. However, upon excitation, the excited electron is in a different orbital. Thus, the spin configuration can change: the two electrons in the single occupied orbitals are either still paired (singlet) or parallel (triplet).

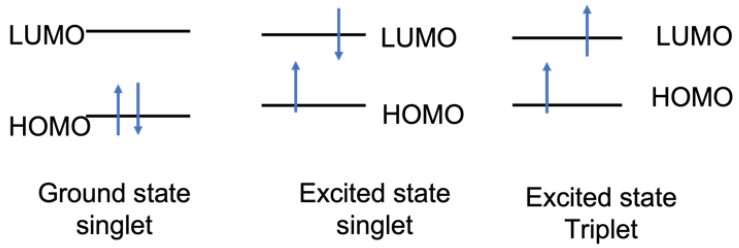

Figure 1.6 *shows the spin state for ground singlet, excited singlet, and triplet state.*

1.4.3 El Sayed's rule and Heavy atom effect

When a singlet state non-radiatively decays into a triplet state, that process is known as intersystem crossing (ISC). Conversely, a triplet transition to a singlet is named reverse ISC (rISC). Since ISC is forbidden by rules of conservation of angular momentum, ISC processes generally happen on longer timescales, e.g. behave 10^{-6} to 10^{-3} s. However, El Sayed's rule

describes that the rate of intersystem crossing is relatively large if the non-radiative transition involves a change of orbital type. This is because a change in orbital angular momentum compensates for the change in spin angular momentum. The allowed types of singlets to triplet transitions for organic materials, shown in Figure 1.7, could happen in crossing two kinds of transition, while the vertical transitions are formally forbidden.

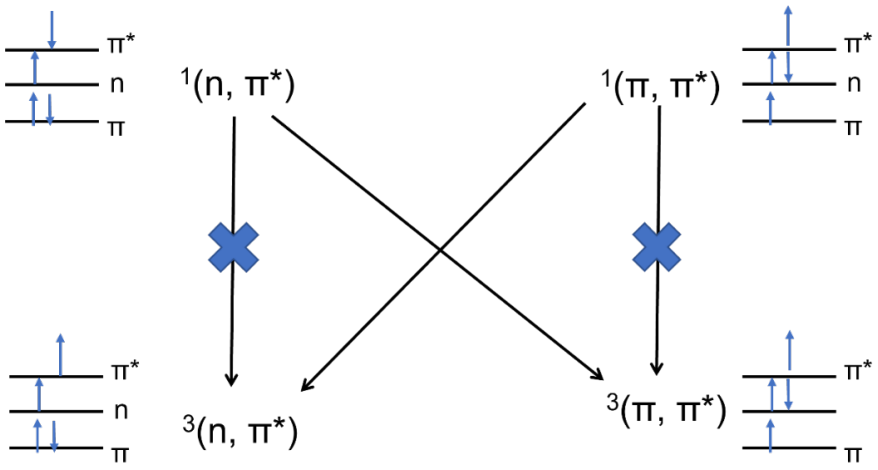

Figure 1.7 *Scheme illustrates the EI-Sayed rule as any change in the spin of an electron is compensated by a change in its orbital motion. The superscript number 1 is singlet, 3 is triplet. n or π is the paired of electrons excited from n or π orbital and π* represents the electron being excited to the π* orbital. The two-arrow pointing direction (state) is described as spin up and spin down.*

The ISC is most common in heavy atom molecules, like platinum porphyrin, zinc porphyrin; it increases the possibility for spin/orbital interaction and a change in spin is more favourable. The energy difference between S_1 and T_1 is also known as the singlet-triplet splitting energy ΔE_{ST}, as displayed in Figure **1.8**. The low band gap conjugated materials showing a smaller ΔE_{ST} could potentially result in rISC and thermally activated delayed fluorescence (as reported in pristine Y6 film)[22].

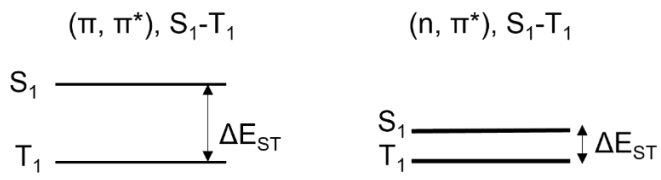

Figure 1.8 *Scheme shows the larger energy gap between the first excited singlet (S_1) and triplet states (T_1).*

1.5 Photophysics of organic solar cells

The device performance of OSCs is mainly controlled by the photophysical process of the excited states in terms of the mechanism aspect, which is mainly reflected in the generation of the excited state after photoexcitation and the subsequent decay processes. The fundamental principle of the excited states and the charge photogeneration process will be introduced in the following sections.

1.5.1 Exciton formation

Relatively higher device performance of OSCs can be achieved by additional electron deficient electron acceptors that create a driving force for exciton diffusion to the D/A interface and dissociate to free charge carriers. In the absence of exciton dissociation to free charge carriers, those localised excitons will undergo radiative or non-radiative decay, causing an energy loss process. For example, radiative decay includes the fluorescence and phosphorous processes, and the non-radiative decay processes: internal conversion and intersystem crossing. The driving force (ΔE) for electron transfer was defined as the energy difference between the LUMO level of electron D and A materials. For hole transfer, the D and A energy difference of the HOMO level, as shown in Figure 1.9. Since the close physical distance between electron D and A, the electron transfer process only results in a modest spatial separation between electron and hole around 0.5 to 1 nm.[23] At this spatial distance, the electron and hole are still loosely bound, named charge transfer state (CT state). Therefore, the driving force for electron transfer can also be represented by the energy difference between the singlet exciton state and the CT state.

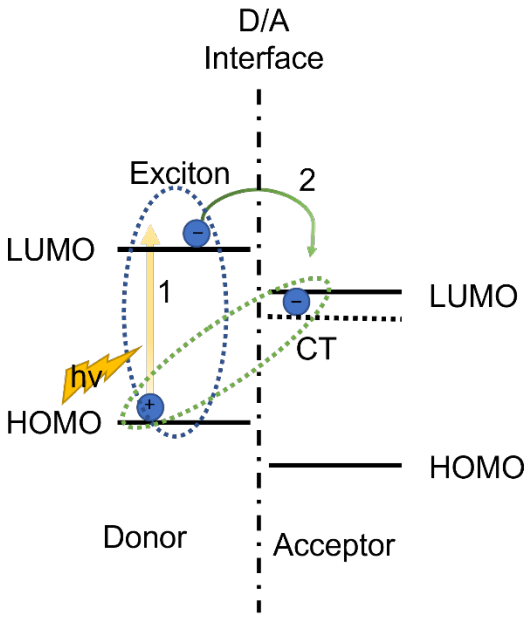

Figure 1.9 *Scheme for exciton generation after photoexcitation in electron D and A blend OSC. Light absorption (1) is greater or equal to the bandgap of the polymer, the electron from polymer donor is excited to the higher energy LUMO level and left with a hole in the ground state. The electron and hole are often called negative and positive polarons, including a charge and its reorganisation energy to the surroundings. The donor electron can then transfer to the lower energy LUMO level of the acceptor (2) due to the driving force for exciton diffusion and dissociation. The blue dash circle represents the Frenkel exciton, and the green dash circle is the CT state at the D/A interface.*

1.5.2 Exciton diffusion

As shown in Figure 1.10, the photogenerated localised exciton is initially formed in the pure D or A domain or both (depending on the excitation wavelength and the absorption cross-section of D and A molecules). The efficiency for exciton diffusion to the D/A interface is related to the exciton lifetime and strongly to the morphology of the bulk heterojunction blend, in terms of the domain size and purity. The possibility of exciton diffusion to the D/A interface can be characterised by exciton lifetime and diffusion length.[24] The longer exciton diffusion length represents that they have more chances to diffuse toward the D/A interface and dissociate into free charge carriers. The charge photogeneration process is competing with exciton decay back to the ground state. In other words, the longer exciton diffusion length means exciton is less likely radiative decay or non-radiative back to the ground state.

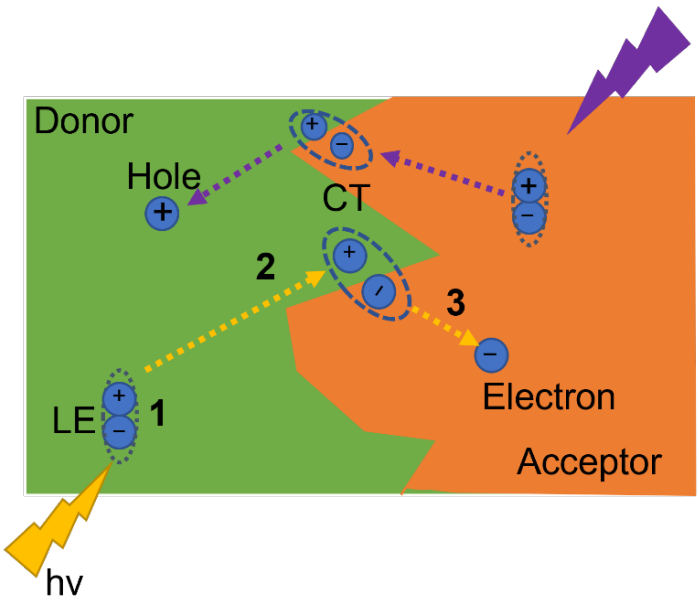

Figure 1.10 *Scheme to show the photogenerated excited state after light absorption in pure D, A domain and the D/A interface, including the localised Frenkel exciton (LE), charge transfer (CT) state, the free charge carries: electron and holes. (1) is the light absorption by donor or acceptor materials creating the strong bound electron and hole in bulk D or A domain. (2) exciton diffusion to the D/A interface, generating a CT state. (3) CT dissociation to form free charge carriers.*

The fully separated charge carriers with their surrounding structural distortion are polarons. Electron is defined as negative polarons; the hole is termed positive polarons.[25,26] Furthermore, since charge photogeneration is also determined by the driving force between D and A, it is necessary to optimise HOMO to LUMO energies in the D and A blend systems.

As mentioned in section 1.2, the electron deficient fullerene was used as a traditional electron acceptor to create a driving force with polymer for exciton diffusion and dissociation to free charges. The ideal morphology for a higher performance polymer:fullerene OSCs have been found with a bi-continuous network of D and A phases to increase interfacial area within the bulk heterojunction blend. The sufficient percolation pathways consisting of the bi-continuous network of D and A phases enable continuous electrons and holes being collected by the electrodes and minimise the charge back recombination. The typical exciton lifetime is in the range from ps to ns, and the exciton diffusion length around 5 nm to 20 nm was observed in polymer:fullerene blend systems.[27]

More recently, the emergence of NFAs further improved the PCE of OSCs with an even negligible or smaller driving force. Unlike the low absorption range of fullerene, NFAs show

the potential to absorb a wide range of light to near infrared. The exciton diffusion length in crystalline NFAs is reported to be around 20 to 47 nm, which is double the distance of the fullerene-based OSCs.[28] At the same time, a more rigid conjugated core structure is investigated in the high performance polymer:NFAs blends, which means a smaller energy disorder in the blend, facilitating the exciton dissociation and electron mobility. It should be noted that photogenerated exciton can be observed in both polymer D and NFA domains after light absorption; one of the reasons is because of the wide ground state absorption range for conjugated organic materials, as introduced in section 1.2.

1.5.3 Energy transfer

NFA exciton could also be observed in polymer:NFA blend systems via a non-radiative energy transfer process from the higher energy donor (D*) to the neutral acceptor (A) with the selectively polymer photoexcitation. Consequently, a higher energy A (A*) will be created along with a neutral D in the ground state. Generally, the energy transfer process can be classified into two categories: Förster resonant and Dexter energy transfer.

As shown in Figure 1.11, Förster resonant energy transfer (FRET) is based on dipole-dipole interactions, the oscillating dipole in D* induces an oscillating dipole in A. Since the conservation of energy, the reduced energy from D* to D is equal to the energy obtained by A to A*.

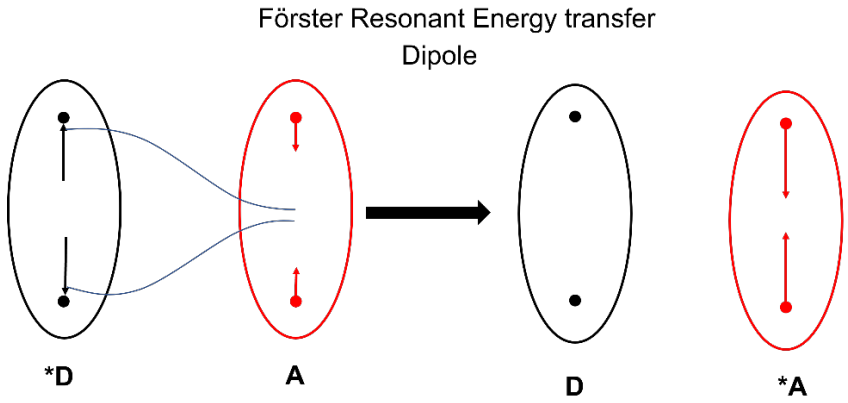

Figure 1.11 *Scheme for Förster resonant energy transfer, the circle represents the dipole of donor (D) and acceptor (A) of material, and the arrow's length and direction mean the dipole's strength. D* and A* are the higher energy D and A.*

This type of energy transfer is commonly regarded as a long-ranged (through space) transfer process, occurring when a donor emission spectrum significantly overlaps with the acceptor

absorption spectrum. It is normally observed with a D-A distance separation in the range of 1-10 nm.[29–31] The efficiency of FRET is determined by the distance between donor and acceptor as r^{-6}, it decreases dramatically as the distance between D and A increases, with the expression displayed in 1.4.

$$k_{FRET} = \frac{1}{\tau_D}\left(\frac{R_0}{r}\right)^6 \qquad (1.4)$$

Where k_{FRET} is the rate coefficient of Förster resonant energy transfer, τ_D is the lifetime of the donor. R_0 is the Förster radius which is the distance at energy transfer with 50% efficiency, and the Förster radius can be defined by equation 1.5.

$$R_0^6 = \frac{9\Phi_{PL}K^2}{128\pi^5 n^4} J_F \qquad (1.5)$$

Where Φ_{PL} is the photoluminescence quantum yield, K is an orientation factor to allow for the directional nature of the dipole-dipole interaction, n is the refractive index, and J_F is the Förster overlap integral between the photoluminescence spectra of the donor and absorption spectrum of the acceptor.

Dexter energy transfer models the exchange of electrons between electron D and A, and thus requires a significant molecular orbital overlapping between D and A. [32,30] It is regarded as short-ranged through the bond transfer process, in length scales less than 1 nm. As exhibited in Figure 1.12, when D* is in close contact with the A molecule, an excited state electron from the LUMO level of D* will be transferred to the LUMO level of A*; at the same time, a ground state electron from the HOMO level of A will be transferred to the HOMO level of D. In π-conjugated materials, delocalisation of electrons results in energy lowering as D* and A approach to each other, the distance and interaction between D and A causes a shift to lower energy states ($E_{D^*\text{-}A} > E_{D\text{-}A^*}$). The efficiency of Dexter energy transfer (k_D) is related exponentially to the distance separation between electrons D and A shown in equation 1.6.

$$k_D = KJ_D e^{\left(\frac{-2r}{L}\right)} \qquad (1.6)$$

Where K is a parameter related to specific orbital interaction, J_D is the dexter overlap integral between the emission spectrum of D and absorption spectrum of A, r is the separation distance between D and A, and L is the sum of van der Waals radii of D and A.

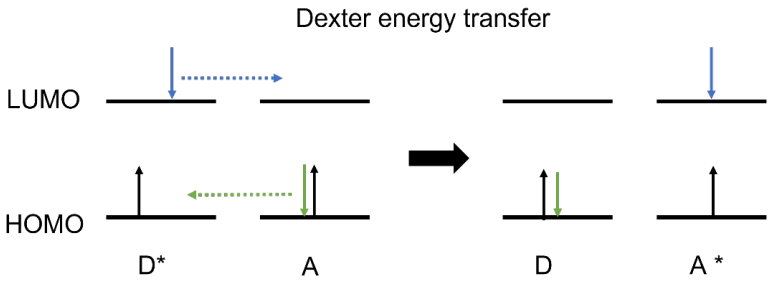

Figure 1.12 *Scheme for Dexter energy transfer enables the diffusion of triplet excitons. The horizontal lines are HOMO and LUMO energy levels of donor and acceptor materials. The dash arrows represent simultaneous rearrangement of the electronic configuration.*

Both FRET and Dexter energy transfer can occur for singlet excitons, as there is no change in spin multiplicity. However, for the triplet exciton, the highly possible energy transfer process is Dexter energy transfer because the change in spin multiplicity could couple to a change in angular momentum (T_D-T_A).[29,32–34] The triplet exciton diffusion length could exceed μm in certain conjugated polymer that is longer than singlet exciton. [46–48]

1.5.4 Electron transfer and Marcus Theory

When D and A phases are intimately mixed in the blend OSCs, excitons can be generated directly at the D/A interface, avoiding exciton diffusion. Electron transfer from high energy D to neutral A is another alternative way for charge photogeneration as opposed to energy transfer, resulting in positive (D^+) and negative (A^-) polarons, as shown in Figure 1.13. Such an electron transfer process can occur extremely rapidly on the femtosecond time scale. [35–37]

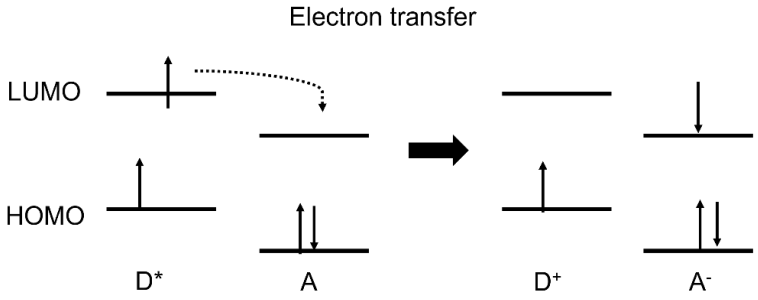

Figure 1.13 *Scheme for electron transfer from a higher energy electron donor (D*) to a neutral acceptor (A), resulting in a donor cation (D^+) and acceptor anion (A^-).*

Marcus theory is used to describe the electron transfer process in the D/A interface, and it was first reported in 1956[38], and has been successful applied to photoinduced charge transfer in the conjugated polymer blend.[39–42] The non-adiabatic electron transfer between the initial

and final state was represented by two intersecting potential energy curves as a function of the nucleus rearrangement, as illustrated in Figure 1.14. Born-Oppenheimer approximation states that electron motion occurs much more rapidly compared to nuclear motion, and nuclear configuration does not change during electronic transitions. The intersection points therefore represented the same molecular geometry and potential energy for the initial and final state. Marcus theory states that the electron transfer process is an activated process with activation barrier $\Delta G^{\ddagger}$ that could be expressed in terms of the Gibbs free energy ΔG^0 and the reorganisation energy λ, as illustrated in equation 1.7:

$$\Delta G^{\ddagger} = \frac{(\lambda + \Delta G^0)^2}{4\lambda} \qquad (1.7)$$

The reorganisation energy refers to the energy required for the reactant and surrounding medium to adopt the equilibrium geometry. The rate coefficient of electron transfer (k_{ET}) is determined by Fermi's Golden Rule that states k_{ET} is directly related to the perturbation matrix of the initial and final state. In other words, the rate of electron transfer can be investigated by comparing the magnitude of $-\Delta G^0$ to λ. The maximum k_{ET} can be obtained when $-\Delta G^0 = \lambda$ is the barrierless region. A Marcus invert region is defined as the $-\Delta G^0 > \lambda$, the undesired reverse recombination process to the ground states is highly activated.

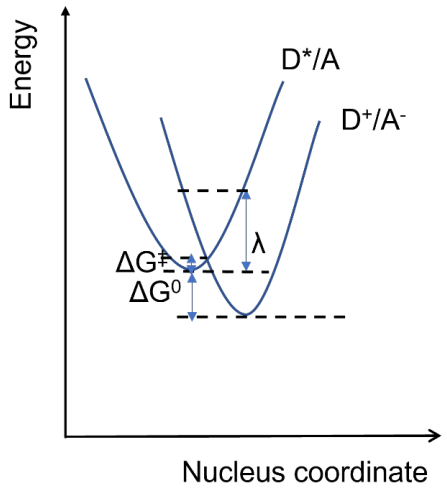

Figure 1.14 *Schematic to illustrate Marcus theory represented by the potential energy curves of the initial state (D*/A) and final state (D^+/A^-). $\Delta G^{\ddagger}$ is the activation barrier, ΔG^0 is the Gibbs free energy, and λ is the reorganisation energy.*

1.5.5 Exciton dissociation and charge separation

Figure 1.15 shows the photophysical process in electron D and A OSC blend systems. In polymer:fullerene blend system, the initially generated S_1 with higher energy can be quenched via a downhill electron transfer process from electron D to A, resulting in a formation of a hot charge transfer (CT) state (2) with excess thermal or vibronic energy as predicted by Onsager theory.[43] The primary generated hot CT state exist as the columbic electron-hole binding pair.[44] They can either sequentially thermal relax back to stable (localized) CT states or they can dissociate into free charge carriers (3) facilitated by the presence of delocalized states.[45–47] The efficiency of charge separation depends on the magnitude of thermalization length versus the Columbic capture radius. If the distance between electron and holes increase to escape the Columbic capture radius, the free charge carriers can be generated. Such charge separation process is driven by the energy offset between the E_g of donor/acceptor materials and the energy of CT state E_{CT}, (E_g-E_{CT}). The CT state can undergo rapid spin mixing between spin-singlet (^{1}CT) and spin-triplet (^{3}CT) state, due to weak electronic coupling, to form either ground state S_0 or triplet exciton T_1 via non-radiative geminate recombination. When CT states are dissociated into free charge (FC) carriers, not all of FC can be collected by respective electrodes to generate photocurrent. Some of the FCs do not originate from the same CT state, they will reform the bound CT state via non-geminate (bimolecular) charge back recombination.[48,49] Due to the spin-allowed transition, the ^{3}CT state can then decay to the lower energy T_1 via a back electron transfer.

An efficient charge separation could be observed in some polymer:NFA blends with small or negligible driving force. The photocurrent generation is not only relied on electron transfer but also on hole transfer. An ultrafast singlet energy transfer could occur from polymer singlet state to acceptor, proceeding the hole transfer from electron A to D, with the driving force referred to as energy difference in HOMO energy levels. Furthermore, as we introduced in section 1.5.2, a long exciton diffusion length has been observed in NFAs that reduces the requirement for fast interfacial charge transfer. The exciton lifetime plays a decisive role in charge separation efficiency in polymer:NFAs OSCs.[50] Several studies have reported that hybridization of exciton and CT states could occur in blend D/A systems with a small or negligible driving force.[51–53] Karuthedath et al.[54] pointed out that a minimum ionization potential (IP) offset of 0.5 eV is still necessary to ensure efficient NFA-based OSCs' charge

separation. The quadrupole moments observed in NFAs causes energy level bending at the D/A interface, which essentially increases the donor's ionisation energy and decreases the acceptor's electron affinity, causing an increase in the energy of CT states. The formation of this high energy CT state prevents efficient exciton to CT state conversion in low IP offset polymer: NFA blends.

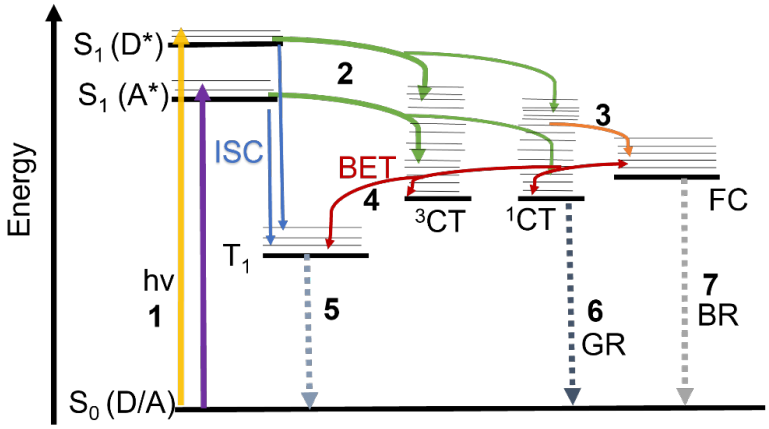

Figure 1.15 *Scheme to show the energy level diagram and summarise the main charge photogeneration process in bulk heterojunction organic solar cell, electron donor and acceptor materials. (1) hv: photoexcitation energy to generation singlet donor (D*) or acceptor (A*) excitons. (S_1) from the ground state S_0; ISC: intersystem crossing; T_1: Triplet state; (5) triplet decay via phosphorescence; (2) ^{1}CT&^{3}CT: singlet charge transfer state and triplet charge transfer states. (3) FC: fully dissociated charge-separated state. (4) BET: charge back recombination process. (6) GR: geminate recombination. (7) BR: bimolecular recombination.*

1.5.6 Charge recombination

The energy levels of the electron D and A are critical to ensure efficient exciton dissociation at the D/A interface.[19] Following with D or A electron transfer, two recombination pathways may compete with photocurrent generation, named geminate and bimolecular recombination.

1.5.6.1 Geminate recombination

Geminate recombination (GR) is referred as monomolecular decay process that obey first-order kinetics.[55] Such first-order kinetics are the decay rate of reaction is independent of the excitation density. Thus, the decay dynamics of excited species with a geminate recombination process are independent of the photoexcitation energy density. The mono-exponential decay shows a linear line on a log-linear scale, as shown in Equation 1.8.

$$\ln[A]_t = \ln[A]_0 - kt \qquad (1.8)$$

$[A]_t$ is concentration of the species at time t, $[A]_0$ is the initial concentration of the species at time zero and t is the lifetime.

Geminate recombination generally refers to recombination of a bound electron and hole in a CT state. However, GR also observed with two charges after escaping their coulombic attractive force but remained confined by the physical size of their respective domain. Such that each electron can only recombine with its original hole, this process is also named as GR.[19]

1.5.6.2 Bimolecular recombination

In contrast, bimolecular recombination describes second-order decay dynamics because of the combination of two fully separated charges not from the same CT state back to the ground state. It shows an excitation-dependent behaviour as the BR decay rate depends on the population of charges. BR competes with charge transport to the electrodes and negatively influences photocurrent generation. The recombination rate of GR compared to BR usually occurs on short timescales, e.g. within a few picoseconds.[56] Efficient organic solar cells require the separation distance between electrons and holes generated from excitons beyond the Coulombic capture distance (>5nm) to avoid rapid GR.

Pure second-order recombination is typically not found in the decay dynamics in organic solar cells because of the existence of trap states in the deeper density of states distribution. Since the conjugated system with random chain length and delocalisation properties are the components of OSCs, the HOMO or LUMO is described as the density of states distribution rather than a certain energy value. Instead of the second-order recombination, the decay dynamics of two charges are characteristic of bimolecular recombination, fitted by a power law, which shows the linear line on a log-log scale, as displayed in Equation 1.9.[57–59]

$$A \propto t^{-\alpha} \qquad (1.9)$$

t is time and α is the power law coefficient. The value of α gives indication of the energetic distribution of trap states. When the power law decay with α less than 1, it is characterised by the bimolecular recombination of trap carriers having an exponential tail of polaron trap states, named trap limited bimolecular recombination. When α is 1, the power law decay is pure bimolecular recombination. Alternatively, the charge density can be fitted to a stretched exponential decay and used to give information about the dispersion of the system,[60,61] as shown in Equation 1.10.

$$A_t = A_0 * \exp\left(-\frac{t}{\tau}\right)^{\beta} \qquad (1.10)$$

Where t is time, τ is the lifetime of transient species, and β is the stretched exponential factor. When β<1, it shows that there is more than one decay pathway for charge recombination. When β=1, this corresponds to truly mono-exponential decay kinetics. [62,63]

1.5.7 Triplet state

The decay rate of triplet states is shown to obey the first-order decay rate in the nanosecond to microsecond timescales (10^{-7}-10^{-3} s^{-1}). The presence of triplet state with state energy above the oxygen energy 0.98 eV can be demonstrated by the oxygen dependence transient absorption measurements, the higher energy triplet states could transfer their energy to the low energy oxygen, resulting in a triplet quenching.[64,65] It should be noted that the singlet oxygen state could also be produced as a by-product that harms cells and impairs signalling events.[66]

As shown in Figure 1.15, triplet state (T_1) can be created via several different ways, ISC or geminate recombination from CT state, or BR (charge back recombination) through a spin mixing of FCs. The spin mixing process occurring in OSCs is associated with the structure of organic materials. Since organic materials consists of light weights atoms, like carbon, oxygen, nitrogen, sulphur, oxygen, and hydrogen it shows a weak spin-orbital coupling, resulting in an inefficient transition between excitonic states of different spin multiplicity. Therefore, the triplet lifetimes are typically longer than the singlet states. For organic polymers, triplet exciton back transfer is only possible if the D triplet state energy is lower than that of the CT state (<0.1 eV), that is usually to be the case with singlet and triplet splitting energy (ΔE_{ST}) around 0.6 to 0.7 eV.[67]

In terms of fullerene-based OSCs, Benson-Smith et al.[68] reported that fullerene triplet was observed in polymers with high ionisation potential (IP) blending with fullerene films. The energy level of polaron was higher than fullerene triplet state in the polymer blend with high IP. Such fullerene triplet formation in the polymer:fullerene blend illustrated via energy transfer process from donor singlet exciton to acceptor, and this process can compete with the more desirable electron transfer process.[69] Dyer-Smith et al. [70] specifically demonstrated that triplet formation via energy transfer occurs in the blend polyfluorene with fullerene systems when the energy offset is around 1.6 eV between the HOMO level of donor and

LUMO level of acceptor. Meanwhile, they pointed out the triplet formation also shows strongly influenced by the morphology of the blend film, in competition with the exciton dissociation at the D/A interface.

Conventionally, triplet formation is regarded as OSCs' major energy loss process. Whether or not triplet state formation is related to spin mixing geminate or non-geminate recombination is still under debate. Dimitrov et al.[71] studied two closely related polymer-fullerene blend with polymer fluorination systems, they reported that triplet exciton was observed in the low device performance fluorination blend systems, which is formed through the spin mixing on nanosecond timescale of the initially generated bound polaron pairs.[72] They concluded that triplet exciton observation is associated with geminate recombination of bound polaron pairs. However, unlike fullerene triplets, polymer triplets show no limitations to the device performance in OSCs.[7374]Such triplet was observed in a polymer:fullerene (ICBA) blend system with polymer triplet level is much lower than either the polymer or fullerene singlet states, and fullerene triplet energy level is close to the CT state. Instead of the energy loss through the lowest energy level polymer triplet, non-radiative decay was observed via the fullerene triplet. It is suggested that the excited state recombination process was determined by the thermodynamics and kinetically controlled. Privitera et al[49] reported that the triplet formation on polymer:fullerene blend system is significantly created via the geminate recombination. This is because fullerene is known to be intercalated in the side chain of some polymers in the blend solar cell. The initially generated electron-hole pairs are deeply trapped to allow ISC to occur. A pure D and A domains are required to prevent triplet formation in polymer: fullerene blend films.

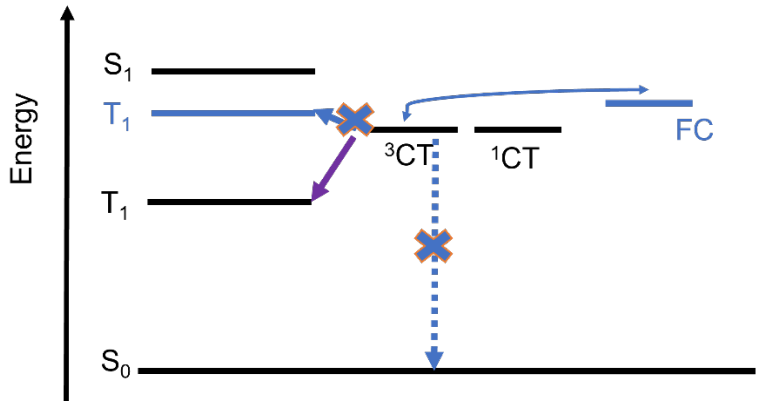

Figure 1.16 *Scheme illustrates the energetic state in OSCs, with a large ΔE_{ST} (black) and a small ΔE_{ST} (blue). Blend system with a large ΔE_{ST} shows a much lower T_1 state and the ^3CT could decay to the low energy T_1 state via geminate recombination. However, in the blend system with small ΔE_{ST}, the decay process for ^3CT to T_1 is forbidden and the long-lived ^3CT shows the possibility of recreating FC state. The extra yield of FC from CT state is beneficial for OSC device performance.*

Interestingly, the triplet formation has also been observed in high performance polymers with NFAs OSCs. Gillett et al. studied a series of polymers with NFAs and demonstrated that non-geminate NFA triplet formation occurs in preference to geminate triplet formation. For example, the Y6 triplet formation is observed in the high efficiency PM6:Y6 blend film. As shown in Figure 1.16, such non-geminate recombination could occur due to the energy level of the local T_1 being higher than ^3CT state, resulting in a thermodynamically forbidden decay process from ^3CT to T_1.[75] Instead, since the ^3CT exists with a longer lifetime (decay to ground state also forbidden), it can either rISC to ^1CT or re-dissociate into FCs.[76] The re-generation of FCs could contribute to the high performance device performance. Such non-geminate triplet is generally observed with a smaller ΔE_{ST} in either polymer or NFAs with a strong Intramolecular charge transfer (ICT) effect.[77,78] The ICT effect could raise the energy of the T_1 and the intermolecular CT state. Wang et al. reported the non-geminate triplet formation could be suppressed in a polymer blend with fluorinated IDIC-based NFA containing enhanced ICT effect. They found an enhanced charge carrier lifetime and improved device performance. The improved efficiency of OSCs was attributed to the lower energy level of the ^3CT and ^3LE than the T_1 in the blend film.[79]

1.6 Role of morphology to charge photogeneration.

The nanomorphology of the D/A blend films is the other critical factor for charge photogeneration. It has been reported photogenerated excited state shows different

interactions to the morphology of the blend films, in terms of the domain size, domain purity (composition of the mixed D/A domain) and degree of crystallinity. If the domain size is too large (aggregated), the limited exciton diffusion length could inhibit exciton diffusing to the D/A interface within the exciton lifetimes.[80] In contrast, if the domain size is too small, the physical charge separation domain size is smaller than the Columbic attractive radii, such that the electron-hole pair cannot escape Columbic attractive radii and decay via geminate recombination.[81] In addition, a high degree of bimolecular recombination could also occur between the FCs because of the intermixed D/A domain.[82] Thermal annealing, as reported, shows potential to enhance the crystallinity of the film and increase the phase segregation in the blend film. For the NFAs-based OSCs, excessive aggregation can be controlled by the side chain and crystallinity of the NFAs. The morphology of the blend NFAs film can be controlled by the twisted and bulky side chain of NFAs, and the planar core structure could also provide π-π stacking, facilitating electron or hole mobility. In consequence, controlling the morphology of the photoactive layer and optimal phase segregation could substantially improve the device performance of OSCs.

1.7 Development of Organic solar cell

1.7.1 polymer/fullerene solar cell

Historically, polymer-based bulk heterojunction organic solar cells have used polymers as electron donors and fullerene derivatives as electron acceptor materials. Fullerene derivatives have played a dominant role in electron acceptors in the last two decades because of their ball-like fully conjugated 3D structure, strongly facilitating charge delocalization and transport at the photoactive layer of organic solar cells.[83] A breakthrough of the OSC efficiency of 2.5% was reported by Shaheen et.al in 2001,[84] they realised the morphology of the blend films could affect the device performance. They studied the blend film of the polymer poly[2-methoxy-5-(3',7'-dimethyloctyloxy)-1,4-phenylenevinylene] (MDMO-PPV) and the fullerene acceptor $PC_{60}BM$ with two solvents containing different polarity. Later on, the new investment of crystalline polymer poly(3-hexythiophene-2,5-diyl) (P3HT) boosted the efficiency of organic solar devices to around 4.4%.[85] Yang et al. found that even better device performance can be achieved by controlling the morphology of the film, such as the thermal annealing conditions or evaporation speed of solvent during the film formation. As a consequence, the ideal morphology for the bulk heterojunction films should facilitate the

exciton dissociation, which can be represented by the large interpenetrating network between electron D and A materials.[86] Following these contributions, a range of polymer materials centred on the concept of heterojunction structures are the subject of widespread research. Over the past two decades, these fullerene-based systems have shown a rich library with the understanding of the polymer performance in OSC, and a steady growing efficiency was as higher to reach 12.1 % in 2017 with a ternary blend structure by two polymers and one fullerene acceptor PC70BM.[87] This efficiency is in the medium range of photovoltaics compared to the commercialised solar cell.

Besides the promising charge transport property, there are several serious drawbacks limiting the wide use of fullerene in organic devices. Since fullerene is based on the C_{60} molecule, it shows a spherical structure with high symmetry properties. Such symmetric property of fullerene means that only dipole-forbidden electronic states are found in the low excitation energy region, resulting in poor light absorption in the solar spectrum range.[88] The fixed energy-level tunability of fullerene also restricts the light-harvesting ability of the fullerene-based organic solar cells.[89,90] The lability of morphology and chemical stability of fullerenes also increase uncertainties in organic solar cells.[91] There are two or three phases in the photoactive layer of organic solar cells, including pure D or A phase and D/A interface. Such metastable morphology could degrade the blend films and provide charge species which undergo different recombination pathways, lowering the efficiency of OSCs.

1.7.2 Polymer/Non-fullerene solar cell

Rapid development of non-fullerene acceptors (NFA) has recently attracted more attention as an alternative to fullerene acceptors to boost the power conversion efficiency of OSCs. NFAs are versatile in comparison to fullerene acceptor. One advantage of the NFAs over fullerene is their easily tunable energy levels that allow NFA OSCs to achieve high V_{oc} than the conventional based OSCs. Moreover, NFAs can offer a better light absorption capability with a significantly higher extinction coefficient than fullerene acceptors. In addition, NFAs can absorb broad range of wavelengths to the near infrared with a small energy bandgap. Therefore, a higher J_{sc} can be achieved by combining the strong absorption capability and the wider absorption range. In addition, since there is a wide range of electron donor materials investigated for fullerene organic solar cells, it provides reasonable design strategies for immediate use in NFA organic solar cells. The proper chemical and electrical structure

matching in electron donor and acceptor materials also increase the chemical and morphological stability of NFA organic solar cells. The efficiency has reached 19% in a ternary device with the polymer D18 and NFAs Y6 and BS3TSe-4F under certain ratios.[92]

There are three main types of NFAs have been synthesized so far; one is the wide bandgap pyridine (PDI) oligomers with twisted and /or 3D structures. The other type comprises narrow bandgap small molecules based on linearly fused-ring acceptor-donor-acceptor (A-D-A) aromatic backbones with four side chains located on two sp^3 hybridised carbon atoms near the centre atoms, such as the indacenodithiophene (IDT) based molecules. The third type is named Y series acceptor with a A-DA'D-A structure. The DA'D core was represented as a ladder-type electron deficient central fused ring with benzothiadiazole fragment to fine tune its absorption and electron affinity.

As described early, Tang first made the relatively efficient OPV based on the bilayer structure of electron D and A material. He used a perylene tetracarboxydiimide (PDI) derivative as an electron acceptor that was the first NFA material used in heterojunction OPVs. In 2010, Sharma et al. modified the PDI acceptor with an extra bulky side chain that enhanced light absorption and improved the electron mobility. They reported that the efficiency of the OSC consisting of the polymer and PPI could reach to 3.17%. [93] Since the planar structure of the PDI and derivatives, the morphology of the blend films prefers to form aggregated NFAs domain that is harmful for exciton transfer and dissociation. With the learning from the structure of the fullerene acceptors, the 2D planar structure of PDI was transferred to a 3D-like twisted structure that highly provide chances for polymer and NFAs intercalated to each other. In 2013, Zhao et al. reported a twisted spirobifluorene PDI ($SF\text{-}PDI_2$) was blended with P3HT and the efficiency was reported of 2.35%. Although the efficiency was not high, it shows a dramatic suppression of the NFAs aggregation. In 2016, Liu et al. used the $SF\text{-}PDI_2$ acceptor to blend with a more suitable polymer donor P3TEA, and the efficiency was boosted to 9.5%.[94] The enhanced efficiency due to the twisted structure of PDI suggests that the intramolecular twisting should be minimised to enhance the charge transport capability of SMAs, provided that the degree of molecular aggregation is low enough to achieve a reasonable small domain size.

The linearly fused D-A-D NFA structure was inspired by the CN-PPV acceptor, which was reported in pioneering work in BHJ OPVs.[95] This acceptor shows electrons can be delocalised effectively along the conjugated backbone of CN-PPV. Hall *et al.* reported this is because of the functional group of CN with strong electron negativity. A significant milestone in NFA-based OSCs development was made by Zhan et al. in 2015. [96] They reported a high performing fused-ring electron acceptor (FREA) named ITIC blended with the polymer PTB7-Th showing a power conversion efficiency to 6.8%. At the same time, they also studied the fullerene blend PTB7-Th with PC60BM, showing a slightly higher device in the NFA blend. They reported that the optimized device performance with NFA was due to the reasonably good morphology with suppressed NFA aggregation. The key is the unique ITIC structure with a fused core unit indacenodithieno[3,2-b]thiophene (IDTT) possesses four out-of-plane 4-hexyphenyl side chains. These bulky side chains are not only facilitating the solubility but also prevent the self-aggregation of ITIC. At the same time, the end group 1,1-dicyanomethylene-3-indanone (IC) of ITIC shows a good π-π stacking which accelerate the electron transfer rate.

The improvement of the NFA OSCs device performance has been achieved based on the effectively tunable NFA energy level, optical properties, solubility, crystallinity and electron mobility, which can be controlled by the structure of A-D-A type molecules. The fused-ring core, end group unit and side chain are three structural features that manipulate the intramolecular charge transfer (ICT) effect. In the following year 2016, Li et al.[97] reported an enhanced device performance of 12.1 % was found in the blend system ITIC-M with the polymer PBDB-T. In comparison to the ITIC, ITIC-M shows a larger energy bandgap with an increase in the lowest unoccupied molecular orbitals (LUMO) than ITIC, incorporating electron donating groups like methyl or methoxy into the end-capping units of the ITIC. In 2017, Zhao et al. reported a 12.1% NFA OPV device performance based on the polymer donor FTAZ and the NFA ITIC-Th.[98] In contrast, ITIC-Th shows with a smaller bandgap and a decrease in the LUMO than the ITIC, by incorporating 5-hexylthiophenyl side chains. The easy planarization of the sulfur (S) atom and the S-S intermolecular interaction helps the electron transfer rate. The resulting smaller energy bandgap of ITIC-Th shows a red shift absorption with improved light absorption property and molecular extinction coefficient. In addition, Hou et al. have reported that the LUMO level of ITIC can be further reduced by the electron-deficient functional atom fluorine (F) to the end-capped units. They obtained a further

improved device efficiency to 13.1% with a blended system of NFAs named ITIC-4F to the polymer PBDB-T-SF (also named PM6).[99] Because of the strong electron-pulling effect on the end groups, the intramolecular interaction was enhanced in ITIC-4F. Therefore, an enhanced near-infrared absorption was observed for ITIC-4F. Compared to the ITIC, ITIC-4F consisting of the extra electron deficient end group shows strong and broad absorption but also helps the π-π stacking with electron D polymer. The crystalline D/A mixed domain facilitates exciton dissociation and electron mobility. It should be noted that the electron-rich IDT core in ITIC-related NFAs was not involved in the π-π stacking as the steric hindrance by the surrounded bulky side chains. Later, the intramolecular push-pulling effect was applied to other NFAs and with properly matching with the energy level to the polymer, a PCE up to 16.6% was observed in a single junction OSC blending PM6 with the ITIC type NFAs M32[100], and 17.4% PCE was obtained in a tandem OSC with polymer PTB7-Th and fullerene $PC_{60}BM$ and a NFA O6T-4F.[101]

The emergence of Y series acceptors has further promoted the development of OSCs. In early 2019, Zhou et al firstly reported the NFA Y6, and the single junction OSC consisting with the polymer PM6 with Y6 could reach the PCE to 15.7%.[102] One year later, Ding et al reported an improved PCE reach to 18.2% observed in Y6 blend with the polymer D18 for single junction.[103] One of the reasons for the high device performance of Y6 with polymer could be attributed to its unique twisted chain structure that helps compatibility of Y6 with different polymer donor materials, and increase the solubility. The twisted chain structure of Y6 was found closely affected by its four side chains. Two of the side chains were attached to the inside pyrrole rings and the two attached at the outside thiophene rings. Due to the steric hindrance between the inside chains, the molecular structure of Y6 shows a certain degree of twisted and the two inside chains are far apart. In 2020, Yao et al reported an optimized Y6 correlated NFAs named BTP-eC9. It shows a slightly enhanced device performance with the polymer PM6 to 17.8%.[104] The modification of BTP-eC9 was based on the structure Y6 but with optimized side chains by inducing chlorine atoms and elongated the inside chain from ethylhexyl to butyloctyl and shorted the outside chain from undercyl to nonyl. The modified side chain in BTP-eC9 suggests a more ordered intermolecular packing that facilitating the electron mobility.

With the new investigation for the structure to property in either ITIC or Y6 and their derivatives, the OPV device performance can become more efficient, cost effective and versatile. Before the potential benefits of the OPVs can be realized, significant advantages must be taken to better understand the fundamentals of the electron D organic semiconductors and the NFAs which enable further development of this technology.

1.8 Aims of this Thesis

Solution processable OSCs have attracted considerable attention in recent years with rapid device efficiency. The improvement is largely a consequence of newly designed NFAs, providing a series of options to match with electron donor polymer and covering a broader spectral range than the fullerenes.

This thesis aims to study the charge and triplet photogeneration and the effect of nanomorphology in fullerene and non-fullerene based OSCs. The studied NFAs consist of ITIC-based and Y series materials. Triplet states are traditionally considered harmful for device stability and performance, but their recent discovery in high-performing NFA OSCs brings their exact role in device performance into question. Furthermore, charge photogeneration mechanisms in NFA OSC blends are still not fully understood, this thesis aims to address some of the unexplored issues in longer timescale range.

In the first results chapter, chapter 3, charge photogeneration is explored in an efficient polymer: fullerene blend film where the donor polymer plays an important role in controlling the blend morphology. Bimodal polarons are generated in polymer-dominated domains and mixed domains influenced by fullerene induced ordering. In addition, polymer triplet formation was identified for the first time in this high-performing system via charge back recombination.

With the understanding of the photophysical process of PffBT4T-based polymer in fullerene blend systems, a subsequent study was carried out to study charge photogeneration and the morphology effect in PffBT4T-C9C13 blending with ITIC and Y series NFAs. Chapter 4 studied charge photogeneration in polymer blends with five different NFAs. Triplet states are detected in three of the studied systems and one of these blend films show the highest charge population. The reason for that is attributed to the dissociation of interfacial states to form

charges compete with triplet states formation. Charge photogeneration yields are explained in terms of morphology and triplet formation of each blend film.

Chapter 5 focus on the charge photogeneration in polymer PM6 and three PDI related NFAs with A-DA'D-A structure. A high fill factor and small voltage loss was observed in PM6 with two of the PDI related NFAs. It is valuable to study the correlation between the charge photogeneration with the strong phase segregation PDI related films to explore photophysical mechanism behind such blend system.

1.9 References

1 B. Franta, *Env Polit*, 2021, **30**, 663–668.

2 M. B. Hayat, D. Ali, K. C. Monyake, L. Alagha and N. Ahmed, *Int J Energy Res*, 2019, **43**, 1049–1067.

3 K. Ardani, P. Denholm, T. Mai, R. Margolis, T. Silverman and J. Zuboy, *Solar Futures Study*, 2035.

4 M. C. Scharber, D. Mühlbacher, M. Koppe, P. Denk, C. Waldauf, A. J. Heeger and C. J. Brabec, *Advanced Materials*, 2006, **18**, 789–794.

5 A.E. Becquerel, *Compt. Rend. Acad. Sci.*1839, **9**, 561

6 A. Pochettino, *Acad. Lincei Rend.* 1906, **15**, 355.

7 C. W. Tang and A. C. Albrecht, *J Chem Phys*, 1975, **62**,2139–2149.

8 B. Hideki Shirakawa, E. J. Louis, A. G. Macdiarmid, C. H. W A N K Chiang, *J. chem. Soc, Chem. Commun* 1977, **2**, 578-580.

9 C. W. Tang, *Appl Phys Lett*, 1986, **48**, 183–185.

10 C. Deibel and V. Dyakonov, *Reports on Progress in Physics*, 2010, **73**, 096401.

11 G. Yu, K. Pakbaz, C. Zhang and A. J. Heeger, *Molecular Crystals and Liquid Crystals Science and Technology. Section A. Molecular Crystals and Liquid Crystals*, 1994, **256**, 543–548.

12 W. Shockley and H. J. Queisser, *J Appl Phys*, 1961, **32**, 510–519.

13 X. Guo, N. Zhou, S. J. Lou, J. Smith, D. B. Tice, J. W. Hennek, R. P. Ortiz, J. T. L. Navarrete, S. Li, J. Strzalka, L. X. Chen, R. P. H. Chang, A. Facchetti and T. J. Marks, *Nat Photonics*, 2013, **7**, 825–833.

14 A. de Sio, F. Troiani, M. Maiuri, J. Réhault, E. Sommer, J. Lim, S. F. Huelga, M. B. Plenio, C. A. Rozzi, G. Cerullo, E. Molinari and C. Lienau, *Nat Commun*, 2016, **7**, 13742.

15 K. Wang, H. Chen, J. Zhang, Y. Zou and Y. Yang, *Journal of Physical Chemistry Letters*, 2021, **12**, 3928–3933.

16 J. L. Wang, K. K. Liu, J. Yan, Z. Wu, F. Liu, F. Xiao, Z. F. Chang, H. Bin Wu, Y. Cao and T. P. Russell, *J Am Chem Soc*, 2016, **138**, 7687–7697.

17 K. Sun, Z. Xiao, S. Lu, W. Zajaczkowski, W. Pisula, E. Hanssen, J. M. White, R. M. Williamson, J. Subbiah, J. Ouyang, A. B. Holmes, W. W. H. Wong and D. J. Jones, *Nat Commun*, 2015, **6**, 6013.

18 C C. H. Lee, G. Yu, D. Moses and A. J. Heeger, *Picosecond transient photoconductivity in poly(p-phenylenevinylene)*,1994, **49**, 2396.

19 T. M. Clarke and J. R. Durrant, *Chem Rev*, 2010, **110**, 6736–6767.

20 H. J. Queisser, *Mater Sci Eng B Solid State Mater Adv Technol*, 2009, **159–160**, 322–328.

21 T. Saito, T. Nishimura, J. Y. Yoon, J. Kölzer, D. Iizasa, M. Kammermeier, T. Schäpers, J. Nitta and M. Kohda, *Phys Rev Res,*2022, **4**, 043217.

22 S. I. Natsuda, Y. Sakamoto, T. Takeyama, R. Shirouchi, T. Saito, Y. Tamai and H. Ohkita, *Journal of Physical Chemistry C*, 2021, **125**, 20806–20813.

23 T. Richards, M. Bird and H. Sirringhaus, *Journal of Chemical Physics*, 2008, **128**,234905.

24 C. J. Brabec and J. R. Durrant, *Solution-Processed Organic Solar Cells*, 2008,**33**, 670-675.

25 J. L. Brédas, J. E. Norton, J. Cornil and V. Coropceanu, *Acc Chem Res*, 2009, **42**, 1691–1699.

26 F. Piersimoni, D. Cheyns, K. Vandewal, J. V. Manca and B. P. Rand, *Journal of Physical Chemistry Letters*, 2012, **3**, 2064–2068.

27 J. L. Brédas, J. Cornil and A. J. Heeger, *Advanced Materials*, 1996, **8**, 447–452.

28 Y. Firdaus, V. M. le Corre, S. Karuthedath, W. Liu, A. Markina, W. Huang, S. Chattopadhyay, M. M. Nahid, M. I. Nugraha, Y. Lin, A. Seitkhan, A. Basu, W. Zhang, I. McCulloch, H. Ade, J. Labram, F. Laquai, D. Andrienko, L. J. A. Koster and T. D. Anthopoulos, *Nat Commun*,2020, **11**, 5220.

29 W. A. Luhman and R. J. Holmes, *Adv Funct Mater*, 2011, **21**, 764–771.

30 G. D. Scholes, *Annu Rev Phys Chem*, 2003, **54**, 57–87.

31 R. Koeppe and N. S. Sariciftci, *Photochemical and Photobiological Sciences*, 2006, **5**, 1122–1131.

32 D. L. Dexter, *J Chem Phys*, 1953, **21**, 836–850.

33 X. Gong, S. H. Lim, J. C. Ostrowski, D. Moses, C. J. Bardeen and G. C. Bazan, *J Appl Phys*, 2004, **95**, 948–953.

34 T. Richards, M. Bird and H. Sirringhaus, *Journal of Chemical Physics*, 2008, **128**, 234905.

35 C. J. Brabec, G. Zerza, G. Cerullo, S. de Silvestri, S. Luzzati, J. C. Hummelen and S. Sariciftci, *Chemical Physics Letters,* 2001, **340**, 232-236.

36 A. A. Bakulin, D. S. Martyanov, D. Y. Paraschuk, M. S. Pshenichnikov and P. H. M. Van Loosdrecht, *Journal of Physical Chemistry B*, 2008, **112**, 13730–13737.

37 B. Kraabel, C. H. Lee, D. McBranch, D. Moses, N. S. Sariciftci and A. J. Heeger, *Chem Phys Lett*, 1993, **213**, 389–394.

38 R. A. Marcus, *J Chem. Phys*. 1956, **24**, 966

39 G. Zhou, M. Zhang, Z. Chen, J. Zhang, L. Zhan, S. Li, L. Zhu, Z. Wang, X. Zhu, H. Chen, L. Wang, F. Liu and H. Zhu, *ACS Energy Lett*, 2021, **6**, 2971–2981.

40 Y. Zhong, M. Causa', G. J. Moore, P. Krauspe, B. Xiao, F. Günther, J. Kublitski, R. Shivhare, J. Benduhn, E. BarOr, S. Mukherjee, K. M. Yallum, J. Réhault, S. C. B. Mannsfeld, D. Neher, L. J. Richter, D. M. DeLongchamp, F. Ortmann, K. Vandewal, E. Zhou and N. Banerji, *Nat Commun*, 2020, **11**, 833

41 O. Kwon, V. Coropceanu, N. E. Gruhn, J. C. Durivage, J. G. Laquindanum, H. E. Katz, J. Cornil and J. L. Brédas, *Journal of Chemical Physics*, 2004, **120**, 8186–8194.

42 Y. X. Liu, M. A. Summers, S. R. Scully and M. D. McGehee, *J Appl Phys*, 2006, **99**, 093521

43 G. Jaffe and H Zanstra, *Onsager*, P. Langevin, 1932, **39**, 12.

44 J. Lee, K. Vandewal, S. R. Yost, M. E. Bahlke, L. Goris, M. A. Baldo, J. V. Manca and T. Van Voorhis, *J Am Chem Soc*, 2010, **132**, 11878–11880.

45 A. A. Bakulin, A. Rao, V. G. Pavelyev, P. H. M. van Loosdrecht, M. S. Pshenichnikov, D. Niedzialek, J. Cornil, D. Beljonne and R. H. Friend, *Science (1979)*, 2012, **335**, 1340–1344.

46 D. Liraz and N. Tessler, *Chemical Physics Reviews*, 2022, **3**, 031305.

47 B. Bernardo, D. Cheyns, B. Verreet, R. D. Schaller, B. P. Rand and N. C. Giebink, *Nat Commun*, 2014, **5**, 3245

48 A. J. Gillett, A. Privitera, R. Dilmurat, A. Karki, D. Qian, A. Pershin, G. Londi, W. K. Myers, J. Lee, J. Yuan, S. J. Ko, M. K. Riede, F. Gao, G. C. Bazan, A. Rao, T. Q. Nguyen, D. Beljonne and R. H. Friend, *Nature*, 2021, **597**, 666–671.

49 A. Privitera, J. Grüne, A. Karki, W. K. Myers, V. Dyakonov, T. Q. Nguyen, M. K. Riede, R. H. Friend, A. Sperlich and A. J. Gillett, *Adv Energy Mater*,2022, **12**, 2103944.

50 A. Classen, C. L. Chochos, L. Lüer, V. G. Gregoriou, J. Wortmann, A. Osvet, K. Forberich, I. McCulloch, T. Heumüller and C. J. Brabec, *Nat Energy*, 2020, **5**, 711–719.

51 F. D. Eisner, M. Azzouzi, Z. Fei, X. Hou, T. D. Anthopoulos, T. J. S. Dennis, M. Heeney and J. Nelson, *J Am Chem Soc*, 2019, **141**, 6362–6374.

52 T. F. Hinrichsen, C. C. S. Chan, C. Ma, D. Paleček, A. Gillett, S. Chen, X. Zou, G. Zhang, H. L. Yip, K. S. Wong, R. H. Friend, H. Yan, A. Rao and P. C. Y. Chow, *Nat Commun*, 2020, **11**, 5617

53 D. Qian, Z. Zheng, H. Yao, W. Tress, T. R. Hopper, S. Chen, S. Li, J. Liu, S. Chen, J. Zhang, X. K. Liu, B. Gao, L. Ouyang, Y. Jin, G. Pozina, I. A. Buyanova, W. M. Chen, O. Inganäs, V. Coropceanu, J. L. Bredas, H. Yan, J. Hou, F. Zhang, A. A. Bakulin and F. Gao, *Nat Mater*, 2018, **17**, 703–709.

54 S. Karuthedath, J. Gorenflot, Y. Firdaus, N. Chaturvedi, C. S. P. De Castro, G. T. Harrison, J. I. Khan, A. Markina, A. H. Balawi, T. A. Dela Peña, W. Liu, R. Z. Liang, A. Sharma, S. H. K. Paleti, W. Zhang, Y. Lin, E. Alarousu, D. H. Anjum, P. M. Beaujuge, S. De Wolf, I. McCulloch, T. D. Anthopoulos, D. Baran, D. Andrienko and F. Laquai, *Nat Mater*, 2021, **20**, 378–384.

55 I. Montanari, A. F. Nogueira, J. Nelson, J. R. Durrant, C. Winder, M. A. Loi, N. S. Sariciftci and C. Brabec, *Appl Phys Lett*, 2002, **81**, 3001–3003.

56 T. Hahn, S. Tscheuschner, F. J. Kahle, M. Reichenberger, S. Athanasopoulos, C. Saller, G. C. Bazan, T. Q. Nguyen, P. Strohriegl, H. Bässler and A. Köhler, *Adv Funct Mater*, 2017, **27**, 1604906.

57 S. Ryu, N. Y. Ha, Y. H. Ahn, J. Y. Park and S. Lee, *Sci Rep*, 2021, **11**, 16781

58 Y. Liu, K. Zojer, B. Lassen, J. Kjelstrup-Hansen, H. G. Rubahn and M. Madsen, *Journal of Physical Chemistry C*, 2015, **119**, 26588–26597.

59 C. G. Shuttle, B. O'Regan, A. M. Ballantyne, J. Nelson, D. D. C. Bradley and J. R. Durrant, *Phys Rev B Condens Matter Mater Phys*, 2008, **78**, 1–4.

60 J. Nelson, *Phys Rev B Condens Matter Mater Phys*, 1999, **59**, 15374–15380.

61 J. Guo, J. M. Marin-Beloqui and T. M. Clarke, *JPhys Materials*, 2021, **4**, 1–12.

62 C. Fŕy, B. Racine, D. Vaufrey, H. Doyeux and S. Cińa, *Appl Phys Lett*, 2005, **87**, 1–3.

63 K. C. Benny Lee, J. Siegel, S. E. D. Webb, S. Lévêque-Fort, M. J. Cole, R. Jones, K. Dowling, M. J. Lever and P. M. W. French, *Biophys J*, 2001, **81**, 1265–1274.

64 F. Willrinson, 1997, **69**, 851-858

65 F. Wilkinson and A. A. Abdel-Shafi, 1997, **101**, 30

66 L. Mattsson Hultén, M. Holmstr and B. Soussi, 1999, **27**, 1203-1207.

67 A. Köhler and H. Bässler, *Materials Science and Engineering: R: Reports*, 2009, **66**, 71–109.

68 J. J. Benson-Smith, L. Goris, K. Vandewal, K. Haenen, J. V. Manca, D. Vanderzande, D. D. C. Bradley and J. Nelson, *Adv Funct Mater*, 2007, **17**, 451–457.

69 J. J. M. Halls, J. Cornil, D. A. dos Santos, D.-H. Hwang, A. B. Holmes, J. L. Bré and R. H. Friend, *Phys Rev B*, 1999, **60**, 5721

70 C. Dyer-Smith, L. X. Reynolds, A. Bruno, D. D. C. Bradley, S. A. Hoque and J. Nelson, *Adv Funct Mater*, 2010, **20**, 2701–2708.

71 S. D. Dimitrov, S. Wheeler, D. Niedzialek, B. C. Schroeder, H. Utzat, J. M. Frost, J. Yao, A. Gillett, P. S. Tuladhar, I. McCulloch, J. Nelson and J. R. Durrant, *Nat Commun*, 2015, **6**, 6501

72 P. C. Y. Chow, S. Albert-Seifried, S. Gélinas and R. H. Friend, *Advanced Materials*, 2014, **26**, 4851–4854.

73 C. W. Schlenker, K. S. Chen, H. L. Yip, C. Z. Li, L. R. Bradshaw, S. T. Ochsenbein, F. Ding, X. S. Li, D. R. Gamelin, A. K. Y. Jen and D. S. Ginger, *J Am Chem Soc*, 2012, **134**, 19661–19668.

74 S. Karuthedath, J. Gorenflot, A. Melianas, Z. Kan, M. Kemerink and F. Laquai, *Journal of Physical Chemistry Letters*, 2020, **11**, 2838–2845.

75 D. Veldman, S. C. J. Meskers and R. A. J. Janssen, *Adv Funct Mater*, 2009, **19**, 1939–1948.

76 W. Chang, D. N. Congreve, E. Hontz, M. E. Bahlke, D. P. McMahon, S. Reineke, T. C. Wu, V. Bulović, T. van Voorhis and M. A. Baldo, *Nat Commun*, 2015, **6**, 6415

77 M. S. Kotova, G. Londi, J. Junker, S. Dietz, A. Privitera, K. Tvingstedt, D. Beljonne, A. Sperlich and V. Dyakonov, *Mater Horiz*, 2020, **7**, 1641–1649.

78 L. Yang, W. Gu, L. Lv, Y. Chen, Y. Yang, P. Ye, J. Wu, L. Hong, A. Peng and H. Huang, *Angewandte Chemie*, 2018, **130**, 1108–1114.

79 R. Wang, C. Zhang, Q. Li, Z. Zhang, X. Wang and M. Xiao, *J Am Chem Soc*, 2020, **142**, 12751–12759.

80 R. Adel, E. Gala, M. J. Alonso-Navarro, E. Gutierrez-Fernandez, J. Martín, M. Stella, E. Martinez-Ferrero, A. De La Peña, A. Harbuzaru, M. M. Ramos, R. P. Ortiz, J. L. Segura and M. Campoy-Quiles, *J Mater Chem C Mater*, 2022, **10**, 1698–1710.

81 A. Yazmaciyan, M. Stolterfoht, P. L. Burn, Q. Lin, P. Meredith and A. Armin, *Adv Energy Mater*, 2018, **8**, 1703339

82 P. Westacott, J. R. Tumbleston, S. Shoaee, S. Fearn, J. H. Bannock, J. B. Gilchrist, S. Heutz, J. Demello, M. Heeney, H. Ade, J. Durrant, D. S. McPhail and N. Stingelin, *Energy Environ Sci*, 2013, **6**, 2756–2764.

83 N. S. Sariciftci, L. Smilowitz, A. J. Heeger and F. Wudl, *Synthetic Metals*, 1993, **59**, 333-352

84 S. E. Shaheen, C. J. Brabec, N. S. Sariciftci, F. Padinger, T. Fromherz and J. C. Hummelen, *Appl Phys Lett*, 2001, **78**, 841–843.

85 G. Li, V. Shrotriya, J. Huang, Y. Yao, T. Moriarty, K. Emery and Y. Yang, *Nat Mater*, 2005, **4**, 864–868.

86 M. Reyes-Reyes, K. Kim and D. L. Carroll, *Appl Phys Lett*, 2005, **87**, 083506

87 T. Kumari, S. M. Lee, S. H. Kang, S. Chen and C. Yang, *Energy Environ Sci*, 2017, **10**, 258–265.

88 G. Li, C. W. Chu, V. Shrotriya, J. Huang and Y. Yang, *Appl Phys Lett*, 2005, **86**, 253503.

89 Y. He, H.-Y. Chen, J. Hou and Y. Li, *J Am Chem Soc*, 2010, **132**, 1377–1382.

90 P. P. Shanbogh and N. G. Sundaram, *Resonance*, 2015, **20**, 123–135.

91 P. Cheng and X. Zhan, *Chem Soc Rev*, 2016, 45, 2544–2582.

92 W. Gao, F. Qi, Z. Peng, F. R. Lin, K. Jiang, C. Zhong, W. Kaminsky, Z. Guan, C. S. Lee, T. J. Marks, H. Ade and A. K. Y. Jen, *Advanced Materials*, 2022, **34**, 1–11.

93 G. D. Sharma, P. Suresh, J. A. Mikroyannidis and M. M. Stylianakis, *J Mater Chem*, 2010, **20**, 561–567.

94 J. Liu, S. Chen, D. Qian, B. Gautam, G. Yang, J. Zhao, J. Bergqvist, F. Zhang, W. Ma, H. Ade, O. Inganäs, K. Gundogdu, F. Gao and H. Yan, *Nat Energy*, 2016, **1**, 16089.

95 S. M. Walker, *Carolrhoda Books*, 2005.

96 Y. Lin, J. Wang, Z. G. Zhang, H. Bai, Y. Li, D. Zhu and X. Zhan, *Advanced Materials*, 2015, **27**, 1170–1174.

97 S. Li, L. Ye, W. Zhao, S. Zhang, S. Mukherjee, H. Ade and J. Hou, *Advanced Materials*, 2016, **28**, 9423–9429.

98 F. Zhao, S. Dai, Y. Wu, Q. Zhang, J. Wang, L. Jiang, Q. Ling, Z. Wei, W. Ma, W. You, C. Wang and X. Zhan, *Advanced Materials*, 2017, **29**, 1700144

99 W. Zhao, S. Li, H. Yao, S. Zhang, Y. Zhang, B. Yang and J. Hou, *J Am Chem Soc*, 2017, **139**, 7148–7151.

100 Y. Ma, M. Zhang, S. Wan, P. Yin, P. Wang, D. Cai, F. Liu and Q. Zheng, *Joule*, 2021, **5**, 197–209.

101 L. Meng, Y. Zhang, X. Wan, C. Li, X. Zhang, Y. Wang, X. Ke, Z. Xiao, L. Ding, R. Xia, H.-L. Yip, Y. Cao and Y. Chen, *Sci,* 2018, **361**, 6407.

102 J. Yuan, Y. Zhang, L. Zhou, G. Zhang, H. L. Yip, T. K. Lau, X. Lu, C. Zhu, H. Peng, P. A. Johnson, M. Leclerc, Y. Cao, J. Ulanski, Y. Li and Y. Zou, *Joule*, 2019, **3**, 1140–1151.

103 Q. Liu, Y. Jiang, K. Jin, J. Qin, J. Xu, W. Li, J. Xiong, J. Liu, Z. Xiao, K. Sun, S. Yang, X. Zhang and L. Ding, *Sci Bull (Beijing)*, 2020, **65**, 272–275.

104 Y. Cui, H. Yao, J. Zhang, K. Xian, T. Zhang, L. Hong, Y. Wang, Y. Xu, K. Ma, C. An, C. He, Z. Wei, F. Gao and J. Hou, *Advanced Materials*, 2020, **32**, 1908205.

Chapter 2 Experimental techniques

This chapter discusses the experimental details used in the thesis including the source of materials samples preparation, characterisation, and analytical process. It begins with the sample (films and solutions) preparation and followed by the characterisation methods, for example, the vibronic transitions investigated by steady state absorption and photoluminescence emission spectroscopy. Atomic force microscopy (AFM) and grazing incident X-ray diffraction (GIXRD) were used to determine the film morphology in terms of the root-mean-square surface roughness (Rq) for AFM and the d-spacing between layers (crystalline or amorphous domain) for GIXRD. The cation or anion formation generated in pure film were monitored by the spectroelectrochemistry in terms of a series of applied voltage below their first oxidation or reduction band. The excited states generated or decay in the films were monitored by different timescales of the transient absorption spectroscopy. The nano-to-millisecond transient absorption spectroscopy (μs-TAS) was used to study the decay dynamics of longer lifetime transient species, such as the photogenerated charges or triplets. Picosecond TAS (ps-TAS) was used to study the transient species with shorter lifetime, for example, the decay of excitons, CT states, or the formation and decay of polarons or triplet states.

2.1 Materials

Polymer Poly[(5,6-difluoro-2,1,3-benzothiadiazol-4,7-diyl)-alt-(3,3’’’-di(2-nonyltridecyl)-2,2’,5’,2’’,5’’,2’’’-quaterthiophen-5,5’’’-diyl)] PffBT4T-C9C13 (PCE12) was purchased from Ossila with Mw = 123,796, PDI=1.68. Polymer Poly[(5,6-difluoro-2,1,3-benzothiadiazol-4,7-diyl)-alt-(3,3’’’-di(2-nonyltridecyl)-2,2’,5’,2’’,5’’,2’’’-quaterthiophen-5,5’’’-diyl)] (PffBT4T-2OD) was bought from 1-Material (M_w=100,000, PDI=1.5-2.5). The control material polystyrene (PS) was purchased from Sigma-Aldrich.

Triplet sensitisers zinc tetraphenyl-porphyrin (ZnTpp) and the platinum porphyrin (PtOEP) were purchased from Sigma-Aldrich.

Fullerene acceptors $PC_{60}BM$ (99%) and $PC_{70}BM$ (99%) were bought from Solenne BV.

Non-fullerene acceptors *(ITIC series and Y6)* 3,9-bis(2-methylene-(3-(1,1-dicyanomethylene)-indanone))-5,5,11,11-tetrakis(4-hexylphenyl)-dithieno[2,3-d:2’,3’-d’]-s-indaceno[1,2-b:5,6-

b']dithiophene (ITIC), and 3,9-bis(2-methylene-(3-(1,1-dicyanomethylene)-indanone))-5,5,11,11-tetrakis(4-hexylthienyl)-dithieno[2,3-d:2',3'-d']-s-indaceno[1,2-b:5,6-b']dithiophene (ITIC-Th or IT-Th), and 3,9-bis(2-methylene-(3-(1,1-dicyanomethylene)-6,7-difluro)-indanone))-5,5,11,11-tetrakis(4-hexylphenyl)-dithieno[2,3-d:2',3'-d']-s-indaceno[1,2-b:5,6-b']dithiophene (ITIC-2F or ITIC-4F or IT-4F), and the 2,2'-((2Z,2'Z)-((12,13-bis(2-ethylhexyl)-3,9-diundecyl-12,13-dihydro-[1,2,5]thiadiazolo[3,4-e]thieno[2",3":4,5]pyrrolo[3,2-g]thieno[2'3':4,5]thieno[3,2,b]indole-2,10-diyl)bis(methanylylidene))bis(5,6-difluoro-3-oxo-2,3-dihydro-1H-indene-2,1-dilidene))dimalononitrile (Y6 or BTP-4F) were purchased from Ossila.

(PDFC series) Anti-PDFC, Syn-PDFC and PDFC-Ph were synthesised by Zhong's group[1] from Shanghai Jiao Tong University, Shanghai, China.

Solvents The solvents chlorobenzene (CB, 99.9%), dichlorobenzene (DCB, 99.9%), chloroform (CF, 99.9%), and the additive 1,8-diiodooctane (DIO) and the additive 1-chloronaphthalene (CN, 99%.9) were purchased from Sigma-Aldrich.

2.2 Sample Preparation

A general solution and film fabrication procedure will be introduced in this section, but the specific experimental details are located in the experimental section in each chapter, which varies from material to material.

Solutions All solutions were initially prepared outside the glovebox and then transferred into the glovebox with certain heating temperature depending on the types of materials, with a stirring rate 500 rpm. The Freeze-Pump-Thaw (FPT) method was used to extract air (oxygen) from the sample solution with minimum three repeating cycles until there was no bubbling in the cuvette during the thaw process. The solution concentration made for the TA measurements was generally around 0.01 mg mL^{-1}.

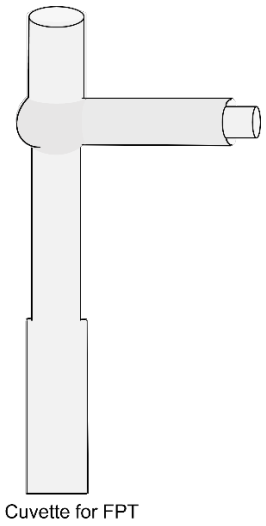

Figure 2.1 *Cuvette for Freeze-Pump-Thaw to remove oxygen in solution with three repeat cycles.*

Film Films are deposited on glass substrate with size 1.0 x 1.0 cm^2, which was purchased from VWR and the size of glass substrate was cut by hand. Thin films were made by spin coating (spin coater, Ossila) inside the glovebox under nitrogen atmosphere. All the glassware used to make PffBT4T-C9C13 and PffBT4T-2OD thin films was preheated at 100 °C on the hotplate for at least 30 minutes. The hot solution was then deposited onto 1 cm^2 glass substrates within 18 seconds to make uniform thin film with a spin rate of 800 rpm for 60 seconds to ensure the reproducibility of the films. The reason to control the hot solution transferring time from sample vial to the glass substrate is because of the strong pre-aggregation behaviour in the polymer solution, the best quality film can be made from hot solution with temperature above 85 °C. As shown in Figure 2.2, polymer solution temperature showed a decreasing trend as a function of time after the hot solution was removed from the hot plate. Same procedures were applied to make the PffBT4T-C9C13 correlated blend films: PffBT4T-C9C13 with fullerene and NFAs. Annealed blend films of PffBT4T-C9C13:$PC_{70}BM$ and PffBT4T-2OD:$PC_{70}BM$ were achieved by heating up the film at 80 °C for 5 minutes on the hotplate, which were made directly on films after spin coating. For the PM6 with PDFC films in Chapter 5, they were made with standard yellow pipette tips under room temperature.

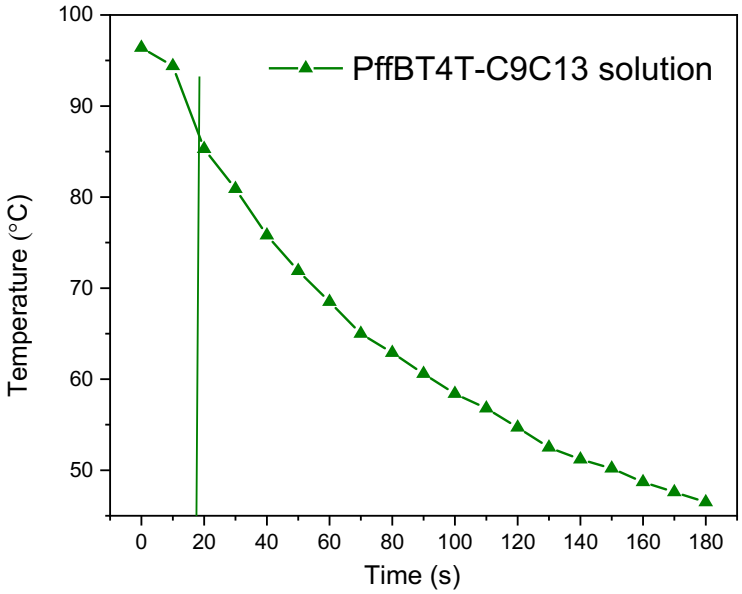

Figure 2.2 *Temperature variation for hot solution as a function of time for the sample vial removing from the hot plate to film glass substrate.*

2.3 Ground state ultraviolet-visible (UV-vis) absorption spectroscopy

Generally, spectroscopic studies begin with the measurement of ground state absorption spectra for semiconductors (polymer or NFAs) range from 300 to 1100 nm. The absorption range was used in a range from 0.6 to 0.8, that is good to gain best balance between high signal to noise ratio whilst avoiding non-linear effects and probing attenuation during the following transient absorption spectroscopy study. For solution, the absorption range was in the range from 0.2 to 0.4 to avoid triplet-triplet annihilation under high solution concentration.

When the light passing through the sample, the absorption of molecule at specific energies allows electronic transition from the ground state to the excited state. Absorption (A) is calculated by comparing the differences in the transmitted light intensity with and without the sample, as describe by the equation 2.1.

$$A = -\log T = -\log \frac{I}{I_0} \qquad (2.1)$$

Where A is the absorption, T is the transmittance, I is the intensity of transmitted light through the sample and I_0 is the intensity of incident light. For solution samples, the correlation

between the measured absorption and the concentration of the solution obeys the Beer-Lambert law, as the equation 2.2.

$$A = \varepsilon\, c\, l \qquad (2.2)$$

Where ε is the molar extinction coefficient (L mol^{-1} cm^{-1}), c is the solution concentration (mol L^{-1}) and l is the light path length (0.2 cm in our case).

The temperature dependence ground state absorption spectrum was recorded with a Perkin Elmer Lambda 365 from 300 nm to 1100 nm at ambient atmosphere and the sample holder was connected to the external water bath and heating pump (Grant) with temperature range 20 to 90 °C as shown in Figure 2.3.

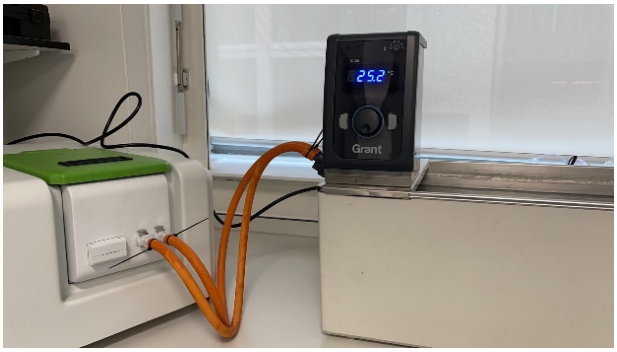

Figure 2.3 *Setup for ground state absorption spectroscopy connected with a water bath for temperature dependence measurements.*

2.4 Photoluminescence (PL) spectroscopy

The PL spectroscopy is used to measure the photon emission of the excited states for electron donor and acceptor materials decay back to a ground state, after the photoexcitation process. PL spectroscopy plays an important role to justify the effectiveness of acceptor materials for charge photogeneration in blend films. Generally, for polymer:fullerene blends, the polymer exciton will be quenched at the D/A interface, and the PL quenching can be estimated by the height (PL intensity) ratio of the blend to the pristine polymer film. However, both D and A exciton could be quenched in polymer/non-fullerene (NFA) acceptor blend. It is hard to solely calculated the PL quenching for specific type of exciton. Therefore, the PL quenching was calculated by the area of the blend film to the total area of the pristine D and NFA films based on their corresponding PL spectrum.

Photoluminescence emission spectra were obtained with a Fluorolog-3 Spectrometer (Horiba). The 450 W xenon short arc lamp provided the excitation. The spectra were measured at 100 accumulated exposures of 0.1 s. Correction were made by subtracting the background and accounting for the detector and lamp response. PL spectrum was made with normalised per sample absorption at the excitation wavelength. The temperature dependence PL measurement for NFAs was performed with extra TC 1 temperature controller (Quantum northwest) and a liquid cooling system (Koolance EXT-440) with the temperature range from 20 to 80 °C, as shown in Figure 2.4.

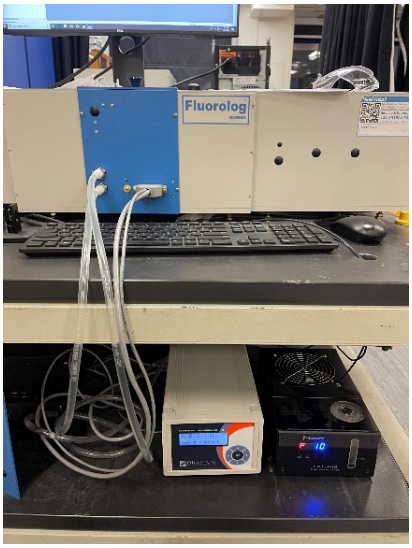

Figure 2.4 *Setup for the temperature dependence photoluminescence spectrum measurement.*

2.5 Atomic force microscopy (AFM)

Atomic force microscopy (AFM) is subset of scanning force microscopy (SFM) which is one of the notable tools for imaging matter at nanoscale. The information is gathering by probing the surface with a peak force mode. It overcomes the limitation of the traditional contact-mode-based conductive techniques to damage sample or probe tip contamination and provide direct, precise force control for high resolution imaging. This is facilitated by the presence of a piezoelectric crystal that allows for the detection of miniscule changes in attractive and repulsive force. A schematic of AFM is shown in Figure 2.5. AFM images were recorded by Bruker Dimension Icon in ScanAsyst peak force mode. Cantilevers used for AFM were Bruker scanasyst-Air with a nominal radius of 4 nm.

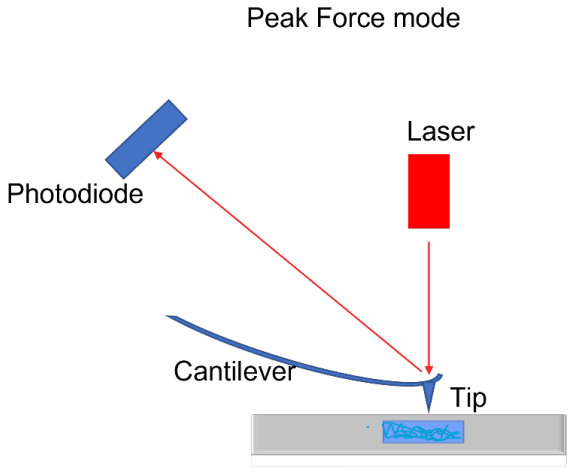

Figure 2.5 *Schematic diagram for AFM microscopy in peak force mode*.

AFM operated by allowing an extremely sharp tip located at the end of the cantilever in a closer proximity to the sample films. Different forces in the film will either attract or repel the tip. AFM images monitors the interactive forces between the sample and the tip, as the inter-atomic van der Waals attractive or repulsive force. These force between the tip and the film is measured directly by the deflection of the cantilever. A real feedback loop (not force trigger) keeps the peak force constant.

AFM amplitude parameters, root-mean-square roughness (R_q) and average roughness (R_a) were estimated by the software named NanoScope analysis under the surface roughness mode. The linear correlation for the height was obtained under the section mode. The distance between the crystalline domain of the material was estimated by the x-axis distance between the highest adjacent peak. The width of the crystalline domain was obtained by the averaging value of peaks' FWHM.

2.6 Grazing incidence X-ray diffraction (GIXRD)

Figure 2.6a shows the measurement configuration for PANalytical EMPYREAN, a high-resolution X-ray diffractometer schematically. The X-ray source Copper (Cu) cathode, driven by 40 kV high voltage, generates the incident X-ray beam, and then a monochromator is used for selecting the $Cu_{k\alpha1}$ emission line (λ=1.54059 Å). The intensity of the diffracted beam can be measured by the CCD detector mounted on the same goniometer as the X-ray source. The angle between the incident X-ray and the sample surface is θ, while the angle enclosed by the incident beam and the diffracted is denoted as 2θ. The incident slit (IS) defines the size of the incident X-ray.

X-ray diffraction analysis was carried out using a Bruker AXS D8 Advanced X-ray diffractometer in grazing-incidence mode with parallel beam optics equipped with a LynxEye silicon strip detector and copper source (Cu Kα1, 1.54056 Å and Kα2, 1.54439 Å) run at 40kV, 40mA. The angular range was 4˚ to 30˚ 2θ counted at 0.05° /sec with a data step of 0.05° using a 1° grazing incidence angle (θ) on the films. All the GIXRD samples were spin-cast on glass substrates.

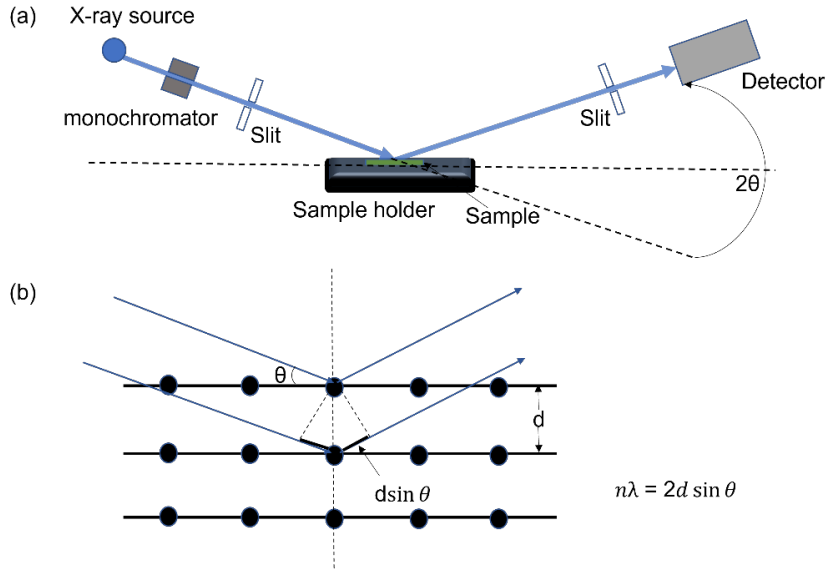

Figure 2.6 *(a) Schematic diagram for GIXRD diffractometer (b) Diagram to show Bragg's law for d-spacing calculation between two adjacent layers.*

The polymer contains certain crystalline and amorphous domains as a conjugated organic molecule. Sometimes, it could also show a completely amorphous structure. Due to the amorphous domain of the polymer, the GIXRD pattern of the polymer display as a relatively broad band. This is also true for the NFA, conjugated molecules. For the organic materials, the π- π stacking (010) layer usually located around 15 to 18 nm^{-1}. The d-spacing between layers can be estimated via Bragg's law, as shown in equation 2.3, and the equation can be deduced based on Figure 2.6b.

$$n\lambda = 2d \sin\theta \qquad (2.3)$$

Where n is number of electrons, d is the distance between two layers and θ is the incident angle.

The π-π stacking coherence length was calculated by the Scherrer's equation:

$$\Gamma = \frac{K\lambda}{\beta \cos\theta} \qquad (2.4)$$

Where r is the mean size of the ordered domains, which may be smaller or equal to the grain size. K is the dimensionless shape factor as a constant 0.94, λ is the incident X-ray wavelength 1.54059 Å, β is the linear broadening at half the maximum intensity (FWHM), in radians, and θ is the Bragg angle.

2.7 Cyclic voltammetry (CV) and Spectroelectrochemistry (SEC)

CV was measured with a three-electrode configuration, with the Pt mesh as the counter electrode, $Ag/AgNO_3$ as the reference electrode, and the film on ITO substrate as the working electrode. The electrolyte used was 0.1 M tetrabutylammonium hexaflurophosphate in acetonitrile. It should be noted that the non-fullerene acceptors showed less stable behaviour in this electrolyte solution as they could be dissolved to some extent along with the increased applied voltage. It suggests that the reduction reaction of the NFAs in acetonitrile is irreversible, and this is likely because of the subsequent chemical reaction triggered by the electron transfer process. More than 10 films were made for each NFAs from the same solution and spin coating speed to avoid this reproducibility issue. The cyclic voltammograms for each NFAs material were measured under the condition of degassing with N_2 or Ar for at least 20 minutes. The reproducible solution was chosen as the same CV shape from different films. A small amount of ferrocene was added into the electrolyte as the final step for the reduction peak position correction.

SEC was employed to confirm the polymer cation and NFA anions' position for polymer and non-fullerene acceptors in their pristine thin films. In order to observe the change in the absorption in response to the applied potential, the same three-electrode configuration and electrolyte were used as shown in Figure 2.7.

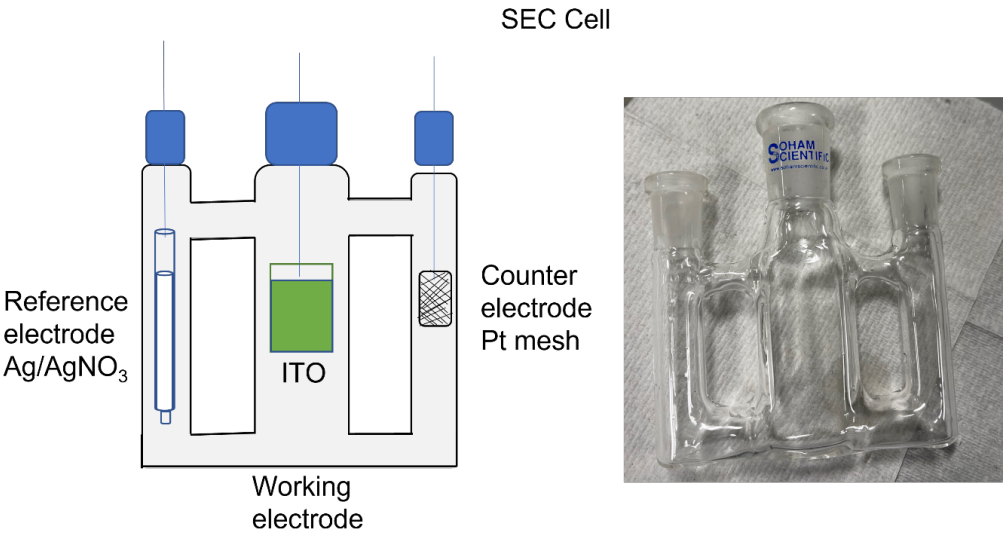

Figure 2.7 *Schematic diagram for spectroelectrochemitry (SEC) cell, ITO coated with NFAs or polymer thin films as working electrode, Ag/AgNO₃ as reference electrode, and platinum mesh (Pt) as counter electrode.*

As the CV curve for each NFA was measured first, the applied potential range was selected to be lower than the first reduction peak's voltage to avoid over-reducing the film and generating by-products. A collimated beam 10 mW halogen lamp (Ocean optics) was used as a light source, passing through the sample which was placed in an airtight 1 cm path length quartz cuvette cell, and degassed for more than 20 minutes. The cell was then inserted into the UV-Vis spectrometer with the absorption mode. After passing through the cell, the beam was re-collimated and focused into an optical fibre used for detection. Two CCD cameras were used, enabling spectra to be captured from in the visible region from 650 nm to 950 nm (Ocean Maya 2000) and from 1000 to 1700 nm (Ocean Insight NIR quest). Potentials were applied using an IVIUM VERTEX potentiostat using custom built LABVIEW software.

2.8 Transient absorption spectroscopy (TAS)

Transient absorption spectroscopy (TAS) is one of the pump-probe techniques that detect the optical properties of short-lived excited transient species in the photoactive layer of organic solar cells, capable of probing processes on 10^{-14} s and 10^{-2} s timescales. To be more specific, it can be used to measure the non-radiative decay, like triplet states which tend to be relatively non-emissive, or the formation and decay of CT states, the excitation of trap electrons and holes in the NIR region, free charge generation and recombination process. In addition, the negative TA signals can be used to analyse the ground state bleaching or

stimulated emission process. The stimulated emission process is the induced emission of a photon from an excited state, via interaction with the prob light. There are three timescales of TAS to detect transient species formed and decay during charge photogeneration, such as picosecond TAS (1 ps – 10 ns), and microsecond TAS (0.1 μs - 1 ms). For my projects, the nanosecond to millisecond (ns-μs-TAS) were mainly used to study the triplet and free charges decay process. Picosecond TAS was used in Chapter 5 to study the ultrafast photophysical process in perylene diimide based NFAs with polymer PM6.

The core for pump-probe μs-TAS is to employ a shorter intense laser pulse to populate the excited state, and the continuous steady white light probe is used to measure changes in absorption as a function of wavelength and time. The absorption intensity by the excited species is defined as:

$$\Delta A_t = A_t - A_0 \tag{2.5}$$

Where A_t is the absorption of excited state as a function of time, A_0 is the absorption of the sample not being excited. The absorption by excited state is the transient absorption (optical density: OD). Therefore, the absorption by the excited states can be expressed by:

$$\Delta OD_t = OD_t - OD_0 \tag{2.6}$$

Where ΔOD_t is the change in absorption after time duration t, OD_t is the absorption of excited state as a function of time, OD_0 is the absorption of sample is not excited.

On the timescales in the ns to s range, the time dependence of the T_n-T_1 decay process is determined by the lifetime of the T_1 state from which the absorption occurs.

2.8.1 Nanosecond to millisecond (ns-μs TAS)

A pump-probe ns-μs TA spectroscopy set-up was used to measure the TA spectra and kinetics for the excited species with a lifetime greater than 5ns to s. For example, the triplet lifetime can be estimated from the mono-exponential decay fitting. The general scheme for the ns-μs TAS experimental setup shown in Figure 2.8.

The Nd:YAG laser pulse was employed to excite the sample by passing through either film or solution in a quartz cuvette, with and without the presence of the probe white light and entering a monochromator to select the specific wavelength. Generally, a series of wavelengths starting from the pump wavelength to 1700 nm with 25 nm wavelength interval

to plot TA spectrum for a sample in different timescales, and the kinetic decay dynamics for transient species were measured in specific wavelengths with bandpass filters. The bandpass filters are used to avoid the white light effect[1] and also for wavelength selectivity. The photodiode detectors directly detected the potential difference upon exposure to light and sent to amplifier to enlarge the signals. The oscilloscope recorded the change of the voltage.

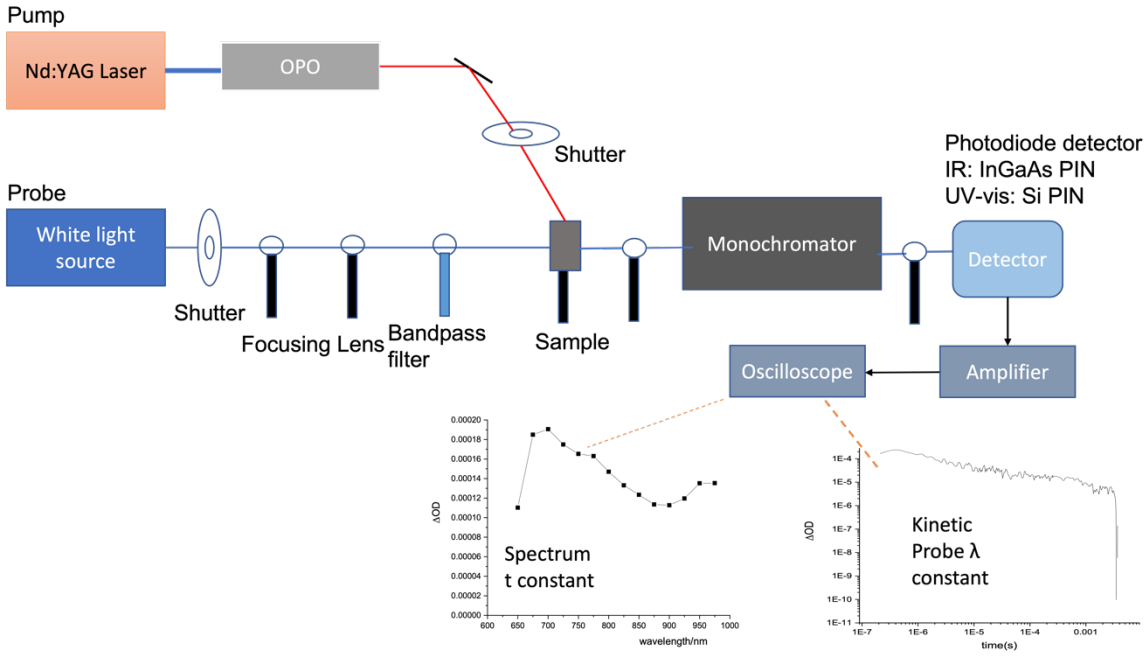

Figure 2.8 *The scheme of microsecond transient absorption spectroscopy setup. The TAS system consists of a pump laser and probe lamp sources. The other components in the system include a monochromator for probe wavelength selection, a detector to monitor the signal peaks and a signal amplifier. The spectrum diagram shows the formation of transient species in organic thin film based on ΔOD against wavelength, and the kinetic diagram shows the decay dynamics of the transient species based on ΔOD against time.*

The setup details: Laser pulses (repetition rate 10 Hz, pulse duration 6 ns) were generated by a Nd:YAG laser (Spectra Physics, INDI-40-10). The 1064 nm fundamental is frequency doubled to yield 532 nm light, which is then subsequently mixed with the 1064 nm fundamental to give an output of 355 nm. The 355 nm output beam is then used to seed a beta barium borate optical parametric oscillator (OPO) (Versascan L-532, GWU). Excitation wavelengths were selected by an OPO, and the excitation density was set in the range between 0.3 and 120 μJ cm^{-2} using neutral density filters, measured by an ES111C power sensor (Thorlabs). The probe light was provided by a quartz tungsten halogen lamp (IL1, Bentham). Probe wavelength selectivity was achieved using bandpass filters and a Cornerstone 130 monochromator (Oriel

Instrument) before the detector. The TA signals were recorded with both Si (400 - 1000 nm) and InGaAs (950 nm -1700 nm) photodiodes which was used one by one. The signal from the photodiodes was preamplified and sent to the main amplification system with an electronic filter (Costronic Electronics), which was connected to an oscilloscope (Tektronics, DPO4034 B) and PC.

The InGaAs detector monitors the probe wavelength from 900 to 1700 nm, and the silicon photodiode detects in the range from 400 to 1000 nm. The monitor records a change in voltage signal related to the fractional change in OD of the sample by:

$$\frac{V_{(t)}-V_{(0)}}{V_{(0)}} = \frac{10^{-OD_t}-10^{-OD_0}}{10^{-OD_0}} = 10^{-OD_t+OD_0} - 1 \quad (2.7)$$

As the $10^{-x} \approx 1 - x \ln 10$ when x is a small number, then the equation 2.7 can be expressed as:

$$\frac{\Delta V_{(t)}}{V_{(0)}} = 1 - \Delta OD \ln 10 - 1 = \Delta OD \ln 10 \quad (2.8)$$

So ΔOD can be expressed as:

$$\Delta OD = \frac{1}{2.303}\frac{\Delta V_{(t)}}{V_{(0)}} \quad (2.9)$$

2.8.1.1 Triplet extinction coefficient calculation

Since triplets have been observed in the polymer PffBT4T-C9C13 with both the fullerene and different non-fullerene blend systems in Chapter 3 and 4, it is valuable not only to know how the triplet formed but also to quantitively know triplet states formed in their polymer blend films. To quantify the population of triplet formation in the blend film, the first step is to calculate the triplet extinction coefficient for certain materials.

As we know, triplets can be generated via intersystem crossing by a high triplet energy level sensitizer. Given a known molar extinction coefficient of the triplet sensitizer, when the sensitizer is directly excited by the pump wavelength in the mixed sensitizer:NFAs solution, thereafter the high energy triplet sensitizer could via energy transfer to create a lower energy triplet on an NFA acceptor of unknown triplet extinction coefficient. After excitation of the donor/sensitizer, there are three possible pathways that could occur in the sensitizer: acceptor blend systems:

(i) the decay of donor by means other than energy transfer with a first order rate constant k1,

$$^3D\ (triplet\ donor) \overset{k_1}{\rightarrow} {}^1D(siglet\ ground\ state\ donor) \quad (2.10)$$

(ii) the energy transfer process itself with a pseudo first-order rate constant k_Q[A], the overall decay of the donor/sensitizer triplet ^{3}D is therefore $k_2 = k_1 + k_Q$[A].

$$^3D + {}^1A\ (siglet\ ground\ state\ acceptor) \overset{k_Q}{\rightarrow} D + {}^3A\ (triplet\ acceptor) \quad (2.11)$$

(iii) the decay of triplet acceptor, with the rate constant k_3,

$$^3A \overset{k_3}{\rightarrow} {}^1A\ (siglet\ ground\ state\ acceptor) \quad (2.12)$$

Using microsecond transient absorption spectroscopy, the unknown triplet-triplet molar absorption coefficient can be obtained by comparison with that of the donor sensitizer by equation 2.13. [2]

$$\frac{\varepsilon_T^D}{\varepsilon_T^A} = \frac{\Delta OD^D}{\Delta OD^A} \quad (2.13)$$

where ε_T^D is the triplet extinction coefficient for known donor compound, ε_T^A is the triplet extinction coefficient for unknown acceptor material. ΔOD^D is the maximum absorbance reached for the triplet-triplet absorption peak of the donor, and ΔOD^A is the maximum absorbance of the acceptor triplet at their respective wavelength maxima.

The NFAs shows negligible absorption under the excitation wavelength (425 nm) for the triplet sensitizer, so Land's additional correction [2] for ^{3}A when it is also formed via direct excitation is negligible for the NFAs studied in this thesis. If the decay of the acceptor triplet occurs simultaneously with its creation via energy transfer, a maximum in ΔOD will form. In such cases, considering the kinetics of successive reactions enables the following equation:

$$\Delta OD_{max}^A = \Delta OD^A \left(-\frac{lnk_2/k_3}{\frac{k_2}{k_3}-1} \right) \quad (2.14)$$

Where ΔOD_{max}^A is the maximum ΔOD observed in the acceptor triplet absorbance in the presence of the donor. Finally, a correction must also be applied for ^{3}D decay during the

energy transfer process, necessary in situations where k_1 is non-negligible. Since this is the case for ZnTPP, a correction factor of $\frac{k_2}{k_1+k_2}$ is applied.

2.8.1.2 Triplet yield calculation in solution and film

The molar extinction coefficient of the triplet may differ from solution to the solid phase film sample. To address this issue, a correction factor methodology was used by considering the change in absorption cross-section, σ, for the ground state from solution to film. The molar extinction coefficients of the ground state (ε_{GS_soln}) of each NFA have been measured in chlorobenzene with three different low concentrations (10^{-6} – 10^{-5} M range), where ε_{GS_soln} is established from the gradient of a plot of absorbance vs concentration. Absorption cross-section is then calculated using the known relationship:

$$\sigma_{GS\_soln} = \frac{\varepsilon_{GS\_soln} ln10}{N_A} \quad (2.15)$$

Where $\sigma_{GS\text{-}soln}$ is the absorption cross-section in solution, and N_A is Avogadro's number; also noting that an additional factor of 1000 is required for unit equivalence. Film absorption coefficients (α) are also converted to absorption cross section ($\sigma_{GS\text{-}solid}$) via $\sigma_{GS\text{-}solid} = \alpha/N_i$, where N_i is the number density of the initial state. N_i for the ground state can be established from the mass density and molecular weight.

Next, the following equation is applied to establish the correction factor for each NFA:

$$\sigma_{GS\_solid} = A\sigma_{GS\_soln} \quad (2.16)$$

Where A is the correction factor, the values for ε_{GS_solid} have been obtained from literature[3], except for ITIC-Th, for which none could be found and thus an extrapolation procedure was used. The correction factor is then applied to the ε of the NFA triplet, assuming that any change in σ of the ground state from solution to solid will occur similarly for the triplet state. The results are presented in the table below.

The triplet yield in pristine solution can be calculated using the Beer-Lamber Law $A=\varepsilon cl$, where ε is the triplet extinction coefficient, c is the concentration of solution, and l is the path length of the cuvette. For triplet formation in the NFA blend films with PffBT4T-C9C13, we can then apply the estimated film triplet ε using the following equation:

$$n_T = \frac{\Delta OD.A_v}{1000.\varepsilon_T.d} \quad (2.17)$$

Where n_T is the triplet yield in cm^{-3}, ΔOD is corrected for absorbance, A_v is Avogadro's number, ε_T is the molar extinction coefficient of the triplet, and *d* is the film thickness.

2.8.2 Picosecond transient absorption spectroscopy (ps-TAS)

Ps-TAS was performed at the Lord Porter Laser Laboratory, University of Sheffield, and measured by Dr James Shipp. A Ti:Sapphire regenerative amplifier (Spitfire ACE PA-40, Spectra-Physics) provided 800 nm pulses (40 fs FWHM, 10 kHz, 1.2 mJ). 520 and 665 nm pulses for excitation were generated from the fundamental 800 nm with a commercially available optical parametric amplifier (TOPAS, Light Conversion). White light super-continuum probe pulses in the range 430 – 700 nm or 800 – 1500 nm regions was generated in situ using 2 % of the Ti:Sapphire amplifier output, focused on a CaF_2 or YAG crystal, respectively. Detection was achieved using a commercial transient absorption spectrometer (Helios, Ultrafast Systems) using CMOS sensor for the UV-vis or an InGaAs detector for NIR spectral range. The relative polarisation of the pump and probe pulses was set to the magic angle of 54.7˚ for anisotropy-free measurements.

2.8.2.1 Data analysis for ps-TA spectrum and decay

The same type of information could be obtained from the ps-TA data and µs-TA data, including the spectral shape for short-lived transient species and their decay lifetime. However, there are several different excited states that could be generated in the ultrafast timescales, such as the localised exciton (tight bound electron and hole), CT state (relatively larger distance between electron and hole), or triplet state. Free triplet or polaron are generally shown with a longer lifetime in ns to µs timescales. However, the triplet formation can also be observed in the ps range via singlet intersystem crossing in the time range from ten to hundred picoseconds.

Due to different refractive index of light in the glass substrates, the white light, including all the probe wavelength does not reach the sample at the same time (chirp), resulting in different time zero (t=0 ps) for different wavelengths, which distorted the TA spectrum. Therefore, the software initially treated the raw ps-TA data with the build-in function named Surface Xplorer, which involves the subtraction of the background noise, chirp correction and time zero correction. Since the complexity of the transient species observed in the picosecond

timescales, genetic algorithm (GA) was employed to deconvolute the TA spectrum and decay dynamics for excited states from the whole ps-TA data, which was designed by Prof Richard Friend group members, University of Cambridge. It worked through the reconstitution of the ps-TA data into basic components by using a linear combination of the spectra gives the species with the smallest residual. Firstly, GA is performed by using a user-specified excited state spectrum as the reference and guesses the number of species in certain samples by analysing the raw ps-TA data. The user-specified excited state spectrum is usually to be the initially generated excited state defined as the exciton state obtained from the pristine polymer or NFA ps-TA spectra. Then it selects the spectrum best fits the data, making small changes to their form, called 'mutations', and 'reproducing' these together, new species generate more guesses. This process is then repeated iteratively until there is little variation between generations, indicating that the GA converges on the solution that can best reconstructed the dataset.[4,5] Care must be taken to ensure the absolute minima, not local minima. Confidence with the GA solution can be gained when repeated runs with different starting reference spectrum converge to the same excited state decay dynamics for certain samples.

2.9 References

1 A. Azeez and K. S. Narayan, *Journal of Physical Chemistry C*, 2021, **125**, 12531–12540.

2 E. Amouyal, R. Bensasson and E. J. Land, *Photochem Photobiol*, 1974, **20**, 415–422.

3 R. Kerremans, C. Kaiser, W. Li, N. Zarrabi, P. Meredith and A. Armin, *Adv Opt Mater*, 2020, **8**, 2000319.

4 K. Kikuchi, Y. Kurabayashi, H. Kokubun, Y. Kaizu and H. Kobayashi, *J Photochem Photobiol A Chem*, 1988, **45**, 261–263.

5. J. S. Seixas De Melo, J. Pina, F. B. Dias and A. L. Maçanita, *Applied Photochemistry*, 2013, **36**, 533–585.

Chapter 3 Bimodal polarons as a function of morphology in high efficiency PffBT4T-based polymer/fullerene blends for organic solar cells

3.1 Introduction

The high-performance fullerene-based organic solar cell (OSC) was observed with a bulk heterojunction (BHJ) structure. In such solar cell, it contains two components, electron donor (D) and acceptor (A) material, and spherical fullerenes tend to intercalate with polymer to form an interpenetrating network that is important for efficient charge separation at the D/A interface. However, if the mixed D/A domain is too small, the large interfacial area may trap electrons under a bimolecular recombination that is detrimental to electron migration. It is essential to control the morphology of the D/A blends and find an optimal morphology combination of excellent optical and electronic properties. In other words, for fullerene based OSCs, controlling the morphology of the polymer in photoactive BHJ film is the most important prerequisite step.

PffBT4T-based polymers have been shown with temperature-dependent aggregation (TDA) properties that could facilitate the formation of well-segregated D/A domains without excessive intermixing.[1] They show strong interchain aggregation in solution at room temperature. Heating polymer solutions above 60 °C cause the aggregation to disperse. Meanwhile, they contain a sufficiently pure polymer domain with a reasonably small crystalline size that could improve electron mobility, by controlling the temperature and time for polymer aggregation. [2] The BHJ OSCs consisting of TDA polymer PffBT4T-2OD with $PC_{70}BM$ fullerene acceptor show excellent device performance with power conversion efficiency around 11%. [3] Yan et al. further reported an improved efficiency of fullerene-based OSCs with TDA polymer PffBT4T-C9C13, showing an increasing side chain alkyl length than PffBT4T-2OD, as the structure is shown in Figure 3.1. They suggested that a small difference in the side alkyl chain length would significantly influence the polymer domain size and purity. In addition to tuning morphology using solution temperature, further modifications to the polymer blend morphology can be achieved using processing additives and thermal annealing.[2]

Due to their temperature-dependent aggregation properties, PffBT4T-based polymers have attracted a great deal of attention in morphology studies. However, spectroscopy and

photophysical studies for these high-efficiency polymers are scarce,[4, 5] especially for PffBT4T-C9C13. Of particular interest, however, is how the fine-tuning of morphology enabled by these polymers affects their photophysical properties. We will focus on fullerene blends, primarily because fullerenes' transient species are well-characterised and of weak absorption cross-section, thereby enabling the polymer transient species to dominate the spectra.

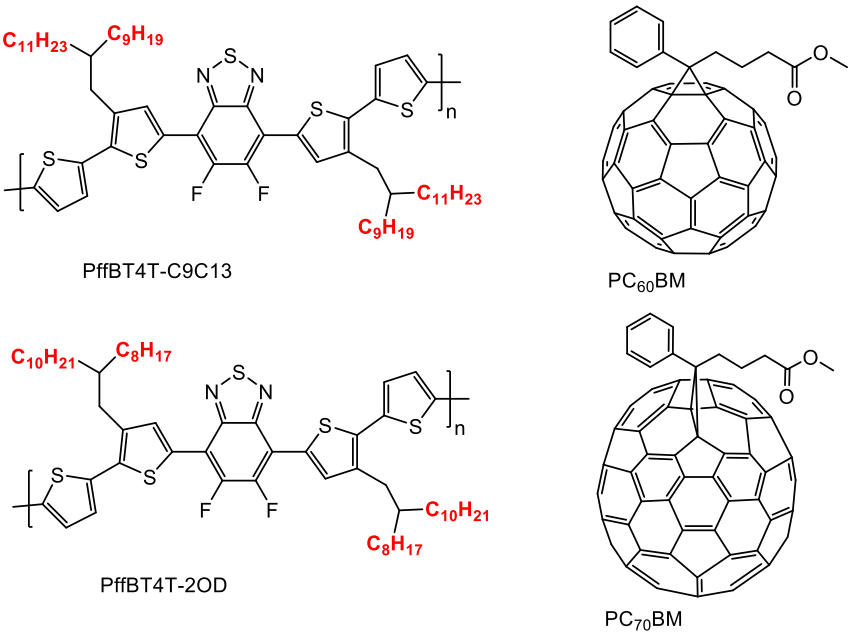

Figure 3.1 *Structure for the polymer donor PffBT4T-C9C13, PffBT4T-2OD and fullerene acceptor $PC_{70}BM$.*

Since the reproducibility issues have been addressed in the PffBT4T- analogue polymers as reported in chapter 2, including the uniform film making and stable film keeping conditions, it is important to move to the next step to investigate the photophysical processes in the high device performance PffBT4T-C9C13: $PC_{70}BM$ and PffBT4T-2OD: $PC_{70}BM$ blend systems. This chapter will focus on the correlation between charge photogeneration and recombination in the blends and the morphology of PffBT4T-C9C13:$PC_{70}BM$ and PffBT4T-2OD:$PC_{70}BM$ blends.

Nanosecond to millisecond transient absorption spectroscopy (ns-µs TAS) is employed to study the photophysical process in these two blend films in terms of different D/A compositions and made with/without thermal annealing. The polaron yields created in these two blend films can be measured by ns-µs TAS, which is directly proportional to the device short circuit current and external quantum efficiency. [6,7] Moreover, the long-lived transient species, like triplet, can also be observed and identified in ns-µs TA spectrum. Finally, and

crucially for our purpose here, TAS can resolve different polaron types: bulk versus interfacial polarons have been observed [8], and also delocalised versus localised polarons [9]. The morphology of the polymer PffBT4T-C9C13 and PffBT4T-2OD related films will be characterized by both atomic force microscopy (AFM) and grazing incident X-ray diffraction (GIXRD).

3.2 Experimental

3.2.1 Materials

PffBT4T-2OD was bought from 1-Material (M_w=50,000-100,000, PDI=1.5-2.5), and the PffBT4T-C9C13 was purchased from Ossila (M_w=123,796, PDI=1.68). $PC_{60}BM$ (99%) and $PC_{70}BM$ (99%) were bought from Solenne BV. The solvents chlorobenzene (CB, 99.9%), dichlorobenzene (DCB, 99.9%) and the additive 1,8-diiodooctane (DIO) were purchased from Sigma-Aldrich.

3.2.2 Sample fabrication

The PffBT4T-C9C13:$PC_{70}BM$ (weight ratio 1:1.2) film was prepared from a 10 mg mL^{-1} in CB solution with 3% DIO. The blend PffBT4T-2OD:$PC_{70}BM$ film (weight ratio 1:1.2) was fabricated from a 13 mg mL^{-1} in CB/DCB (1:1 volume ratio) solution with 3% DIO. The pristine PffBT4T- C9C13 and PffBT4T-2OD films were fabricated from 4 mg mL^{-1} and 2 mg mL^{-1} solutions in CB, respectively. The pristine PffBT4T-2OD and PffBT4T- C9C13 solutions were 0.01 mg mL^{-1} in CB. All solutions were initially prepared outside the glovebox and then heated at 100 °C overnight with a stirring rate 500 rpm inside the glovebox. Thin films were made by spin coating inside the glovebox under nitrogen atmosphere. All the glassware used to make thin films was preheated at 100 °C on the hotplate for at least 30 minutes. The hot solution was then deposited onto 1 cm^2 glass substrates to make thin films at a spin rate of 800 rpm for 60 seconds. The PffBT4T-C9C13:$PC_{70}BM$ and PffBT4T-2OD:$PC_{70}BM$ blend films were thermal annealed at 80 °C for 5 minutes on the hotplate.

3.3 Characterisation of the PffBT4T-C9C13 polymer

3.3.1 Steady state absorption and photoluminescence emission spectra

The steady state absorption spectra are used to analyse the crystallinity of the polymer under different conditions (various temperature in solution, blending film with fullerene and after thermal annealing) based on their 0-0 and 0-1 vibronic transitions. Additionally, the excitation wavelength for transient absorption study is also selected from the steady state spectra, which requires an absorption range from 0.4 to 0.8.[10] For the pristine film, the 0-0 vibronic

transition peak is picked as the excitation wavelength for the TAS study, but for the blend film it depends, and it will be discussed in the TAS section.

3.3.1.1 pristine polymer PffBT4T-C9C13 solution

The temperature dependence steady-state absorption spectra of pristine PffBT4T-C9C13 solution are shown in Figure 3.2a, as seen in previous reports for other PffBT4T polymer.[10,11] The pristine polymer solution exhibits a peak maximum at 700 nm and a side band centred at 638 nm, with a band at 450 nm. The most intense band at 638 nm was assigned to 0-0 vibronic transition, and the side band at 638 nm was attributed to 0-1 vibronic transition. Upon an increasing temperature from 25 °C to 75 °C, the vibronic structures at 600 nm and 638 nm disappeared with a new broad, featureless band formed at 550 nm. This indicates the presence of a strong polymer aggregation and enhanced planarity of PffBT4T-C9C13 at room temperature, and an amorphous (less crystalline) structure was formed with increasing temperature.

Figure 3.2b shows the temperature dependence PL emission spectra of the PffBT4T-C9C13 solution. The isosbestic point at 480 nm in Figure 3.2a was chosen as the excitation wavelength for the PL spectra because it more directly quantifies the PL intensity corresponding to the crystallinity of each emissive species at different temperatures. Unlike the absorption spectra, PL spectra show small changes in the spectral shape below 50 °C and two distinctive emissive species are formed with an increasing temperature to 85 °C. One species emitted at 730 nm is assigned to the fully planar aggregated PffBT4T-C9C13, showing higher intensity at low temperatures. The other emissive species at 660 nm (non-aggregated structure) shows a gradually increasing intensity with rising temperature. Since the 730 nm emission band shows no shifting with changing temperature, it is consistent with the assignment to the planar, rigid structure. The apparent rise in PL intensity with increasing temperatures reflects the relative populations of these two species. In general, the planar conformers have a higher quantum yield of fluorescence.[12] As such, the non-aggregated species must still have a strong presence even at room temperature. In contrast, the planar form has largely disappeared at high temperatures.

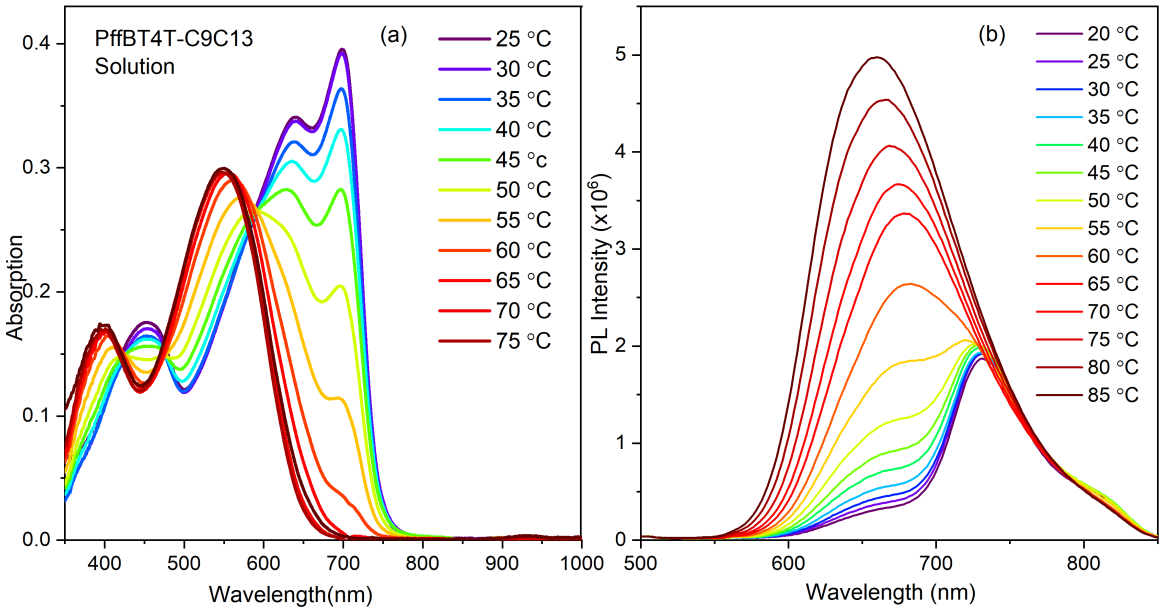

Figure 3.2 *Temperature dependence (a) steady state absorption (b) photoluminescence emission spectra (with an excitation wavelength at 480 nm) for pristine PffBT4T-C9C13 solution with concentration 0.01 mg mL-1 in chlorobenzene.*

3.3.1.2 Pristine and blend film

The normalised steady state absorption spectra for the pristine PffBT4T-C9C13 and PffBT4T-C9C13: PC70BM (weight ratio 1:1.2) blend films before and after annealing are shown in Figure 3.3. A qualitative assessment of PffBT4T-C9C13 film crystallinity can be made from the ratio of the vibronic 0-0 and 0-1 transitions. According to the Franck-Condon Principle, a more rigid crystalline structure inhibits the structural change during electronic excitation and therefore increases the relative intensity of the 0-0 absorption band. The pristine PffBT4T-C9C13 film shows the 0-0 vibronic transition band at 690 nm with a side band (0-1 vibronic transition) at 630 nm. Both absorption band shows a blue-shift relative to the pristine polymer solution, indicating a less crystalline structure than PffBT4T-C9C13 in the solution state. In contrast, the unannealed fullerene blend film exhibits a 10 nm red-shift and a sharper absorption onset compared to the pristine PffBT4T-C9C13 film, indicating a greater crystallinity found in the blend films. This is an unusual observation, as the fullerene is generally regarded to disrupt the crystallinity of the polymer and form an interpenetrating network (amorphous mixed domain).[13–15] However, this abnormally enhanced crystallinity after blending has been reported by Chen et al. in an analogue polymer named PffBT4T-2DT.[10] They have shown that there is no clear d-spacing observed in GIWAXS data for the analogue

pristine PffBT4T-2DT film (indicating a tilted π-π stacking structure), while PffBT4T-C9C13: PC60BM does show d-spacing, evidence of typical parallel π-π stacking.[16] Our absorbance results suggest that a similar evolution is occurring for PffBT4T-C9C13, and the morphology of the film will be discussed further in the next section. A similar fullerene-inducing ordering has been previously observed for the PBTTT: fullerene blends,[17] where the intercalation of small fullerenes between the alkyl chains of the polymer produced extensive co-crystallisation. While the larger fullerenes have resulted in a non-intercalated domain, and the resultant PBTTT domains were more amorphous.

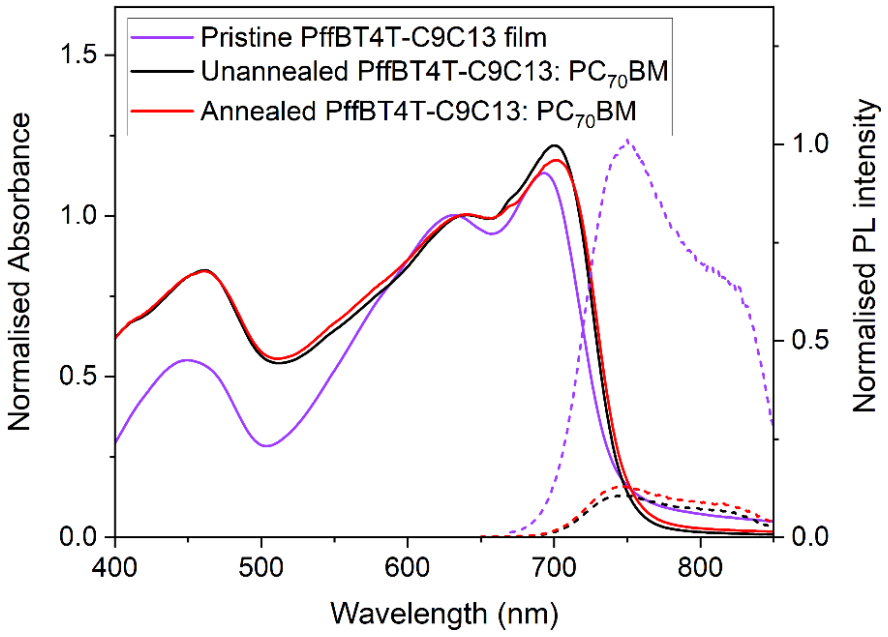

Figure 3.3 *Normalised steady state absorption spectra (solid line) and photoluminescence emission spectra (dash line) for pristine PffBT4T-C9C13 film, unannealed and annealed PffBT4T-C9C13: $PC_{70}BM$.*

The normalised photoluminescence emission spectra for the pristine PffBT4T-C9C13 and blend films are shown as dash lines in Figure 3.3. The PL spectra for pristine film display a strong 750 nm (0-0 vibronic transition) band with a side band at 820 nm (0-1 vibronic transition). Compared to the pristine polymer solution at 25 °C, which shows a planar and aggregated structure with 3 times higher 0-0 band intensity than 0-1 band, the band ratio in the pristine film is 1.7 times lower than its solution. This implies that the pristine PffBT4T-C9C13 film does not possess the same extent of planar rigid structure as the solution at room

temperature. The loss in crystallinity is consistent with the absorption spectra for the pristine film, and the pristine polymer shows the least crystallinity among its solution and blends film states.

PL spectroscopy can also be used as an indicator of exciton quenching, whereby excitons diffuse to the donor/acceptor (D/A) interface and undergo electron transfer. The value of PL quenching can be estimated by the PL intensity difference between the pristine and blend film at the 0-0 vibronic transition peak. The unannealed PffBT4T-C9C13: $PC_{70}BM$ (black dash line) is therefore quenched by 90%, indicating a high but not complete level of exciton dissociation when the $PC_{70}BM$ is added. A small increase in PL intensity and a consequent decrease in PL quenching to 87% was found in the blend film after thermal annealing. The small difference in the PL quenching between unannealed and annealed blend films suggests that the morphology changes after annealing have little impact on the number of excitons reaching the D/A interface. The reason for the high PL quenching in blend films is possible because the PffBT4T-C9C13 exciton diffusion length is greater than the polymer domain size and therefore, it can easily diffuse to the D/A interface before relaxing to the ground state.

3.3.2 Morphology

To understand further the morphology variation of the films with the addition of fullerene and after annealing, AFM is used to study the surface morphology of the film by comparing the average surface roughness, and GIXRD gives information about the extent of the polymer crystallinity domain by analysing the (010) layer of the PffBT4T-C9C13 at 16 nm^{-1}.

3.3.2.1 Atomic force microscopy

AFM height and topography images of pristine PffBT4T-C9C13 and unannealed and annealed blend PffBT4T-C9C13 with $PC_{70}BM$ are shown in Figure 3.4. The average surface roughness (Ra) obtained from the height images from Figure 3.4a to 3.4c increased from the pristine (2.4 nm) to the unannealed blend (6.4 nm) to the annealed blend film (16 nm). The increase in the film roughness show that phase segregation is induced by the addition of $PC_{70}BM$ and enhanced via thermal annealing. The topography of these films (figure 3.4 d to 3.4 f) clearly shows the formation of a larger domain upon thermal annealing.

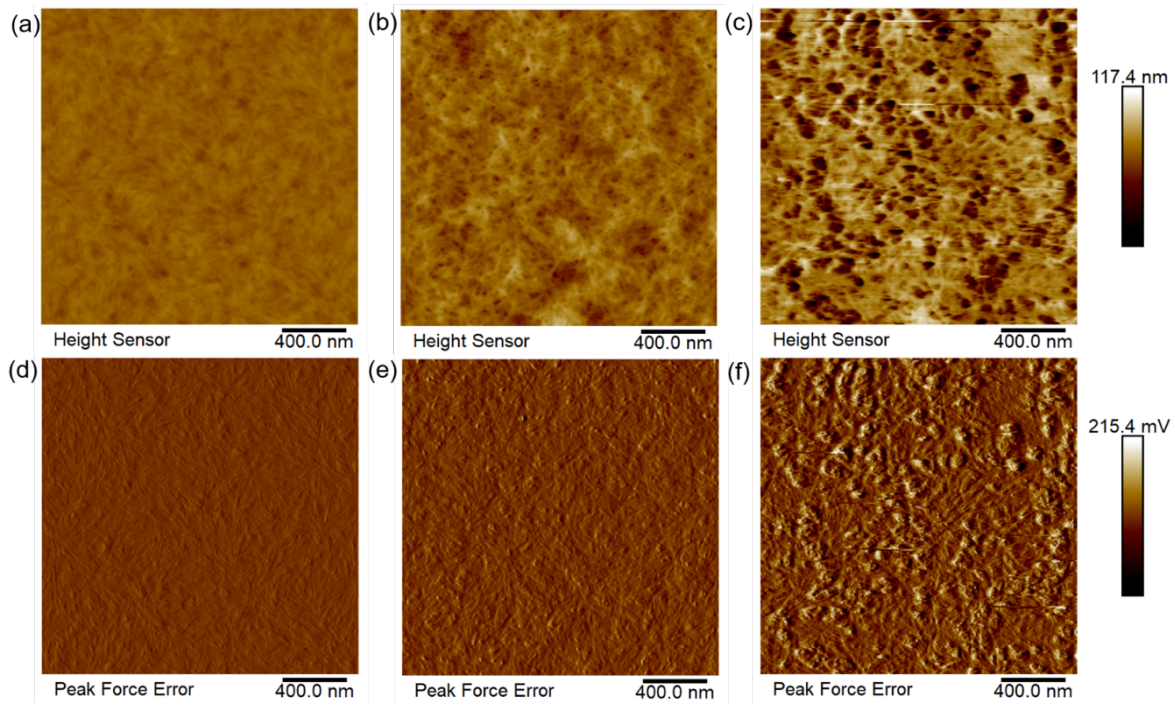

Figure 3.4 *AFM images of phase and topography of pristine PffBT4T-C9C13 (a and d), unannealed PffBT4T-C9C13: $PC_{70}BM$ (1:1.2) (b and e) and annealed PffBT4T-C9C13: $PC_{70}BM$ (1:1.2) blend film (c and f) from left to right and top to bottom. Scale bars are 400 nm. (Note: a larger scale bar was found in the annealed blend than the rest two films, reflected by the pale images colour in the pristine and unannealed blends.)*

3.3.2.2 Grazing incident X-ray diffraction

The GIXRD patterns for pristine PffBT4T-C9C13 and its unannealed and annealed blend with PC70BM are shown in Figure 3.5. In general, the signal intensities of all PffBT4T-C9C13 samples were substantially reduced compared to the literature analogue PffBT4T-2OD.[18] Previous GIXRD measurements in another PffBT4T-C9C13 analogue, PffBT4T-2DT, showed that the (010) peak at 16 nm^{-1} was weakly apparent and it was denoted as amorphous tilted π-π stacking. A similar situation was found in the pristine PffBT4T-C9C13 film: the (010) peak at 16 nm^{-1} shows a very small intensity, indicating less crystalline tilted π-π stacking. However, the (010) peak of the blend films show a significantly greater intensity than the pristine film. To show the intensity difference between the blend and pristine film, the integrating factor was calculated and represented by the ratio of the integrating area of the unannealed blend to the pristine film from 15 nm^{-1} to 17 nm^{-1}. The (010) peak for the PffBT4T-C9C13: $PC_{70}BM$ blend exhibited a greater integrated area by a factor of 1.6 compared to the pristine polymer film (corrected per absorbance). Since the integrated peak area indicates the relative amount

of crystalline polymer domain in the film, a greater crystallinity for the blend film was found compared to the pristine polymer. The enhanced crystallinity with the addition of $PC_{70}BM$ blend is consistent with the steady state absorbance and the AFM results, suggesting that this enhanced crystallinity in the blend is related to the fullerene induced ordering. As such, given that non-unity domain purity has been observed in the PffBT4T-C9C13: $PC_{70}BM$, the mixed D/A domain for the blend shows a higher crystallinity than the pure pristine polymer domain. As I mentioned above, this enhanced crystallinity in the blend is very unusual as the addition of fullerene typically perturbs the crystallinity of the polymer, and the mixed domain is amorphous. For the PffBT4T-C9C13: $PC_{70}BM$ blend system, the reverse case is true. Combing the AFM and GIXRD results, the enhanced crystallinity in the blend can therefore be attributed to the fullerene induced ordering.

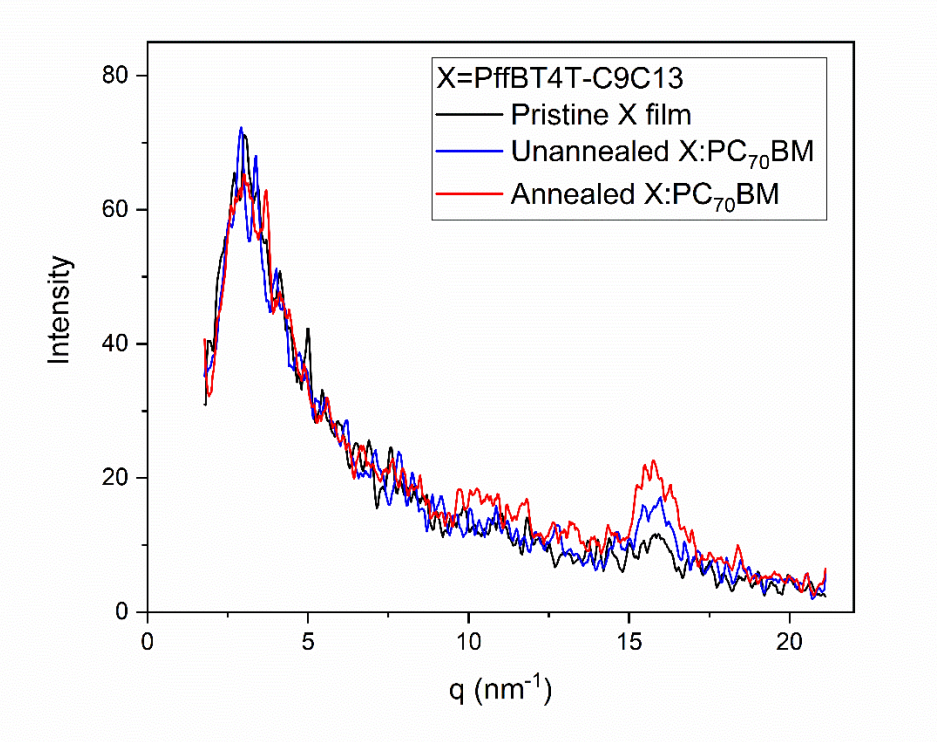

***Figure 3.5**. Grazing -incidence X-ray diffraction of PffBT4T-C9C13 films and its unannealed and annealed blends with $PC_{70}BM$.*

The annealed PffBT4T-C9C13: $PC_{70}BM$ blend shows an even higher (010) peak intensity than the unannealed blend, which gives an integrating factor of 1.3 compared to the unannealed blend. This increased intensity suggests a further enhancement of film crystallinity after thermal annealing. Considering the AFM results for greater surface roughness (2.5 times

higher than unannealed blend) and bigger domain size (topography images), the fullerene-induced ordering domain size may become bigger for the blend film after annealing. However, this large difference in crystallinity (measured by AFM and GIXRD) after annealing was not observed in the steady state absorption and PL spectra. A possible explanation could be that the spectroscopic technique measured a 1 x 1 cm^{-2} area while the morphological equipment focuses on a small, localised area in great detail. It has been previously reported by Peng et al. that strong thermal annealing conditions can lead to prominent fullerene extrusion.[13] Although their thermal annealing condition was more extreme than ours in terms of both temperature and time, a degree of fullerene extrusion cannot be discounted, and this could contribute to the greater phase segregation and domain coarsening we observed in the AFM. Since the fullerene extrusion and enhanced fullerene-induced ordering - which are not mutually exclusive - have opposing spectroscopic effects (the former decreases the vibronic 0-0/0-1 ratio while the latter increases it), this could account for the lack of change in the steady state absorbance spectra.

3.3.3 SEC for polymer cation determination

SEC was employed to identify the charge carriers formed in the pristine PffBT4T-C9C13 film, as shown in Figure 3.6a. The SEC spectra for PffBT4T-C9C13 exhibit an electrooxidation induced bleaching of the ground state absorption bands at 450 nm, 638 nm and 700 nm (negative intensity). In addition, there are two initial generated positive bands shown at 760 nm and 1550 nm. An apparent band shift in high voltage is observed from 760 nm to a broad band around 850 nm. In analogy with the assignment of the absorption spectra of charges in P3HT, the 760 nm band can be attributed to the delocalised polarons inhibiting at the PffBT4T-C9C13 crystalline polymer,[19,20] and the 850 nm band can be assigned to bipolaron.[21] It should be noted that bipolaron formation is regarded as two holes in polymer on a single molecular site.[22] In general, it is considered to be negligible in organic materials because of the coulomb repulsion force between holes. However, it has been reported that strong energetic disorder in organic thin films can facilitate bipolaron formation in the density of state tail and bipolaron formation can be achieved by hole hopping from high energy site to low energy site.[23] The highly disorder in organic thin films provides large interfacial charge density, resulting in a facilitation of bipolaron formation. This is consistent with the amorphous PffBT4T-C9C13 polymer domain with the evidence by the AFM and GIXRD results. In addition, the assignment

of the bipolaron formation also is consistent with the 0.2 eV red shift to the polaron formation and the value of it is affected by the film disorder.[24] The broad SEC band at 1550 nm can be attributed to the HOMO to SOMO electronic transition (P1 transition) of the polarons, and 760 nm band can be ascribed to the SOMO to LUMO transition (P2 transition).[25,2627]

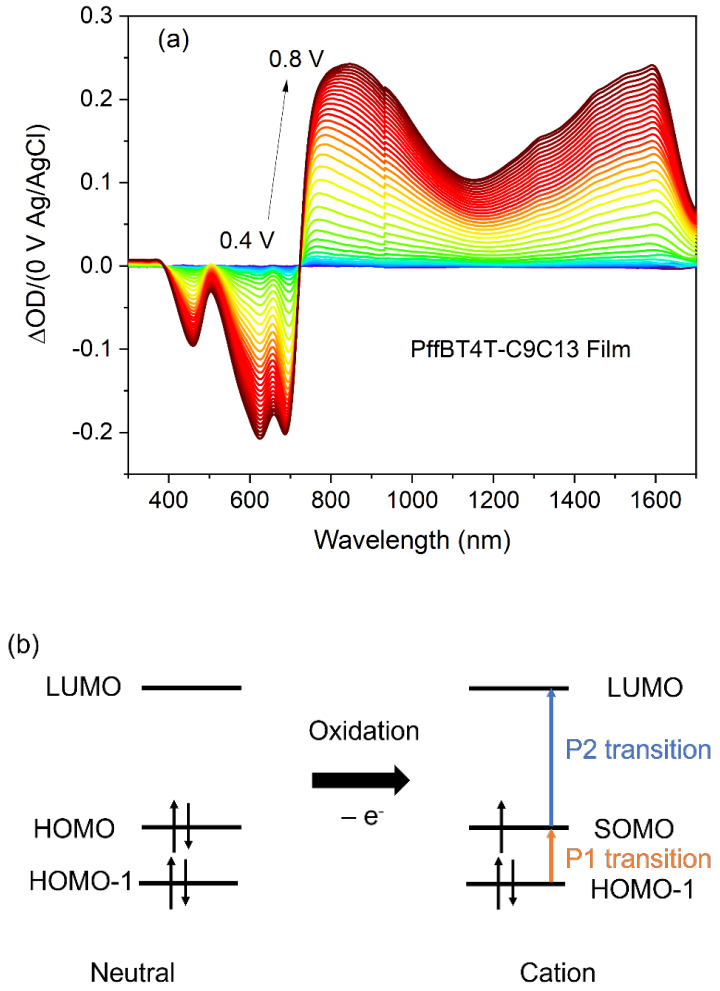

Figure 3.6 *(a) SEC absorption spectra for polymer PffBT4T-C9C13 film with an applied voltage from 0.4 V to 0.8 V. (b) Schematic illustration of the HOMO-LUMO transition in neutral polymer and following oxidation, two polaron transition arises: P1 transition (HOMO to SOMO), P2 transition (SOMO to LUMO).*

3.3.4 nanosecond-microsecond transient absorption spectroscopy (ns-μs TAS)

Since the high device performance (12%) was found in the PffBT4T-C9C13: $PC_{70}BM$ organic photovoltaics (after annealing at 80 °C for 5 mins), it is crucial to understand the photophysics process behind it. Nanosecond to millisecond TAS can be used to investigate the long-lived excited state species, which is the optimal tool to study charge and triplet formation and

decay dynamics of the polymer PffBT4T-C9C13 and its blends with fullerenes. The characterisation process begins with the pristine polymer film and solution to identify the charge and triplet spectra which are used to simplify the photophysics investigation process in the polymer: $PC_{70}BM$ blend systems.

3.3.4.1 Characterisation of pristine polymer

Normalised (to maximum 6.5) TA spectrum for pristine PffBT4T-C9C13 film is shown as a green triangle solid line in Figure 3.7. It displays a single peak around 725 nm which can be attributed to the polymer polarons due to the power law decay kinetics and lack of oxygen dependence (Figure 3.8a). The precise wavelength of the polymer polarons cannot be identified from TAS due to the polymer ground state bleaching overlapping the photoinduced absorption peak.

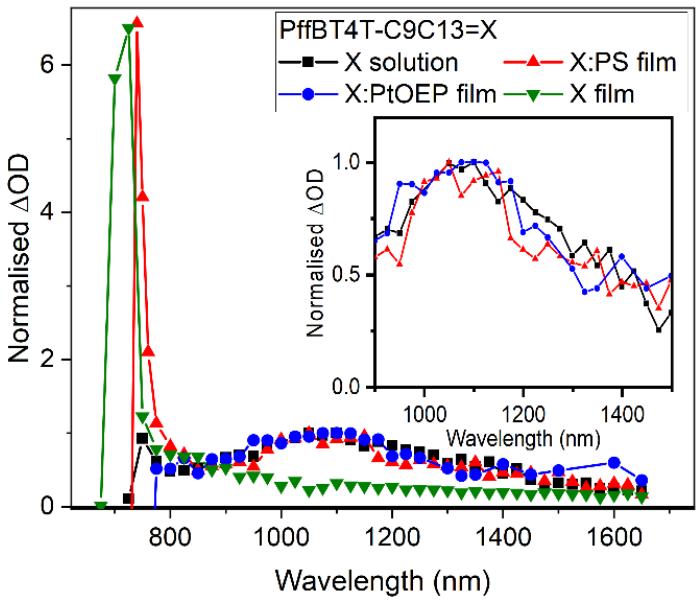

Figure 3.7 *Normalised transient absorption spectra for pristine PffBT4T-C9C13 solution, film, blend PffBT4T-C9C13:PS (3:2), and PffBT4T-C9C13:PtOEP (3:2) films. An excitation wavelength of 600 nm was used for both pristine solution and film because higher excitation densities were required: 34 μJ cm^{-2} and 114 μJ cm^{-2}, respectively. An excitation wavelength of 700 nm and excitation density 65 μJ cm^{-2} were used for the PffBT4T-C9C13:PS (3:2) blend film. An excitation wavelength of 545 nm (to excite the porphyrin) and an excitation density 30 μJ cm^{-2} were used for the blend PffBT4T-C9C13:PtOEP (3:2) film.*

The normalised (to 1) TA spectrum for pristine PffBT4T-C9C13 solution is shown as the black square solid line in Figure 3.7. The TA spectra for pristine solution show a broad absorption centred at 1080 nm. This band is assigned to be polymer triplets, as evidenced by the strong,

reversible oxygen dependence and mono-exponential kinetics (Figure 3.8b). To check the spectrum shift from solution to the condensed phase (film), a triplet sensitisation experiment was performed using the well-known triplet sensitiser platinum octaethylporphyrin (PtOEP).[28] Normalised (to 1) TA spectra for PffBT4T-C9C13: PtOEP (3:2) film as displayed as blue circle solid line in Figure 3.7. The excitation wavelength 545 nm was chosen to selectively excite PtOEP (Figure 3.8c). The triplet PtOEP formed efficiently, and the lower energy polymer triplet can be formed via energy transfer. The TA spectra for PffBT4T-C9C13: PtOEP (3:2) film exhibit a broad band centred at 1050 nm. Since the PtOEP triplet was discovered below 800 nm (Figure 3.8d) in the same ratio blend film with polystyrene (PS) (PtOEP: PS with ratio 2:3), the 1050 nm band generated in the PffBT4T-C9C13: PtOEP film can be confidently assigned to polymer PffBT4T-C9C13 triplet.

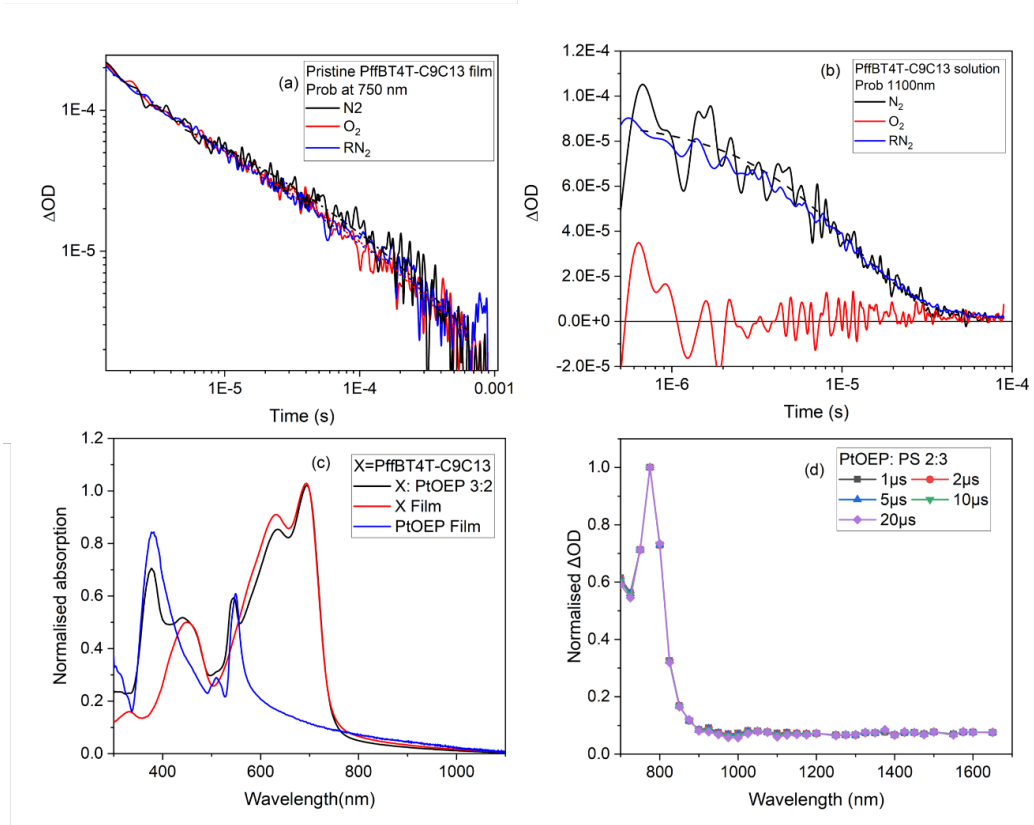

Figure 3.8 *(a) Oxygen-dependent decay dynamics of pristine PffBT4T-C9C13 film at probe wavelength 750 nm with pump wavelength of 600 nm and excitation energy of 114 μJ cm^{-2}. (b) Oxygen-dependent decay dynamics of pristine PffBT4T-C9C13 solution probing at 1100 nm (solid line) and fitted with mono-exponential decay (dash line), with pump wavelength of 600 nm and excitation energy of 34 μJ cm^{-2}. (c) Normalised (to 1) steady-state absorption spectra of pristine PffBT4T-C9C13 film, solution, PtOEP film, and bend film PffBT4T-C9C13: PtOEP (3:2). (d) Normalised (to 1 at 775 nm) TA spectra evolution of PtOEP:PS (2:3) with an excitation wavelength of 545 nm and using 30 μJ cm^{-2}.*

Control blend PffBT4T-C9C13:PS were also assessed in the ratio of 1:1.2 and 3:2, as shown in Figure 3.9a. The TA spectrum with the blend ratio 1:1.2 only showed the formation of the polymer polarons peaked around 750 nm while the polymer: PS (3:2) blend films not only exhibit the formation of polarons around 725 nm but also the polymer triplet centred at 1050 nm. The new appearance of the polymer triplet generated in the 3:2 control blend – in contrast to the pristine film (only the polaron generated as shown in Figure 3.7 and 3.9a) – could be due to the greater intermolecular interaction in the more condensed films enabling fast triplet-triplet deactivation, leaving a negligible triplet population on the μs timescales. The lack of polymer triplet formation was also observed in an even less condensed 1:1 control blend, and this could be due to the large phase segregation causing a weak intermolecular interaction for spin-orbit coupling mediated triplet generation. Figure 3.9b shows the oxygen dependence decay dynamics for the polymer triplets generated in the PffBT4T-C9C13: PS (3:2) blend. Interestingly, the polymer triplets have not been fully quenched in the PS control blend under oxygen atmosphere. In contrast, it was fully quenched when they were generated in the pristine polymer solution (Figure 3.8b). The lower oxygen sensitivity of the polymer triplet formed in the control blend suggests that the triplet energy level is lower in the condensed phase than its in solution, thereby inhibiting the quenching process (closer to the S_1 energy of oxygen). Indeed, the polymer S_1 minimum energy can be estimated by the crossing point of the steady state absorbance and PL emission spectra (Figure 3.3) of the pristine PffBT4T-C9C13 film, and the T_1 energy was previously reported to be typically 0.6 to 0.7 eV lower than S_1 energy in polymer.[29] Therefore, the S_1 energy of PffBT4T-C9C13 can be calculated at around 1.71 eV and the T_1 energy can be estimated at around 1.01 eV, which is around the S_1 energy of the oxygen (0.98 eV).

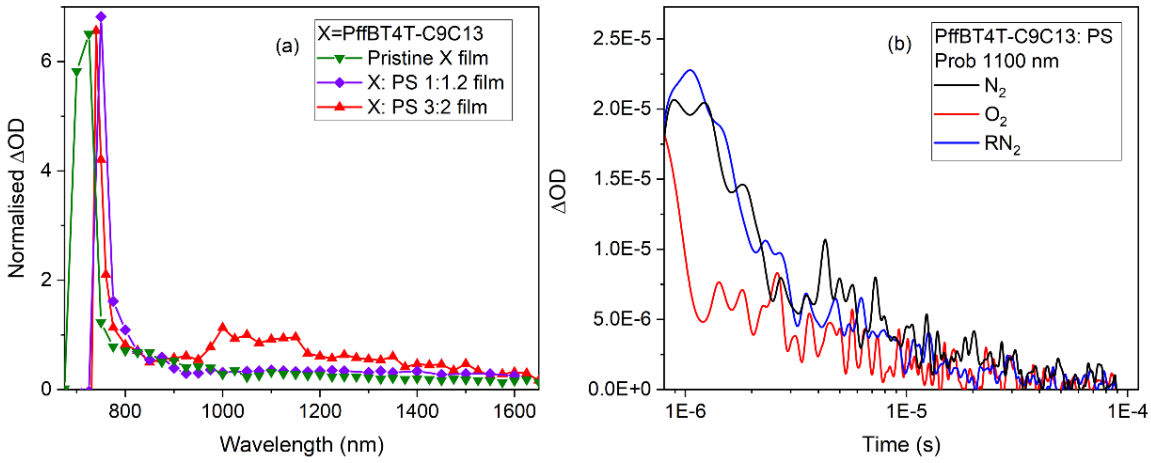

Figure 3.9 *(a) Normalised TA spectra for pristine PffBT4T0C9C13 film and the control blend PfBT4T-C9C13 with polystyrene in blend ratio 1:1.2 and 3:2. (b) Oxygen dependence decay dynamics of PffBT4T-C9C13:PS (3:2) at probe wavelength 1100 nm with pump wavelength at 700 nm and excitation density 65 μJ cm^{-2}. Note that the PffBT4T-C9C13:PS (1:1.2) blend film showed little evidence of triplets, and thus we use the 3:2 blend ratio as a control for examining a disperse polymer matrix instead.*

3.3.4.2 Characterisation of blend films

To analyse the TA spectra for the blend films, spectral evolution is first used to show the number of transient species generated in the blend films. The transient species generated in the blend films are assigned based on the spectral position to the polymer polarons and triplet formation in section 3.3.3 and 3.4.4.1 Spectral evolutions for the unannealed and annealed PffBT4T-C9C13: $PC_{70}BM$ blend films are displayed in Figure 3.10a and 3.10b, respectively. Both these spectra show three TA bands <750 nm, 900 nm and 1100 nm. These three bands show a smoother and more distinct spectral shape after thermal annealing, especially the 900 nm peak exhibiting a slightly larger FWHM and an increasing relative ΔOD at longer timescales which indicate the generation of transient species with longer lifetime. Note that the observed 1600 nm band on the PffBT4T-C9C13 SEC spectrum has not been detected by ns-μs TAS, this might because of the fast decay rate of the P1 transition.

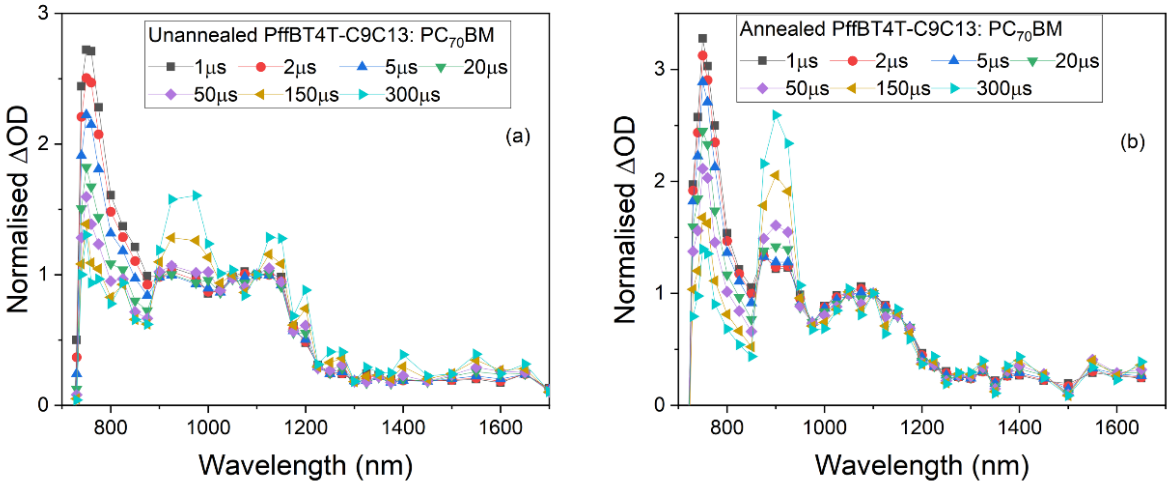

Figure 3.10 *Time evolution of the TA spectra of (a) unannealed PffBT4T-C9C13:$PC_{70}BM$ blends at different timescales. (b) Annealed PffBT4T-C9C13:$PC_{70}BM$ blend films at different timescales. An excitation wavelength of 700 nm and excitation density 4 μJ cm^{-2} was used for both unannealed and annealed PffBT4T-C9C13:$PC_{70}BM$ blend films.*

Normalised TA spectra of unannealed PffBT4T-C9C13:$PC_{70}BM$ film compared to the control transient spectra are shown in Figure 3.11a, the <750 nm peak matches well with the polymer polaron peak generated in the pristine polymer film spectra, and the 1100 nm band shows a good overlap with the polymer triplet spectrum. Thus, unannealed PffBT4T-C9C13 blend with $PC_{70}BM$ displayed both the polymer polaron and triplet formation. However, none of the pristine films, control blend film or triplet sensitised film's spectra show the 900 nm band formation, indicating that the formation of it is due to the addition of fullerene. This 900 nm band is unlikely to derive from either the $PC_{70}BM$ anion or triplet as the $PC_{70}BM$ triplet position is around 1.94 eV[30, 31] and the anion is around 1300 nm.[32] As we observed an enhanced crystallinity in the fullerene blend, the 900 nm band most likely originated from the crystalline domain, so it is important to understand whether the 900 nm band is characterised by the polymer or the fullerene? Since the strong TA signal at 900 nm was observed in the annealed blend PffBT4T-C9C13 with $PC_{70}BM$, to examine whether the 900 nm band was related to the $PC_{70}BM$, the $PC_{60}BM$ was first used to replace the role of $PC_{70}BM$ (with same blend ratio and annealing conditions) in the blend film. As shown in Figure 3.11b, the 900 nm band is still present when switching the acceptor from $PC_{70}BM$ to $PC_{60}BM$, suggesting that the 900 nm band is related to the PffBT4T-C9C13 rather than the fullerene. It also should be noted that the spectra position of <750 nm and 1100 nm do not shift when altering the acceptor,

consistent with the assignment of the polymer polarons and triplet, respectively. Furthermore, a series of other experiments were also performed to identify the long-lived 900 nm band related to the polymer, including altering the blend polymer to fullerene ratio, different excitation wavelengths and after thermal annealing. When increasing the percentage of fullerene in the blend film with polymer from 10% to 50%, the intensity of the 900 nm bump shows a stronger TA signal, as shown in Figure 3.11 c. Furthermore, normalised TA spectra of unannealed PffBT4T-C9C13: $PC_{70}BM$ (Figure 3.11d) were measured with two different excitation wavelengths at 700 nm and 455 nm. 700 nm as the maximum peak in polymer absorption spectra (selectively excited polymer[30]), the TA spectra show the 900 nm band appears more predominately with 700 nm excitation wavelength than 455 nm (large amounts of $PC_{70}BM$ also absorb at 455 nm). In combination with the intense 900 nm TA signal obtained after thermal annealing and enhanced film crystallinity, it is, thus, the polymer related 900 nm band can be assigned to polymer polarons that are localised in the fullerene-induced ordering domains. This assignment is consistent with the narrowness of the band (the polarons exist in a relatively homogeneous environment) and previous literature assignments of bimodal polarons located in different morphological environment.[33]

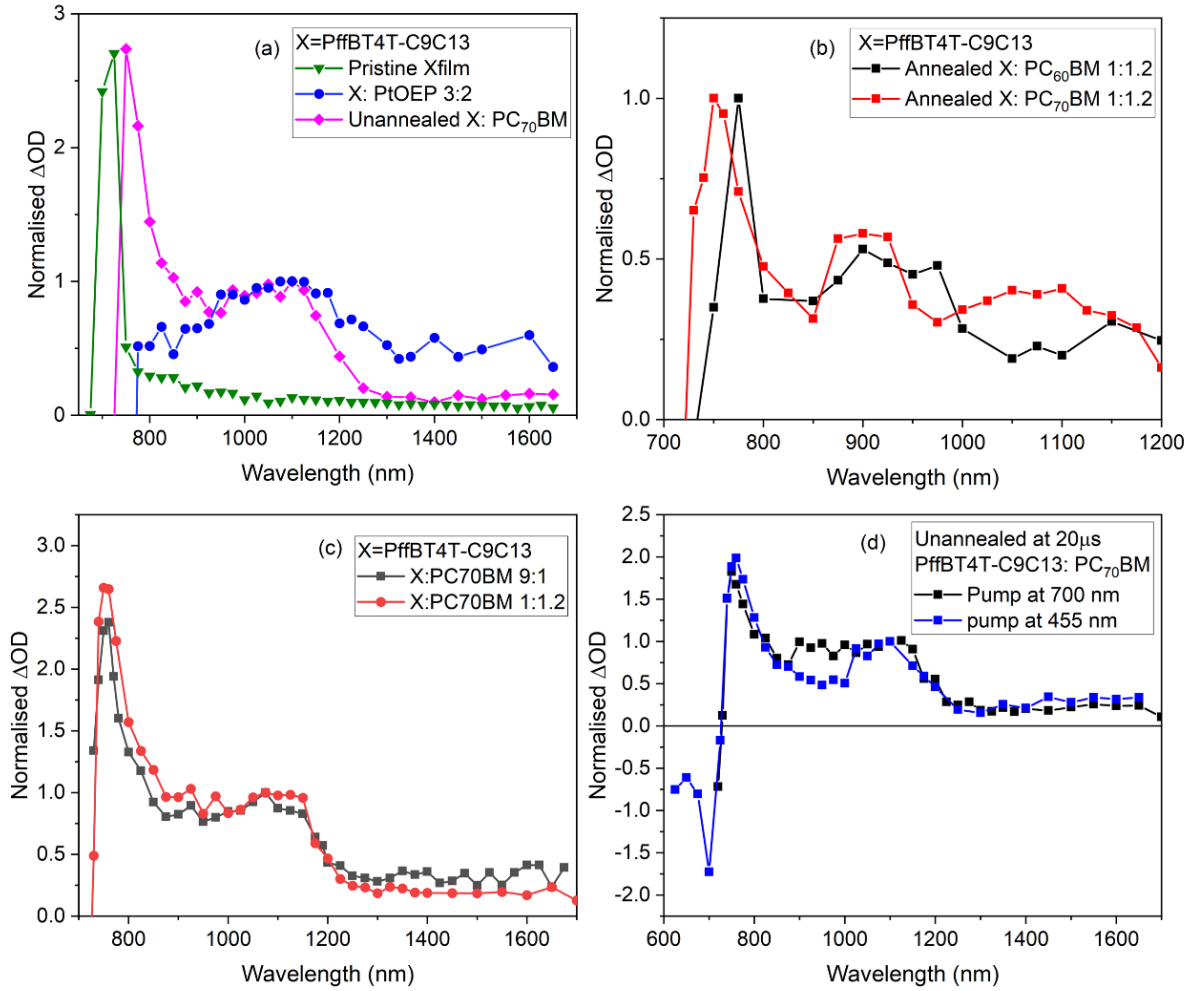

Figure 3.11 *(a) Normalised TA spectra of unannealed PffBT4T-C9C13:$PC_{70}BM$ film compared to the control transient spectra. (b) Normalised transient spectra of annealed PffBT4T-C9C13:$PC_{60}BM$ and PffBT4T-C9C13:$PC_{70}BM$ blend film with weight ratio 1:1.2 at 20 μs. Normalised transient spectra of unannealed PffBT4T-C9C13:$PC_{70}BM$ blend film (c) with weight ratio 9:1 and 1:1.2 at 1 μs, pump at 700 nm (d) with weight ratio 1:1.2, pumped at 700 nm and 455nm and measured at 20 μs, with excitation energy 4.6 and 3.6 μJ cm^{-2}, respectively.*

Several additional TA measurements of the annealed blend films were used to understand the 900 nm band further, such as how the mixed domain crystallinity affects the lifetime of the 900 nm polymer polarons. As shown in Figure 3.12a and 3.12b, three annealed blend films (made under the same annealing conditions) were characterised by the ground state absorption spectra and TA spectra. It was noted that the 900 nm band appeared reproducibly in all three annealed blend films. Furthermore, increasing polaron populations were formed with a reduced vibronic 0-0/0-1 peak ratio (across the natural sample-to-sample variation). This observation is consistent with the increased lifetime of the 900 nm band after thermal

annealing in comparison with the unannealed films (Figure 3.3 and Figure 3.10b). While this reduced vibronic ratio could indicate lower crystallinity, as explained in Figure 3.3, Peng *et al*'s work suggests that this could also be due to increases in fullerene extrusion[34], which can occur upon thermal annealing.

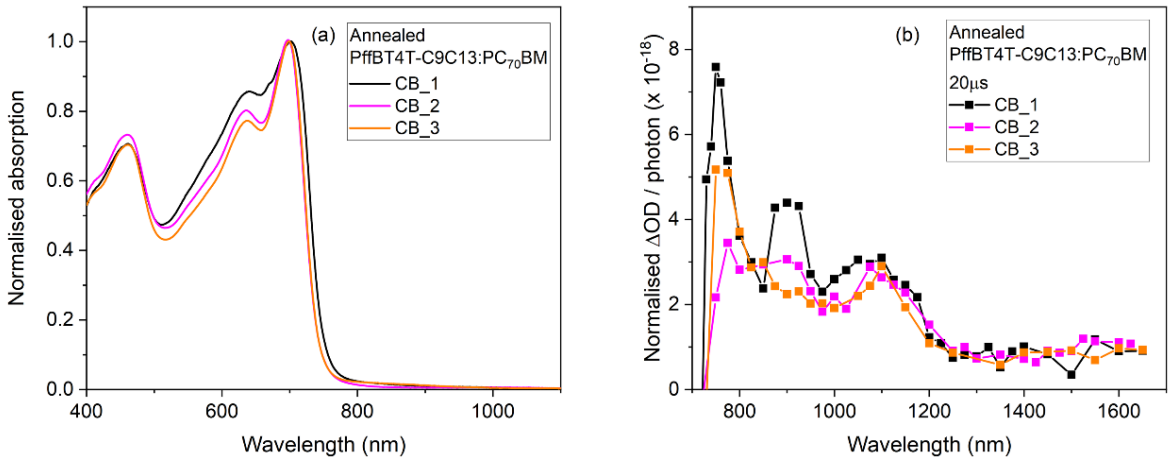

Figure 3.12 *(a) Normalised ground state absorption spectra of annealed PffBT4T-C9C13: $PC_{70}BM$ blend films across the natural sample-to-sample variation. (b) Corresponding normalised (per photon absorbed) transient absorption spectra of annealed PffBT4T-C9C13:$PC_{70}BM$ blend films in chlorobenzene with repeat experiments CB-1, CB-2 and CB-3. The TA spectra were obtained at 20 μs, with pump wavelength at 700 nm and excitation energy around 5 μJ cm^{-2}.*

Now that the spectral position and assignment of the polymer polarons and triplets in blend films have been determined, it is necessary to know the decay process of these transient species to deduce the photophysical process behind them. The presence of the close spectral position of three transient species leads to complex decay kinetics. Figure 3.13 shows the excitation energy dependence decay dynamics at 750 nm and 1100 nm in PffBT4T-C9C13: $PC_{70}BM$ before and after annealing. For all the probe wavelengths, stretched exponential ($\Delta OD \propto e^{(-t/\tau)^{\beta}}$) decay dynamics were observed. In general, the decay kinetics for polarons obey a diffusion-limited bimolecular recombination fitted with a power law decay kinetics, while the triplet typically decays via a mono-exponential decay. However, the stretched exponential decay is related to multiple decay pathways in a dispersive environment.[35,36] The value of β is named the stretched exponential factor (a distribution factor), and it represents the preferential decay to the power law or monoexponential. When the β value is equal to 1, the decay is equivalent to the monoexponential decay, while β value approach to 0 represents a power law decay.

Energy dependence decay dynamics were measured at 750 nm and 1100 nm in both unannealed and annealed blend films, along with plotting for the optical density as a function of excitation density (Figure 3.13 a-e). For polymer polarons, the energy dependence decay dynamics were measured at 750 nm, as displayed in Figure 3.13a (unannealed) and 3.13b (annealed). A reasonably good stretched exponential fitting is used to fit the 900 nm band kinetics with the β value increased from 0.25 to 0.34 after annealing and the lifetime increased from 3 μs to 20 μs. It is suggested that an increased dispersity of the polymer domain after annealing is beneficial to extend polaron lifetimes.

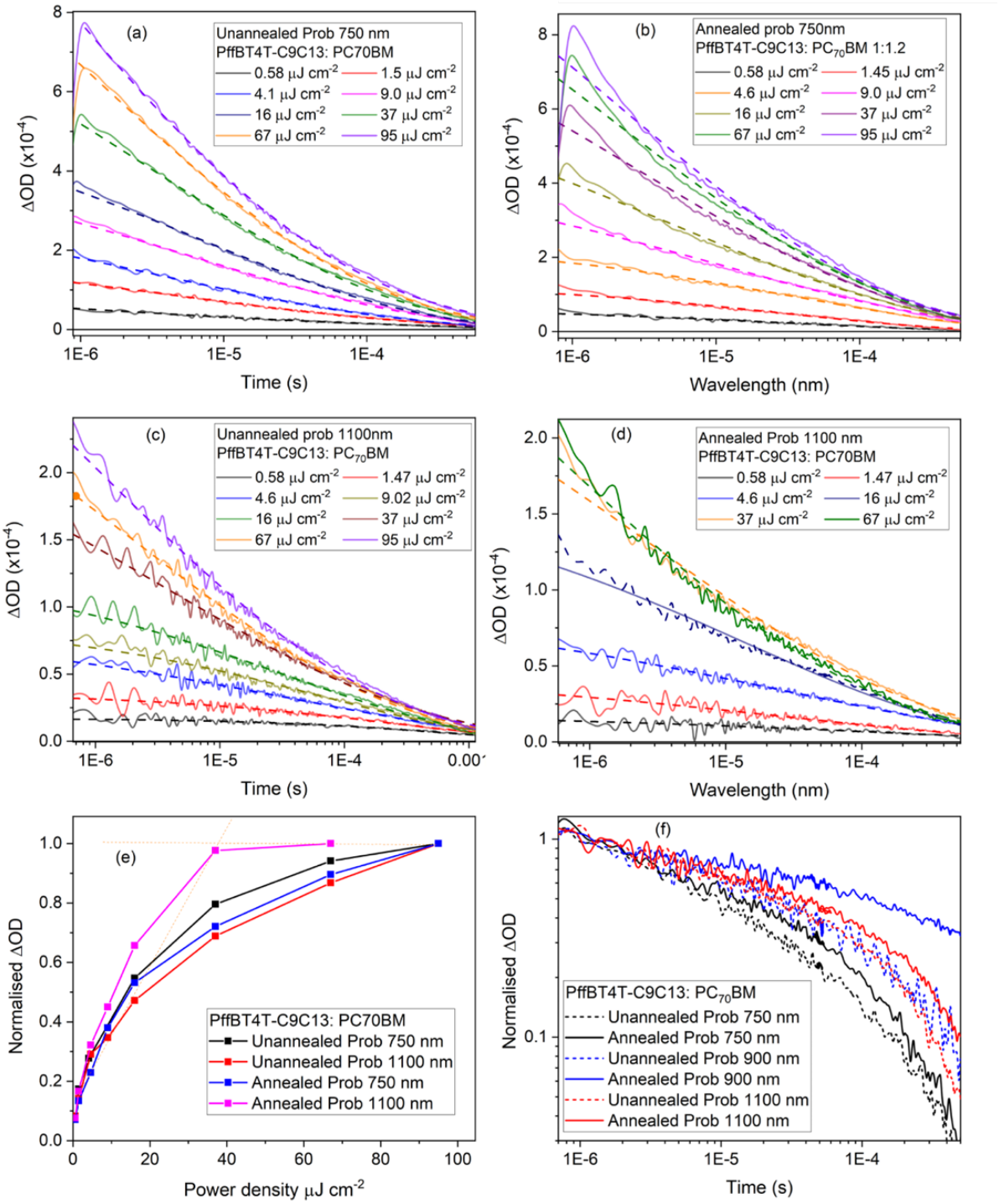

Figure 3.13 *Energy dependence decay dynamics of unannealed (a) probing at 750 nm (c) probing at 1100 nm and annealed PffBT4T-C9C13:$PC_{70}BM$ film (b) probing at 750 nm and (d) probing at 1100 nm with weight ratios 1:1.2, probing at 750 nm and 1100 nm with a range of excitation density from 0.6 to 95 μJ cm^{-2}. (e) Normalised (to 1) trends for optical intensity in function of excitation density for both unannealed and annealed blend PffBT4T-C9C13: $PC_{70}BM$ probe at 750 nm and 1100 nm. (f) Normalised (to 1 at 1 μs) decay dynamics of unannealed and annealed PffBT4T-C9C13:$PC_{70}BM$ (1:1.2) blend films at probe wavelengths of 750 nm, 900 nm, and 1100 nm, with an excitation wavelength of 700 nm and excitation density 4 μJ cm^{-2}.*

Nevertheless, the energy dependence kinetics obtained at 1100 nm shows a fast decay at high excitation density before and after annealing, as shown in Figures 3.13c and 3.13d, respectively. The saturation point can be clearly seen in Figure 3.13e as the crossing point of the dashed line. The β value is around 0.32 in the lower excitation regime (<37 μJ cm^{-2}), whereas it is down to 0.20 with excitation above 37 μJ cm^{-2}. The same energy dependence decay dynamics occurred in polymer triplets generated in the annealed blend but with a different saturation energy at 67 μJ cm^{-2} (β value changed from 0.28 to 0.18). The decrease in β value can be accounted for a contribution of the power law, suggesting a likely attribution to the presence of triplet-triplet annihilation, which can result in additional charge formation under high excitation energy conditions. Moreover, the triplet lifetime was observed to show a slightly increasing from 35 μs to 40 μs before and after annealing in PffBT4T-C9C13: $PC_{70}BM$ blend. Comparing the β value for the 1100 nm band before and after annealing, the reduced β value indicates a less dispersive environment for triplet formation after annealing, which shows little impact on the triplet lifetime.

Due to the spectral proximity of the 900 nm band to the other two strong bands formed in the blend films, the kinetics of 900 nm can be contaminated by either side of the strong peak. The energy dependence decay dynamics at 900 nm band, therefore, would not be discussed. However, the comparison kinetics of 900 nm band to the other two bands exhibited that an obviously longer lifetime was observed for 900 nm band after annealing (τ = 28 μs to τ = 266 μs), as shown in 3.13f. The value of τ was obtained from the stretched exponential fitting to the 900 nm decay of corresponding unannealed and annealed films. The stretched exponential of 900 nm band fitting with a decrease β value from 0.34 to 0.25, which suggests a contribution of power-law decay for the annealed blend. Since the presence of power law is related to Gaussian tails of trap states, these results imply that the ordered polarons in the annealed blend are more influenced by trap states; this would also explain the sensitivity of polarons' lifetime to the local morphology. The observation of stretched exponential kinetics for the PffBT4T-C9C13: $PC_{70}BM$ blend films is therefore consistent with the observed triplet and polarons overlapping absorption bands, and also the morphological variation.

To evaluate the relative populations of each transient species, the TA spectra per photon absorbed were assessed for each sample, as shown in Figure 3.14. Considering the PffBT4T-C9C13 polymer triplet formation at 1100 nm, the triplets' population in the blend is much

higher than any other polymer-only films, like the pristine polymer and control blend with PS (3:2). It should be aware that although the $PC_{70}BM$ triplet also absorbs around 1100 nm,[37] the strong similarity between the $PC_{60}BM$ and $PC_{70}BM$ blend with PffBT4T-C9C13 films indicates that the 1100 nm band is only attributed to the PffBT4T-C9C13 triplet. Since the increased polymer triplet population was observed in the polymer: fullerene blend, in comparison with the pristine film, the triplet must therefore arise from the charge carrier back recombination via a spin-mixing charge transfer state, as the Jablonski diagram in Figure 3.19. Similar to the polymer triplet, the polymer polarons generated at 750 nm and 900 nm also show an increase in charge population in the blend than other polymer-solely films. When increasing the fullerene content from 10% to 55%, both the triplet and polymer polaron population also increases. The higher polaron population in the blend systems leads to an enhancement of the triplet population through this back-transfer process, as has been observed in other OSC blends.[2838–40] It is also interesting to note that the triplet population is unaffected by annealing or acceptor identity, which is consistent with the similar triplet lifetime as we observed in the energy dependence kinetics at 1100 nm (Figure 3.13c and 3.13d).

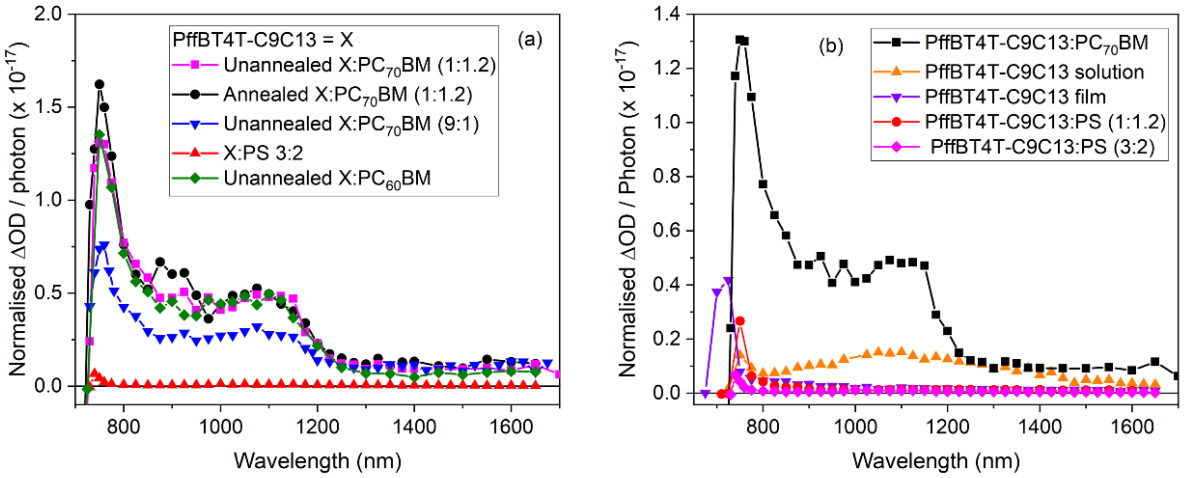

Figure 3.14 *(a) Normalised (per photon absorbed) TA spectra of unannealed PffBT4T-C9C13: $PC_{70}BM$ (1:1.2 and 9:1) and annealed PffBT4T-C9C13: $PC_{70}BM$. All spectra excited at 700 nm with excitation density around 4 μJ cm^{-2}. An excitation wavelength of 700 nm and excitation density 65 μJ cm^{-2} was used for PffBT4T-C9C13:PS (3:2) blend film. All spectra were obtained at 1 μs. (b) Normalised (per photon absorbed) TA spectra of pristine PffBT4T-C9C13 film and solution and the blend PffBT4T-C9C13:PS (3:2) and unannealed PffBT4T-C9C13:$PC_{70}BM$ films.*

Thermal annealing of the PffBT4T-C9C13: $PC_{70}BM$ with a blend ratio 1:1.2 increases the two polaron populations at 1 μs, consistent with the longer charge carrier lifetime observed. The

fullerene-induced ordering polaron at 900 nm has a greater relative population increase (~40%) compared to the 750 nm polarons (~20%) upon annealing. This is consistent with the morphology data, in which we concluded that the enhanced crystallinity and domain size upon annealing is related to a greater predominance of the fullerene-induced ordering regions.

3.4 Characterisation of the PffBT4T-2OD polymer

It is known that the PffBT4T-2OD is a promising organic polymer donor that shows good device performance with $PC_{70}BM$. The power conversion efficiency for the blend system after annealing at 80 °C for 5 min can reach 9.3%. The only difference between PffBT4T-C9C13 and PffBT4T-2OD is that the side chain length of the former is one methyl group longer than that of the latter. The device performance for the PffBT4T-C9C13 is slightly better than the PffBT4T-2OD blend with $PC_{70}BM$ organic photovoltaics (11% VS 9.3%).

The ground state absorption spectra of the pristine PffBT4T-2OD and PffBT4T-2OD blend with $PC_{70}BM$ film before and after annealing are shown in Figure 3.15a. It can see clearly that the 0-0 vibronic transition in all three films peaks at 695 nm and the 0-1 vibronic transition at 635 nm. The 0-0/0-1 vibronic transition ratio in pristine PffBT4T-2OD film is greater than in unannealed blend, followed by annealed blend films. This indicates that the pristine PffBT4T-2OD film shows the greatest polymer crystallinity, and the fullerene-induced ordering no longer exists. The enhanced crystallinity in the pristine PffBT4T-2OD is consistent with the previously reported by Liu *et al.* by using GIWAX.[18] Normalised (per absorption) PL quenching with the addition of $PC_{70}BM$ and after annealing are shown as dash lines in Figure 3.15a. The PL quenching yield for the PffBT4T-C9C13: $PC_{70}BM$ show a reduction in quenching from 94% to 84% upon thermal annealing. The lower PL quenching after annealing represents a smaller number of excitons being quenching due to the larger phase segregation; fewer excitons can reach the D/A interfacial area.

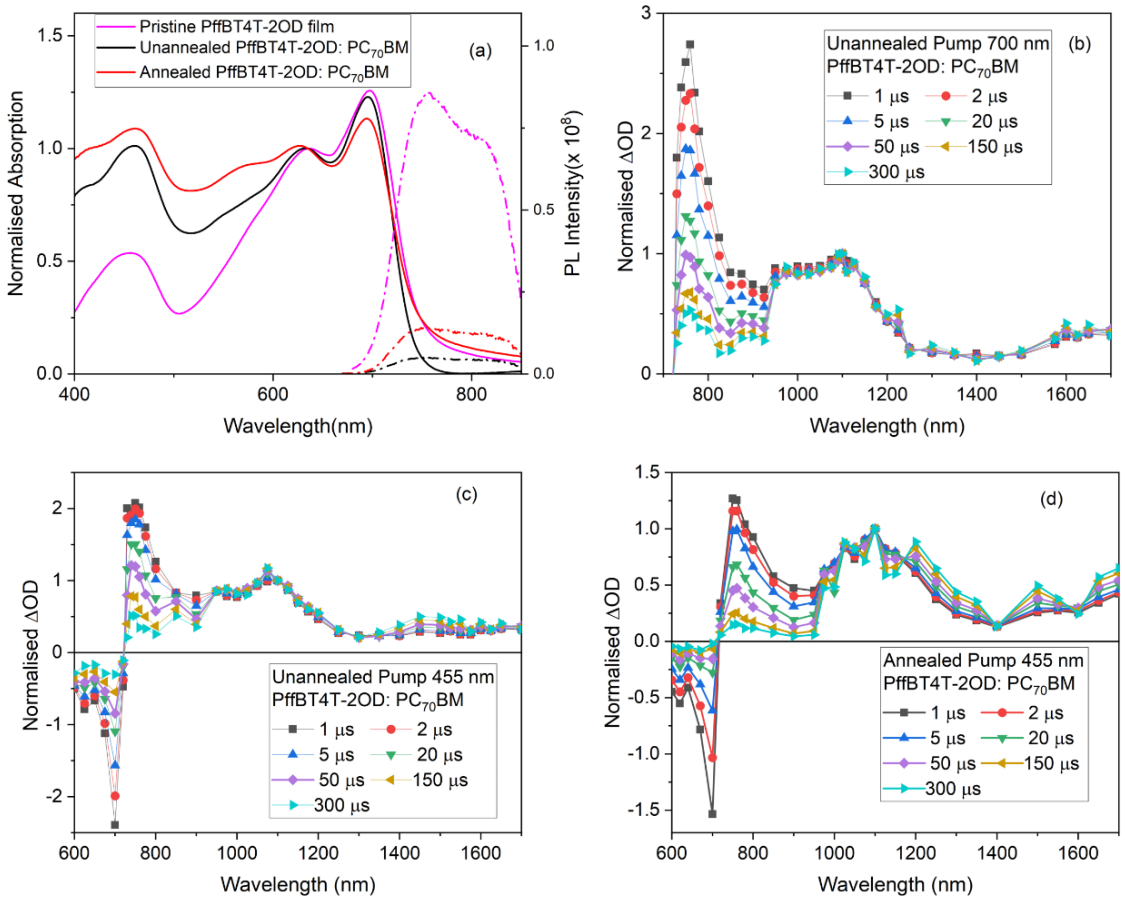

Figure 3.15 *(a) Normalised (to 1 at 635 nm) steady state absorption for pristine PffBT4T-2OD film, unannealed and annealed PffBT4T-2OD:$PC_{70}BM$ (w/t 1:1.2). Normalised (per absorption) photoluminescence emission spectra for pristine PffBT4T-2OD, unannealed and annealed PffBT4T-2OD: $PC_{70}BM$ blend films, obtained with excitation at 650 nm. (b) Spectral evolution of unannealed PffBT4T-2OD:$PC_{70}BM$ blend film excited at 700 nm with excitation density around 4 μJ cm^{-2}. (c) Spectral evolution of unannealed (d) annealed PffBT4T-2OD:$PC_{70}BM$ blend film excited at 455nm with excitation density around 4 μJ cm^{-2}.*

The TA spectral evolution of the unannealed PffBT4T-2OD: $PC_{70}BM$ (Figure 3.15b) shows a similar band position and shape to the PffBT4T-C9C13: $PC_{70}BM$ film with a <750 nm band and 1100 nm band, consistent with the small structural change in polymer. As such, the <750 nm band can be assigned to polymer polarons, and 1100 nm band is attributed to polymer triplets. Interestingly, along with the polaron formation at <750 nm and triplet generated at 1100 nm, there is another weak band around 1600 nm with both excitation at 700 nm and 455 nm. Considering the similar TA spectral position at 1600 nm to the SEC spectra cation formation in PffBT4T-C9C13 film (Figure 3.6a), the 1600 nm can therefore be attributed to PffBT4T-2OD cation. The polaron population formed at 1600 nm has little impact with the excitation

wavelength and annealing (Figure 3.15c and 3.15d), indicating that this type of polaron is generated in a pure polymer domain. It should be noted that there is no evidence of the 900 nm band for PffBT4T-2OD: $PC_{70}BM$, neither before nor after annealing. This is consistent with band assignment to polymer polarons localised in fullerene-induced ordered domains in the PffBT4T-C9C13: $PC_{70}BM$: no such fullerene-induced ordering was observed for PffBT4T-2OD.[41]

For the 1100 nm assignment in PffBT4T-2OD: $PC_{70}BM$ blend system, it should be noted that a previous spectroscopic study using ps-TAS assigned the 1100 nm band to polarons.[42,43] However, our assignment of this band to triplets shows the importance of using longer timescale ns-µs TAS with a series of control experiments to assign peaks. Importantly, ns-µs TAS cannot only identify the triplet or polaron formation but also assess the triplet population and infer the process of triplet formation. For example, if the triplet population scales proportionally with the polaron population, this indicates the triplets form via a polaron back recombination mechanism. The decay kinetics for triplet before and after annealing are shown in Figure 3.16a, it shows that annealing has little impact on the triplet decay, which means the triplet decay independently to the surrounding crystallinity of their environment. This behaviour is in accordance with a monomolecular process such as triplet relaxation, where crystallinity plays a minor role, in contrast to bimolecular process like polaron recombination.

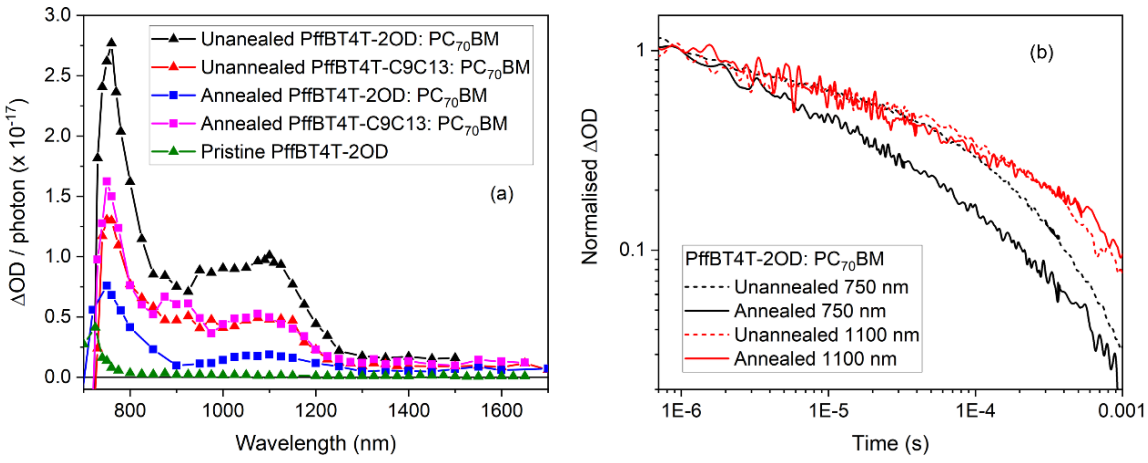

Figure 3.16 *(a) Normalised (per photon absorbed) TA spectra comparison of pristine PffBT4T-2OD film and unannealed and annealed PffBT4T-2OD:$PC_{70}BM$ and PffBT4T-C9C13:$PC_{70}BM$ blends (1:1.2) with excitation wavelength 700 nm at 1 µs. (b) Normalised (to 1 at 1 µs) decay dynamics of unannealed and annealed PffBT4T-2OD: $PC_{70}BM$ blend, obtained with probe wavelengths of 750 nm and 1100 nm with excitation wavelength 700 nm and excitation density 4 µJ cm^{-2}.*

When comparing unannealed PffBT4T-2OD: $PC_{70}BM$ and PffBT4T-C9C13: $PC_{70}BM$, although the <750 nm and 1100 nm bands in the TA spectra are identical, there are a number of differences between the two systems in terms of transient population and kinetics, particularly upon annealing. The PffBT4T-2OD: $PC_{70}BM$ shows a substantially higher polaron population at 750 nm (1µs) compared to the PffBT4T-C9C13: $PC_{70}BM$, thermal annealing of PffBT4T-2OD: $PC_{70}BM$ decreases the polaron population by a factor of 3.5 (Figure 3.16a). In contrast, annealing does not strongly influence the 750 nm polaron formation in the PffBT4T-C9C13: $PC_{70}BM$. The similar polaron to triplet ratio between the two blend systems suggests that polaron back recombination occurs to a similar extent in both systems and thus this cannot be the reason for the difference in behaviour. However, the decay dynamics at 750 nm shown in Figure 3.16b exhibit a considerably faster decay after annealing (the reverse is true for PffBT4T-C9C13). The distribution factor β for the PffBT4T-2OD: $PC_{70}BM$ blend film changes from 0.42 to 0.18 after annealing and their corresponding polaron lifetime is shorter from 56 µs to 0.25 µs. Given the similar polaron to triplet ratio, this suggests that the PffBT4T-2OD polymer polarons have an additional decay pathway upon annealing. The smaller β value after annealing indicates a contribution of trap-limited power law and a less dispersive environment for the annealed PffBT4T-2OD: $PC_{70}BM$ film.

The morphology of the pristine PffBT4T-2OD film, PffBT4T-2OD: $PC_{70}BM$ before and after annealing at 80 °C and 150 °C were studied by AFM (Figure 3.17). From the PffBT4T-2OD series' height images, the average surface roughness was found in pristine PffBT4T-2OD (2.84 nm) to the unannealed blend (5.6 nm) and annealed blend at 80 °C (5.2 nm) and at 150 °C (5.74 nm). The increased surface roughness from pristine to the unannealed blend film shows that phase segregation is induced upon blending. Unlike the increased surface roughness found in the PffBT4T-C9C13: $PC_{70}BM$ blend after annealing, similar surface roughness was found in the unannealed and annealed pffBT4T-2OD: $PC_{70}BM$ blend, even with a heating temperature at 150 °C. Zhang *et al.*[44] have previously pointed out that the surface morphology of PffBT4T-2OD: $PC_{70}BM$ is not representative of the bulk morphology for this blend, and that correlation lengths do indeed increase upon annealing. Combining the TA spectra results and AFM, our hypothesis for the additional decay pathways for polarons is perhaps through the fast geminate recombination back to the ground state in more crystalline, polymer-rich domains of the film.

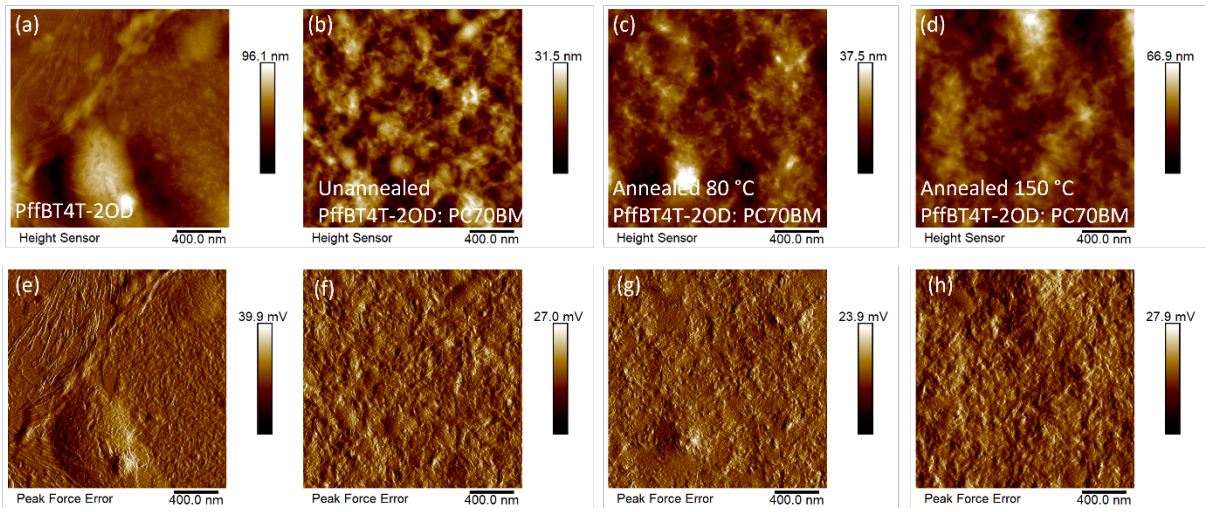

Figure 3.17 *AFM images of phase and topography of unannealed PffBT4T-2OD:$PC_{70}BM$ (1:1.2) (a and c) and annealed PffBT4T-2OD: $PC_{70}BM$ (1:1.2) blend film (b and d) from left to right and top to bottom. Scale bars are 400nm.*

3.5 Discussion

From the spectroscopic study, the significant difference between the PffBT4T-C9C13: $PC_{70}BM$ and PffBT4T-2OD: $PC_{70}BM$ blend systems is the formation of the 900 nm TA band that appears in the former blend. Meanwhile, the morphological study also shows unusual observations in the PffBT4T-C9C13: $PC_{70}BM$ blend, which shows an enhanced crystallinity with the addition of fullerene than the pristine polymer films. Considering both two aspects, the sharp 900 nm band has been assigned to polymer polarons that localised in a fullerene induced ordering (crystalline) domain. This assignment is consistent with the increased intensity of the 900 nm band with fullerene weighting, annealing and excited with polymer dominated wavelength. Importantly, this assignment is consistent with the absence of the fullerene induced ordering for the PffBT4T-2OD: $PC_{70}BM$ and the subsequent absence of the 900 nm band.

Enhanced phase segregation and crystallinity was discovered in PffBT4T-C9C13: $PC_{70}BM$ after thermal annealing, as represented by the schematic diagram 3.18a-b, (marked as the brown square). This results in a longer lifetime of the 900 nm polymer polaron. Based on some repeat TA measurement on annealed blend, the lifetime of 900 nm polaron highly depend on the crystallinity of the mixed domain: the more crystalline the fullerene induced ordered region, the longer the polaron lifetime. The reduced distribution parameter β after annealing gives a good indication of the contribution of power law decay. Since the presence of the power law is related to a Gaussian tail of trap states, these results imply that the ordered polarons in the

annealed blend are more affected by trap states; this would explain the sensitivity of these polarons' lifetime to the local morphology. This could have profound OSC device implications in terms of efficient extraction of charge carriers.

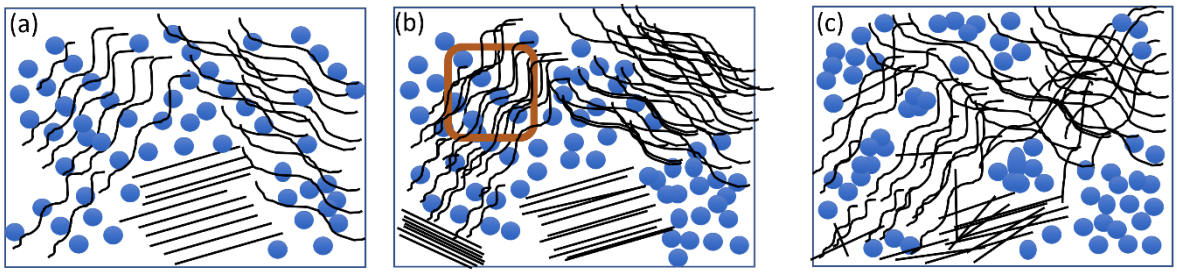

Figure 3.18 *Scheme diagram illustrates the feature of pure polymer, $PC_{70}BM$ and the mixed polymer/$PC_{70}BM$ domain, that proceeding (a), (b) with/without thermal annealing for PffBT4T-C9C13 and (c) PffBT4T-2OD. The curve and straight line represented the crystalline and disorders for polymer and the blue solid circle represented $PC_{70}BM$. The dark brown squared region represented the fullerene-induced crystalline domain. Note: no fullerene-induced ordering formed in unannealed and annealed blend PffBT4T-2OD: $PC_{70}BM$, so they were drawn in one figure.*

An intriguing question comes up is that why the 900 nm fullerene-induced ordering polymer polaron is exhibited in the PffBT4T-C9C13: $PC_{70}BM$ blend but not in the PffBT4T-2OD: $PC_{70}BM$ films. It has been reported by Ye *et al.* that the marginally shorter alkyl chain length can lead to changes in film morphology. Face-on orientation becomes more pronounced compared to the edge-on with longer alkyl chain length[45,46]. Furthermore, the donor/acceptor miscibility reduces.[47] While orientation relative to the substrate is important for organic photovoltaic performance, it is less relevant to optical spectroscopy without the studying of polarisation. Hence, the orientation cannot explain the difference between these two blend systems. As the 900 nm band is generated in a mixed D/A domain, it can be strongly affected by the miscibility of the D and A materials. Miscibility of the fullerene could have large impact on the D and A spatial separation, affecting both the charge generation and recombination process. A greater miscibility for the PffBT4T-2OD: $PC_{70}BM$ is consistent with the high charge population at 1 µs for unannealed PffBT4T-2OD: $PC_{70}BM$ blend, and greater PL quenching. Therefore, the absence of 900 nm band formation in the PffBT4T-2OD: $PC_{70}BM$ blend is likely due to the greater miscibility between the polymer and fullerene.

Another important aspect, observed for both PffBT4T-C9C13:$PC_{70}BM$ and PffBT4T-2OD:$PC_{70}BM$, is the pronounced polymer triplet formation. Because the polymer triplet population scales proportionally with polaron population, and also increases with fullerene weighting, it is most likely that the triplets are being formed from charge carrier back recombination (Figure 3.19). The back-electron transfer triplet electron-hole pair states can lead to a population of energetically low-lying triplet states.[48] Whether this is dominated by geminate or non-geminate triplet formation is unknown. However, considering that the 1100 nm triplet band is also observed in ultrafast spectroscopy, having been assigned to polarons in previous literature reports for other PffBT4T polymers [49, 50, 20,] this suggests that geminate recombination is likely to play a role for these blends. However, a contribution from non-geminate recombination is also highly likely. A comparison of the triplet decay kinetics on μs timescales (Figure 3.20) shows that the fullerene blends' polymer triplet decay much more slowly compared to the inert polystyrene blend's polymer triplet (which must only be formed via standard intersystem crossing). The implication of this is that the polymer triplet population in the fullerene blends is being regenerated via non-geminate charge recombination simultaneously with its decay, thereby retarding the overall kinetics. However, it is noteworthy that non-geminate triplet formation may not affect device performance if charge carrier mobilities are high enough: charges can be extracted prior to the recombination process [51].

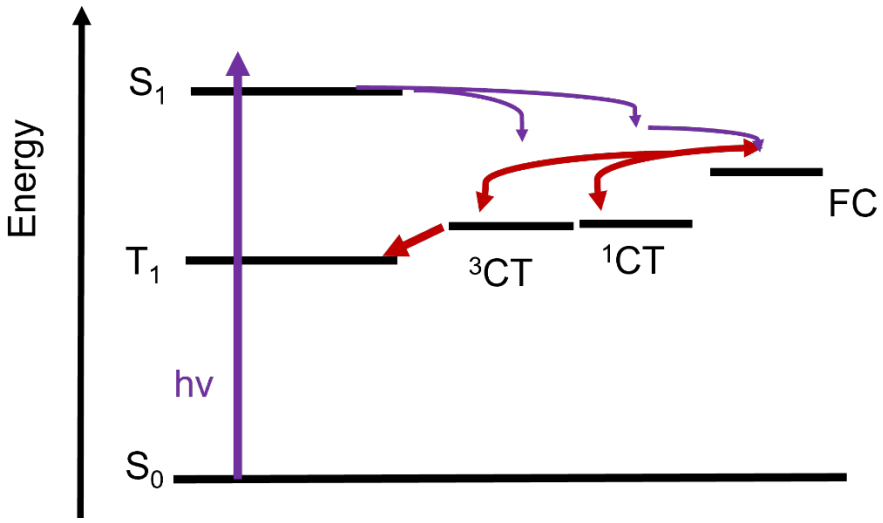

Figure 3.19 *Schematic representation of free charge carriers back recombination process to form low energy triplet state (T_1) through the intermediate ^3CT state.*

The identification of significant triplet populations in PffBT4T-C9C13:$PC_{70}BM$ and PffBT4T-2OD:$PC_{70}BM$ blends, both of which are capable of > 10 % device efficiencies, is, therefore, an important step. Not only does it highlight the value of TAS on microsecond timescales, but it also reveals yet more high-efficiency blends in which triplets are present to a significant level, across all timescales.[52] In the case of PffBT4T-C9C13:$PC_{70}BM$ and PffBT4T-2OD:$PC_{70}BM$ blends, the triplet kinetics change very little or not at all upon thermal annealing, suggesting that despite being formed via charge carrier recombination (presumably at a donor/acceptor interface), they become primarily localised within pristine polymer domains that are unaffected by annealing (annealing of pristine PffBT4T polymer films is known to induce negligible morphological changes [20]). The polymer triplet decay kinetics are also similar with lower fullerene weightings (**Figure 3.20**), and in $PC_{60}BM$ blends, which is also consistent with this conclusion. This sequestration into the pristine polymer domains is likely to mean that the energy is lost, and thus the charge recombination in this case is a loss pathway.

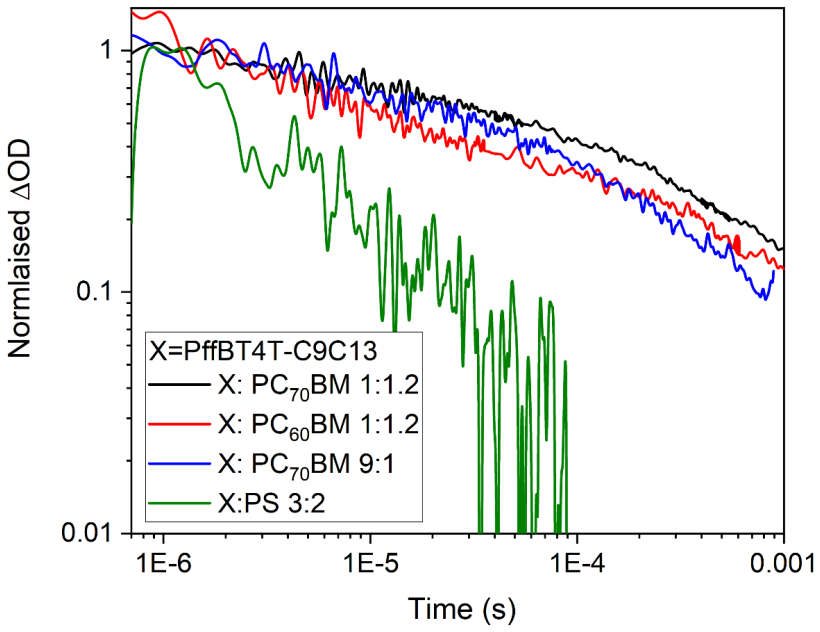

Figure 3.20 *Normalised (to 1 at 1μs) decay dynamics of unannealed PffBT4T-C9C13:$PC_{70}BM$ film with weight ratios 1:1.2 and 9:1, unannealed PffBT4T-C9C13:$PC_{60}BM$ (1:1.2), and PffBT4T-C9C13:PS (3:2) blend films, using a probe wavelength of 1100 nm, excitation wavelength of 700 nm, and excitation density of 65 μJ cm^{-2}.*

Finally, the comparison of PffBT4T-C9C13:$PC_{70}BM$ and PffBT4T-2OD:$PC_{70}BM$ blends to their device performance is discussed. Despite the large differences in photophysics observed here,

the two blends have very similar device efficiencies, with annealed PffBT4T-2OD:$PC_{70}BM$ showing slightly higher efficiency (10.0 %) compared to PffBT4T-C9C13:$PC_{70}BM$ (9.3 %) in CB[3]. Assuming the two polymer polarons have similar absorption cross-sections, annealed PffBT4T-C9C13:$PC_{70}BM$ displays a greater polaron population at 750 nm at 1 μs and slower decay kinetics compared to PffBT4T-2OD:$PC_{70}BM$. However, we have shown that PffBT4T-C9C13:$PC_{70}BM$ is substantially less crystalline than PffBT4T-2OD:$PC_{70}BM$, and this is likely to be accompanied by a reduced charge carrier mobility [3, 53, 54]. Since the mobility-lifetime product ($\mu\tau$) is often considered a figure of merit in determining device performance [55], these two factors may cancel one another out, essentially leading to similar device performances. It should also be noted that PffBT4T-2OD:$PC_{70}BM$ displays an unusual field-assisted exciton separation and thus would exhibit greater charge generation in an operational device.[56]

3.6 Conclusions

A morphology and spectroscopic study of PffBT4T-C9C13 and its fullerene blends before and after annealing is presented in this chapter. Unusually, the pristine polymer film displays the lowest crystallinity, with the significant enhancement in crystallinity in the blend attributed to fullerene induced ordering and a more significant predominance of π-π stacking. Thermal annealing of the blend led to even greater enhancements in film crystallinity and phase segregation.

On microsecond timescales, evidence of polymer triplets generated via charge carrier recombination is observed for PffBT4T-C9C13:$PC_{70}BM$, both before and after thermal annealing. Bimodal polymer polarons are also observed: fast-decaying polarons in pristine polymer domains and polarons localised in the fullerene-induced ordered regions, which decay more slowly. The lifetime of the latter polaron is strongly morphology-dependent and displays characteristics of trapping. All three transient species decayed via stretched exponential kinetics, not at all common for organic photovoltaic materials. Here, we attribute such kinetics to the spectral proximity of three distinct species in different morphologies, leading to multiple decay pathways.

PffBT4T-2OD – which varies from PffBT4T-C9C13 by only the alkyl chain length – displays quite different spectral behaviour. No evidence of fullerene-induced ordering is observed, and this

is accompanied by the loss of the trapped polymer polaron at 900 nm: these observations were attributed to enhanced donor/acceptor miscibility for PffBT4T-2OD. Despite the large differences in photophysics, a comparison to the literature shows that PffBT4T-C9C13 and PffBT4T-2OD based solar cells exhibit similar device performances. We attribute this to the more amorphous PffBT4T-C9C13 blend possessing both slower charge carrier recombination kinetics but also lower charge carrier mobility. This highlights how crystallinity and polymer miscibility lead to large changes in charge generation, recombination, and mobility for two very similar materials in terms of chemical structure, demonstrating how morphology control is key for OSC device efficiency.

3.7 References

1 Z. Chen, P. Cai, J. Chen, X. Liu, L. Zhang, L. Lan, J. Peng, Y. Ma and Y. Cao, *Advanced Materials*, 2014, **26**, 2586–2591.

2 Y. Zhang, A. J. Parnell, F. Pontecchiani, J. F. K. Cooper, R. L. Thompson, R. A. L. Jones, S. M. King, D. G. Lidzey and G. Bernardo, *Sci Rep*, 2017, **7**, 1–12.

3 J. Zhao, Y. Li, G. Yang, K. Jiang, H. Lin, H. Ade, W. Ma and H. Yan, *Nat Energy*, 2016, **1**, 15027.

4 Y. Zhang, A. J. Parnell, O. Blaszczyk, A. J. Musser, I. D. W. Samuel, D. G. Lidzey and G. Bernardo, *Physical Chemistry Chemical Physics*, 2018, **20**, 19023–19029.

5 H. Cha, S. Wheeler, S. Holliday, S. D. Dimitrov, A. Wadsworth, H. H. Lee, D. Baran, I. McCulloch and J. R. Durrant, *Adv Funct Mater*, 2018, **28**, 1–11.

6 T. M. Clarke, A. Ballantyne, S. Shoaee, Y. W. Soon, W. Duffy, M. Heeney, I. McCulloch, J. Nelson and J. R. Durrant, *Advanced Materials*, 2010, **22**, 5287–5291.

7 H. Cha, C.-H. Tan, J. Wu, Y. Dong, W. Zhang, H. Chen, S. Rajaram, K. S. Narayan, I. McCulloch and J. R. Durrant, *Adv Energy Mater*, 2018, **8**, 1801537.

8 J. M. Marin-Beloqui, K. J. Fallon, H. Bronstein and T. M. Clarke, *Journal of Physical Chemistry Letters*, 2019, **10**, 3813–3819.

9 J. Guo, H. Ohkita, S. Yokoya, H. Benten and S. Ito, *J Am Chem Soc*, 2010, **132**, 9631–9637.

10 Z. Chen, P. Cai, J. Chen, X. Liu, L. Zhang, L. Lan, J. Peng, Y. Ma and Y. Cao, *Advanced Materials*, 2014, **26**, 2586–2591.

11 H. Hu, P. C. Y. Chow, G. Zhang, T. Ma, J. Liu, G. Yang and H. Yan, *Acc Chem Res*, 2017, **50**, 2519–2528.

12 B. Xu and S. Holdcroft, *Macromolecules*, 1993, **26**, 445.

13 H. Hoppe and N. S. Sariciftci, *J Mater Chem*, 2006, **16**, 45–61.

14 A. Serbenta, O. v. Kozlov, G. Portale, P. H. M. van Loosdrecht and M. S. Pshenichnikov, *Sci Rep*,2016, **6**, 36236.

15 H. Kang, W. Lee, J. Oh, T. Kim, C. Lee and B. J. Kim, *Acc Chem Res*, 2016, **49**, 2424–2434.

16 D. Baran, T. Kirchartz, S. Wheeler, S. Dimitrov, M. Abdelsamie, J. Gorman, R. S. Ashraf, S. Holliday, A. Wadsworth, N. Gasparini, P. Kaienburg, H. Yan, A. Amassian, C. J. Brabec, J. R. Durrant and I. McCulloch, *Energy Environ Sci*, 2016, **9**, 3783–3793.

17 J. Wade, S. Wood, E. Collado-Fregoso, M. Heeney, J. Durrant and J. S. Kim, *Journal of Physical Chemistry C*, 2017, **121**, 20976–20985.

18 Y. Liu, J. Zhao, Z. Li, C. Mu, W. Ma, H. Hu, K. Jiang, H. Lin, H. Ade and H. Yan, *Nat Commun*, 2014, **5**, 4007.

19 W. Zhang, R. Hu, D. Li, M. M. Huo, X. C. Ai and J. P. Zhang, *Journal of Physical Chemistry C*, 2012, **116**, 4298–4310.

20 W. Zhang, R. Hu, X. Zeng, X. Su, Z. Chen, X. Zou, J. Peng, C. Zhang and A. Yartsev, *Polymers (Basel)*, 2019, **11**, 408.

21 R. Dhanker, C. L. Gray, S. Mukhopadhyay, S. Nunez, C. Y. Cheng, A. N. Sokolov and N. C. Giebink, *Nat Commun*, 2017, **8**, 2252

22 C. Tengstedt, W. Osikowicz, W. R. Salaneck, I. D. Parker, C. H. Hsu and M. Fahlman, *Appl Phys Lett*, 2006, **88**, 1–3.

23 M. Oehzelt, N. Koch and G. Heimel, *Nat Commun*, 2014, **5**, 4174.

24 M. B. Qarai, R. Ghosh and F. C. Spano, *Journal of Physical Chemistry C*, 2021, **125**, 24487–24497.

25 R. Hu, W. Zhang, L. M. Fu, J. P. Zhang and X. C. Ai, *Synth Met*, 2013, **169**, 41–47.

26 X. M. Jiang, R. Österbacka, O. Korovyanko, C. P. An, B. Horovitz, R. A. J. Janssen and Z. V. Vardeny, *Adv Funct Mater*, 2002, **12**, 587–597.

27 J. Guo, H. Ohkita, H. Benten and S. Ito, *J Am Chem Soc*, 2009, **131**, 16869–16880.

28 F. Etzold, I. A. Howard, N. Forler, A. Melnyk, D. Andrienko, M. R. Hansen and F. Laquai, *Energy Environ Sci*, 2015, **8**, 1511–1522.

29 A. Köhler and H. Bässler, *Materials Science and Engineering R: Reports*, 2009, **66**, 71–109.

30 P. C. Y. Chow, S. Albert-Seifried, S. Gélinas and R. H. Friend, *Advanced Materials*, 2014, **26**, 4851–4854.

31 S. Karuthedath, J. Gorenflot, Y. Firdaus, W. Y. Sit, F. Eisner, A. Seitkhan, M. K. Ravva, T. D. Anthopoulos and F. Laquai, *Adv Energy Mater*, 2019, **9**, 1802476.

32 J. Fulara, M. Jakobi and J. P. Maier, *Chem Phys Lett*, 1993, **206**, 203–209.

33 J. Guo, H. Ohkita, S. Yokoya, H. Benten and S. Ito, *J Am Chem Soc*, 2010, **132**, 9631–9637.

34 Z. Peng, X. Jiao, L. Ye, S. Li, J. J. Rech, W. You, J. Hou and H. Ade, *Chemistry of Materials*, 2018, **30**, 3943–3951.

35 J. Albero, Y. Zhou, M. Eck, F. Rauscher, P. Niyamakom, I. Dumsch, S. Allard, U. Scherf, M. Krüger and E. Palomares, *Chem Sci*, 2011, **2**, 2396–2401.

36 J. Nelson, *Phys Rev B, 1999, **59**, 15374*

37 Keiderling C 2017 PhD Thesis Imperial College London

38 A. J. Gillett, A. Privitera, R. Dilmurat, A. Karki, D. Qian, A. Pershin, G. Londi, W. K. Myers, J. Lee, J. Yuan, S. J. Ko, M. K. Riede, F. Gao, G. C. Bazan, A. Rao, T. Q. Nguyen, D. Beljonne and R. H. Friend, *Nature*, 2021, **597**, 666–671.

39 D. G. Bossanyi, Y. Sasaki, S. Wang, D. Chekulaev, N. Kimizuka, N. Yanai and J. Clark, *JACS Au*, 2021, **1**, 2188–2201.

40 S. Holliday, R. S. Ashraf, A. Wadsworth, D. Baran, S. A. Yousaf, C. B. Nielsen, C. H. Tan, S. D. Dimitrov, Z. Shang, N. Gasparini, M. Alamoudi, F. Laquai, C. J. Brabec, A. Salleo, J. R. Durrant and I. McCulloch, *Nat Commun*, 2016, **7**, 11585.

41 W. Ma, G. Yang, K. Jiang, J. H. Carpenter, Y. Wu, X. Meng, T. McAfee, J. Zhao, C. Zhu, C. Wang, H. Ade and H. Yan, *Adv Energy Mater*, 2015, **5**, 1501400

42 Z. Hamid, A. Wadsworth, E. Rezasoltani, S. Holliday, M. Azzouzi, M. Neophytou, A. A. Y. Guilbert, Y. Dong, M. S. Little, S. Mukherjee, A. A. Herzing, H. Bristow, R. J. Kline, D. M. DeLongchamp, A. A. Bakulin, J. R. Durrant, J. Nelson and I. McCulloch, *Adv Energy Mater*, 2020, **10**, 1903248.

43 Y. Dong, H. Cha, J. Zhang, E. Pastor, P. S. Tuladhar, I. McCulloch, J. R. Durrant and A. A. Bakulin, *Journal of Chemical Physics*, 2019, **150**, 104704.

44 Y. Zhang, A. J. Parnell, F. Pontecchiani, J. F. K. Cooper, R. L. Thompson, R. A. L. Jones, S. M. King, D. G. Lidzey and G. Bernardo, *Sci Rep*, 2017, **7**, 44269.

45 M. Li, P. J. Leenaers, M. M. Wienk and R. A. J. Janssen, *J Mater Chem C Mater*, 2020, **8**, 5856–5867.

46 J. Zhao, Y. Li, G. Yang, K. Jiang, H. Lin, H. Ade, W. Ma and H. Yan, *Nat Energy*, 2016, **1**, 15027.

47 R. Ma, G. Li, D. Li, T. Liu, Z. Luo, G. Zhang, M. Zhang, Z. Wang, S. Luo, T. Yang, F. Liu, H. Yan and B. Tang, *Solar RRL*, 2020, **4**, 2000250.

48 S. D. Dimitrov, S. Wheeler, D. Niedzialek, B. C. Schroeder, H. Utzat, J. M. Frost, J. Yao, A. Gillett, P. S. Tuladhar, I. McCulloch, J. Nelson and J. R. Durrant, *Nat Commun*, 2015, **6**, 1–8.

49 H. Cha, S. Wheeler, S. Holliday, S. D. Dimitrov, A. Wadsworth, H. H. Lee, D. Baran, I. McCulloch and J. R. Durrant, *Adv Funct Mater*, 2018, **28**, 1–11.

50 Y. Dong, H. Cha, J. Zhang, E. Pastor, P. S. Tuladhar, I. McCulloch, J. R. Durrant and A. A. Bakulin, *J Chem Phys*, 2019, **150**, 104704.

51 C. W. Schlenker, K. S. Chen, H. L. Yip, C. Z. Li, L. R. Bradshaw, S. T. Ochsenbein, F. Ding, X. S. Li, D. R. Gamelin, A. K. Y. Jen and D. S. Ginger, *J Am Chem Soc*, 2012, **134**, 19661–19668.

52 S. Karuthedath, J. Gorenflot, A. Melianas, Z. Kan, M. Kemerink and F. Laquai, *Journal of Physical Chemistry Letters*, 2020, **11**, 2838–2845.

53 C. H. Woo, C. Piliego, T. W. Holcombe, M. F. Toney and J. M. J. Fréchet, *Macromolecules*, 2012, **45**, 3057–3062.

54 M. D. McGehee, N. C. Cates, R. Gysel, J. E. P. Dahl and A. Sellinger, *Chemistry of Materials*, 2010, **22**, 3543–3548.

55 C. Vijila, S. P. Singh, E. Williams, P. Sonar, A. Pivrikas, B. Philippa, R. White, E. Naveen Kumar, S. Gomathy Sandhya, S. Gorelik, J. Hobley, A. Furube, H. Matsuzaki and R. Katoh, *J Appl Phys*, 2013, **114**, 184503.

56 A. Weu, T. R. Hopper, V. Lami, J. A. Kreß, A. A. Bakulin and Y. Vaynzof, *Chemistry of Materials*, 2018, **30**, 2660–2667.

Chapter 4 Quantifying triplet formation in conjugated polymer/ non-fullerene acceptor blends

4.1 Introduction

As introduced in Chapter 3, the TDA polymers play an important role in controlling the morphology of BHJ fullerene blend films to realise high performance devices. In contrast, a relatively poor device performance was observed for OSCs consisting of the TDA polymer with NFAs. For instance, an efficiency of 10.8% was observed for the PffBT4T-2OD with $PC_{70}BM$ solar cell,[1] while a lower efficiency of 4% was produced with NFA blend with the same polymer.[2] It was reported that relatively high-performance state-of-art NFA based OSCs need to match with a reduced crystalline polymer, despite their low performance with fullerene acceptors. Such different requirement of polymer morphology for the fullerene and NFA-based OSCs reveals different dominated photophysical processes occurring from fullerene to NFA blend systems.

Since the triplet state is shown with the lowest energy in the blend system, its formation and the following decay process are generally regarded as a non-radiative energy loss process. However, several high performance NFA based OSCs have illustrated that a high yield of triplet formation was observed in the blend system.[3–6] Gillett et al[7] reported that Y6 triplet formation observed in highly efficient PM6:Y6 blend systems (18%) occur preferentially through bimolecular charge back recombination. Several blend films without evidence for BR also show that triplet formation can be created via ISC from a singlet state or generated through a back electron transfer from a CT state. The rate of ISC is controlled by the magnitude of spin-orbit coupling and the energy difference between the singlet and triplet states (exchange energy). In general, BR of free charge carriers can be detected in ns-µs while ISC and back electron transfer recombination occurs on fast ps timescales.[8]

Triplet formation can also depend on the morphology of the active layer. For example, Rao et al. have shown that the charge delocalisation enabled by ordered fullerene domains promotes CT state separation over the competing process of back electron transfer to create triplets.[9] As shown in figure 4.1, the triplet preferentially forms in the amorphous domain, which provides small mixed D/A area (green area) in which charges can recombine to form CT state that decays through an electron back transfer to the low energy T_1 state. In polymer:NFA

blend systems, triplet formation is also correlated with morphology. Gillet et al. studied the polymer PTB7-Th with NFA: IEICO-0F and IEICO-2F blend, and have shown that the D/A spatial distance affects the relative energy of the ^{1}CT and ^{3}CT states. A hybridisation of ^{1}CT and localised exciton (S_1) occurs when D/A is displayed with a closer spatial distance, resulting in a destabilised ^{3}CT decaying to T_1 and a stabilised ^{1}CT state.

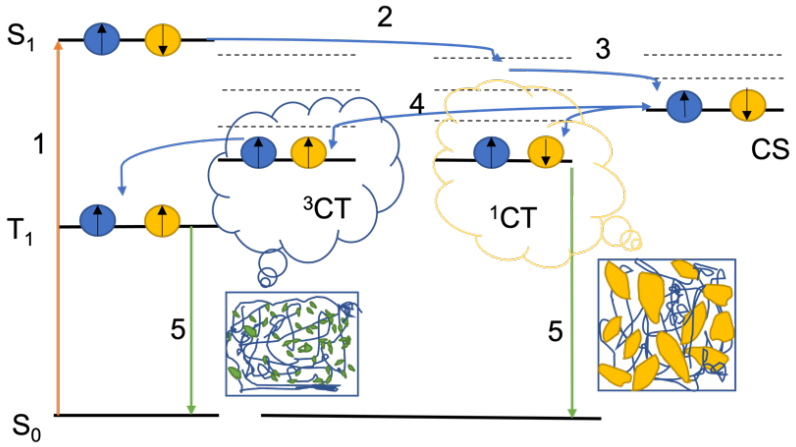

Figure 4.1 *State energy level diagram for triplet generation and charge back recombination to form triplet, which depends on the morphology of the film. (This figure is redrawed based on Rao's paper[9]). 1. The S_1 state was initially excited, and it could via radiatively decay to the ground state or/ and non-radiatively decay 2. to form a charge transfer (^{1}CT) state at the D/A interface, which could be 3. dissociate to form the charge separations state (CS). However, 4. if the energy level of the CT state is close to the CS state, the dissociated CS state can recombine to re-generate the ^{1}CT or ^{3}CT state with ratio 1:3, depending on the local morphology of the blends. The ^{1}CT state would prefer form in the crystalline domain and the ^{3}CT state generated in relatively amorphous domain. 5. non-radiative decay for T_1 and ^{1}CT state.*

Surprisingly, high PCE is also accompanied by a high triplet yield which is counterintuitive as triplet often viewed as an energy loss pathway. However, triplet state exists as an intermediate excited state in OSCs, which is difficult to be directly detected, like singlet excitons or free charge carriers. Therefore, this leads to the poorly understood exact role of triplet in OSCs. Since triplet is not directly photogenerated nor extracted from the OSC devices, triplet parameters such as their absorption cross-section, actual population, and quantum yield of generation and decay are often difficult to measure accurately.

In this chapter, triplet sensitisation experiment is used as an effective way to calculate the NFA triplet extinction coefficient (ε) and quantify triplet yield in the pristine and blend NFA films. NFA triplet state can be created via energy transfer from the high energy sensitizer

triplet state, and the value of ε of NFAs could be calculated on the base of the reference sensitizer ε value. However, if the triplet energy of the target material is higher than the sensitiser triplet energy, the energy transfer process is forbidden, as shown in Figure 4.2. When the ε of the triplet state has been determined for NFAs, their corresponding triplet yield can be calculated according to the Beer-Lambert law in either their pristine or blending systems with polymer.

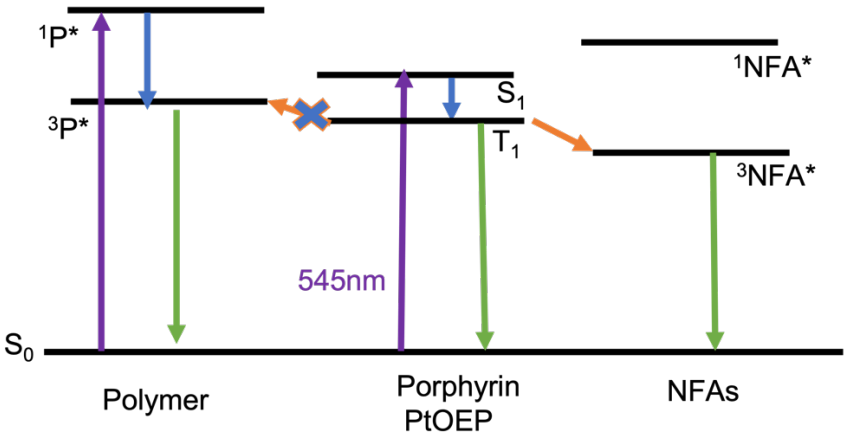

Figure 4.2 *Jablonski type diagram showing the utilisation of porphyrin triplet states for NFAs triplet extinction coefficient determination via energy transfer, while the energy transfer is forbidden from PtOEP triplet to pristine polymer due to the high energy level of polymer.*

In this chapter, charge photogeneration and morphology studies were performed on the same TDA polymer PffBT4T-C9C13 as Chapter 3 [10] and four well-known NFAs, including ITIC, ITIC-Th, ITIC-2F and Y6. The chemical structures of the donor and acceptors are shown in Figure 4.3. To choose the appropriate non-fullerene acceptors for a given polymer donor, the first thing to consider is to create a series of driving forces for electron or hole transfer to study any correlation between the driving force to the charge photogeneration. ITIC and Y6 series are promising NFAs, showing reasonably good OSCs device performance with TDA polymers.

ITIC series' NFAs is a section of fused-ring electron acceptors (FREAs) that have achieved tremendous success in pushing the PCE of the OSCs. FREAs were proposed to exhibit some unique molecule packing features due to the large steric hindrance of the bulky side chains. Yi and co-workers performed molecular dynamics (MD) simulations and predicted that ITIC would favour a π-π stacking of the end-capped 1,1-dicayanomethylene-3-indane IC groups

over the conventional π-π stacking of the core indacenodithieno[3,2-b]-thiophene IDTT group. Mai et al. demonstrated that a common π-π stacking of the long-range structure ordering along the backbone direction originated from favoured end-group π-π stacking in ITIC and ITIC-Th.[11] The thienyl side chain in ITIC-Th deepens molecular energy levels relative to the phenyl group in ITIC, providing a strong S-S interaction that adopts a tighter π-π packing and better crystallinity.[1213] Fluorination has been shown as an effective way to suppress triplet formation and improve device performance by optimal triplet energy alignment.[14] ITIC-2F and Y6 were chosen as fluorinated NFAs to be studied with the TDA polymer. ITIC-2F shows enhanced inter/ intramolecular interactions due to non-covalent F-H and S-F interactions, improving crystallinity and facilitating charge transfer.[15] In addition, the existence of the fluoride group in the ITIC-2F suggests a potential for high polarization and reduced Columbic interaction between electrons and holes.[16] Y6 as the new FREA with A-DA'D-A architecture wherein the D core is replaced by the fused DA'D core involving an electron-deficient benzothiadiazole moiety.[17] It gives a wider absorption range to the near-infrared and a lower energy loss. Y6 as a prototypical high-achiever NFA shows a capable of OPV device efficiencies of 18% blending with D18 [18], even higher to 19% ternary with D18 and BS3TSe-4F with certain ratios.[19] Notably, PffBT4T-C9C13 blends with fullerenes exhibited strong tendencies to polymer triplet formation, despite its high performance in OSCs, and morphology-dependent bimodal polaron formation. The energy levels for these materials are presented in Table 4.1, which are calculated as the energy onset of the cyclic voltammetry (CV) in Figure 4.10.

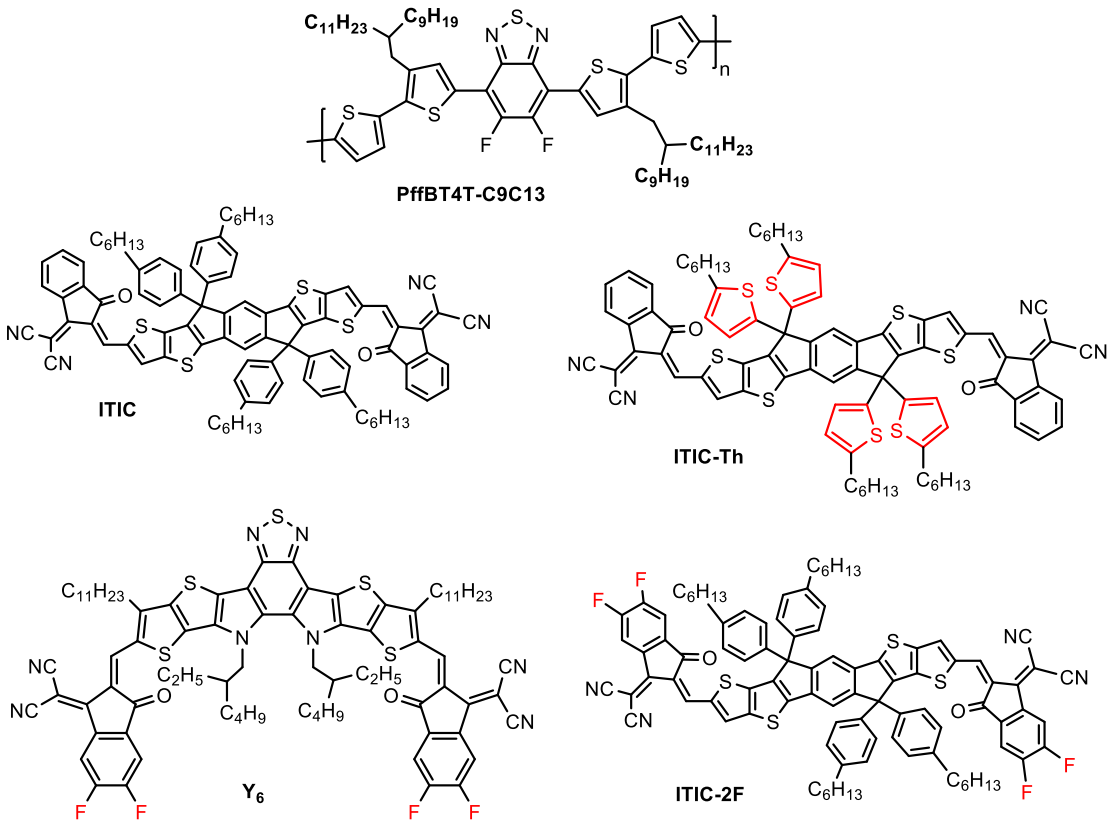

Figure 4.3 *Chemical structure for polymer PffBT4T-C9C13 and non-fullerene acceptors IDFBR, ITIC, ITIC-Th, ITIC-2F.*

In this chapter, the triplet formation and decay were studied by ns-µs TAS. As the triplet via ISC or spin mixing CT state generally occurred in picoseconds, it rarely is identified by our setup, but we can't negligible their formation on fast timescales. Atomic force microscopy (AFM) and grazing incident X-ray diffraction (GIXRD) will be used to study the morphology of the polymer and NFAs in their pristine and blend films.

4.2 Experimental

4.2.1 Materials

The polymer PffBT4T-C9C13 was sourced from Ossila (Mw= 123,796, PDI=1.68). The NFAs ITIC, ITIC-Th, ITIC-2F, and Y6 were all purchased from Ossila. The control material polystyrene (PS), the triplet sensitiser zinc tetraphenyl-porphyrin (ZnTpp), the solvent chlorobenzene (CB, 99.9%), and the additive diiodooctane (DIO) were purchased from Sigma-Aldrich.

4.2.2 Sample preparation

All the solutions were prepared outside the glove box and then transferred inside the glove box with stirring rate 450 rpm overnight. All the pristine acceptors' solutions (ITIC, ITIC-Th, ITIC-2F and Y6) were made with concentration 0.01 mg mL^{-1} in CB for

triplet position determination by TAS. Freeze-pump-thaw procedure was used to extract air from solutions for TAS measurements. Thin films were made by spin coating inside the glove box onto 1 cm^2 glass substrates under nitrogen atmosphere. The pristine acceptors' films were fabricated from 10 mg mL^{-1} in CB solutions, heated overnight at 40°C and spin coated at 900 rpm. All polystyrene (PS):acceptor blend films were made with a weight ratio 1:1.2 from 12 mg mL^{-1} in CB solution, heated at 40 °C and spin coated with spin rate of 900 rpm. The glass substrates and glass pipette to make blend films PffBT4T-C9C13 with non-fullerene acceptors were pre-heated at 100 °C for 20 minutes, and blend films were made by spin coating from hot solution at a spin rate of 900 rpm for 60 seconds. All PffBT4T-C9C13/acceptor blend films were made with a weight ratio 1:1.2 from 10 mg mL^{-1} in CB and 3 % DIO at a spin rate of 900 rpm and heating at temperature of 100 °C. For the sensitisation experiment, both ZnTpp and non-fullerene acceptors solution were made with concentration 7 x 10^{-6} M in CB, and the blend solution ZnTpp with non-fullerene acceptors was made with a molar ratio 1:1. All the films measured for this chapter are freshly made.

4.3 Results

As introduced above, the triplet states have been widely observed in NFAs blending with polymer OSCs. In this chapter, NFAs' triplet spectrum was identified by ns-µs TA measurements in solid (pristine and PS:NFAs' film) and solution phases. The PS:NFAs' films were used to mimic the morphology of polymer: NFAs blend, and to reveal the impact of morphology to the decay of NFAs triplet. PS was used as an inert material. Some of the key results for the NFAs were summarised in Table 4.1

Table 4.1 *Summary of singlet and triplet parameters for the materials studied. The HOMO level of PffBT4T-C9C13 and the LUMO level of acceptors were obtained from cyclic voltammogram (Figure 4.10). 3P* refers to the polymer triplet.*

	S_1 energy (eV)	HOMO (eV)	LUMO (eV)	PLQE (%)	^{3}NFA* ε (x 10^4mol L^{-1} cm^{-1})	Triplet τ solution (µs)	^{3}NFA* τ in blend (µs)	^{3}P* τ in blend (µs)
PffBT4T-C9C13	1.71	-5.34	-3.63	-	-	12	-	-
ITIC	1.66	-5.68	-4.02	77	2.7	1.6	23	33
ITIC-Th	1.67	-5.75	-4.08	68	5.7	6.0	8.5	-
ITIC-2F	1.61	-5.79	-4.18	90	3.9	6.0	>6	36
Y6	1.48	-4.99	-3.94	95	5.9	1.1	-	-

4.3.1 Steady state absorption and photoluminescence emission spectra

The normalised steady state absorption spectra of the pristine polymer PffBT4T-C9C13 and non-fullerene acceptors ITIC, ITIC-Th, ITIC-2F and Y6 films, the control blend films polystyrene (PS) with NFAs and the polymer:NFAs blend films are shown in Figure 4.4. The steady state absorption spectra of pristine PffBT4T-C9C13 film peak at 690 nm with a shoulder at 630 nm.[10] The 0-0 vibronic transition was found at 685 nm in ITIC-Th film and red shifted to 695 nm in ITIC film and further to the red at 720 nm in ITIC-2F film. For the low bandgap Y6 film, the 0-0 vibronic transition was found at 820 nm and a shoulder at 730 nm. The ground state absorption spectra of the blended ITIC series show different variations with the addition of polymer. ITIC blend with PffBT4T-C9C13 spectrum displays a narrower breadth than either of their individual components. PffBT4T-C9C13:ITIC blend film contains the FWHM of 0.35 eV which is less than pristine PffBT4T-C9C13 (0.52 eV) and ITIC (0.41 eV). The blend film of PffBT4T-C9C13:ITIC-Th has the FWHM of 0.4 eV, which is less than pristine ITIC-Th film (0.45 eV) and the polymer. Furthermore, the intensity ratio of the 0-0 and 0-1 bands is greater in the ITIC and ITIC-Th blends compared to the pristine components. Both two observations suggest that enhanced crystallinity was found in the blend ITIC and ITIC-Th films, which was also observed in the PffBT4T-C9C13:fullerene blend system and found to be due to acceptor-induced ordering.

However, for the ITIC-2F blend with PffBT4T-C9C13, the breadth of the ground state absorption spectrum is 0.48 eV which is an intermediate value between the polymer and ITIC-2F (0.41 eV). The 0-0 to 0-1 band intensity ratio decreases compared to its PS:ITIC-2F film but slightly increases to the pristine polymer. The intermediate FWHM value and the smaller 0-0/0-1 intensity ratio to each component give an indication that the ITIC-2F induced ordering is less obvious in the PffBT4T-C9C13:ITIC-2F film. The ground state absorption spectrum for PffBT4T-C9C13:Y6 blend show both the polymer and Y6 contributions, with both the components showing a clear red-shifts relative to the pristine film, potentially indicating an enhanced crystallinity for both the donor and acceptor domains.

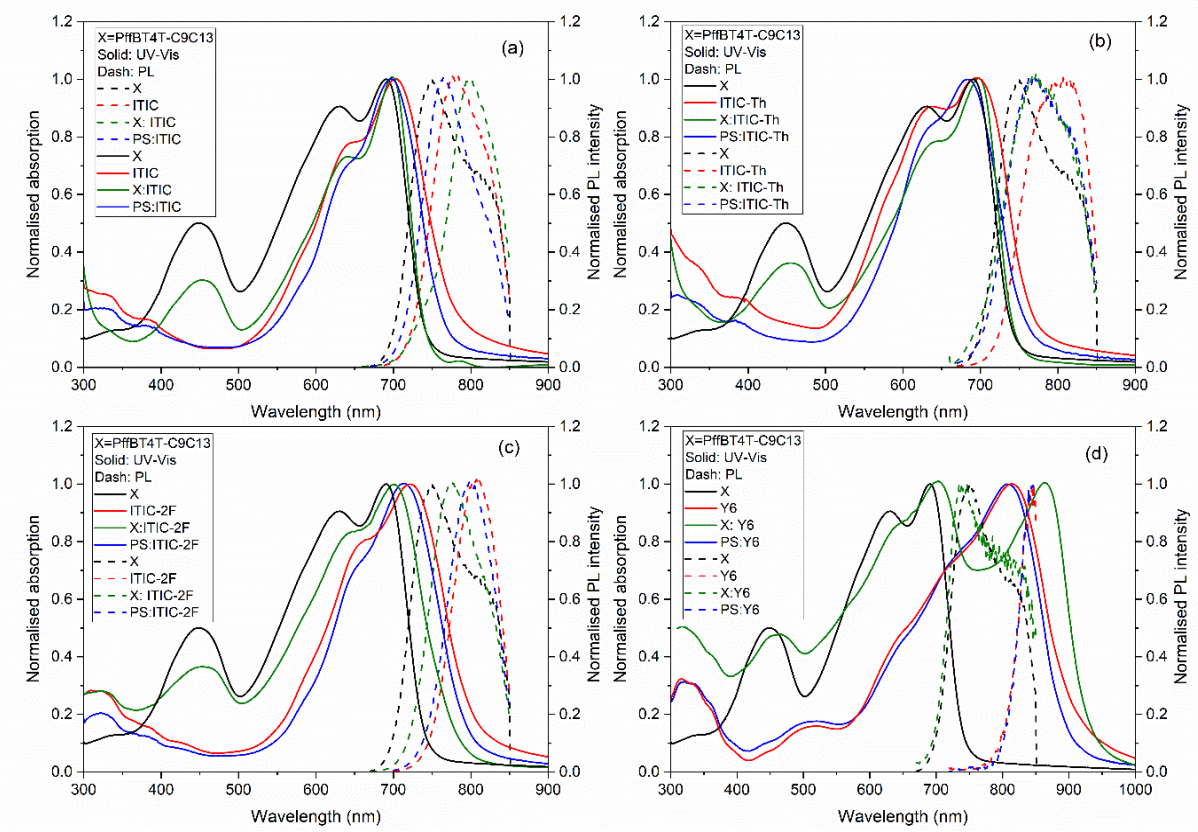

Figure 4.4 *Normalised steady state absorption spectra (solid lines) and photoluminescence emission spectra (dash lines) for (a) pristine PffBT4T-C9C13, ITIC, PS:ITIC and PffBT4T-C9C13:ITIC films. (b) pristine PffBT4T-C9C13, ITIC-Th, PS:ITIC-Th (1:1.2) and PffBT4T-C9C13:ITIC (1:1.2) films. (c) pristine PffBT4T-C9C13, ITIC-2F, PS:ITIC-2F and PffBT4T-C9C13:ITIC-2F films (d) pristine PffBT4T-C9C13, Y6, PS:Y6 and PffBT4T-C9C13:Y6 films*

Photoluminescence (PL) emission spectroscopy was used to analyse the role of NFA in the PffBT4T-C9C13 blend films. The normalised PL emission spectra for the pristine polymer and NFAs are shown as dash lines in Figure 4.4, with an excitation wavelength of 650 nm. Since both the polymer and acceptors absorb at 650 nm, the PL spectra of the blend films contain a combination of both components. As shown in all four figures, the PL spectrum for PffBT4T-C9C13 shows a main emission peak at 750 nm with a shoulder around 825 nm. All three ITIC series' blends with PffBT4T-C9C13 reveal interesting behaviour: red or blue shifted PL emission band of the blend relative to the pristine components. For the PffBT4T-C9C13:ITIC blend, the PL spectrum displays the main peak at 798 nm and a shoulder at 740 nm. However, the main peak position of the blend ITIC is red-shifted relative to PL of pristine polymer and the ITIC films. The PL spectrum of PS:ITIC film is used to show the effect of the dispersive environment on the ITIC emission, and it exhibits the main peak at 765 nm, which is 15 nm

blue-shifted to the PL of ITIC film. Hence, the red-shifted in the ITIC blend cannot be attributed to the dispersion of the ITIC in the blend film and it is more likely due to the D/A interaction in the blend film.

In contrast, the PL spectrum for ITIC-Th blended with polymer (Figure 4.4b) exhibit an identical PL spectrum to the PL spectrum of the PS:ITIC-Th film. Such blend PL spectral overlapping of the ITIC-Th with polymer and PS indicates the PL emission in the polymer:ITIC-Th blend originated from the ITIC-Th aggregates that formed could be due to the strong intermolecular S-S interaction. As shown in Figure 4.5, the normalised (per absorption) emission spectra for pristine polymer, NFAs and their blend films with PS and polymer have exhibited further evidence for the formation of ITIC-Th clusters. In comparison to the PL emission intensity of the pristine to the ps blend film, all pristine NFA film shows lower PL emission intensity than the PS:NFAs films, revealing an aggregation induced PL quenching. Although all pristine NFA PL spectra display aggregation-induced quenching than the ps blend film, ITIC-Th shows considerably less predominated. This implied the formation of ITIC-Th aggregation in pristine ITIC-Th film, which is hard to be dispersed by additional PS. Therefore, the identical PL spectrum polymer:ITIC-Th to PS:ITIC-Th implies the possible presence of ITIC-Th clusters, which may contain the remaining PL. Another possibility that cannot be ignored is the singlet energy transfer from the polymer to the NFA. If the energy levels of the S_1 state of the polymer and NFA are similar, a hybrid energy state between the polymer and NFA S_1 states can be generated at the D/A interface.

For the PffBT4T-C9C13:ITIC-2F film, the normalised PL spectrum appears an intermediate PL emission peak between the polymer and ITIC-2F, but the high PL quantum yield of the ITIC-2F makes it difficult to assess the relative contributions. The PL spectrum of PffBT4T-C9C13:Y6 film is dominated by the polymer, and this can be attributed to the greater proportion of light being absorbed by the polymer at the excitation wavelength of 650 nm.

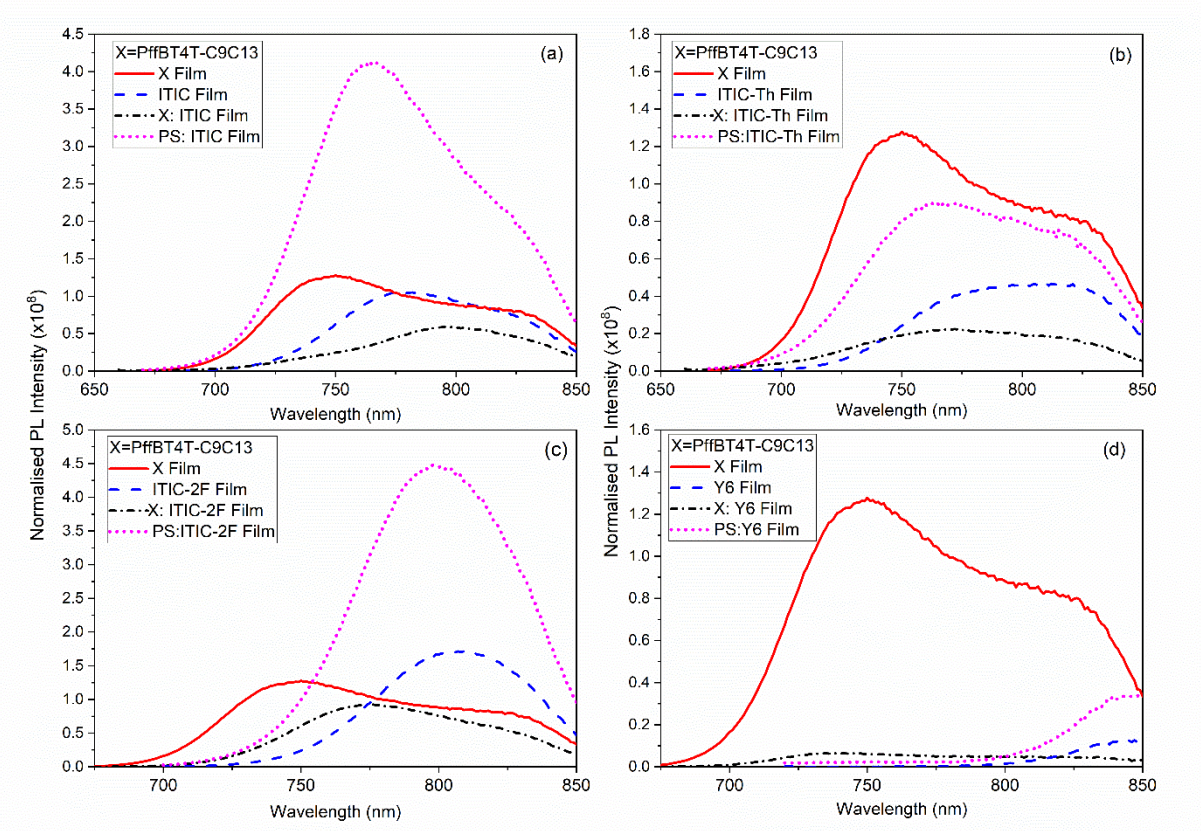

Figure 4.5 *Normalised (per absorbance) photoluminescence emission spectra of (a) PffBT4T-C9C13: ITIC film and (b) PffBT4T-C9C13: ITIC-Th film (c) PffBT4T-C9C13: ITIC-2F film (d) PffBT4T-C9C13: Y6 film, compared to the pristine components and the PS: NFAs' control blends, with excitation wavelength at 650 nm.*

To estimate the extent of polymer exciton to charge carriers, the yield of polymer PL quenching was calculated from PL spectra as shown in Figure 4.6, with an excitation wavelength 455 nm. It should be noted that 455 nm excitation wavelength mainly excites polymer but there is still a minor absorption contribution from NFA (Figure 4.6a). To minimise the influence by NFA on the value of polymer PL quenching, the polymer PL emission quenching was estimated by the ratio of the PL intensity of the polymer:NFA blend at 700 nm to the sum of PL intensities of the pristine polymer and NFA films. At 700 nm, the PL intensity of NFAs was as smaller as <10% to the polymer, and the uncertainty in the estimated polymer PL quenching yield was raised from the contribution of NFAs, that was around $\pm$5%. The PffBT4T-C9C13:ITIC-Th blend showed the least polymer PL quenching to 68%, which is consistent with the hypothesis of the formation of ITIC-Th cluster in the polymer blend. The highest PL quenching was observed in the PffBT4T-C9C13:Y6 film to be 95%, and that is likely because of the long exciton lifetime and consequently of long exciton diffusion length of Y6.

PL quenching of PffBT4T-C9C13:ITIC was estimated to be 77 %, while the fluorinated ITIC-2F with PffBT4T-C9C13 blend shows the efficiency around 90%. The increased PL quenching from ITIC to ITIC-2F blend potentially assisted by the greatest driving force for electron transfer and a favourable blend morphology.

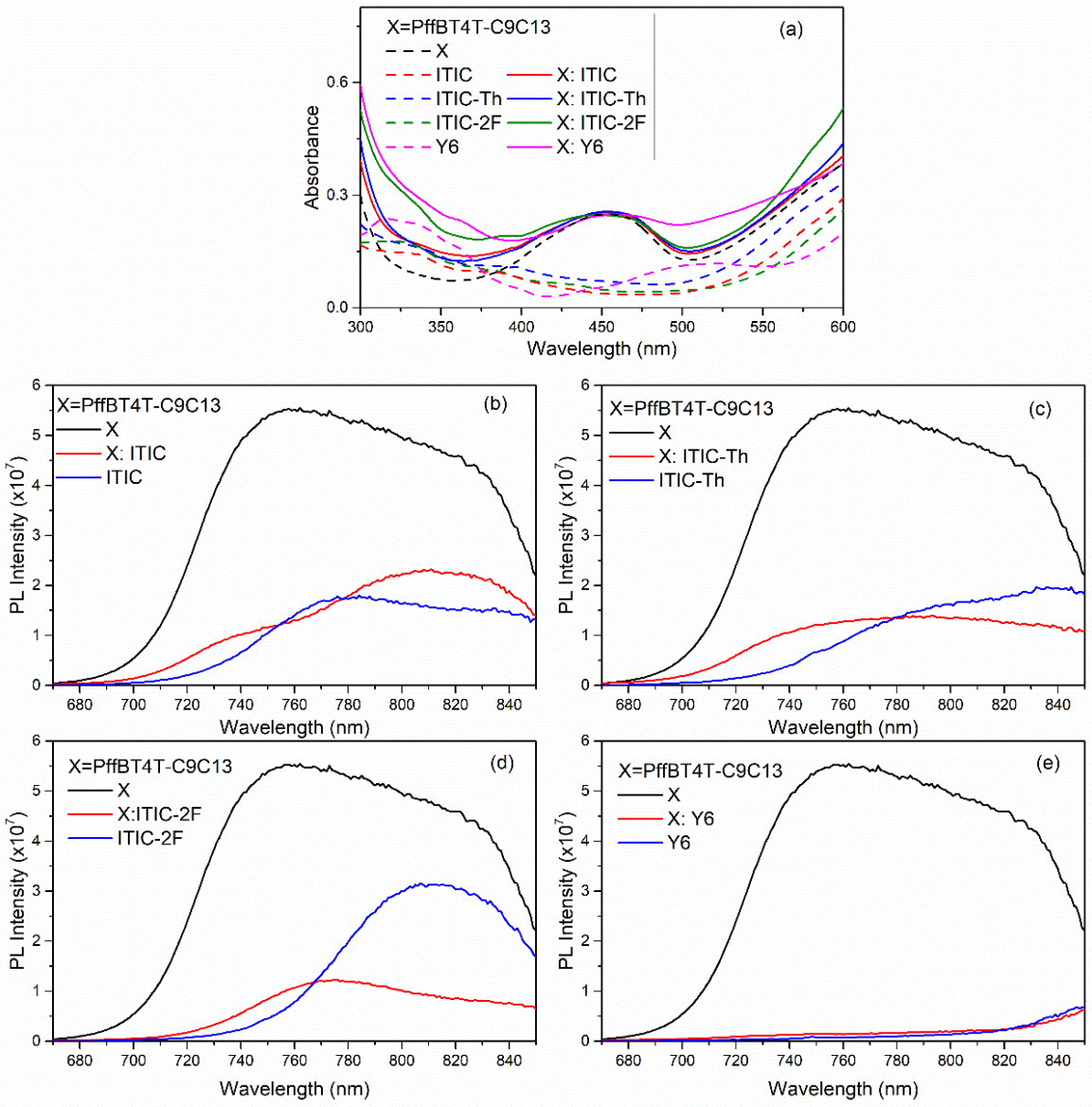

Figure 4.6 *(a) Zoom of the 455 nm absorbance peak of PffBT4T-C9C13 used to estimate PL quenching yield, showing the minimal NFA absorbance. Photoluminescence emission spectra of (b) PffBT4T-C9C13: ITIC film, (c) PffBT4T-C9C13: ITIC-Th film, (d) PffBT4T-C9C13:ITIC-2F film, and (e) PffBT4T-C9C13:Y6 film, compared to the pristine components, with 455 nm excitation wavelength.*

4.3.2 Atomic force microscopy AFM

AFM was employed to understand the morphology of the blending of PffBT4T-C9C13 with different NFAs, as shown in Figure 4.7. The R_q value was estimated from the height images of

the blend and pristine films. For the PffBT4T-C9C13 with ITIC series blends, the R_q varies from ITIC blend (4.1 nm) to ITIC-2F blend (5.1 nm) to ITIC-Th blend (5.6 nm), all the blend surface roughness is larger than the pristine polymer (2.4 nm). The increased R_q from the pristine polymer to the blend films indicates the formation of phase segregation is induced with the addition of the NFAs. In particular, the largest R_q observed in the PffBT4T-C9C13: ITIC-Th blend potentially reveals the largest domain size of ITIC-Th compared to the other two NFAs, which is consistent with the hypothesis made based on the PL results.

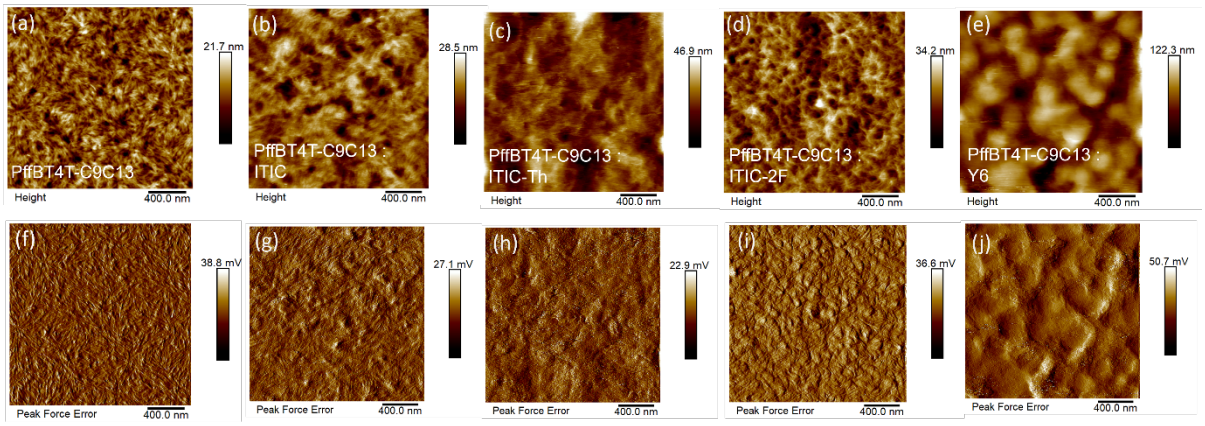

Figure 4.7 *AFM images of phase and topography for (a and e) pristine PffBT4T-C9C13, (b and f) PffBT4T-C9C13:ITIC, (c and g) PffBT4T-C9C13:ITIC-Th, (d and h) PffBT4T-C9C13:ITIC-2F. Scale bars are 400 nm.*

However, the surface roughness of PffBT4T-C9C13:Y6 blend is substantially higher than the ITIC series blends, with R_q around 17 nm. This large surface roughness blending with PffBT4T-C9C13 contrasts with smooth films reported for PM6:Y6, which shows similar morphology to the pristine PM6 film. Therefore, there is a high probability that the enhanced R_q is related to the inherent Y6. As shown in Figure 4.8a-d, the surface roughness of Y6 was further investigated in the pristine Y6 and PS:Y6 film. Pristine Y6 film is relatively smooth with R_q 2.2 nm while a larger R_q 6.6 nm was observed in the PS:Y6 film. Therefore, the large domain size showing in Y6 blend with PS can be attributed to the Y6 induced ordering. As such, the higher surface roughness value observed in the PffBT4T-C9C13: Y6 film can be attributed to the considerable Y6 phase segregation, indicating low miscibility between the two components. Considering the similar morphology of the Y6 blends to the PS:Y6 film, this may suggest an extensive surface covering of pure Y6. In contrast, the pristine ITIC series' films are very smooth, with R_q value of less than 1 nm (Figure 4.8e-p).

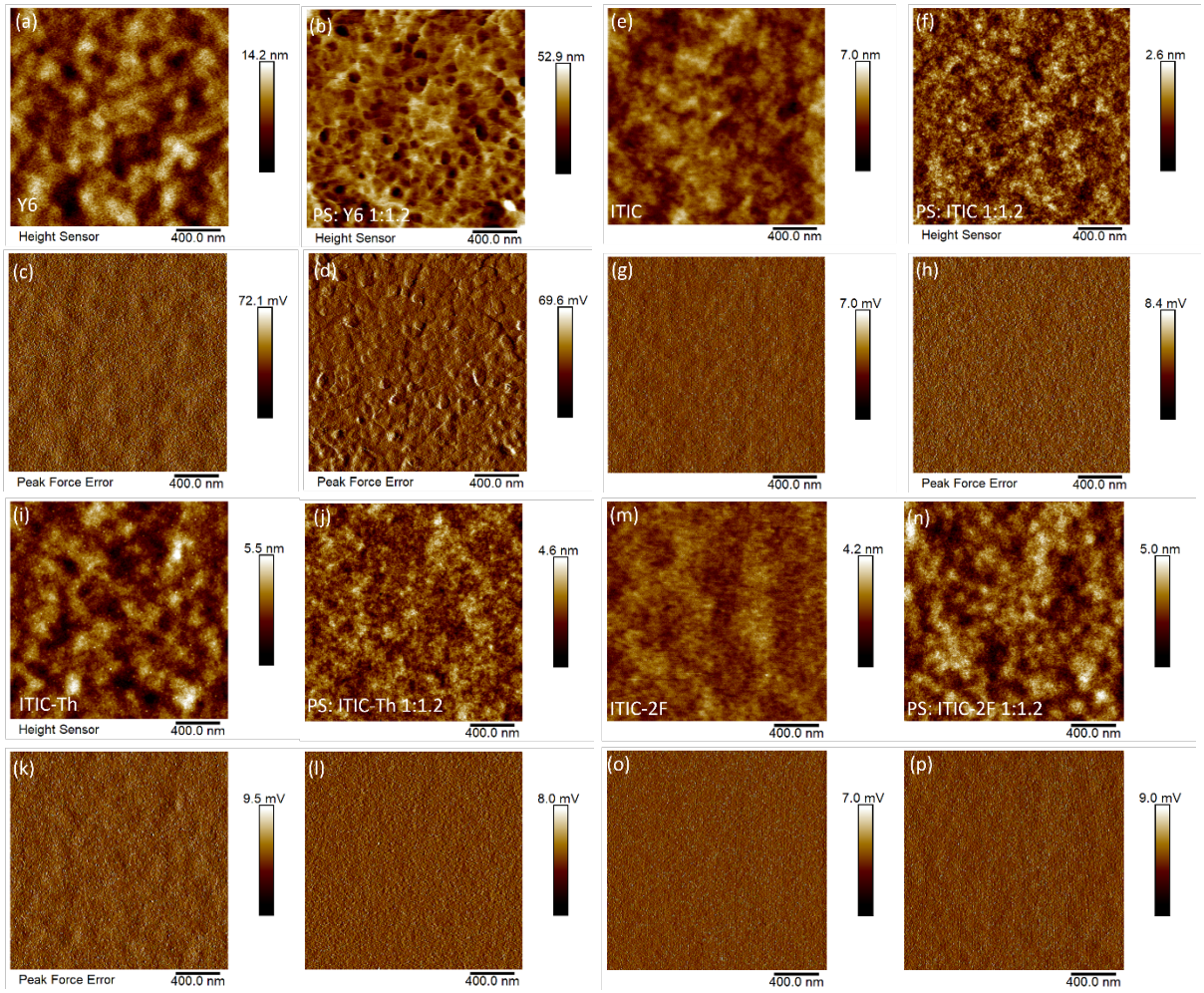

Figure 4.8 *AFM images of phase and topography for (a and c) Y6, (b and d) PS:Y6 (1:1.2); (e and g) ITIC, (f and h) PS:ITIC (1:1.2); (i and k) ITIC-Th, (j and l) PS:ITIC-Th (1:1.2); (m and o) ITIC-2F, (n and p) PS:ITIC-2F (1:1.2),. Scale bars are 400 nm. Comparing the Y6 and PS:Y6 film, an increased roughness from 1.8 nm for Y6 to 5.2 nm for PS:Y6 was found, and an increase in grain size was induced with addition of polystyrene. In contrast, all the ITIC series' films are very smooth, with R_q values of less than 1 nm.*

4.3.3 Grazing incident X-ray diffraction (GIXRD)

GIXRD was employed to examine the molecular packing for pure polymer, NFAs, and blend NFAs with PffBT4T-C9C13 and PS, in a range from 4 to 28 nm^{-1}. The x-axis was measured in 2θ, which was converted to q in the case regardless of the source of excitation wavelength (Figure 4.9a-d).

Previous Chapters have shown an amorphous morphology of pristine polymer PffBT4T-C9C13, with a weak, broad (010) π-π stacking peak around q=16 nm^{-1} (stacking distance d = 0.393 nm).[20] Compared to the polymer, the GIXRD patterns for NFAs display relatively intense, narrow π-π stacking (010) peak but with slightly different peak scattering position and

intensity, occurring around 17 nm^{-1}, which is consistent with previous reported values.[21,22]The relatively weaker and broader (010) π-π stacking peak for a pure ITIC comparing to other NFAs indicates its lower crystallinity which can be explained by its slightly poor self-organisation behaviour with the para-alkyl-phenyl group.[23] For the PS:ITIC series' film, the π-π stacking (010) peaks show a slightly increased peak intensity but do not change massively as the Y6, which gives an indication that the morphology of the ITIC series' NFAs won't be affected as much by the additional PS, this is consistent with the AFM results.

In the polymer: NFA blends, the (010) peak of the polymer becomes increasingly prominent (with the NFA peak still visible as a shoulder), suggesting an enhanced crystallinity of the polymer domain. Similar to the pristine ITIC, PffBT4T-C9C13:ITIC blend shows the least integrating area, indicating the lowest polymer domain size among other PffBT4T-C9C13:NFA blends. In contrast, PffBT4T-C9C13:Y6 exhibits the greatest integrated peak area, and the Y6 shoulder is particularly visible, suggesting both polymer and Y6 show an enhanced crystallinity, a possible result of the low miscibility between polymer and Y6 as observed in the AFM. The largest integrating area estimated from the PS:Y6 film provides further evidence for the enhanced crystallinity due to the Y6 phase segregation.

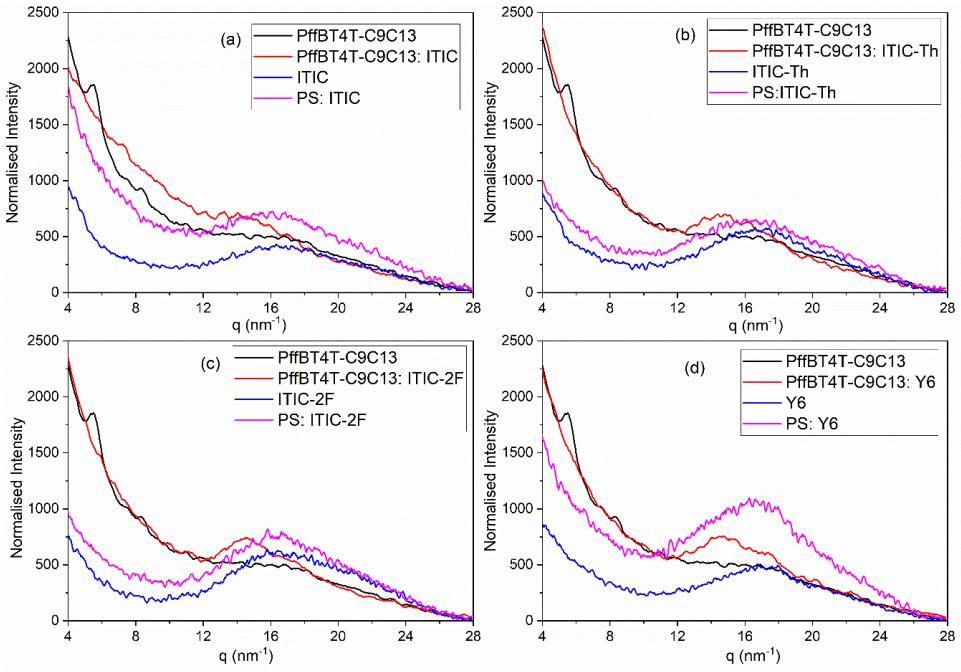

Figure 4.9 *GIXRD (normalised per absorption) for pristine PffBT4T-C9C13 film and (e) ITIC and PffBT4T-C9C13: ITIC (1:1.2) film (f) ITIC-Th and PffBT4T-C9C13: ITIC-Th (1:1.2) film (g) ITIC-2F and PffBT4T-C9C13: ITIC-2F (1:1.2) film (h) Y6 and PffBT4T-C9C13: Y6 (1:1.2) film.*

4.3.4 Cyclic voltammograms

The oxidation potential for polymer and reduction potential for NFAs can be obtained directly from the oxidation/reduction onset of their CVs. The HOMO level of the polymer was estimated by the empirical relation $E_{HOMO} = \left[\left(E_{ox} - E_{ferrecene}\right) + 4.8\right]$ eV and the LUMO level of NFA can be determined by $E_{LUMO} = \left[\left(E_{red} - E_{ferrecene}\right) + 4.8\right]$ eV. Ferrocene was used as an external standard. E_{ox} is the polymer oxidation onset and E_{red} is the NFA reduction onset.

The oxidation onset of the polymer PffBT4T-C9C13 film was observed to be 0.54 eV and the HOMO level was estimated to be 5.34 eV. The same method applied for the NFAs, the LUMO level was determined to be -4.02 eV for pure ITIC film, -4.08 for ITIC-Th film, -4.18 eV for ITIC-2F film and -3.97 eV for Y6 film.

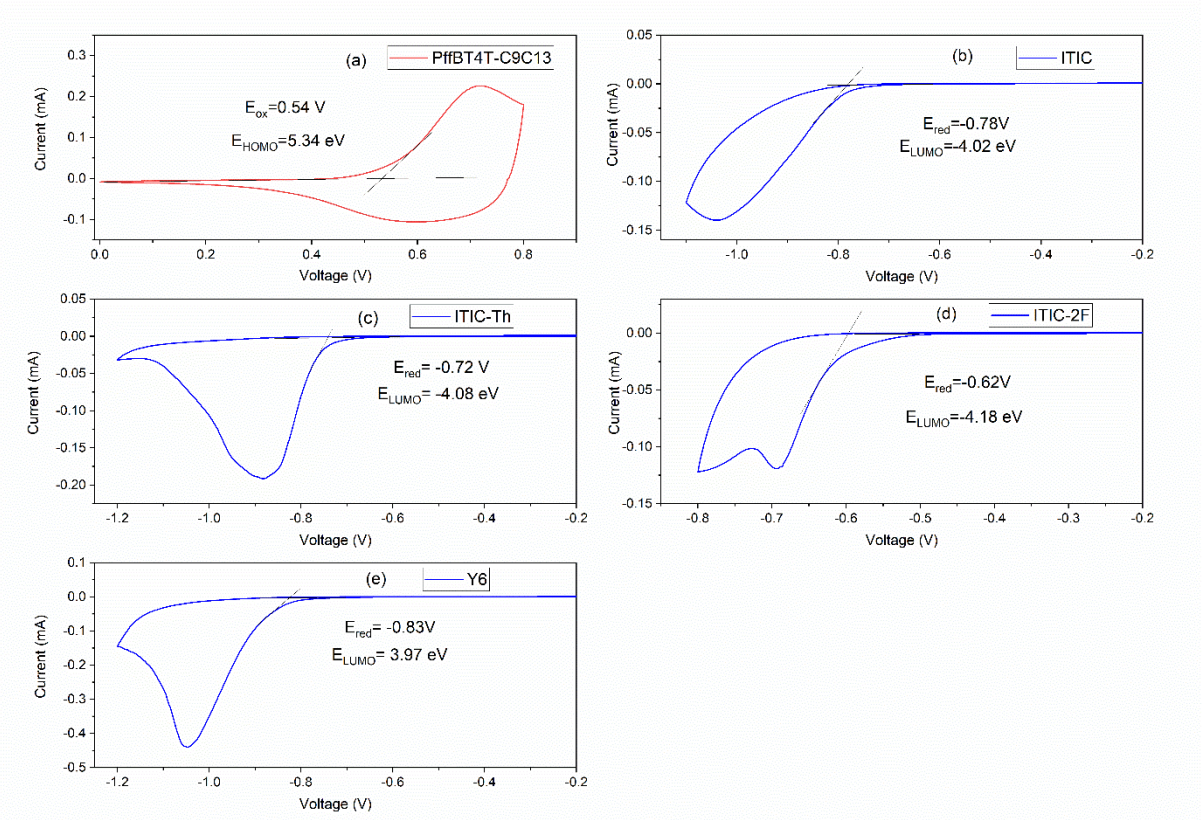

Figure 4.10 *Cyclic voltammogram for PffBT4T-C9C13, ITIC-Th, ITIC, ITIC-2F and Y6 Films in 0.1 M Bu_4NPF6 acetonitrile solution with scan rate at 20 mV s^{-1} on ITO substrate.*

4.3.5 SEC spectra for polymer cation and NFA Anion formation in films

Since the wide absorption range for NFAs, they can also be excited to some extent under the polymer dominated excitation wavelength, resulting in a spectral congestion of both polymer and NFAs' transient species. SEC was used to initially identify the spectral shape of polymer cation and NFAs' anions in the pure polymer or NFA films. The range of applied voltage used for SEC was assessed from their corresponding CVs, ensuring voltages below the first oxidation/reduction peak of certain material to avoid double oxidation/reduction.

The SEC absorption spectra for polymer PffBT4T-C9C13 have been investigated in Chapter 3 (section 3.3.3). Just for a reminding purpose, it is also shown in Figure 4.11a. The SEC absorption spectra for the NFAs films are shown in Figure 4.11b-f, together with the comparison SEC spectra for all four NFAs' anions at their corresponding higher applied voltage. The SEC spectra for ITIC film exhibit electroreduction induced bleaching of the ground state absorption bands at 705 nm and a shoulder at 650 nm as negative intensity. The ITIC anion band was created as a positive intensity at 785 nm. For the ITIC-Th and ITIC-2F film, the electroreduction induced bleaching was at 710 nm and 640 nm, and their anion formation was observed at 797 nm and 792 nm, respectively. The ground state bleaching at 835 nm and 750 nm were determined in the low bandgap Y6 film, and the Y6 anion was created at 870 nm. These NFA anions formation shows different sensitivity to the applied voltage, with the ITIC-2F anion intensity higher than ITIC, Y6 and ITIC-Th. This may because of the relative number of anions generated in their films and the rate of anions mobility. The faster the anion transfer to the electrode, the easier of anions being detected. Although the Y6 and ITIC-Th anions' signal is weak, additional confidence in these results arises from the good correspondence between the peak amplitude and the total charge extracted as a function of voltage as shown in Figure 4.12.

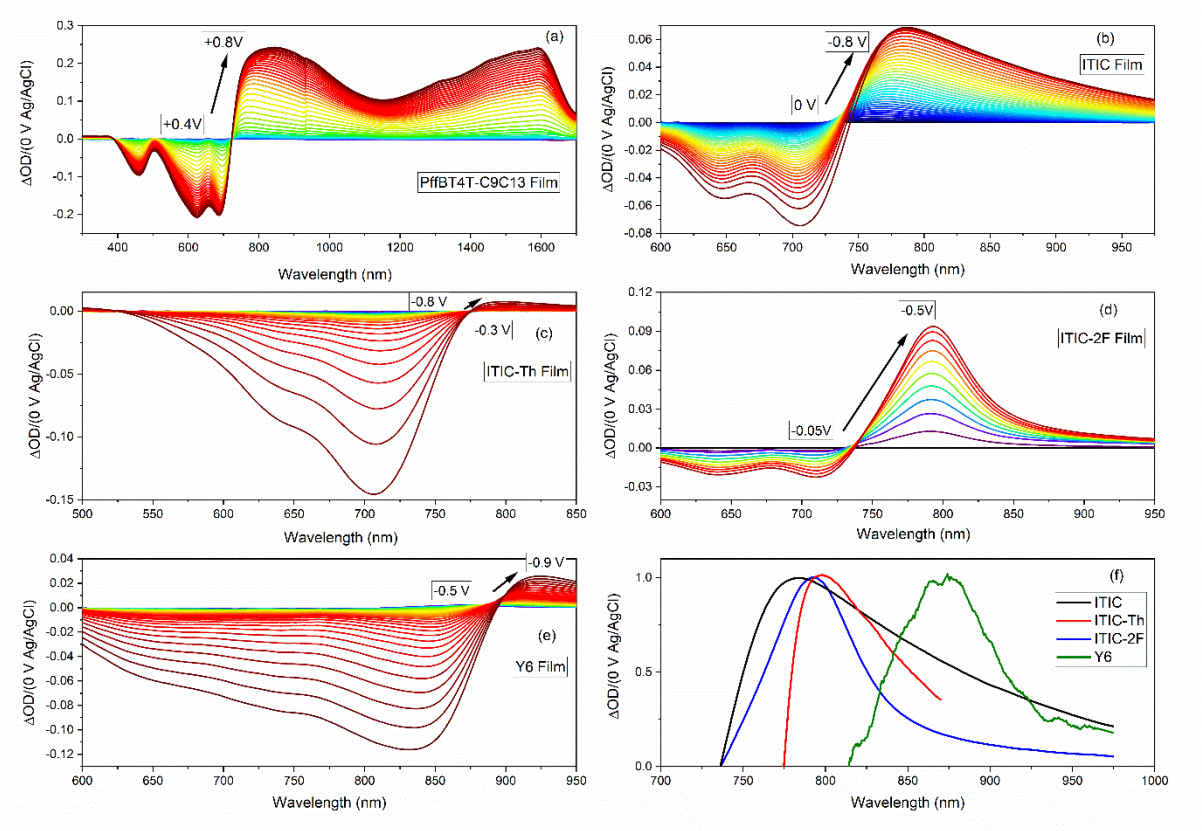

Figure 4.11 *SEC absorption spectra for (a) polymer PffBT4T-C9C13 film and (b) ITIC film, (c) ITIC-Th (-0.9 V), (d) ITIC-2F (-0.5 V) and (e) Y6 (-0.8 V) in 0.1 M TBAP/ acetonitrile with Ag/AgNO3 electrode, plotted versus applied potential from 0 V to 0.8 V for the polymer and 0 V to -0.8 V for ITIC film. (f) Normalised (to 1) absorption spectra for NFA films.*

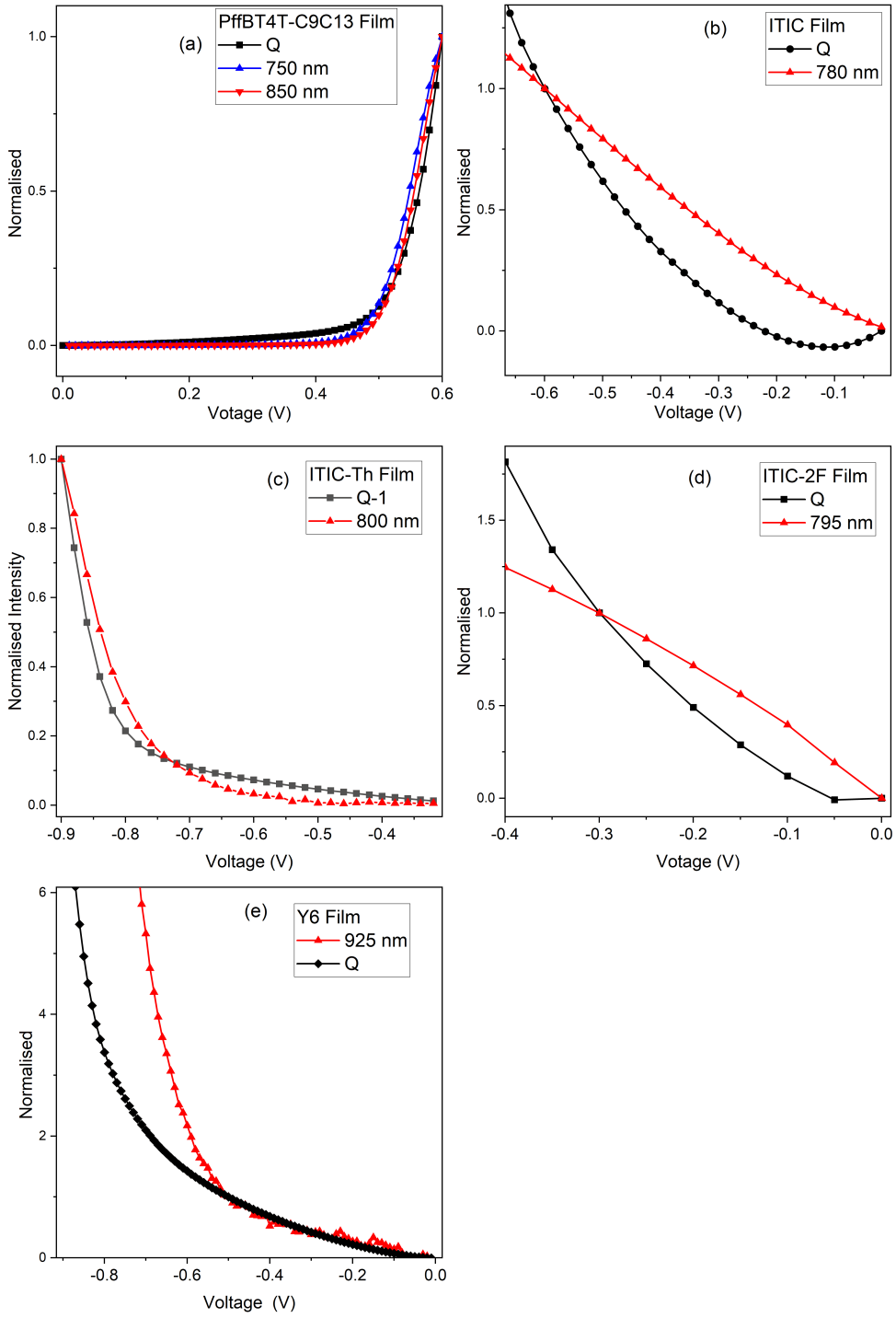

Figure 4.12 *The Normalised comparison spectra for the number of charge generation Q (integration from the JV curve) and the NFAs anion peak variation with a rising applied voltage.*

4.3.6 ns-µs TAS for triplet formation in pristine NFAs solution

Ns-µs TAS was employed to study the charge photogeneration in pristine polymer and NFA solutions. Normalised (to 1) TA spectra for pristine polymer and NFAs solution are shown in

Figure 4.13. The TA spectra for the pristine polymer show a broad absorption band centred at 1080 nm, which was previously assigned to the donor polymer triplet in Chapter 3 (section 3.3.4.1) and is shown here for comparison. The TA spectra for all NFAs showed a broad TA band peak at 1100 nm (ITIC), 1130 nm (ITIC-Th) and further to the red at 1210 nm (ITIC-2F), reflecting the differences in their ground state absorbance spectra. The TA spectrum for the Y6 solution exhibits an even more red-shifted absorption peak at 1360 nm. All of these bands generated in the TA spectra of pristine NFAs band can be attributed to NFAs' triplet as evidenced by the strong, reversible oxygen dependence and mono-exponential decay kinetics, as shown in Figure 4.14. Since the original TA signal amplitude and lifetime were recovered after regeneration of the inert N_2 atmosphere, their corresponding triplet lifetime can be calculated by the mono-exponential fitting as shown in Figure 4.13b. The triplet lifetime decay lifetime for the Y6 is determined to be 1.1 µs, 1.6 µs for ITIC triplet and 6.0 µs for both the ITIC-2F and ITIC-Th triplet.

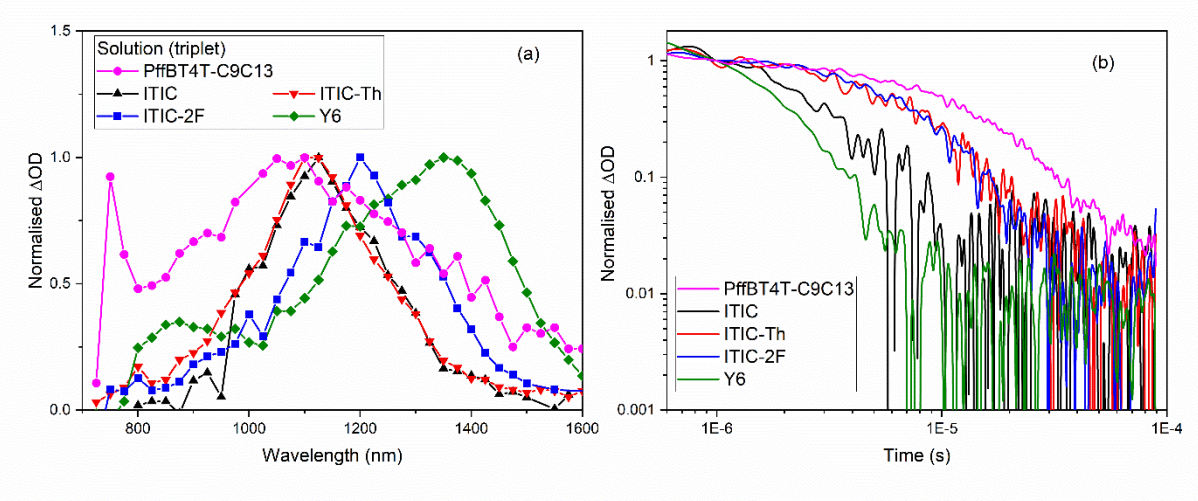

Figure 4.13 *Normalised (to 1) TA spectra for PffBT4T-C9C13, ITIC, ITIC-Th, ITIC-2F and Y6 solutions (d) Normalised (to 1) decay dynamics for PffBT4T-C9C13 (prob at 1100 nm), ITIC (probe at 1100 nm), ITIC-Th (Prob at 1100 nm), ITIC-2F (prob at 1200 nm), Y6 (prob at 1350 nm) solutions. The excitation energies used for above solution is in a range of 16 to 26 µJ cm^{-2}.*

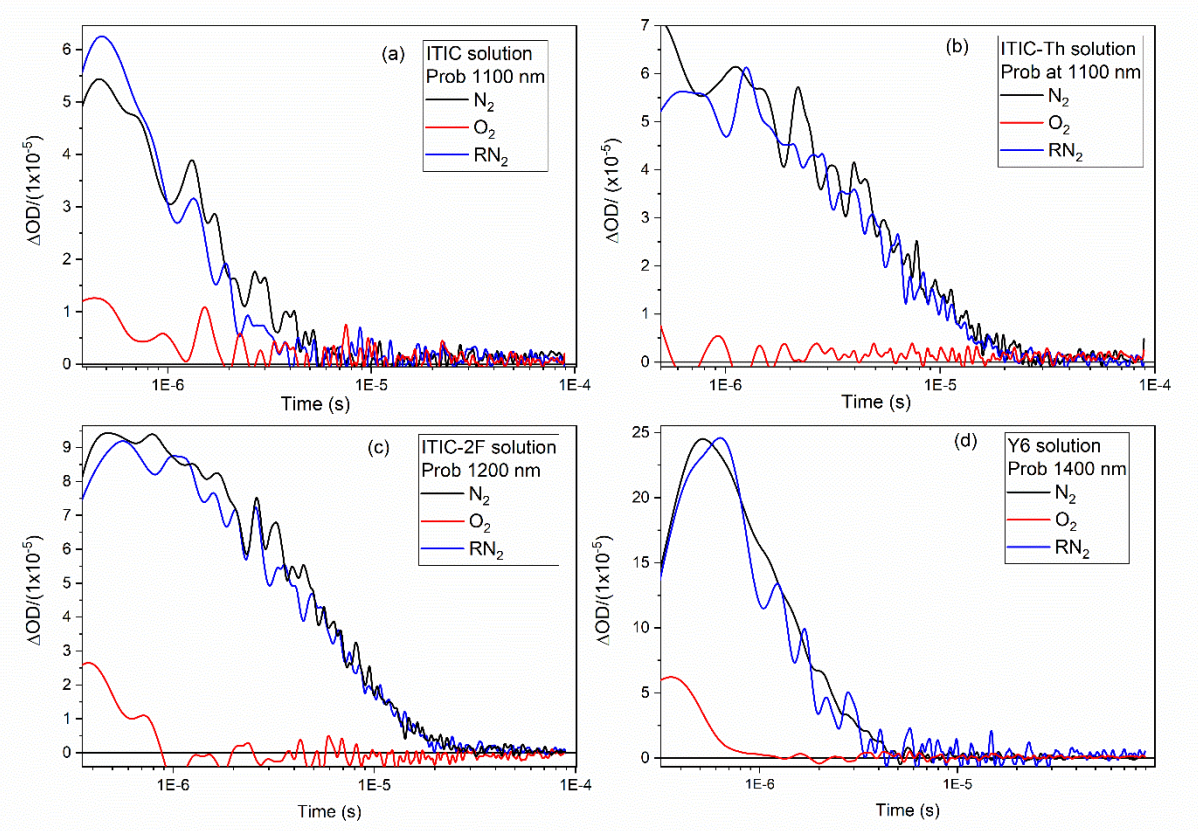

Figure 4.14 *Oxygen dependence decay dynamics for the NFAs solution (a) ITIC (b) ITIC-Th (c) ITIC-2F (d) Y6.*

4.3.7 ns-µs TAS for triplet formation in NFAs films

Because the condensed phase can often incur substantial red-shifts relative to the solution phase, the control blends film with inert PS films under the same weight ratio to the blend also under determined, as shown in Figure 4.15. It is also used to predict the blend film environment to investigate the formation of morphology dependence transient species.

Figure 4.15 shows the normalised (to 1) TA spectra of the NFAs in three phases (pure films, solutions, and PS control blends). The triplet formation generated in Y6 solution was not detected in its PS:Y6 film, and only the Y6 anion feature was observed <925 nm. Since the large ground state bleaching below 890 nm, the positive feature of <925 nm can only be attributed to Y6 anion feature, not despite displaying the actual spectral shape of the Y6 anion. Y6 triplet created in the pristine Y6 film showed a 0.12 eV red shift from the solution. Considering that in its control blend no Y6 triplet was generated, and the crystallinity was increased after blending with polystyrene, we can infer that the Y6 anions preferentially formed in large pristine Y6 domains, which is consistent with the main conclusion made by

Justin et al.[24] In contrast, triplet formation was still detected in all three PS:ITIC series' NFAs. PS: ITIC and PS:ITIC-Th shows a 0.05 eV red-shifted relative to their solution, which is consistent with the red-shift in ground state absorption spectra. While the PS:ITIC-2F shows a significantly broadening triplet TA spectrum than in the solution phase, indicating numerous triplet environments. This hypothesis can be verified by the triplet formation in the pristine ITIC-2F film, which shows the triplet state red-shifted to 1300 nm. The missing TA spectra for the pristine ITIC and ITIC-Th film is because of the small signal-to-noise ratio during the measurement. As such, it is difficult to plot a reliable TA spectrum based on weak signals. The small signal-to-noise ratio could be derived from a small number of transient species left over in µs timescales with their shorter lifetime or other fast second-order loss process. For example, the fast triplet-triplet annihilation process occurred in pristine NFA films due to the formation of NFA aggregation.

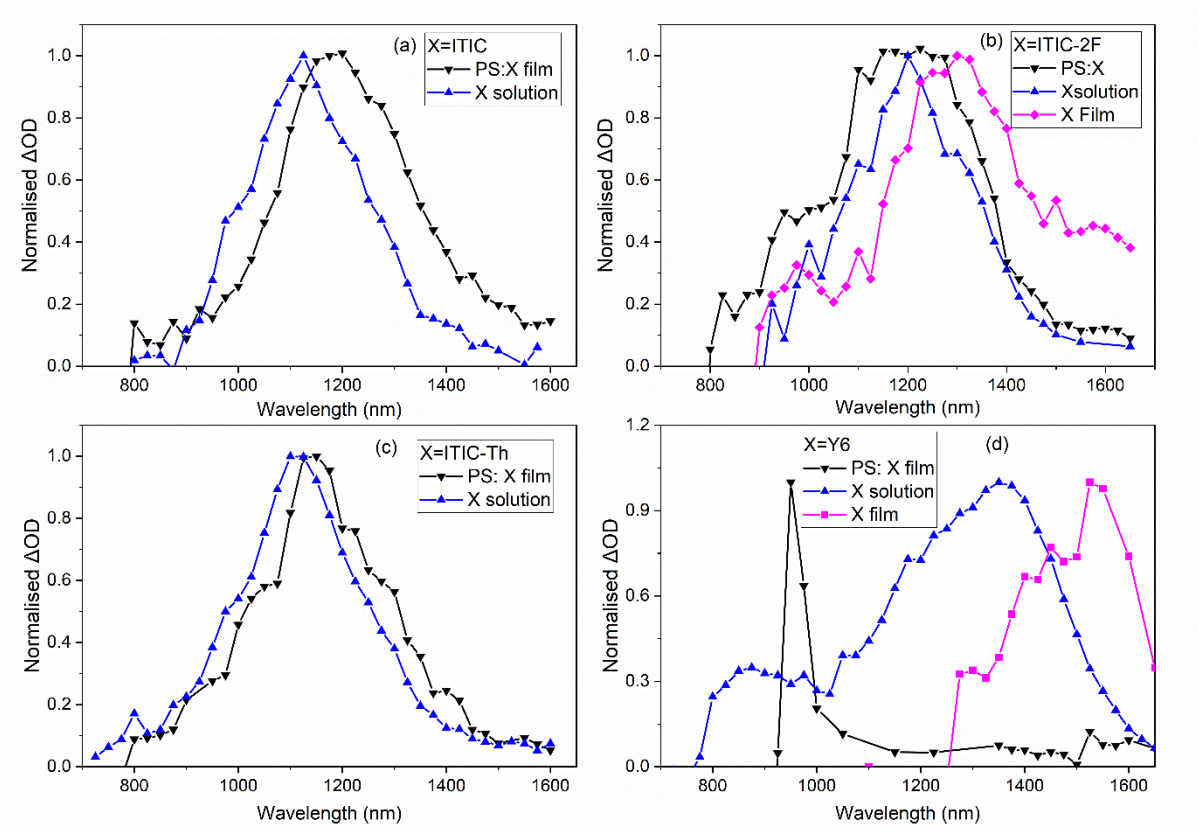

Figure 4.15 *Normalised TA spectra comparison for prisitne NFAs solution with PS: NFAs films (a) ITIC (b) ITIC-Th (c) ITIC-2F (d) Y6.*

In comparison with the triplet decay dynamics in solution to the PS:NFA films, it is found that the triplet lifetime is longer in the control PS blend than in the solution phase, with a mono-

exponential decay lifetime in the range of 120 - 160 µs (Figure 4.16). This is really unusual observation. Since the triplet decays in both phases are mono-exponential, this cannot be accounted for by triplet-triplet annihilation or any other second order loss process.

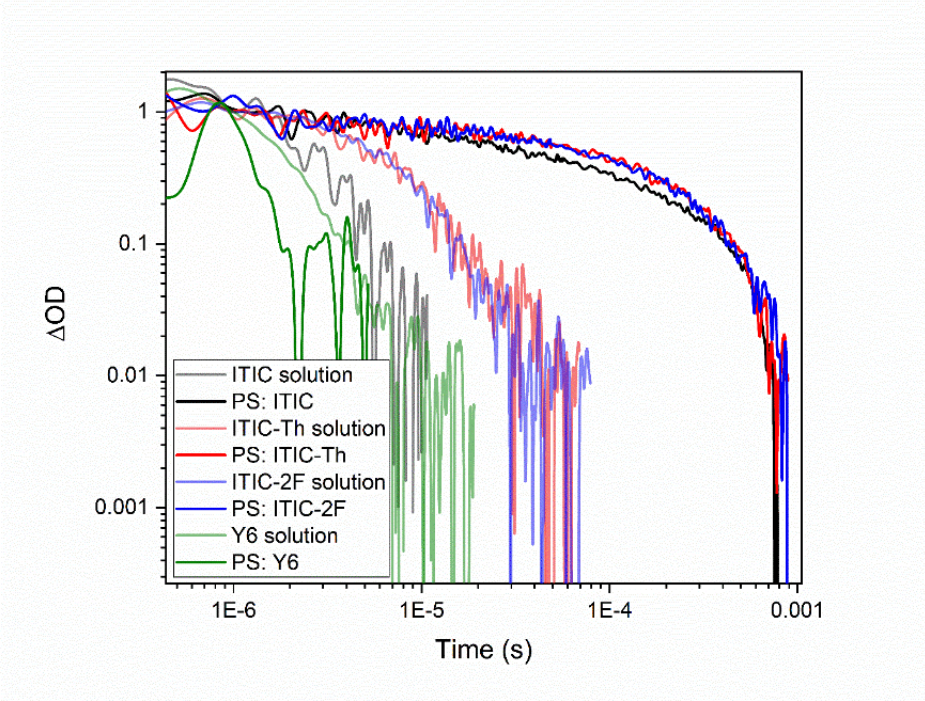

Figure 4.16 *Normalised decay dynamics comparison for prisitne NFA solutions and PS:NFA films.*

4.3.8 Triplet extinction coefficient calculation in solution and film

To quantify the NFA triplet formation, the triplet molecular extinction coefficient for NFAs was calculated in solution. This was accomplished using a sensitisation process with the well-know triplet sensitizer ZnTpp. By selectively exciting at ZnTpp's strong Soret band, effect triplet formation and transfer onto each NFA enables it triplet extinction coefficient to be determined. We used the estimated method outline by Land et al.,[25] including their suggestions for situations when the acceptor triplet decays during its formation, and when the donor triplet decays by means other than triplet transfer.

As show in Figure 4.17, the NFAs shows negligible absorption under the excitation wavelength (425 nm) for the triplet sensitizer, so Land's additional correction [25] for ^{3}A when it is also formed via direct excitation is negligible for the NFAs studied in this thesis. If decay of the acceptor triplet occurs simultaneously with its creation via energy transfer, a maximum in ΔOD will form, which is shown in Figure 4.18.

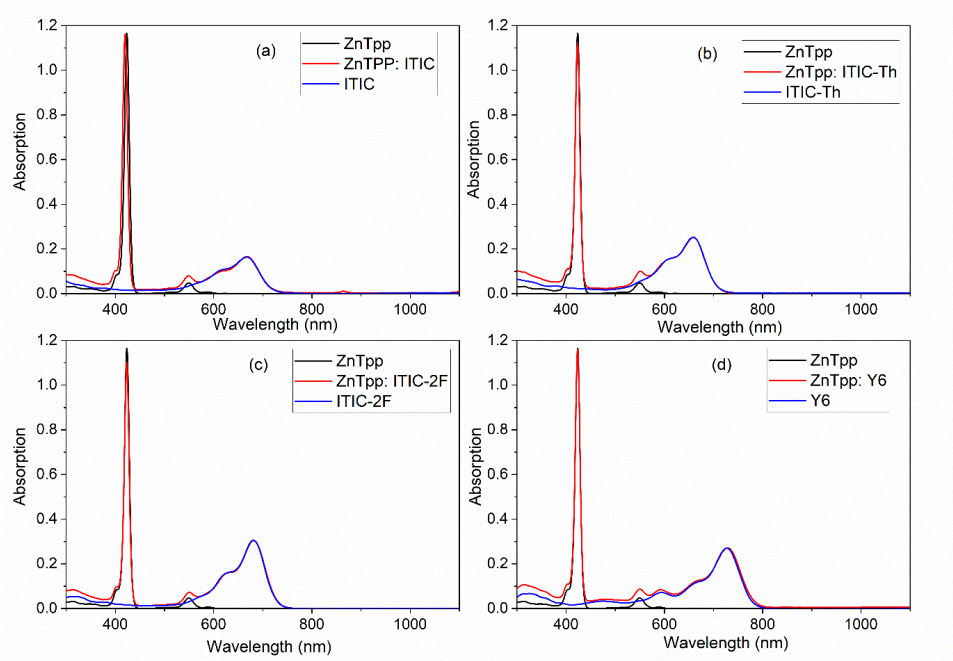

Figure 4.17 *Ground state absorption spectra for pristine and blend donor, acceptor solution (a) ITIC, (b) ITIC-Th (c) ITIC-2F and (d) Y6.*

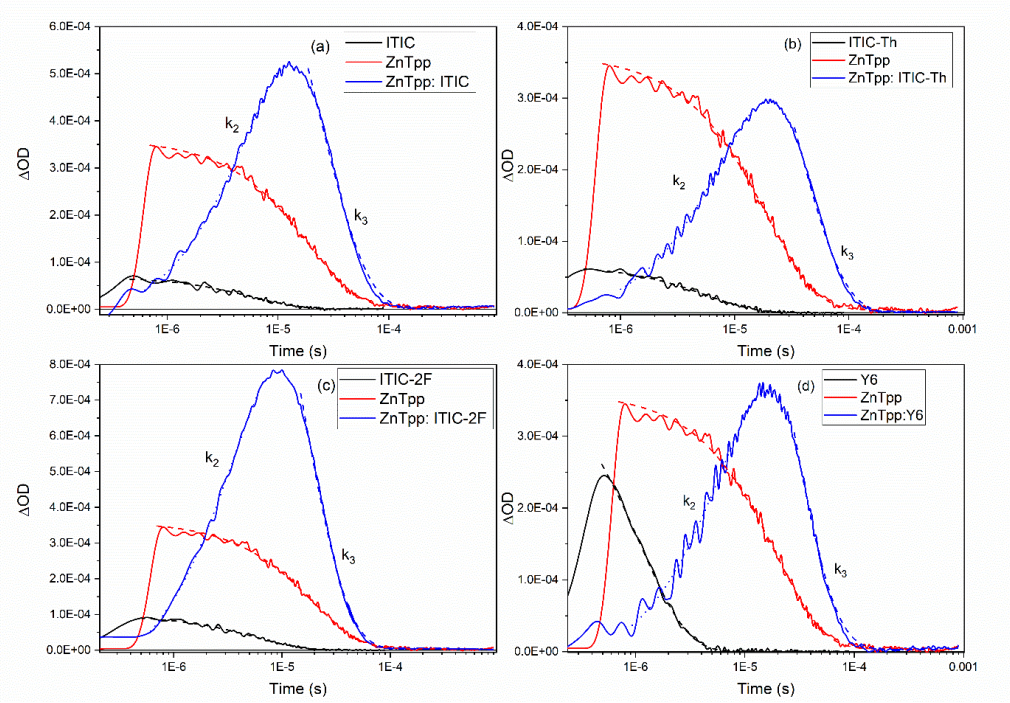

Figure 4.18 *Decay dynamics of (a) ZnTpp: ITIC (1:1), ITIC, and ZnTpp solution, (b) ZnTpp: ITIC-2F (1:1), ITIC-2F, and ZnTpp solution, (c) ZnTpp: ITIC-Th (1:1), ITIC-Th, and ZnTpp solution and (d) ZnTpp: Y6 (1:1), Y6, and ZnTpp solution. All the solution with concentration 7 $\times$ 10^{-6} M and excitation wavelength 426 nm, fitted with mono-exponential decay (dash line)/growth (dot line). The probe wavelength for the ZnTpp solution is at 850 nm; ZnTpp:ITIC, ITIC, ZnTpp:ITIC-Th, and ITIC-Th is probing at 1100 nm; 1150 nm for ZnTpp:ITIC-2F and ITIC-2F; and 1400 nm for ZNTpp:Y6 and Y6 solution.*

ZnTpp acts as the triplet sensitiser with triplet-triplet molar absorption coefficient 9500 M^{-1} cm^{-1}.[26] The TA spectra for pristine ZnTPP and the ZnTPP/NFA sensitised solutions are shown in Figure 4.19. The triplet extinction coefficients for all NFAs solutions are calculated as shown in Table 4.1.

Here we use the ITIC-2F as an example to show the process for the triplet-triplet molar extinction coefficient calculation. As shown in Figure 4.19e, the TA spectrum of ZnTpp:ITIC-2F solution shows that the ZnTPP triplet is located below 900 nm, and the ITIC-2F triplet absorbs maximally at 1150 nm. The ITIC-2F triplet clearly grows in over time (1 µs to 10 µs), a hallmark of the sensitisation process. The kinetics of the ITIC-2F triplet growth and decay were probed at a maximum of 1150 nm (Figure 4.18). Assuming first-order behaviour such that $k_2 = 1/\tau_2$, the time constant τ of the rise (3.2×10^{-6} s) provides k_2 and the decay provides k_3 (1.5×10^{-5} s).[27,26] The ΔOD_{max} of the ITIC-2F triplet is 7.8×10^{-4}. Applying the corrections detailed above, the corrected ΔOD_{max} is 1.5×10^{-3}. Therefore, the triplet molar extinction coefficient can be calculated as $\varepsilon_T^A = \frac{\Delta OD_{max}^A \times \varepsilon_T^D}{\Delta OD^D} = \frac{7.8e{-}4 \times 9500}{3.4e{-}4}$ = 3.92×10^4 M^{-1} cm^{-1}. Full methodology details are given in the experimental section 2.8.1.1, and the NFA triplet extinction coefficients were estimated to be the order of 10^4 L mol^{-1} cm^{-1}, with a range of 2.7 - 6.5 x 10^4 L mol^{-1} cm^{-1} (Table 4.1). We estimated the uncertainty in these values, based on the signal-to-noise of the ΔOD amplitude and fitting errors, to be approximately $\pm$ 0.2 x 10^4 L mol^{-1} cm^{-1}. By applying a correction factor considering the change in absorption cross-section, σ, for the ground state from solution to film, the triplet extinction coefficient in film was estimated as shown in Table 4.2. The detailed methodology was described in section 2.8.1.1.

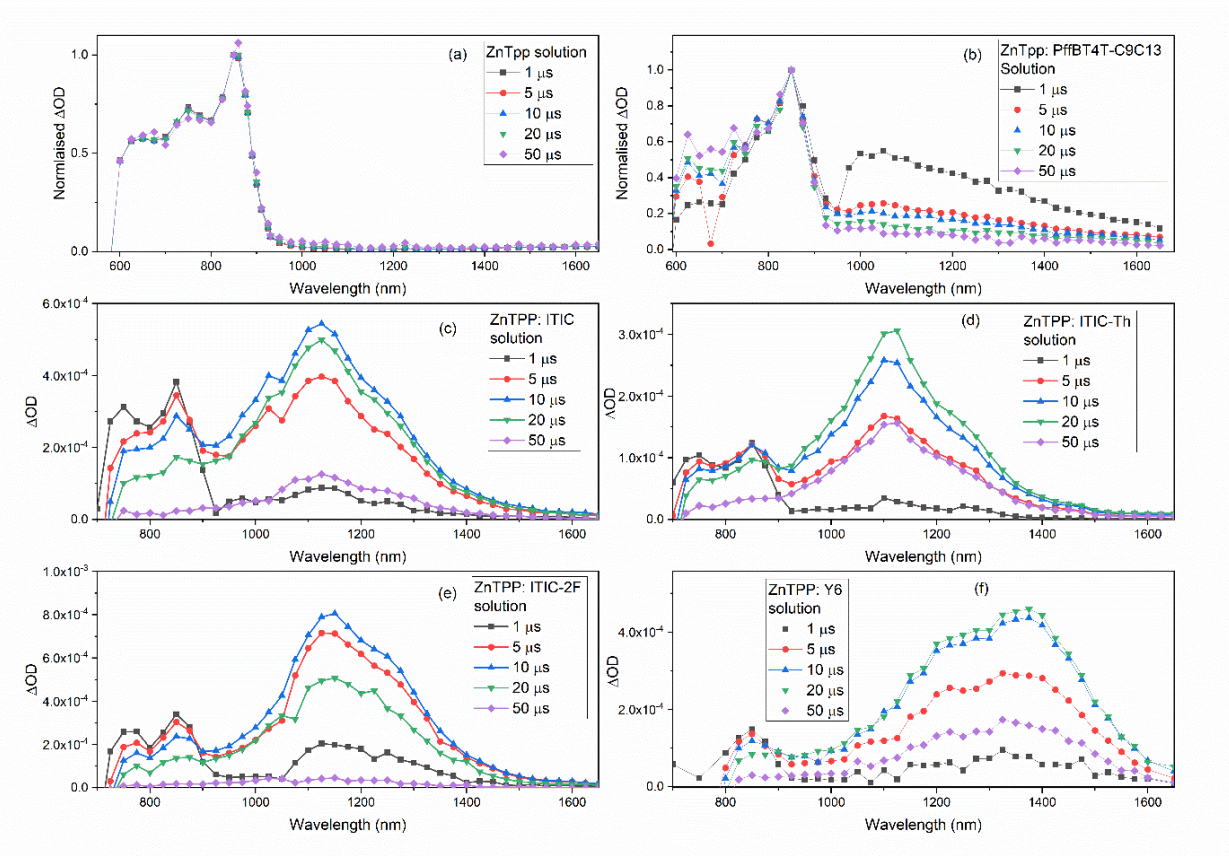

Figure 4.19 *Normalised (to 1 at 850 nm) transient absorption spectra for (a) ZnTpp (7×10^{-6} M) solution with an excitation energy at 30 µJ cm^{-2}, (b) ZnTpp: PffBT4T-C9C13 (7×10^{-6} M: 0.05 mg mL-1) solution with an excitation energy at 25 µJ cm^{-2}. Transient absorption spectra for (c) ZnTpp:ITIC (7×10^{-6} M: 7×10^{-6} M) solution (d) ZnTpp:ITIC-Th (7×10^{-6} M: 7×10^{-6} M) solution, (e) ZnTpp:ITIC-2F (7×10^{-6} M: 7×10^{-6} M) solution with an excitation energy at 12 µJ cm^{-2}, (f) ZnTpp:Y6 (7×10^{-6} M: 7×10^{-6} M) solution. All the spectra were obtained with an excitation wavelength at 426 nm, and excitation energy for all the all the ZnTpp:NFA solutions is around 12-14 µJ cm^{-2}.*

Table 4.2. *Parameters summery for the triplet extinction coefficient calculation in NFA solution and film.*

NFA	ε_{GS_soln} (10^5 L mol^{-1} cm^{-1}	σ_{GS_soln} (10^{-16} cm^2)	α in film (10^5 cm^{-1})[a]	σ_{GS_solid} (10^{-16} cm^2)	A	^{3}NFA* solution ε ($\pm$ 0.2 $\times$ 10^4 L mol^{-1} cm^{-1})	^{3}NFA* film ε ($\pm$ 0.4 $\times$ 10^4 L mol^{-1} cm^{-1})
ITIC	1.6 ± 0.5	6.2	2.4	4.7 ± 0.5	0.76	2.7	2.1
ITIC-Th	1.9 ± 0.5	7.3	-	-		5.7	2.3[b]
ITIC-2F	2.2 ± 0.5	8.4	2.5	5.2 ± 0.5	0.62	3.9	2.4
Y6	2.3 ± 0.5	8.8	2.0	4.0 ± 0.5	0.45	5.9	2.7

a. From Kerremans et al. Adv. Optical Mater. 2020, 8, 2000319.

b. Estimated from extrapolating along the ITIC series, observing that ε_{GS_soln} for ITIC-Th is between that of ITIC and ITIC-2F.

4.3.9 ns-µs TAS for blend PffBT4T-C9C13:Y6 film

Since the NFAs' triplet and anion formation have been investigated for each ITIC, ITIC-Th, ITIC-2F and Y6 as above, and the positive polaron and triplet spectral features have been well-determined in the PffBT4T-C9C13: fullerene blend systems in Chapter 3. ns-µs TAS was further employed to study the photophysical process for the PffBT4T-C9C13 blended with the selected NFAs. The transient absorption spectra were obtained with two pump wavelengths for each PffBT4T-C9C13: NFAs blend system. 455 nm is used to primarily excite the polymer and 700 nm is able to excite both the polymer and ITIC series' non-fullerene acceptors (709 nm was used for the low bandgap Y6 blend). The observed photophyscis are summarised in Joblonski diagram is shown in Figure 4.27.

As shown in Figure 4.20a-b, the spectral evolution of the PffBT4T-C9C13: Y6 blend film at both excitation wavelengths shows that two TA features: one shown as a sharp peak <800 nm and a smooth broadband <950 nm. With supporting evidence by the identical kinetics as shown in Figure 4.17d, these two TA features actually belong to the same transient species that was bisected by the Y6 ground state bleaching. The normalised (to 1) TA spectra for the blend (Figure 4.20c) show that neither polymer triplet nor Y6 triplet is generated in the blend, but rather the formation of transient species is attributed to charge carriers which decay obeys power law dynamics fitting. The assignment of transient species to the polarons is also consistent with the SEC results (Figure 4.11e). It should be noted that the decrease in TA signal <800 nm was due to the white light effect, resulting in a fast decay under high excitation energy. Normalised (per photon) TA spectra for both excitation wavelengths at 1 µs (Figure 4.20e) show that the Y6 negative polarons are generated in equal numbers, which is consistent with the previous report of the ultrafast energy transfer in Y6 blend.[28] Y6 as a low bandgap NFA, its ground state absorption spectrum showed a large overlap with the polymer PL (Figure 4.4d), and this could result in an efficient Förster resonant energy transfer (FRET) from polymer to Y6. Karuthedath et al. reported that the ultrafast energy transfer precedes hole transfer from the acceptor to the donor, and the yield of charge generation is equal at the initial stage. Since the faster decay kinetics were observed when the polymer blend excited at 700 nm than the 455 nm, and this is likely part of the reason for fewer negative

polarons observed with 700 nm excitation at 10 µs (Figure 4.20f). This suggests that the polymer-dominated domains are suitable for long-lived polarons diffusion exhibiting slow decay, while the fast decay at 1100 nm perhaps because of the simultaneous presence of polymer cations and Y6 anions in the D/A mixed domain accelerating the charge recombination process.

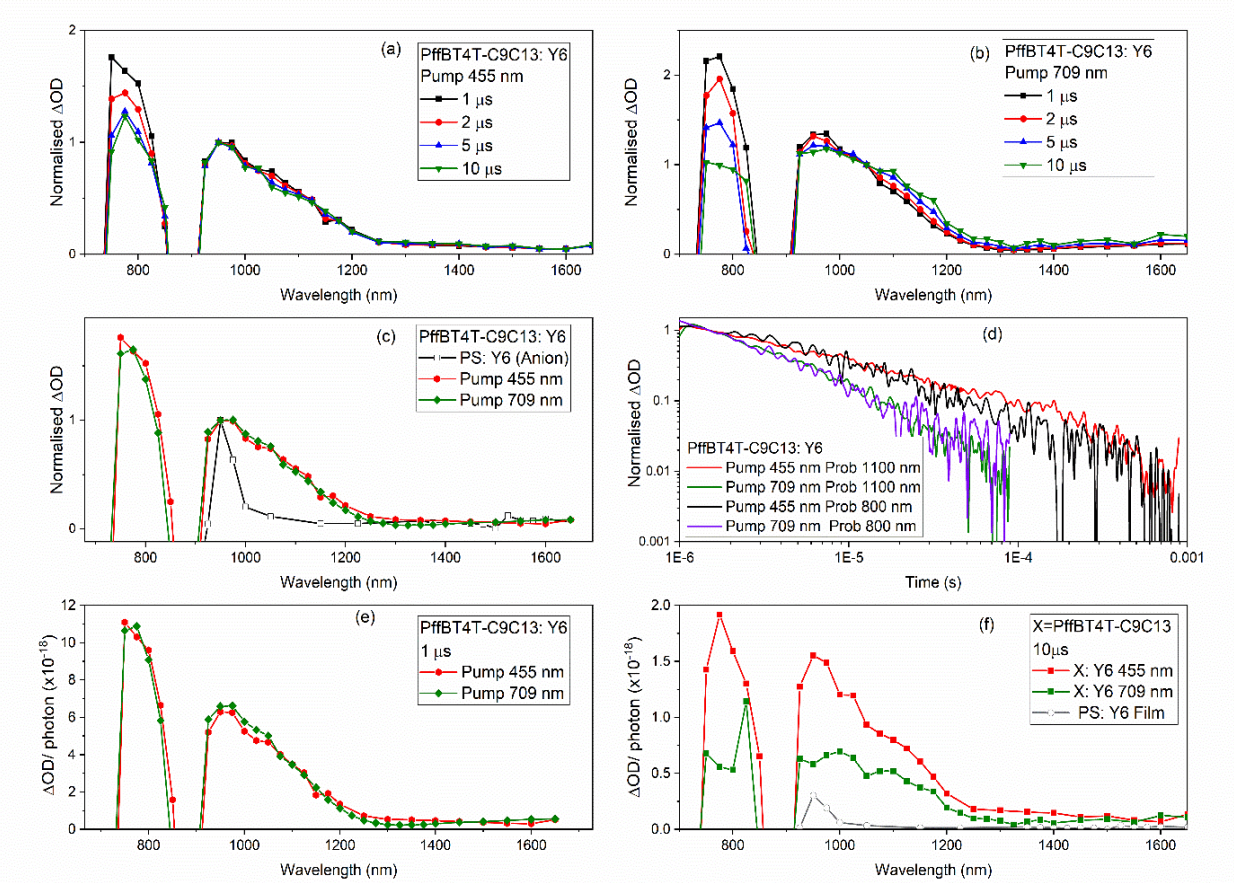

Figure 4.20 *PffBT4T-C9C13: Y6 (a) spectral evolution with excitation wavelength at (a) 455 nm (b) 709 nm. Normalised (to 1) transient absorption spectra of (c) PffBT4T-C9C13: Y6 film and PS: Y6 film. (d) normalised (to 1) decay dynamics for PffBT4T-C9C13: Y6 probing at 1100 nm and 800 nm with two excitation wavelengths at 455 nm and 709 nm. Normalised (per photo absorbed) TA spectra for PffBT4T-C9C13: Y6 at (e) 1 µs and (f) 10 µs. The blend PffBT4T-C9C13: ITIC series (ITIC, ITIC-Th, ITIC-2F) are excited at both 455 nm and 700 nm. PffBT4T-C9C13: Y6 film was excited at 455 nm and 709 nm with excitation energy around 13 µJ cm-2. Films PS with Y6 is excited at 709 nm with excitation energy around 30 µJ cm^{-2}.*

4.3.10 ns-µs TAS for blend PffBT4T-C9C13: ITIC-Th film

In contrast, PffBT4T-C9C13: ITIC-Th displays evidence of both charge carriers and triplet formation. Spectral evolution of PffBT4T-C9C13: ITIC-Th film are shown in Figure 4.21a-d, two types of transient species are formed: one peaked at wavelengths <800 nm and the other a sharp band at 1140 nm under both 455 nm and 700 nm excitation wavelengths but different absolte intensity. To assign these TA features, figure 4.18c displayed a comparison TA blend spectra to the triplet spectrum of PS:ITIC-Th film and the negative polaron spectrum. The ITIC-Th triplet was illustrated to be created in PffBT4T-C9C13:ITIC-Th blend with both excitation wavelengths, that was identical match of the PS:ITIC-Th spectrum in terms of the spectral position, shape and breadth. Furthermore, the considerable increase in relative intensity of the 1140 nm peak when exciting the ITIC-Th directly is strongly indicative of an ITIC-Th species. The <800 and 1000 nm bands are attributed to polymer polarons that are similar spectral shape of the previously seen in the PffBT4T-C9C13: $PC_{70}BM$ blend in Chapter 3. More precisely, the <800 nm was attributed to the polymer polarons generated in the polymer domain and 1000 nm band ascibed as the polymer polarons generated in D/A mixed domains. Moreover, ITIC-Th anions are also observed around 800 nm from the SEC spectrum of ITIC-Th film (Figure 4.11c), thus the assignment of the more intense <800 nm peak is likely a combination of polymer and ITIC-Th polarons.

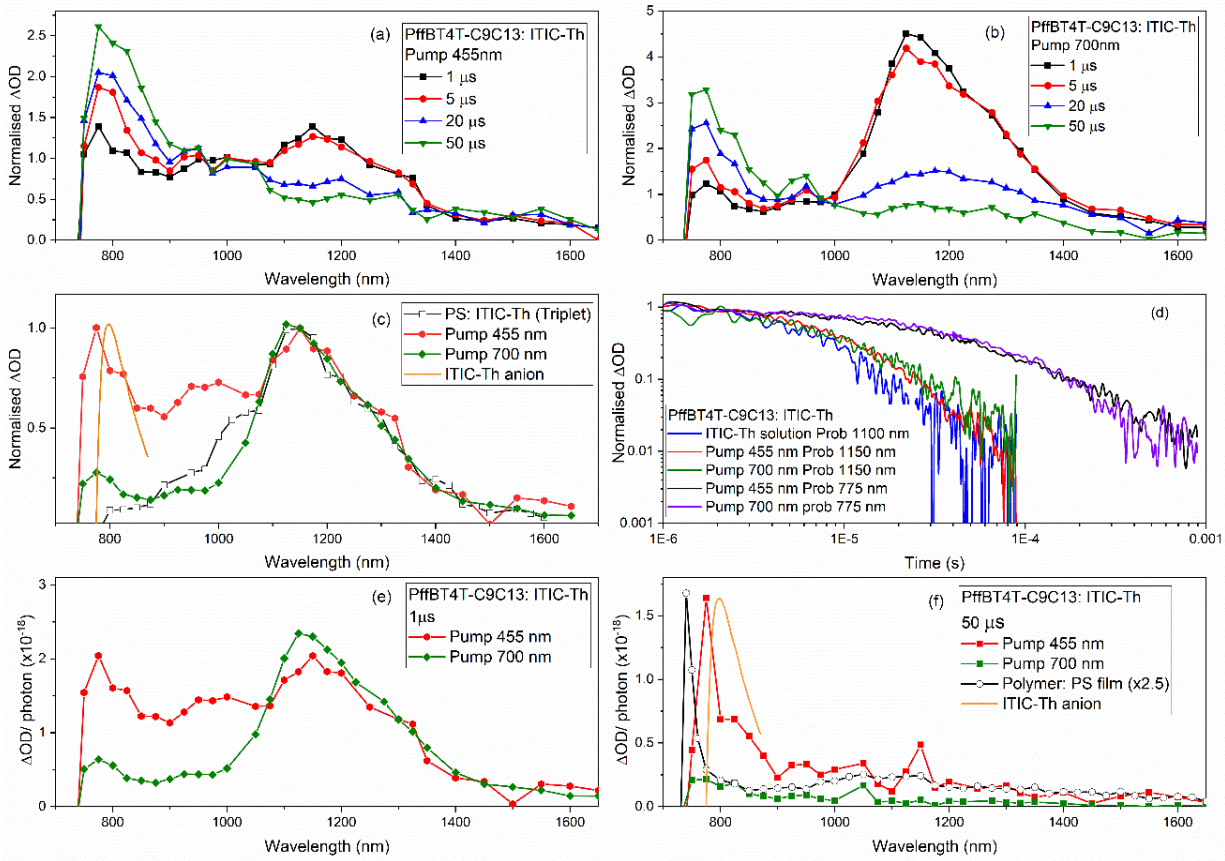

Figure 4.21 *PffBT4T-C9C13: ITIC-Th (a) spectral evolution with excitation wavelength at (a) 455 nm (b) 700 nm. Normalised (to 1) transient absorption spectra of (c) PffBT4T-C9C13: ITIC-Th film and PS: ITIC-Th film and SEC spectra for ITIC-Th film. (d) normalised (to 1) decay dynamics for PffBT4T-C9C13: ITIC-Th probing at 1150 nm and 775 nm with two excitation wavelengths at 455 nm and 700 nm. Normalised (per photo absorbed) TA spectra for PffBT4T-C9C13: ITIC-Th at (e) 1 µs and (f) 50 µs. The blend PffBT4T-C9C13: ITIC -Th were excited at both 455 nm and 700 nm. The excitation energy used for ITIC-Th with polymer blend was 23 µJ cm^{-2}. Film PS with ITIC-Th was excited at 700 nm with excitation energy around 30 µJ cm^{-2}.*

As shown in Figure 4.21d, the ITIC-Th triplet in the PffBT4T-C9C13:ITIC-Th blend decays rapidly with a monoexponential lifetime of 6 µs and reveals more of the charge carriers' spectral features at longer timescales. Interestingly, a similar monoexponential decay lifetime of ITIC-Th triplet in the polymer blend is found as in solution, indicating that ITIC-Th triplet generated in polymer blend is not being regenerated via charge recombination. Furthermore, the appearance of similar ITIC-Th triplet populations was found in the blend irrespective of the excitation wavelength (Figure 4.21e), suggesting that the observation of ITIC-Th triplet due to the presence of energy transfer mechanism (either singlet or triplet), with the ITIC-Th triplet being the lowest energy triplet in the system.

4.3.11 ns-µs TAS for PffBT4T-C9C13 blending with ITIC and ITIC-2F films

Like PffBT4T-C9C13: ITIC-Th, the existence of charge carriers and triplet states was also found in PffBT4T-C9C13: ITIC blend film. The difference is that only ITIC-Th triplet was found in ITIC-Th blend at early timescales, but both polymer and ITIC triplet states were found in the ITIC blend excited at different excitation wavelengths.

As shown in Figure 4.22a-b, the spectral evolution of the PffBT4T-C9C13: ITIC shows three spectral features: excitation wavelength independent long-lived sharp peak at <800 nm, a relatively narrow band at 920 nm and a third excitation-dependent band is generated at 1080 nm with polymer excitation and formed at 1150 nm with ITIC excitation. As with the ITIC-Th blend, the <800 nm and 920 nm bands can be initially attributed to the polymer polarons generated in the pure polymer domain and D/A mixed domain. Considering the formation of ITIC anion generated at 780 nm from SEC results (Figure 4.11b), the <800 nm band in the ITIC blend, therefore, contains both the ITIC anions and the polymer polarons. To make an assignment of the third band in the ITIC blend, normalised (to 1) TA spectra for PffBT4T-C9C13:ITIC blend and the reference TA spectra of the polymer and ITIC triplets provide some clues (Figure 4.22c). The red edge of the 455 nm PffBT4T-C9C13: ITIC TA spectrum matches perfectly with the PffBT4T-C9C13: $PC_{70}BM$ spectrum, indicating the 1080 nm band can be attributed to the polymer triplet. In contrast, the 1150 nm band in 700 nm PffBT4T-C9C13: ITIC TA spectrum show a very similar spectral shape to the TA spectra of ITIC solution and PS: ITIC film, suggesting that the 1150 nm band is ITIC triplet. The appearance of polymer and ITIC triplet at 1 µs with their corresponding excitation wavelengths can possibly be explained by the similar triplet energy level of the polymer and ITIC (the S_1 energy calculated 1.71 VS 1.66 eV), and thus there is no impetus for triplet energy transfer.

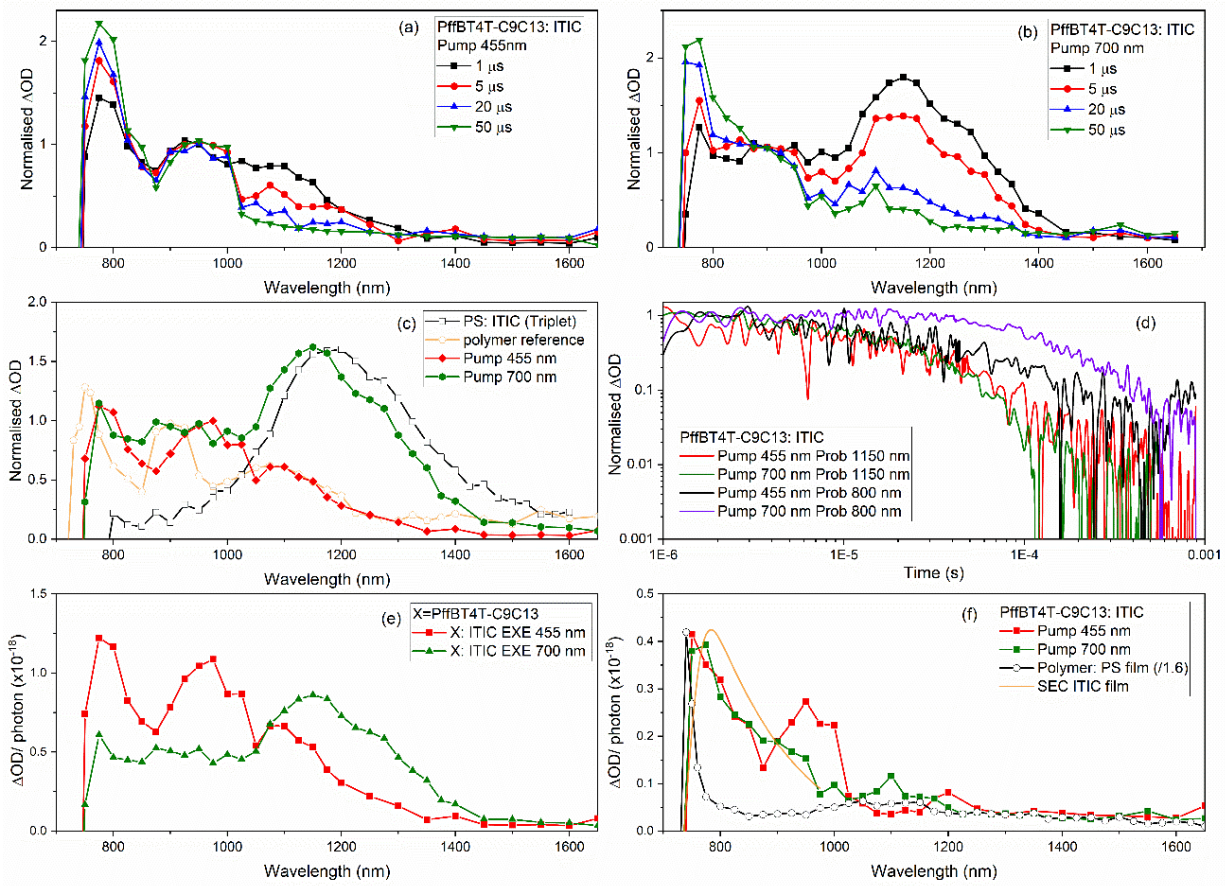

Figure 4.22 *PffBT4T-C9C13: ITIC (a) spectral evolution with excitation wavelength at (a) 455 nm (b) 700 nm. Normalised (to 1) transient absorption spectra of (c) PffBT4T-C9C13: ITIC film, PS: ITIC and PffBT4T-C9C13: PC70BM films (d) normalised (to 1) decay dynamics for PffBT4T-C9C13: ITIC probing at 1150 nm and 800 nm with two excitation wavelengths at 455 nm and 700 nm. Normalised (per photo absorbed) TA spectra for PffBT4T-C9C13: ITIC at (e) 1 µs and (f) 50 µs. The blend PffBT4T-C9C13: ITIC were excited at both 455 nm and 700 nm. The excitation energy used for ITIC with polymer blend was 18 µJ cm^{-2}. Film PS with ITIC was excited at 700 nm with excitation energy around 30 µJ cm^{-2}. The excitation wavelength used for PffBT4T-C9C13:PC70BM is 700 nm with an excitation energy 4 µJ cm^{-2}.*

Normalised (to 1) decay dynamics for the PffBT4T-C9C13 and ITIC triplets in PffBT4T-C9C13: ITIC is exhibited in 4.22d. It is shown that the decay kinetics for both polymer and ITIC triplets is fitted with monoexponential decay with a lifetime 33 µs and 23 µs, respectively, which are longer-lived than their lifetimes in solution (12 µs for polymer and 1.6 µs for ITIC). The prolonged lifetime may have its origin in charge recombination repopulating the triplet state on longer timescales.

Like PffBT4T-C9C13: ITIC, PffBT4T-C9C13: ITIC-2F also exhibits both the charge carriers, polymer and ITIC-2F triplets, with strong excitation wavelength dependence. As the spectral

evolution and normalised (to 1) TA spectra are shown in Figure 4.23a-c, the dual polaron peaks are generated at <800 nm and 950 nm, the polymer triplet are formed at 1080 nm with polymer excitation and ITIC-2F triplet formed as an intense broad band centred at 1200 nm with ITIC-2F excitation. There is another band around 1600 nm showing a longer lifetime than the polymer triplet. From the SEC results, the 1600 nm band is also attributed to polymer polarons. Like the other blend in ITIC series, the dual polaron peak at <800 nm shows both the formation of polymer cation and ITIC-2F anion (Figure 4.11d), and the 950 nm band is attributed to the polymer polarons generated in D/A mixed domains. Being different to the blends with ITIC-Th and Y6, the spectral evolution spectra of PffBT4T-C9C13: ITIC-2F give further information that in the late timescales there is a strong contribution to the TA spectrum by triplets, not just polarons (Figure 4.23d,f). Furthermore, the late-time spectrum is roughly the same for both excitation wavelength and the triplet region matches the polymer triplet (Figure 4.23f).

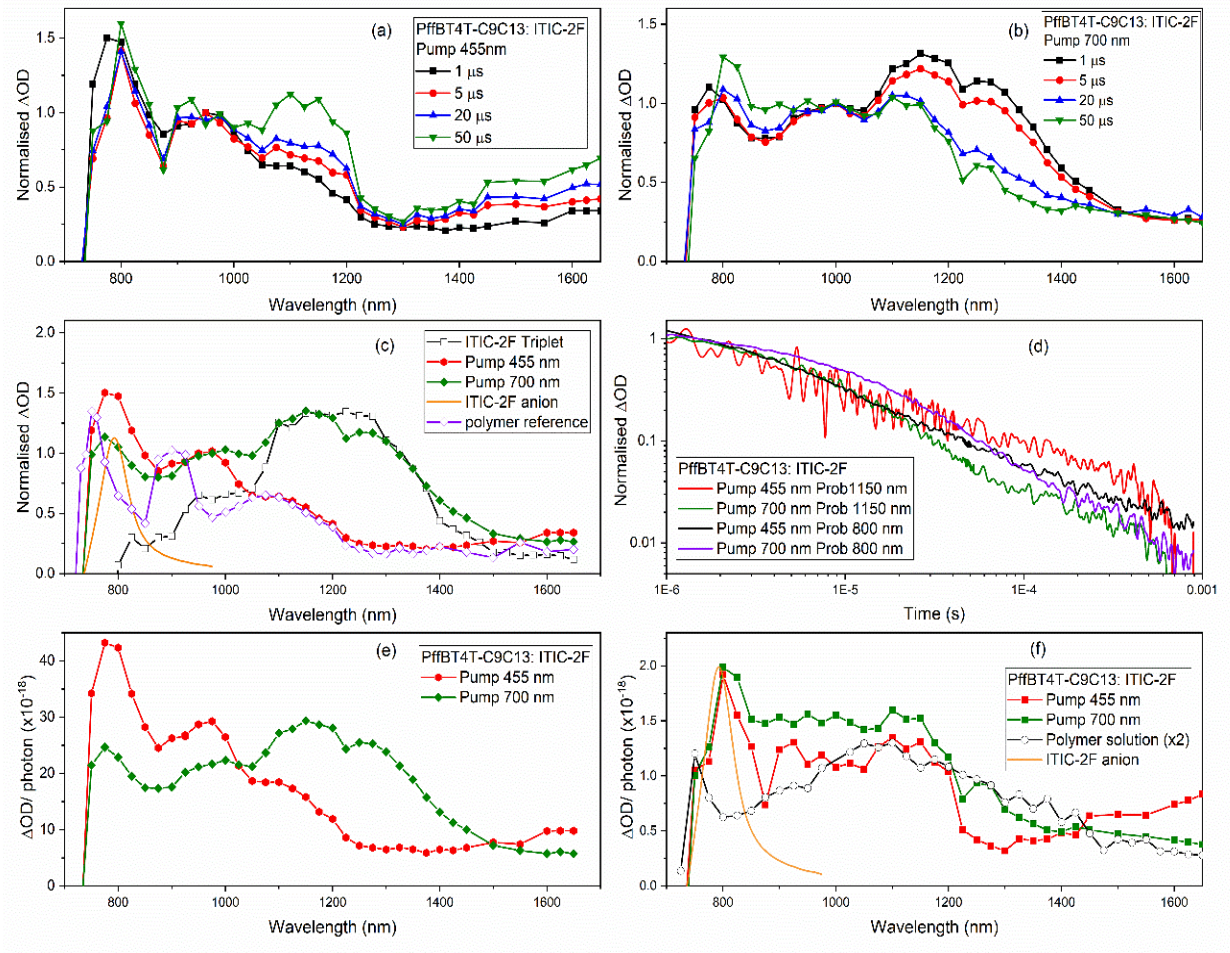

Figure 4.23 *PffBT4T-C9C13: ITIC-2F (a) spectral evolution with excitation wavelength at (a) 455 nm (b) 700 nm. Normalised (to 1) transient absorption spectra of (c) PffBT4T-C9C13: ITIC-2F film, PS: ITIC-2F, SEC spectra and PffBT4T-C9C13: $PC_{70}BM$ films (d) normalised (to 1) decay dynamics for PffBT4T-C9C13: ITIC -2F probing at 1150 nm and 800 nm with two excitation wavelengths at 455 nm and 700 nm. Normalised (per photo absorbed) TA spectra for PffBT4T-C9C13: ITIC-2F at (e) 1 µs and (f) 50 µs. The blend PffBT4T-C9C13: ITIC-2F were excited at both 455 nm and 700 nm. The excitation energy used for ITIC-2F with polymer blend was 10 µJ cm^{-2}. Film PS with ITIC was excited at 700 nm with excitation energy around 30 µJ cm^{-2}. The excitation wavelength used for PffBT4T-C9C13:$PC_{70}BM$ is 700 nm with excitation energy 4 µJ cm^{-2}.*

An examination of triplet decay with 700 nm excitation is shown in Figure 4.23d; it displays a biphasic decay which is consistent with the TA spectra investigation. The ITIC-2F triplet decay is observed until approximately 80 µs, after which time the polymer triplet is more apparent and decays at the same rate as the 455 nm excitation decay. The polymer triplet lifetime contains a long-lived component of 40 µs in the blend, three times longer than the lifetime in solution, indicative of non-geminate recombination. As the black line for polaron decay shown in Figure 4.23d, polymer polarons are the same order of magnitude as the polymer triplet

lifetime, consistent with this hypothesis: triplet generation could form with polaron recombination. Normalised (per photon) TA spectra of ITIC-2F blend also show another interesting observation that the charge yield and triplet population in ITIC-2F is substantially higher than the rest of the ITIC-based blends.

4.4 Discussion

From the spectroscopic study for these polymer:NFA blend films, triplet formation is particularly prevalent in these NFA based blend systems. Since triplet formation is generally regarded as an energy loss pathway, it is important not only to understand how they are formed but also to know their population in different polymer blend films. Therefore, we used sensitisation procedures to estimate the triplet extinction coefficient for each NFAs. The estimated triplet population in both solution and blend based on the calculated triplet extinction coefficient for each NFAs is shown in Figure 4.24a and b, respectively. It should be noted that only NFA-excited TA results were used for the quantification of NFA triplet formation. Because the wavelength (455 nm) used to excite the polymer simultaneously produced polymer triplet state on several films but not all, which is not conductive to the lateral comparative analysis of the triplet state in different NFAs.

In the solution, it is observed that Y6 displays the highest triplet population by a factor of almost four in relative to the lowest population in ITIC-Th. It has been previously reported by Ohkita et al. that Y6 can generate triplets via singlet fission in addition to ISC, and this could account for the highest triplet population in these later timescales.[29] ITIC-2F has the second highest triplet population, an unusual result given its high PL quantum yield: a low ISC efficiency would therefore be expected. However, this could be compensated by its relatively long triplet lifetime. The lowest triplet population found in ITIC-Th solution might be because of the strong S-S intermolecular interaction that facilitated the charge transfer process and less triplet formation.

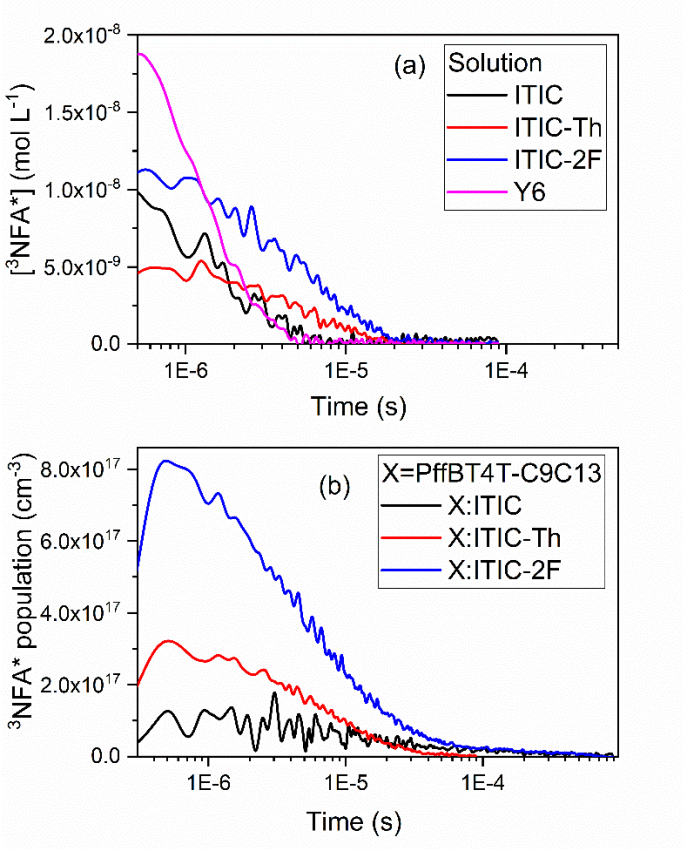

Figure 4.24 *The triplet yield calculated (a) in pristine NFAs solution and (b) in blend PffBT4T-C9C13: NFAs films using 700 nm excitation.*

It is important to noticed that the triplet extinction coefficient of a material can be vary between the solution and the solid phase. A quantitative triplet sensitisation procedure in the solid phase is too difficult to calculate accurately. One of the reasons is the lack of standards with known triplet absorption coefficient in the solid phase. Furthermore, the excited state annihilation process could also lead to inaccurate ε value. Hence, we have addressed this problem by obtaining correction factors for the change in absorption cross section between solution and film for the ground state of each NFA, and then triplet ε in solid phase can be calculated by applying these correction factors to the solution triplet ε as determined in Section 2.2.2. Actually, even to obtain the ground state ε in film is non-trivial, especially for dispersive materials, but this has been achieved by Armin et al for the NFAs: ITIC, ITIC-2F and Y6.[30] The estimated triplet state ε in NFA films are in range from 2-3 x10^4 L mol^{-1} cm^{-1}. However, applying a correction factor does introduce an additional uncertainty, but this is likely to be systematic errors, and this will not significantly affect the results discussed below.

Since there is little evidence of Y6 triplet generated in the polymer blends in ns-µs timescales, only the ITIC related triplet population was estimated in the polymer: NFAs' blend film exhibited in Figure 4.24b. PffBT4T-C9C13: ITIC-2F has the highest NFA triplet population of 8 $\times 10^{17}$ cm^{-3}, significantly greater by a factor of 2.7 than PffBT4T-C9C13: ITIC-Th. The likely origin of this is the non-geminate recombination of charges to create triplets, as also evidenced by the substantially longer triplet lifetime in the blend, thereby providing an additional avenue for populating the triplet state. Previous works have shown that the fluorinated NFAs have suppressed non-geminate triplet formation, for example by stabilizing the ^{3}CT state below the local NFA triplet. Indeed, although the highest triplet population was found in the PffBT4T-C9C13: ITIC-2F, the triplet suppression by fluorination can also be shown under this blend system by comparison with PffBT4T-C9C13: ITIC. This is because PffBT4T-C9C13:ITIC-2F also has the highest charge carrier population (Figure 4.23e) and thus more charges are available to recombine to create triplets. Instead, we can correct the triplet population for charge yield for PffBT4T-C9C13:ITIC-2F and PffBT4T-C9C13:ITIC (noting that PffBT4T-C9C13:ITIC-Th exhibited no evidence of non-geminate triplet formation). PffBT4T-C9C13:ITIC-2F produces 40 times more charge carriers but only 8 times more triplets compared to the ITIC blend, thus we estimate that PffBT4T-C9C13:ITIC-2F produces only one-fifth the number of triplets compared to the ITIC blend per charge carrier.

As we observed that the highest charge carrier populations were found in the PffBT4T-C9C13:ITIC-2F blend (with a large number of triplet formation at the same time), even more than the Y6 blend (charge carrier only generated). This might be explained by the largest driving force in PffBT4T-C9C13:ITIC-2F among other blends for the charge separation which is defined by the difference between HOMO level (0.45 eV) or LUMO level (0.55 eV)of the donor and acceptor. It is well-known that the larger the driving force for charge separation, the higher charge carriers' populations.[31] Furthermore, a higher dielectric constant of the ITIC-2F (5.83) has been reported than Y6 (5.73) and ITIC (4.3).[32] The higher dielectric constant of the ITIC-2F indicates a smaller binding energy between electrons and holes which can facilitate the charge separation process. It is intriguing that PffBT4T-C9C13:ITIC-2F produces such high charge yield, but it also exhibits the lowest PL quenching. However, this could be compensated for by its high PL quantum yield, opening opportunities for photon recycling.

It was also observed that there are considerable differences in the charge carriers dynamics between the blends upon polymer excitation (Figure 4.25), with both PffBT4T-C9C13:ITIC-2F and PffBT4T-C9C13:Y6 both exhibit distinct power law kinetics with α = 0.7 while PffBT4T-C9C13:ITIC and PffBT4T-C9C13:ITIC-Th display a stretch exponential decay kinetics. This can be correlated with the observation that the first two blends also have the highest charge generation yields by order of magnitude. Stretched exponential kinetics are typically associated with multiple decay pathways in a dispersive environment.[33,34] Conversely, the α = 0.7 is very high compared to most other polymer:acceptor blends, and indicates a crystalline, relatively trap-free environment of the polymer domain.[35,36] This can lead to higher charge mobility and greater CT state delocalisation, both of which can facilitate the higher charge carrier photogeneration yields observed for the ITIC-2F and Y6 blends. However, it should be noted that the NFA could also be embedded in the crystalline donor domain facilitating charge back recombination to form triplet states. This does not affect the formation of large pure crystalline polymer domains still exist in the polymer:NFA blend films.

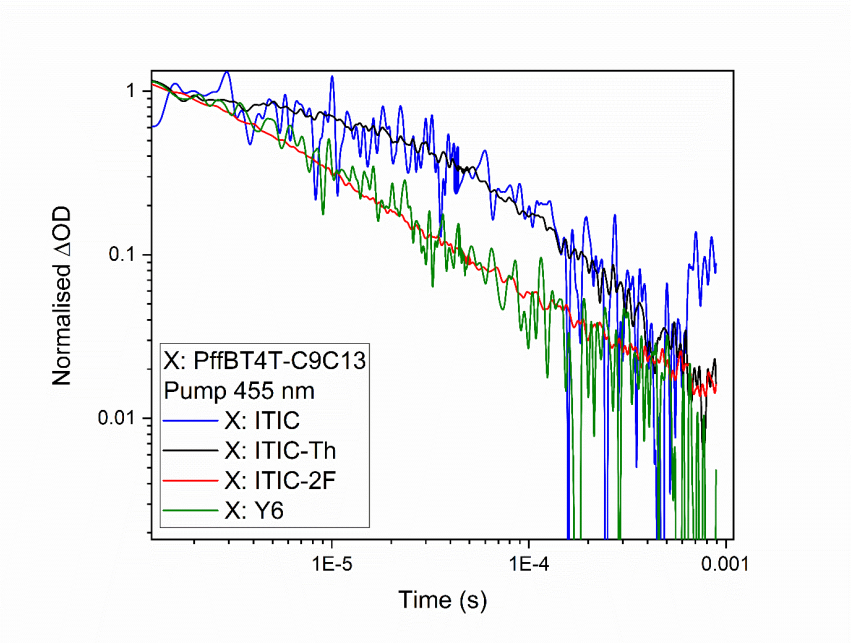

Figure 4.25 *Normalised (to 1) decay dynamics for the polymer polaron in PffBT4T-C9C13 blended with NFAs ITIC (probe at 800 nm), ITIC-Th (probe at 775 nm), ITIC-2F (probe at 800 nm) and Y6 (probe at 800 nm) films. The excitation wavelength 455 nm is used for all the films.*

To exploring the intriguingly high charge carriers and triplet population of the blend PffBT4T-C9C13:ITIC-2F further, a spectroscopic and morphological study of the PffBT4T-C9C13:ITIC-2F

was made as a function of blend ratio, and the TA measurements with two different excitation wavelengths. As shown in Figure 4.26, the charge photogeneration process was detected in the D:A blend with ratio 1:3 and 3:1, and compared to the 1:1.2 blend. It is immediately evident that the 1:1.2 blend produces the highest charge carrier and triplet populations. With excess ITIC-2F in the blend (1:3), or 700 nm excitation (for either 1:3 or 3:1 blends), very few excited state species are still present on μs timescales, indicating rapid relaxation processes back to the ground state. Indeed, the population of triplets and charges under these conditions are very similar to the pristine, or PS blend ITIC-2F films. AFM images for these 3:1 and 1:3 blend ratio films are shown in Figure 4.26c-d, the surface roughness R_q was estimated to be 11.9 nm for 1:3 blend and 7.3 nm for 3:1 blend. These values for rougher than the 1:1.2 blend with R_q 5.1 nm. The increased surface roughness with 1:3 and 3:1 blend ratio in comparison to the 1:1.2 blend indicated that a stronger phase segregation was observed in 1:3 blend than 3:1 blend than 1:1.2 blend films. A particularly interesting observation is that ITIC-2F triplet only exists in the 1:1.2 blend ratio film. Therefore, the NFA triplet formation and smoother surface roughness found in the 1:1.2 blend imply the charge back recombination to form triplet state primarily occurs in well-dispersed, intermixed D/A domains. In contrast, charge recombination is considerably less apparent when large crystalline, segregated domains are present.

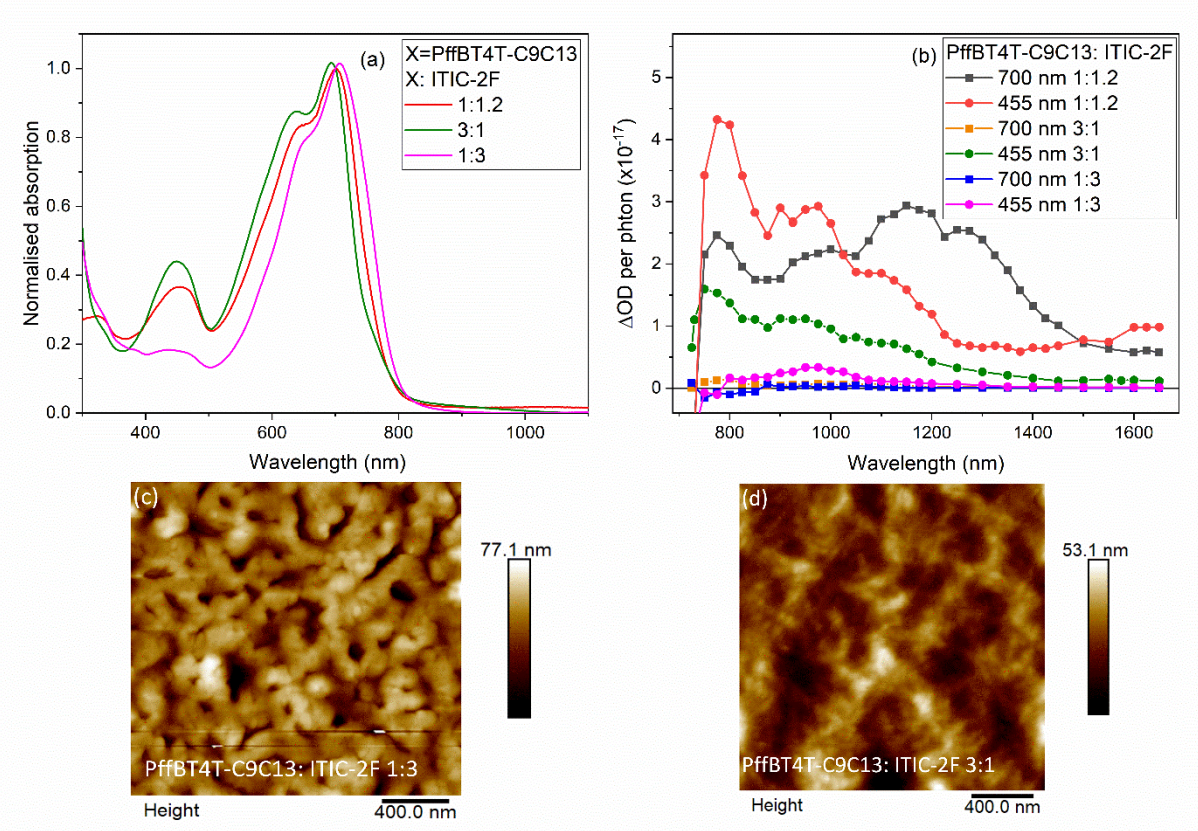

Figure 4.26 *The μs-TA spectra, corrected for photons absorbed, for PffBT4T-C9C13:ITIC-2F blends with weight ratios 3:1, 1:1.2, and 1:3 with excitation wavelengths of 455 and 700 nm (a). AFM images for PffBT4T-C9C13:ITIC-2F 3:1 (b) and 1:3 (c) ratios, noting that the AFM data for the 1:1.2 ratio are displayed in Figure 4.7d and i.*

A summarised photophysical mechanism for all four PffBT4T-C9C13:NFA blend films is shown in Figure 4.27. It has been demonstrated that the formation of charge carriers have been observed in all four NFA based polymer blends, while the NFA triplet formation just been observed in ITIC series blend films with PffBT4T-C9C13 on the μs timescales. For the PffBT4T-C9C13:ITIC-Th blend film, ITIC-Th triplets were produced via the energy transfer process, while ITIC or ITIC-2F blend was created via charge back recombination, and the yield of the triplet is proportional to the charge carrier's population.

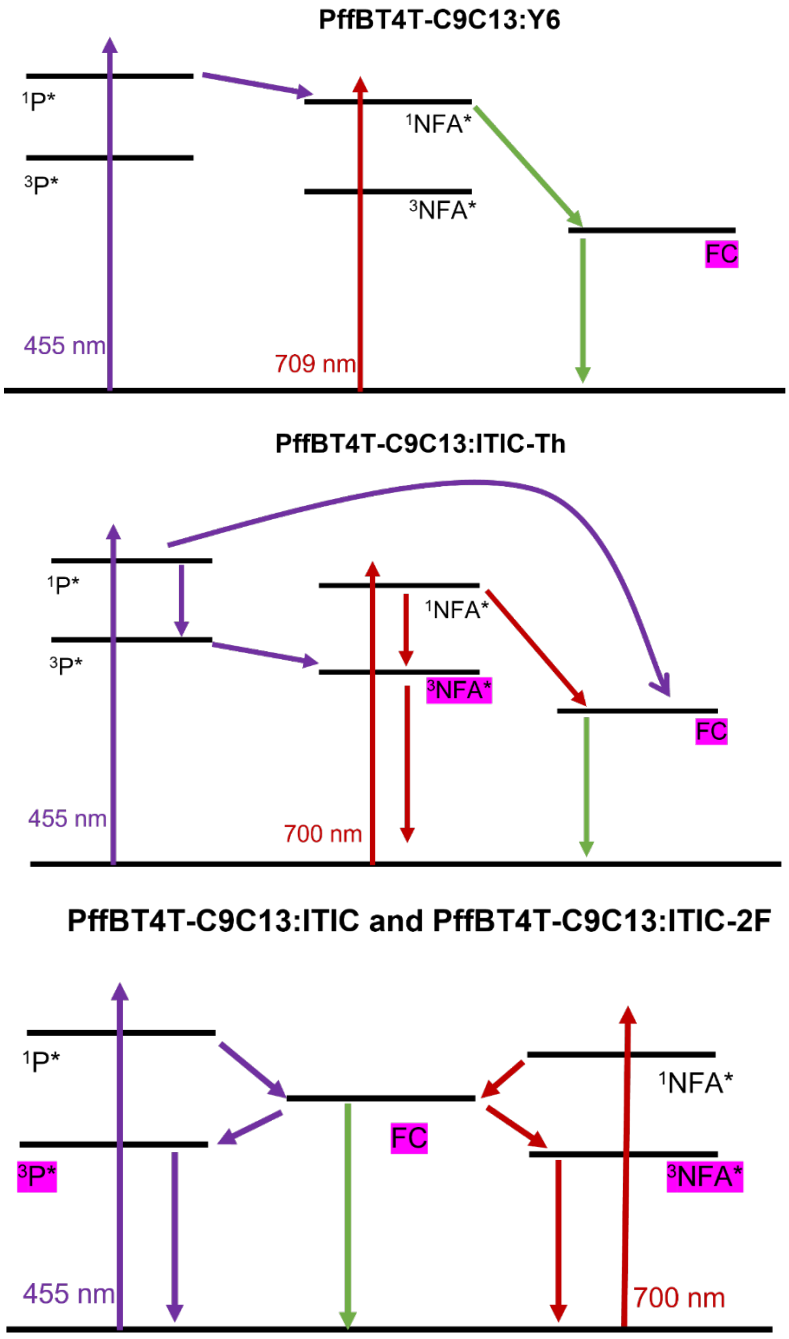

Figure 4.27 *Scheme illustrated the photophysical mechanisms observed in the PffBT4T-C9C13: NFAs blend films. Purple arrow denote polymer (P) excitation with 455 nm pum, while red arrows denote NFA excitation with 700 nm excitation (althouh some polymer excitation is alo present with this pump wavelength). Green arrow denot processes that occur irrespective of excitation wavelength. The excited species highlighted in pink show those present on µs timescales in each blend. Note that the CT state can not be observed in ns-µs TAS, and therefore foucus only on the free charge carriers (FC); however, CT state will certainly contributed during both charge generation and recombination processes.*

The lack of Y6 triplets on the μs timescales is probably related to two aspects. One is the long lifetime of the Y6 singlet exciton and the ultrafast energy transfer enabling efficient exciton quenching despite the large domain size observed.[37] The Y6 blend also has the largest GIXRD integration area of all the blends studied, which is consistent with the lower energetic disorder compared to the ITIC series, as reported by Bredas et al.[38] The ordered domains and fast charge carrier transfer rates enable charge carrier generation to dominate in PffBT4T-C9C13:Y6 films.[39] However, non-geminate triplet formation has been observed in the PM6:Y6,[40] but it should be noted that the PM6:Y6 also presents a very smooth morphology with the two components highly miscible with one another,[41] in contrast to the strongly segregated PffBT4T-C9C13:Y6. The second reason could be the intrinsic charge photogeneration in pure and crystalline Y6 domain,[24] this is consistent with a small difference in charge population between the PS:Y6 film and the PffBT4T-C9C13:Y6 blend film (Figure 4.20f). The efficient intrinsic charge photogeneration in the low bandgap Y6 contributes to the lack of non-geminate triplet formation: if charges are generated in large, relatively pure domains, then D/A non-geminate recombination is less likely to occur.

The prevalence of the NFA triplets and their short lifetime in the PffBT4T-C9C13:ITIC-Th is likely partially related to the ITIC-Th's greater propensity to cluster, an indicated by the morphology and PL results. Furthermore, the similarity in the NFA triplet population, irrespective of excitation wavelength, strongly indicates an energy transfer process. In contrast, the other ITIC series' blend with distinct excitation wavelength dependence. 455 nm primarily excites the polymer, and PffBT4T-C9C13:ITIC and PffBT4T-C9C13:ITIC-2F show the polymer triplet generation, with no evidence of the NFA triplets at all. The energetics of energy transfer does not vary across the polymer:ITIC series, where the S_1 energies of the PffBT4T-C9C13 and ITIC are very similar, and the T_1 energy levels of the ITIC series are calculated to be invariant.[42] However, it has been previously reported by Marina *et al*. that polymorphism and phase behaviour of the ITIC-Th is different to the others in the ITIC series due to differing chemical moiety occurring in the central building block rather than terminal groups, thereby altering intermolecular interactions.[43] The presence of energy transfer in the PffBT4T-C9C13:ITIC-Th could therefore be related to differences in the nanomorphology at the D/A interface, possibly enabling a small reorganisation energy and thus facilitating energy transfer.

Finally, we consider the ramifications of these results for OSC device performance. Firstly, the variation in photophysical mechanisms across the different NFA blends suggests a complex interplay between intrinsic behaviour, energetics, and morphology that dictates that new OSC materials must be considered on their own merits. Our results suggest that charge recombination to form triplets is significantly enhanced when intermixed, well-dispersed domains are present. However, the clear observation that triplet populations also scale with charge carrier populations implies that future research directions must attempt to decouple the two, or alternatively employ strategies to harness triplet states to benefit device performance.

4.5 Conclusions

In summary, the triplet formation and behaviour are studied in blend systems of NFAs (ITIC, ITIC-Th, ITIC-2F and Y6) with a well-studied reference polymer the PffBT4T-C9C13. SEC spectra for the pristine polymer and NFAs' film give information about the polymer cation and NFAs' anion formation to assist in understanding the spectral congestion of the μs TA spectra, and triplet sensitization measurements are used to quantify NFA triplet populations in both solution and solid phases. It has been shown that there are only charge carriers observed in the PffBT4T-C9C13: Y6 films, and ITIC-Th triplets are generated in the PffBT4T-C9C13: ITIC-Th blend. In contrast, both the polymer and NFAs' triplets are generated in the PffBT4T-C9C13: ITIC and ITIC-2F blends, and longer-lived triplet lifetime in the polymer:NFA blends suggest that triplet formation formed via non-geminate recombination. Although triplet formation is suppressed in the fluorinated ITIC-2F relative to ITIC, the extraordinarily high charge carrier population observed in PffBT4T-C9C13: ITIC-2F coupled with the non-geminate recombination mechanism also results in a high triplet population. These results show that while there is no consistent pattern regarding triplet behaviour in NFA blends, triplets are extremely prevalent and can reach very high populations.

4.6 References

1 Y. Liu, J. Zhao, Z. Li, C. Mu, W. Ma, H. Hu, K. Jiang, H. Lin, H. Ade and H. Yan, *Nat Commun*, 2014, **5**, 4007

2 Z. Li, K. Jiang, G. Yang, J. Y. L. Lai, T. Ma, J. Zhao, W. Ma and H. Yan, *Nat Commun*, 2016, **7**, 13094.

3 M. S. Kotova, G. Londi, J. Junker, S. Dietz, A. Privitera, K. Tvingstedt, D. Beljonne, A. Sperlich and V. Dyakonov, *Mater Horiz*, 2020, **7**, 1641–1649.

4 L. Yang, W. Gu, L. Lv, Y. Chen, Y. Yang, P. Ye, J. Wu, L. Hong, A. Peng and H. Huang, *Angewandte Chemie*, 2018, **130**, 1108–1114.

5 A. J. Gillett, A. Privitera, R. Dilmurat, A. Karki, D. Qian, A. Pershin, G. Londi, W. K. Myers, J. Lee, J. Yuan, S. J. Ko, M. K. Riede, F. Gao, G. C. Bazan, A. Rao, T. Q. Nguyen, D. Beljonne and R. H. Friend, *Nature*, 2021, **597**, 666–671.

6 A. Privitera, J. Grüne, A. Karki, W. K. Myers, V. Dyakonov, T. Q. Nguyen, M. K. Riede, R. H. Friend, A. Sperlich and A. J. Gillett, *Adv Energy Mater*, 2022, **12**, 2103944

7 A. J. Gillett, A. Privitera, R. Dilmurat, A. Karki, D. Qian, A. Pershin, G. Londi, W. K. Myers, J. Lee, J. Yuan, S. J. Ko, M. K. Riede, F. Gao, G. C. Bazan, A. Rao, T. Q. Nguyen, D. Beljonne and R. H. Friend, *Nature*, 2021, **597**, 666–671.

8 A. J. Gillett, A. Privitera, R. Dilmurat, A. Karki, D. Qian, A. Pershin, G. Londi, W. K. Myers, J. Lee, J. Yuan, S. J. Ko, M. K. Riede, F. Gao, G. C. Bazan, A. Rao, T. Q. Nguyen, D. Beljonne and R. H. Friend, *Nature*, 2021, **597**, 666–671.

9 A. Rao, P. C. Y. Chow, S. Gélinas, C. W. Schlenker, C. Z. Li, H. L. Yip, A. K. Y. Jen, D. S. Ginger and R. H. Friend, *Nature*, 2013, **500**, 435–439.

10 J. Guo, J. M. Marin-Beloqui and T. M. Clarke, *JPhys Materials*, 2021, **4**, 4

11 J. Mai, Y. Xiao, G. Zhou, J. Wang, J. Zhu, N. Zhao, X. Zhan and X. Lu, *Advanced Materials*, 2018, **30**, 1802888

12 Y. Lin, F. Zhao, Q. He, L. Huo, Y. Wu, T. C. Parker, W. Ma, Y. Sun, C. Wang, D. Zhu, A. J. Heeger, S. R. Marder and X. Zhan, *J Am Chem Soc*, 2016, **138**, 4955–4961.

13 Y. Lin, F. Zhao, Q. He, L. Huo, Y. Wu, T. C. Parker, W. Ma, Y. Sun, C. Wang, D. Zhu, A. J. Heeger, S. R. Marder and X. Zhan, *J Am Chem Soc*, 2016, **138**, 4955–4961.

14 R. Wang, J. Xu, L. Fu, C. Zhang, Q. Li, J. Yao, X. Li, C. Sun, Z. G. Zhang, X. Wang, Y. Li, J. Ma and M. Xiao, *J Am Chem Soc*, 2021, **143**, 4359–4366.

15 K. Reichenbächer, H. I. Süss and J. Hulliger, *Chem Soc Rev*, 2005, **34**, 22–30.

16 A. C. Stuart, J. R. Tumbleston, H. Zhou, W. Li, S. Liu, H. Ade and W. You, *J Am Chem Soc*, 2013, **135**, 1806–1815.

17 J. Yuan, Y. Zhang, L. Zhou, G. Zhang, H. L. Yip, T. K. Lau, X. Lu, C. Zhu, H. Peng, P. A. Johnson, M. Leclerc, Y. Cao, J. Ulanski, Y. Li and Y. Zou, *Joule*, 2019, **3**, 1140–1151.

18 Q. Liu, Y. Jiang, K. Jin, J. Qin, J. Xu, W. Li, J. Xiong and J. Liu, *Sci Bull (Beijing)*, 2020, **65**, 272–275.

19 W. Gao, F. Qi, Z. Peng, F. R. Lin, K. Jiang, C. Zhong, W. Kaminsky, Z. Guan, C. S. Lee, T. J. Marks, H. Ade and A. K. Y. Jen, *Advanced Materials*, 2022, **34**, 1–11.

20 Z. Chen, P. Cai, J. Chen, X. Liu, L. Zhang, L. Lan, J. Peng, Y. Ma and Y. Cao, *Advanced Materials*, 2014, **26**, 2586–2591.

21 A. C. Stuart, J. R. Tumbleston, H. Zhou, W. Li, S. Liu, H. Ade and W. You, *J Am Chem Soc*, 2013, **135**, 1806–1815.

22 H. Zhang, H. Yao, J. Hou, J. Zhu, J. Zhang, W. Li, R. Yu, B. Gao, S. Zhang and J. Hou, *Advanced Materials*, 2018, **30**, 1800613.

23 Q. Fan, Z. Xu, X. Guo, X. Meng, W. Li, W. Su, X. Ou, W. Ma, M. Zhang and Y. Li, *Nano Energy*, 2017, **40**, 20–26.

24 M. B. Price, P. A. Hume, A. Ilina, I. Wagner, R. R. Tamming, K. E. Thorn, W. Jiao, A. Goldingay, P. J. Conaghan, G. Lakhwani, N. J. L. K. Davis, Y. Wang, P. Xue, H. Lu, K. Chen, X. Zhan and J. M. Hodgkiss, *Nat Commun*, 2022, **13**, 2827.

25 E. Amouyal, R. Bensasson and E. J. Land, *Photochem Photobiol*, 1974, **20**, 415–422.

26 K. Kikuchi, Y. Kurabayashi, H. Kokubun, Y. Kaizu and H. Kobayashi, *J Photochem Photobiol A Chem*, 1988, **45**, 261–263.

27 J. S. Seixas De Melo, J. Pina, F. B. Dias and A. L. Maçanita, *Applied Photochemistry*, 2013, **9**, 533–585.

28 S. Karuthedath, J. Gorenflot, Y. Firdaus, N. Chaturvedi, C. S. P. de Castro, G. T. Harrison, J. I. Khan, A. Markina, A. H. Balawi, T. A. dela Peña, W. Liu, R. Z. Liang, A. Sharma, S. H. K. Paleti, W. Zhang, Y. Lin, E. Alarousu, D. H. Anjum, P. M. Beaujuge, S. de Wolf, I. McCulloch, T. D. Anthopoulos, D. Baran, D. Andrienko and F. Laquai, *Nat Mater*, 2021, **20**, 378–384.

29 S. I. Natsuda, Y. Sakamoto, T. Takeyama, R. Shirouchi, T. Saito, Y. Tamai and H. Ohkita, *Journal of Physical Chemistry C*, 2021, **125**, 20806–20813.

30 R. Kerremans, C. Kaiser, W. Li, N. Zarrabi, P. Meredith and A. Armin, *Adv Opt Mater*, 2020, **8**, 2000319.

31 C. Yang, J. Zhang, N. Liang, H. Yao, Z. Wei, C. He, X. Yuan and J. Hou, *J Mater Chem A Mater*, 2019, **7**, 18889–18897.

32 P. Li, J. Fang, Y. Wang, S. Manzhos, L. Cai, Z. Song, Y. Li, T. Song, X. Wang, X. Guo, M. Zhang, D. Ma and B. Sun, *Angewandte Chemie - International Edition*, 2021, **60**, 15054–15062.

33 J. Nelson, *Phys Rev B, 1999, **59**, 15374*

34 J. Albero, Y. Zhou, M. Eck, F. Rauscher, P. Niyamakom, I. Dumsch, S. Allard, U. Scherf, M. Krüger and E. Palomares, *Chem Sci*, 2011, **2**, 2396–2401.

35 J. Guo, H. Ohkita, S. Yokoya, H. Benten and S. Ito, *J Am Chem Soc*, 2010, **132**, 9631–9637.

36 T. M. Clarke, F. C. Jamieson and J. R. Durrant, *Journal of Physical Chemistry C*, 2009, **113**, 20934–20941.

37 A. Classen, C. L. Chochos, L. Lüer, V. G. Gregoriou, J. Wortmann, A. Osvet, K. Forberich, I. McCulloch, T. Heumüller and C. J. Brabec, *Nat Energy*, 2020, **5**, 711–719.

38 G. Kupgan, X. K. Chen and J. L. Brédas, *Mater Today Adv*, 2021, **11**, 100154.

39 W. Zhao, S. Li, H. Yao, S. Zhang, Y. Zhang, B. Yang and J. Hou, *J Am Chem Soc*, 2017, **139**, 7148–7151.

40 A. J. Gillett, A. Privitera, R. Dilmurat, A. Karki, D. Qian, A. Pershin, G. Londi, W. K. Myers, J. Lee, J. Yuan, S. J. Ko, M. K. Riede, F. Gao, G. C. Bazan, A. Rao, T. Q. Nguyen, D. Beljonne and R. H. Friend, *Nature*, 2021, **597**, 666–671.

41 J. Kosco, S. Gonzalez-Carrero, C. T. Howells, T. Fei, Y. Dong, R. Sougrat, G. T. Harrison, Y. Firdaus, R. Sheelamanthula, B. Purushothaman, F. Moruzzi, W. Xu, L. Zhao, A. Basu, S. de Wolf, T. D. Anthopoulos, J. R. Durrant and I. McCulloch, *Nat Energy*, 2022, **7**, 340–351.

42 M. S. Kotova, G. Londi, J. Junker, S. Dietz, A. Privitera, K. Tvingstedt, D. Beljonne, A. Sperlich and V. Dyakonov, *Mater Horiz*, 2020, **7**, 1641–1649.

43 E. Gutierrez-Fernandez, A. D. Scaccabarozzi, A. Basu, E. Solano, T. D. Anthopoulos and J. Martín, *Advanced Science*, 2022, **9**, 2104977.

Chapter 5 Understanding the morphology and charge generation in novel NFA blend systems

5.1 Introduction

As introduced in Chapter 1, the device performance of OSCs is composed of three photovoltaic parameters of the short circuit current density (Jsc), open circuit voltage (V_{oc}) and the fill factor (FF), which ultimately determine the PCE of OSCs. [1] In general, the molecular structure and subsequent morphological characteristics of the active layer are closely related to the macroscopic properties of thin films and can further determine the photovoltaic parameters.[2] In principle, a nanoscale phase-separated blend morphology is required to match with the exciton diffusion length for efficient charge separation.[3,4] The exciton dissociates at the D/A interface initially generated the charge transfer (CT) state,[5] and traditionally, it required a driving force for CT state separation contributing to the charge photogeneration. The driving force for electron transfer is defined as the energy difference between the LUMO level of D and A. In NFA blend systems, due to the high absorptivity of the NFA, hole transfer could also occur efficiently[6], and the driving force for hole transfer can be defined as the difference in HOMO level of the D and A. In NFA blend systems, the OSCs have been observed to show good device performance with a minimal driving force for either electron or hole transfer.[7–10] Reducing the driving force for charge separation, can reduce the energy losses, resulting in a higher V_{oc}, but it may also have a detrimental effect on the yield of free charges.[11–13] Therefore, it is worth exploring the charge photogeneration and recombination in NFA systems with a small driving force. Furthermore, a comprehensive understanding of the charge photogeneration to the morphology study is still to unveil the fundamentals.

In this chapter, a high PCE 12.56% and high FF 81.3% blend D/A system consisting of the polymer PM6 and anti-PDFC NFA will be explored with the hole driving force is only 0.07 eV and electron driving force is 0.15 eV. A slightly lower PCE 10.43 % and FF 77.2% was found in PM6:syn-PDFC with the hole driving force as small as 0.07 eV and electron transfer 0.13eV. However, the least device perforce was observed in PM6:PDFC-Ph blend system with a relatively hole (0.19 eV) and 0.12 eV electron driving force but the least PCE value of 6.53 % and FF of 66%. These three PDFC NFAs were synthesised by Zhong's group from Shanghai Jiao

Tong University, China [14] and a summary of photovoltaic performances for all three PM6 with PDFC NFA blend systems is shown in Table 5.1. As the various device performance was found in these three PDFC NFA with PM6 blend systems, it is interesting to explore the photophysical mechanisms for such high PCE and FF polymer with small driving force blend systems but lower performance with slightly higher driving force.

Table 5.1 *Summary of photovoltaic performance based on polymer PM6:PDFC NFAs bulk heterojunction structure, with thermal annealing at 140° for 5 mins.*

NFA	Voc (V)	Jsc (mA cm^{-2})	FF (%)	PCE (%)
Anti-PDFC	0.97	15.93	81.3	12.56
Syn-PDFC	0.98	13.87	77.2	10.49
PDFC-Ph	1.03	9.64	66.0	6.53

The chemical structure for all three PDFC NFAs and the polymer PM6 are shown in Figure 5.1, along with their HOMO and LUMO levels that were estimated from cyclic voltammograms (Figure 5.5) and the energy bandgap calculated by the crossing point of the ground state absorption and photoluminescence emission spectrum (Figure 5.2). For the PDFC NFAs, they all show the A-DA'D-A architecture and use perylene diimide (PDI) derivatives as the electron-deficient A' part. PDI derivatives generally show excellent chemical and thermal stability and strong light absorption.[15,16] The high rigid planar structure of PDFC was achieved by the large, conjugated planarity of the PDI moiety endowing the acceptors with strong π-π stacking. The D core comprises an electron efficient fused benzothiadiazole moiety. Due to the strong push-pull structure in fused benzothiadiazole moiety, it shows a strong intramolecular charge transfer (ICT) that can extend the absorption to the near-infrared range.[14] Anti-PDFC and syn-PDFC NFA share the same chemical formula, both of these PDFC NFAs show a planar backbone structure.[17] PDFC-Ph shows the same configuration as anti-PDFC, but the side chain of it includes extra 8 phenyl groups. Syn-PDFC displayed a cis configuration, which is often augmented by solvophobic forces that inhibit their strong propensity to self-assembly.[18] The

side chain balances rigidity and the flexibility in a wide range of solvent while still allowing dynamic self-assembly to occur. Therefore, the addition of PM6 could affect a various degree of twist structure of the PDFC self-assembly. The planar structure rather than twisted can facilitate the electron migration from the donor to acceptor, because the planarized DAD enhances the delocalisation of electrons. [19]

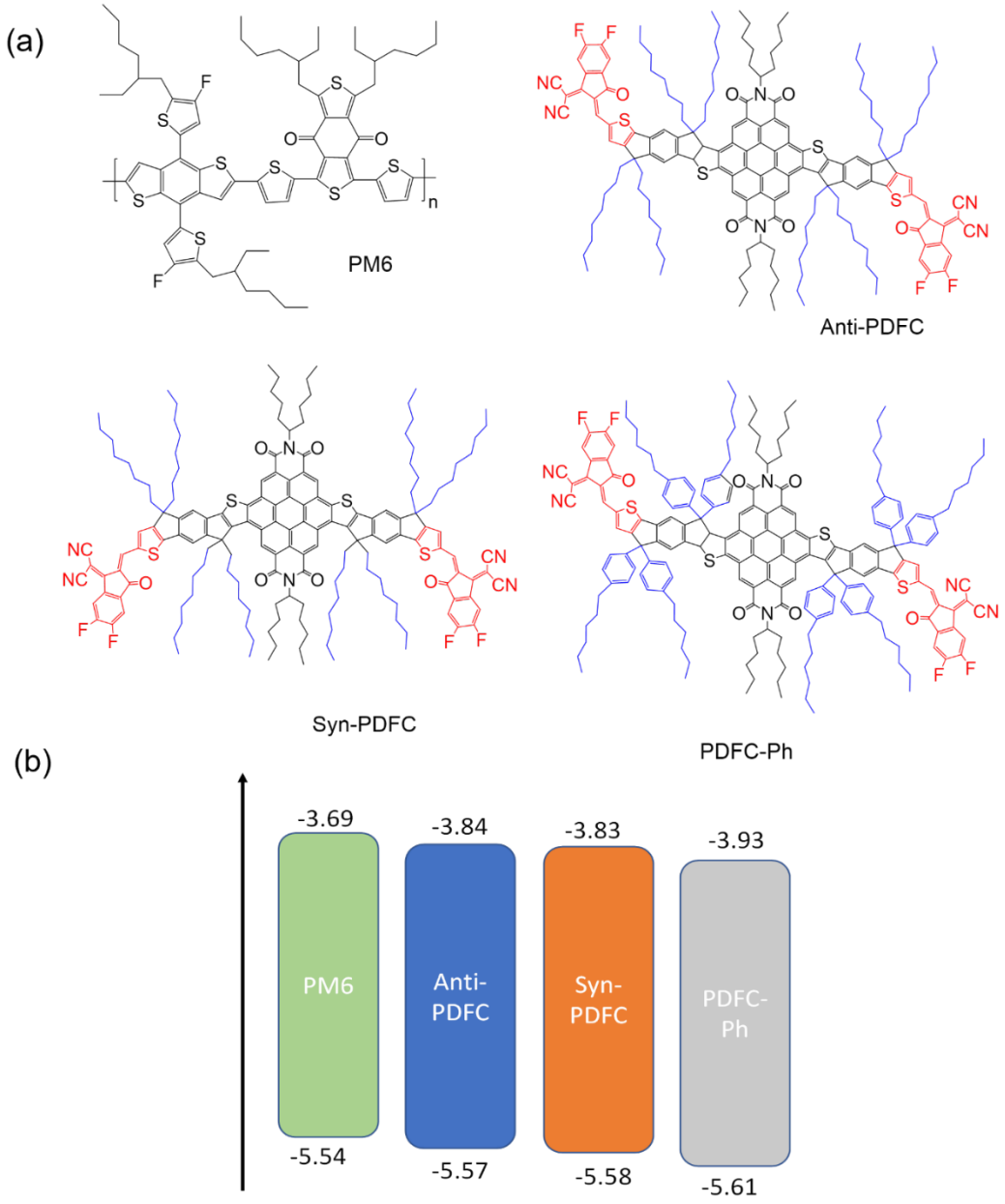

Figure 5.1 *(a) Chemical structures and (b) energy levels for polymer PM6 and NFAs: anti-PDFC, syn-PDFC and PDFC-Ph. The HOMO level of polymer and LUMO level of the NFAs were calculated from their cyclic voltammograms, and the LUMO of polymer and HOMO of NFAs were estimated by* $LUMO_p = HOMO_p + S_1$ *and* $HOMO_{NFA} = LUMO_{NFA} - S_1$.

In this chapter, the charge and exciton photogeneration and recombination process will be studied in the annealed blend PM6 with three different PDFC NFAs by ns-µs TAS and ps-TAS, together with the film morphology study characterised by both AFM and GIXRD. The photophysical process in the annealed blend was initially investigated in pure polymer and PDFC NFAs, followed by studies of annealed blend PM6:PDFC systems. The ns-µs TAS was employed to explore the long-lived transient species photophysical behaviour while the ps-TAS was used to study the short-lived excited state, such as exciton, CT state.

5.2 Experimental

Materials The polymer PM6 was sourced from Ossila (Mw= 100,790, PDI=2.92). The NFA Y6 was purchased from Ossila. Anti-PDFC, syn-PDFC and PDFC-Ph were synthesised by Zhong's group. The triplet sensitiser zinc tetraphenyl-porphyrin (ZnTpp), the solvent chloroform (CF, 99.9%), and the additive 1-chloronaphthalene (CN, 99%.9) were purchased from Sigma-Aldrich. The fullerene acceptors (PC60BM and PC70BM) were purchased from Solenne BV.

Sample preparation All the solutions were prepared outside the glove box and then transferred inside the glove box with a stirring rate 450 rpm overnight and heating temperature at 35°C. All the pristine acceptors' solutions (anti-PDFC, syn-PDFC, PDFC-Ph) were made with concentration 0.01 mg mL^{-1} in chloroform for triplet position determination by TAS. Three times freeze-pump-thaw was used to extract air from solutions for TAS measurements. Thin films were made by spin coating inside the glove box under nitrogen atmosphere. Thin films used for ns-µs TAS were made onto 1 cm^2 glass substrates, but for ps-TAS were made on CaF_2. The pristine NFA acceptors' films were fabricated from 5 mg mL^{-1} in chloroform solutions, and spin coated at 900 rpm. All PM6:acceptor blend films were made with weight ratio 1:1.1 in chloroform and 0.75% CN but with different concentration and spin rate. For the PM6 with syn-PDFC and PDFC-Ph films, the blend films were made from blend concentration at 8 mg mL^{-1} and spin rate at 1500 rpm, while the blend concentration for PM6: anti-PDFC is 10 mg mL^{-1} and spin rate at 2000 rpm. For the PM6 with PC60BM blend films, the blend concentration used was 10 mg mL^{-1} and spin rate at 1000rpm. The blend films were made by spin coating from hot solution at certain spin rate (as mentioned above) for 60 seconds.

5.3 Results and Discussion

5.3.1 Steady-state absorption and photoluminescence emission spectra

The normalised steady state absorption spectra of the pristine polymer PM6 film, and pristine PDFC NFAs anti-PDFC, syn-PDFC, and PDFC-Ph solution and films, and the annealed blend PM6:NFAs films, as displayed in Figure 5.2. The steady state absorption spectrum of pristine PM6 film shows equal intensity peaks at 615 nm and 575 nm which was assigned to the 0-0 and 0-1 vibronic transition, respectively. The nearly equal absorption ratio indicates the polymer PM6 containing less crystalline structure.

For the PDFC NFA solution, the absorption spectrum of anti-PDFC solution shows a narrow peak maximum at 668 nm, while both syn-PDFC and PDFC-Ph solution show the narrow peak maximum at 660 nm, the small breadth of the peak consistent with a relatively ordered morphology.[17] Comparing to the solution, ground state absorption spectra of pristine anti-PDFC film shows the peak maximum at 683 nm for anti-PDFC, and 670 nm for syn-PDFC film and 665 nm for PDFC-Ph film. A 15 nm absorption peak maximum red-shift was observed for anti-PDFC film and 10 nm for syn-PDFC film and 5 nm for PDFC-Ph film, indicating intermolecular packing is enhanced during the film spin coating due to the rigid backbone, and the strong intermolecular π-π interaction and alkyl-alkyl interaction.[17] The molecular absorption coefficient for all NFAs solution was calculated under a series concentration as shown in Figure 5.2d. The greatest value is shown with PDFC-Ph (3.3×10^5 M^{-1} cm^{-1}), followed with the syn-PDFC (3×10^5 M^{-1} cm^{-1}) and the smallest value (2.8×10^5 M^{-1} cm^{-1}) for anti-PDFC.

The ground state absorption spectra of annealed blend anti-PDFC and PDFC-Ph NFAs shows different variations to the syn-PDFC blend. The ground state absorption spectra of annealed PM6:anti-PDFC and PM6:PDFC-Ph blends displayed a red shift relative to the pristine polymer and NFA films, which means the resultant blend films exhibit an enhanced crystallinity for both polymer and NFA domains. In contrast, blending of the polymer and syn-PDFC induces no shifts, and the resultant PM6:syn-PDFC blend absorption spectrum appears to be a simple addition of the individual components. In particular, there is no alternation to the syn-PDFC absorption onset.

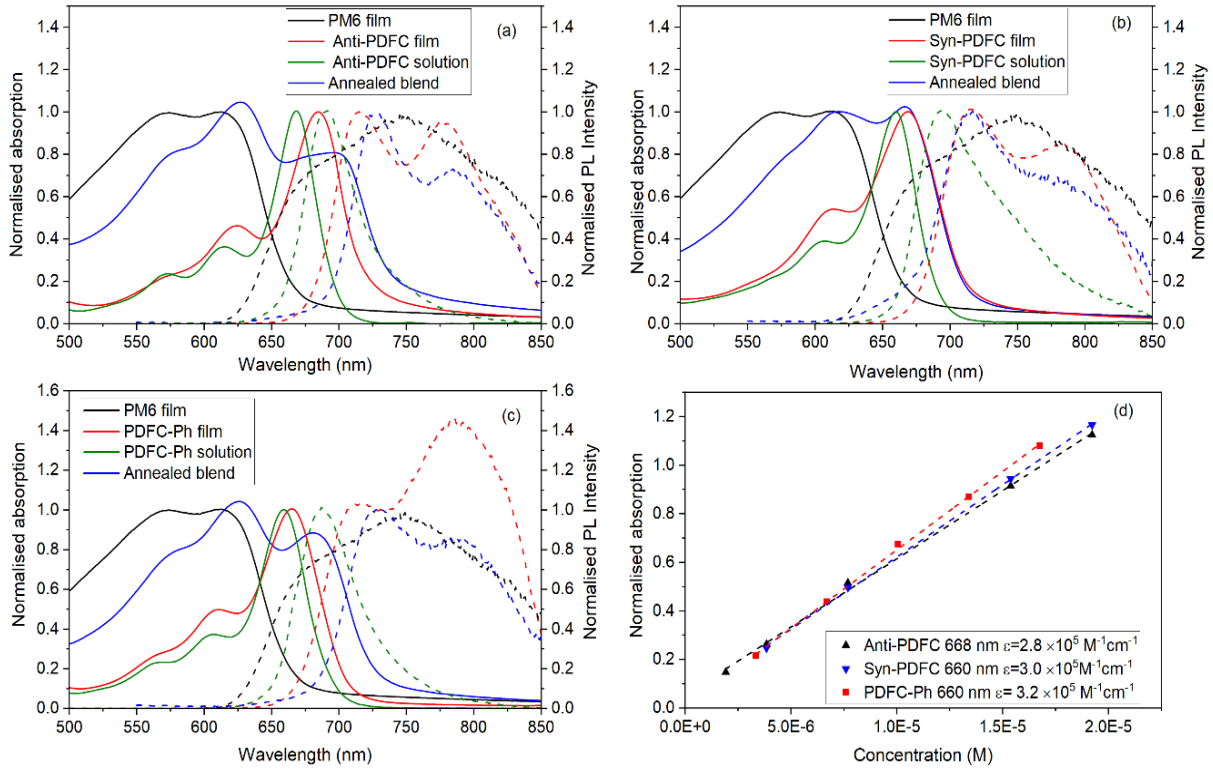

Figure 5.2 *Normalised (to 1) steady state absorption spectra (solid lines) and photoluminescence emission spectra (dash lines) for (a) pristine PM6 film, pristine anti-PDFC film and annealed blend film PM6:anti-PDFC, (b) pristine PM6 film, Syn-PDFC film and annealed blend film PM6: syn-PDFC, (c) pristine PM6 film, PDFC-Ph film and annealed blend film PM6: PDFC-Ph. (d) extinction coefficient calculation for PDFC NFAs in solutions. Annealed blend films were obtained by heating the fresh made blend films at 140 °C for 5 mins. The excitation wavelength 600 nm was used for PL spectra of PDFC series' non-fullerenes, and 520 nm was used for the blend films.*

As dash lines shown in Figure 5.2, normalised PL emission spectra of pristine PM6 film, NFA film, solution and the annealed PM6 with NFA blend films are measured to gain insight into morphology. The excitation wavelength 520 nm was used to dominantly excite the polymer in the annealed blends. As the black dash line exhibited in all three figures, the PM6 film shows a PL maximum at 750 nm and a side band at 685 nm.

The PL spectra of the anti-PDFC and PDFC-Ph solutions peaked at 690 nm, with the FWHM 0.11 eV and 0.13 eV, respectively. In contrast, the PL spectrum of syn-PDFC solution is broader (FWHM of 0.18 eV) and with an emission peak at 695 nm and a side band at 750 nm. The extra side band and a wider breadth of the syn-PDFC solution indicate the contribution of syn-PDFC aggregates in the solution.[17] Compared to the PDFC solution, the aggregate formation becomes more pronounced in pristine NFA films, with evidence that two emissive peaks were

observed in all three pristine PDFC NFA films. The 0-0 vibronic transition is at 716 nm in all three PDFC series' acceptors but with various position and intensity ratios to the 0-1 vibronic transitions. A greater than unity 0-0/ 0-1 PL ratio was found in pristine anti-PDFC, and syn-PDFC film, while a smaller than unity 0-0/ 0-1 (786 nm) ratio appeared in the pristine PDFC-Ph film. According to Spano et al., the greater than unity PL ratio represented the J aggregation, and the reverse is H aggregation.[20] The formation of aggregation in the film could be facilitated by the strong intermolecular interaction.

Surprisingly, for all three polymer:NFA blend films, although, under the excitation of the polymer, the PL spectra display different spectral shapes from the polymer but are similar to the NFAs. It is suggested that an efficient energy transfer process occurred in the annealed PM6:PDFC blend systems from the polymer to the NFAs. A 15 nm red shift and a greater than unity 0-0/0-1 PL ratio was observed in the PM6:anti-PDFC and PM6:PDFC-Ph films in comparison to the pristine NFA, indicating an enhanced J aggregation in the blend. PM6:syn-PDFC film also shows a larger 0-0/0-1 PL ratio (1.5 vs 1.2) but similar emissive bands' position to the pristine syn-PDFC film, which is consistent with the ground state absorption results. The enhancement of the 0-0/0-1 PL ratio in the blend to the pristine NFAs could be attributed to the dispersion of the D polymer, resulting in a D/A mixed domain.

5.3.2 Morphology

The morphology of pristine polymer PM6 and annealed PM6 with PDFC NFA films are characterised by AFM and GIXRD, as shown in Figures 5.3 and 5.4, respectively. Table 5.2 summarises the morphology observations from the AFM and GIXRD, including the surface roughness, d-spacing, and coherence length for π-π stacking, which are estimated from Figures in section 5.3.2.1 and 5.3.2.2.

***Table 5.2**. The parameters of the root-mean-square surface roughness (Rq) of the pristine and annealed blend films obtained from AFM, and the parameters of π-π stacking d-spacing and coherence length calculation from GIXRD.*

	Rq (nm)	π-π stacking plane (nm^{-1})	π-π d-spacing (nm)	FWHM (π-π)(°)	Coherence length (π-π) (nm)
PM6	1.1	-	-	-	
Anti-PDFC	7.35	17.1	0.37	11.2	7.1
Annealed PM6:Anti-PDFC	2.86	16.8	0.37	10.8	7.5
Syn-PDFC	0.87	16.2	0.39	15.1	5.4
Annealed PM6:Syn-PDFC	2.52	17.1	0.37	11.2	7.2
PDFC-Ph	0.78	17.3	0.36	12.5	6.5
Annealed PM6:PDFC-Ph	3.47	16.2	0.39	12.9	6.3

5.3.2.1 Atomic force Microscopy AFM

The morphology of pristine polymer PM6 and annealed PM6 with PDFC NFA films are characterised by AFM with both height and topography images, as shown in Figure 5.3. Rq was estimated from their corresponding height images, and the crystalline structure can be observed from the topography of the films.

As shown in Figure 5.3a-b, the pristine PM6 film shows the needle-like crystalline structure with R_q to be around 1.1 nm, showing a smooth polymer surface domain. However, a substantially high surface roughness with R_q 7.9 nm was observed in PM6:PS film (Figure 5.3i-j), indicating strong phase segregation for PM6 with additional of PS. For pristine PDFC NFAs, the highest R_q 7.35 nm was observed in pristine anti-PDFC film with a nanofibre structure, and the R_q for syn-PDFC (0.87 nm) is closer to the PDFC-Ph film (0.78 nm), but the syn-PDFC exhibited a nano-fibre like structure while featureless morphology was observed in PDFC-Ph film. It should be noted that the nano-fibre-like structure of syn-PDFC indicated that there is still crystalline domain generated in syn-PDFC film.

Although the morphology of pristine anti-PDFC film exhibit large differences between syn-PDFC and PDFC-Ph, the R_q for annealed PM6: anti-PDFC (2.86 nm) is similar to the annealed PM6: syn-PDFC film (2.56 nm), but smaller to the PM6:PDFC-Ph blend film (3.47 nm), as displayed in Figure 5.3 k-p. The low R_q value observed in the annealed syn-PDFC and anti-

PDFC was likely due to the good miscibility between PM6 and syn-PDFC/anti-PDFC, creating a well-mixed D/A domain. In contrast, the larger surface roughness and square packing shape aggregates were observed in the PM6: PDFC-ph film. Since the square packing structure and a larger R_q were observed in PM6:PS film, which is similar to the morphology of the annealed PM6: PDFC-Ph film, the larger R_q value could be attributed to the enhanced crystallinity of the polymer domain. From the topography images, the enhanced phase segregation in annealed blend PM6 with PDFC NFAs films could be clearly demonstrated.

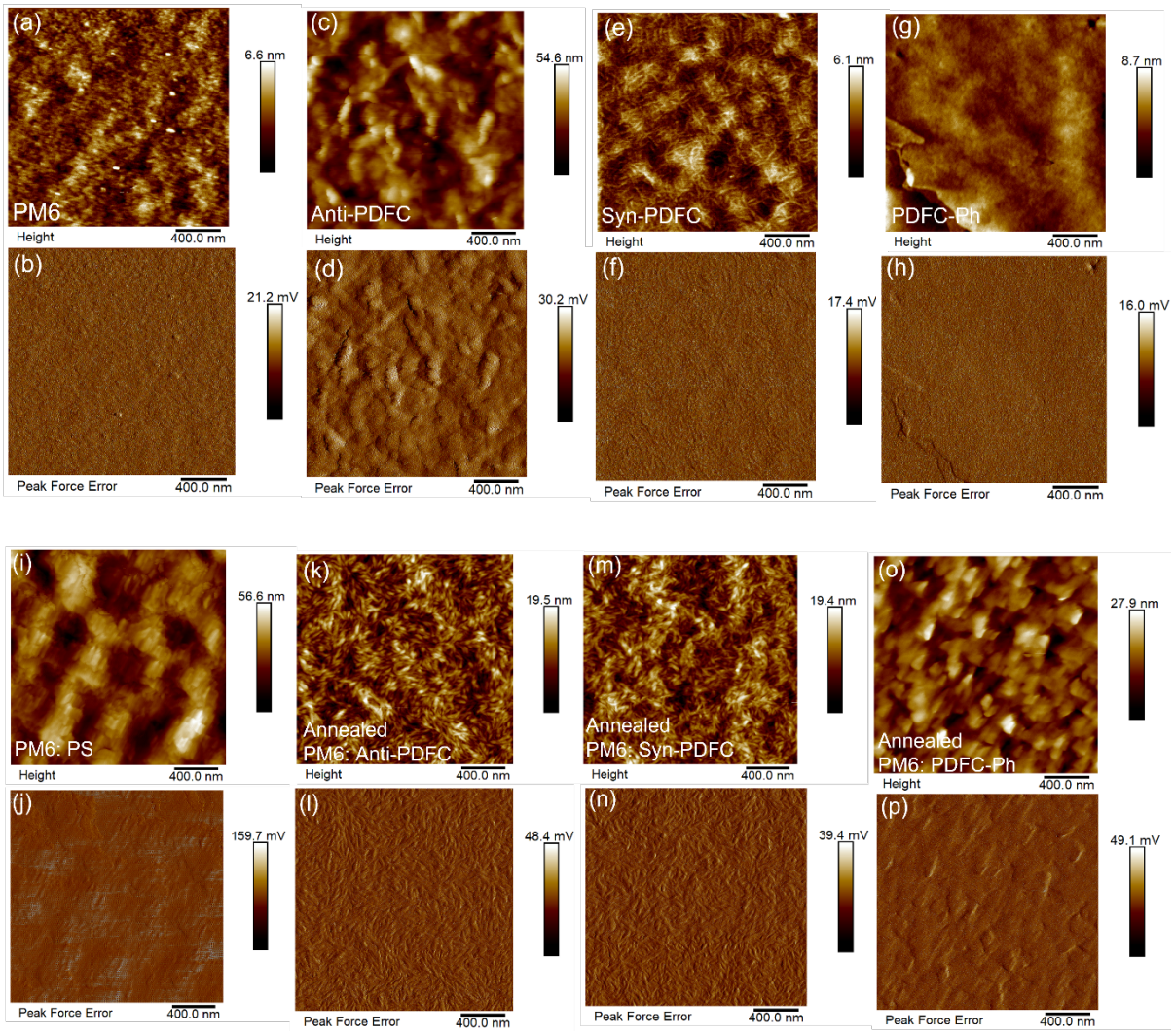

Figure 5.3 *AFM images of height and topography for (a and b) PM6 film, (c and d) Anti-PDFC; (e and f) syn-PDFC, (g and h) PDFC-Ph; (I and j) PM6:PS (1:1.1) (k and l)) annealed PM6:anti-PDFC (1:1.1) (m and n) annealed PM6:Syn-PDFC (1:1.1); (o and p) annealed PM6:PDFC-Ph (1:1.1) films. Scale bars are 400 nm.*

5.3.2.2 Grazing incident X-ray diffraction (GIXRD)

The molecular packing of the pristine anti-PDFC, PDFC-Ph and syn-PDFC films and their annealed blends with PM6 were characterized by GIXRD. The pristine PM6 film shows only shows an increasing baseline to 5 nm^{-1} and no π-π stacking (010) diffraction peak, which is consistent with the literature.[21] The lack of π-π stacking reveals a relatively amorphous domain. The GIXRD pattern for the pristine anti-PDFC and PDFC-Ph displays a broad band around 17 nm^{-1} (d = 0.37 nm) and 16 nm^{-1} (d = 0.39 nm) for syn-PDFC film corresponding to the π-π stacking planes.[14] The sharp bump around 5 nm^{-1} for anti-PDFC and 4 nm^{-1} for PDFC-Ph film was caused by antifact.[22]

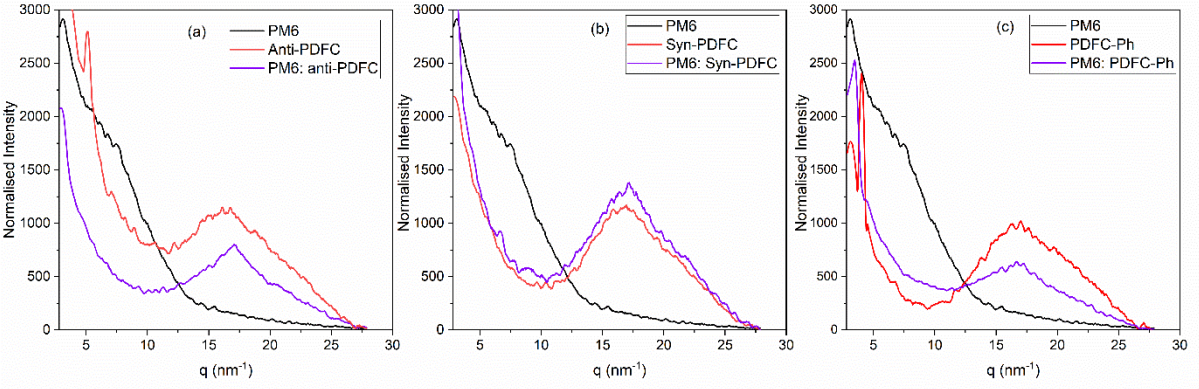

Figure 5.4 *Normalised (per absorption) GIXRD patterns for (a) pristine PM6 film, anti-PDFC and annealed PM6: anti-PDFC films, (b) pristine PM6 film, syn-PDFC and annealed PM6: syn-PDFC films, (c) pristine PM6 film, PDFC-Ph and annealed PM6: PDFC-Ph films.*

For all three annealed: PDFC NFA blends, the GIXRD patterns only show a strong π-π stacking (010) peak to the PDFC feature. The coherence length for π-π stacking was calculated by Scherrer's equation, as introduced in chapter 2.6, which could represent the crystalline π-π stacking domain size in the film. As shown in Figure 5.4a-b, the π-π stacking coherence length of annealed PM6:anti-PDFC is 7.5 nm, which is similar to the annealed syn-PDFC blend (7.2 nm) and higher than the annealed PM6:PDFC-Ph blend (6.3 nm). The similar domain size of anti-PDFC and syn-PDFC blends is consistent with the AFM results. The smaller π-π stacking domain size of the PDFC-Ph blend is consistent with the assignment of the PM6 aggregation rather than the PDFC-Ph aggregates investigated by the AFM results. Interestingly, both anti-PDFC (7.1 nm) and PDFC-Ph (6.5 nm) shows a less than 5% π-π stacking domain size variation from pristine to the annealed blend with PM6. In contrast, syn-PDFC (5.4 nm) shows a 25%

increasing domain size from pristine to the annealed blends, which indicates a good π-π stacking that could accelerate the electron transfer rate.[23,24]

5.3.3 Spectroelectrochemistry

To study the charge generation and recombination process in different annealed blend systems, it is essential to know the spectral identity for each polymer and NFAs transient species. To achieve this, the polymer cation and anion formation was determined by spectroelectrochemistry.

5.3.3.1 Cyclovoltammetry

The oxidation potential for polymer PM6 and reduction potential for PDFC NFAs can be estimated from the oxidation/reduction onset of their CVs, as shown in Figure 5.5. The HOMO level of the polymer and LUMO of the NFAs can then be deduced based on the oxidation/reduction onset. The summarized HOMO and LUMO levels for polymer and NFAs are shown in Figure 5.1.

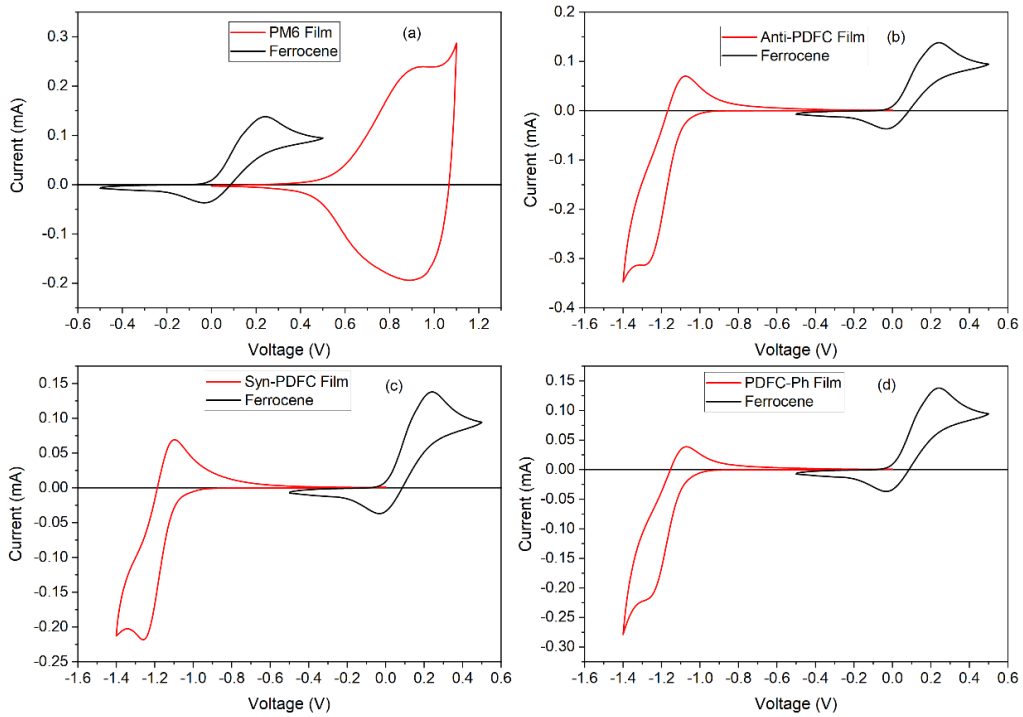

Figure 5.5 *Cyclic voltammogram for PM6, anti-PDFC, syn-PDFC, PDFC-Ph and ferrocene films in 0.1 M Bu_4NPF6 acetonitrile solution with scan rate at 20 mV s^{-1} on ITO substrate.*

5.3.3.2 SEC of PM6 cation

SEC spectrum for pristine PM6 film was measured with applied voltage range from 0.4 to 0.8V, as shown in Figure 5.6a. It exhibits negative intensity peaks at 623 nm with a shoulder at 573

nm, which were assigned to the electrooxidation induced ground bleaching. It should be noted that the ground state bleaching 0-0/0-1 ratio in SEC spectrum is around 1.5, which is larger than the absorption ratio measured by the ground state absorption spectrum. This might be because the highest crystalline polymer chains were oxidised first. Additionally, there are three positive intensity features shown at <700 nm, 900 nm and a tail to 1600 nm. Being different to the assignment of the polymer PffBT4T-C9C13 in Chapter 3, these three positive features are all initially generated under the applied voltages such that they are all assigned to polymer cations. Figure 5.6b shows the peak amplitude and total charge extracted as a function of applied voltages, the curve overlapping for the 1600 nm to the total charge extracted implies that the charge generated at 1600 nm obeys the faradic charge transfer process, while the charge spectra at 700 nm and 900 nm can be easily oxidised at lower applied voltage. The different charge behaviours from 1600 nm to 700 nm or 900 nm might be because of the polymer cations localised in different morphological environments (consistent with the broadness of polymer cyclic voltammograms). It is apparent that the relative intensity ratio of the 700 nm to the 900 nm band increases across the applied voltage range. In general, the crystalline domain has a shallower HOMO and, thus, smaller ionisation potential. Since the 700 nm band become relatively more intense compared to the 900 nm band with increasing voltage, the 700 nm band can be attributed to the polymer cation generated in less ordered domain while the 900 nm band to cations in a more ordered region.

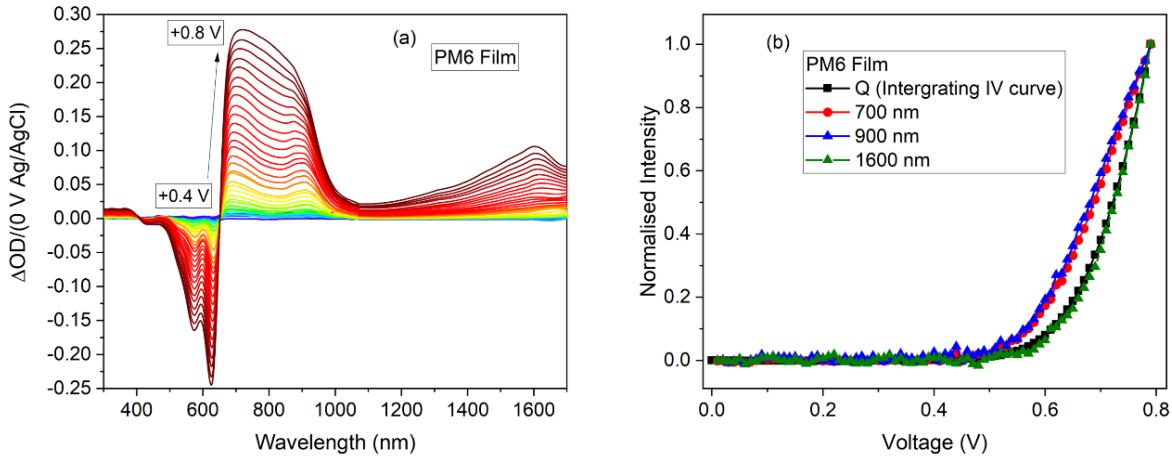

Figure 5.6 *(a) SEC absorption spectra for polymer PM6 film with an applied voltage from 0.4 V to 0.8 V. (b) Normalised peak amplitude and total charge extracted as a function of applied voltages.*

5.3.3.3 SEC for NFA anions

SEC is used to obtain the PDFC anion spectra of the pristine film, as a function of a series of applied voltage, as shown in Figure 5.8. The applied voltage for each film was chosen to start from the voltage with zero current to the first reduction band in order to minimise contamination from any dianions features (Figure 5.7). The first reduction potential was measured from the IV curve as a broad band around -1.04 V for the anti-PDFC, and -1.02 V for syn-PDFC, and -0.8 V for the PDFC-Ph film.

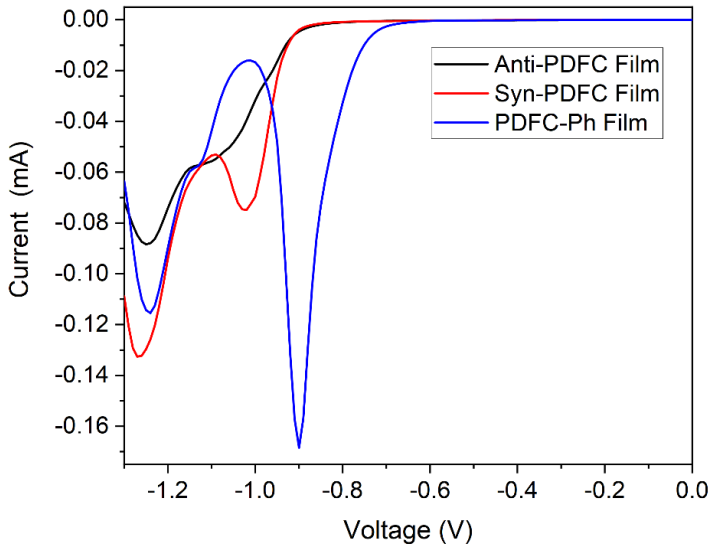

Figure 5.7 *Current to voltage curve for anti-PDFC, syn-PDFC and PDFC-Ph film in 0.1 M Bu4NPF6 acetonitrile solution with scan rate at 20 mV* s^{-1} *on ITO substrate.*

The SEC spectra for PDFC NFAs films are shown in Figure 5.8 as a function of voltage, along with the normalised peak amplitude and charge extracted from the IV curve and anion formation. For all three pristine PDFC films, the PDFC NFAs' anion clearly shows a positive feature around 1600 nm as part of a broad feature that can be seen increasing in amplitude from 1200 nm. The region from 400 - 800 nm also possesses another anion feature but its details are concealed by the large neural molecule bleach. Furthermore, the strong ordered aggregation in the PDFC NFA film produces a large scattering tail out to 1200 nm that obscures any anion features in the TA-relevant region of 800 – 1200 nm. The assignment of anion contribution in all three PDFC NFA films is supported by the good correspondence between the extracted charges and the anion peak amplitude as a function of voltage, as shown in Figure 5.8 b, d, f.

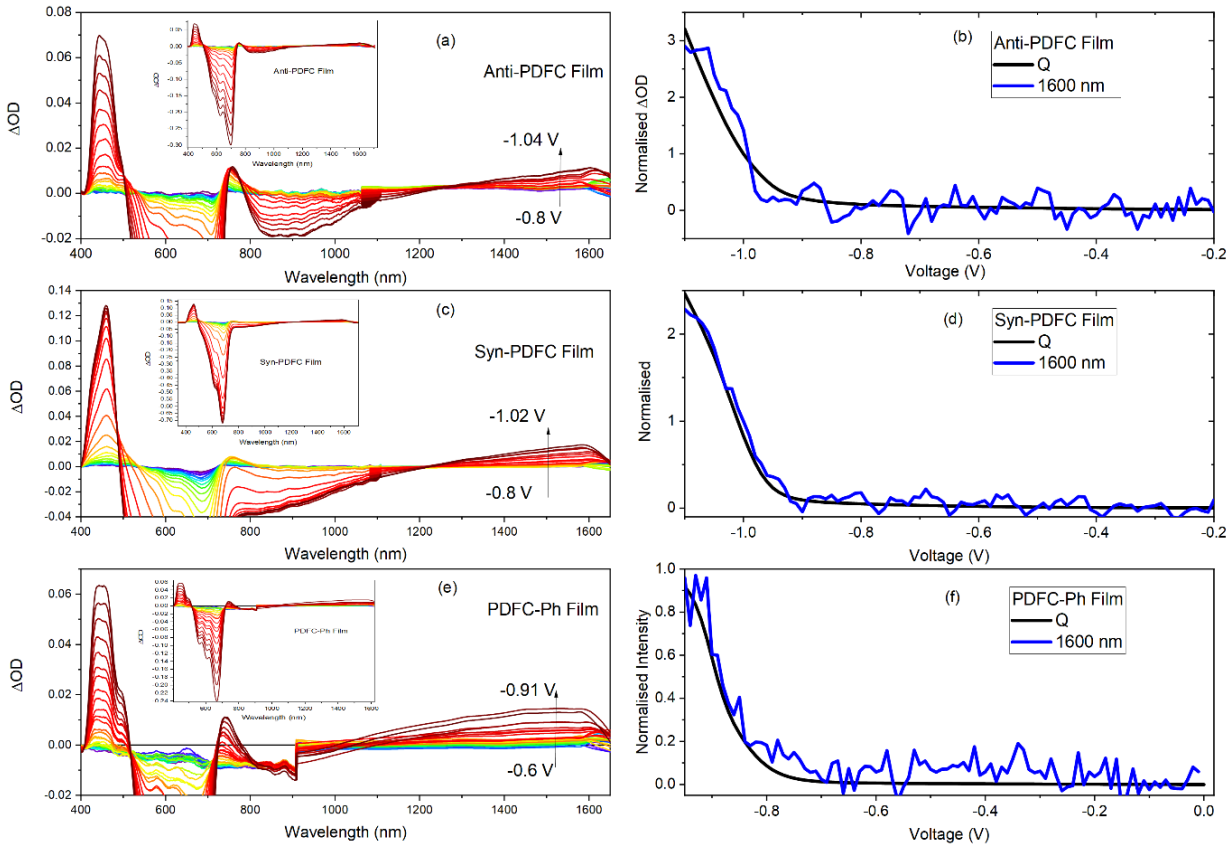

Figure 5.8 *SEC absorption spectra for (a) polymer Anti-PDFC film and (c) Syn-PDFC film, (e) PDFC-Ph film in 0.1 M TBAP/ acetonitrile with Ag/AgNO3 electrode, plotted versus applied potential from -0.6 V to -1.25 V for PDFC films. Normalised total extracted charges and the peak amplitude in the (b)anti-PDFC, (d) syn-PDFC, (f) PDFC-Ph films.*

5.3.4 Nanosecond-microsecond transient absorption spectroscopy

The time-resolved spectroscopy to assess the effects of the minimal energy offsets in both directions. Ns-µs TAS directly monitors the optical absorption of photogenerated transient species in pristine polymer, NFA and polymer:NFA blend films, providing information on the identity, yield and decay mechanisms of these transient species.

5.3.4.1 Triplet and polaron formation in pure PM6 solution and film

Figure 5.9a shows the ground state absorption spectra for pristine PM6 film, solution, triplet sensitizer PtOEP, and the blend films of PM6:PtOEP with ratios 1:1 and 3:1. As shown in Figure 5.9b, the normalised PM6 solution TA spectrum shows a broad band range from 800 nm to 1400 nm and centred at 1100 nm. This band is assigned to be a polymer triplet, as evidenced by the oxygen-dependent mono-exponential decay dynamics (Figure 5.9c).

The normalised TA spectrum for pristine PM6 film (Figure 5.9b) shows a sharp peak maximum at 900 nm and a relatively small intensity <700 nm, and a high-intensity long tail beyond 1600 nm. A slightly oxygen-dependent kinetics was observed for the 900 nm band and the tail to 1600 nm (Figure 5.9e-g), indicating the potential existence both of triplet and charges. The decay dynamics at 900 nm and 1600 nm were fitted with stretch exponential under the nitrogen atmosphere. This indicates a dispersive environment in the pristine PM6 film, resulting in multiple decay pathways consistent with the coexistence of triplet and charge. The same as we discussed the stretched exponential decay in Chapter 3 and 4, the stretched exponential factor approach to 0 shows a preference for the transient species to obey a power law decay, in other way, close to 1, it is more like a monoexponential decay. As the stretch exponential factor 0.13 was obtained for transient species at 900 nm and 0.59 for 1600 nm, we can deduce that the number of charges at 900 nm is greater than the triplet. In contrast, as the relative intensity of 1600 nm band is higher than 900 nm band, it suggests that the number of triplets is higher than the charges at 1600 nm. The greater relative intensity of the 1600 nm polaron band in the TA spectrum compared to the SEC spectrum is likely due to the additional contribution of triplet absorption in the TA spectrum.

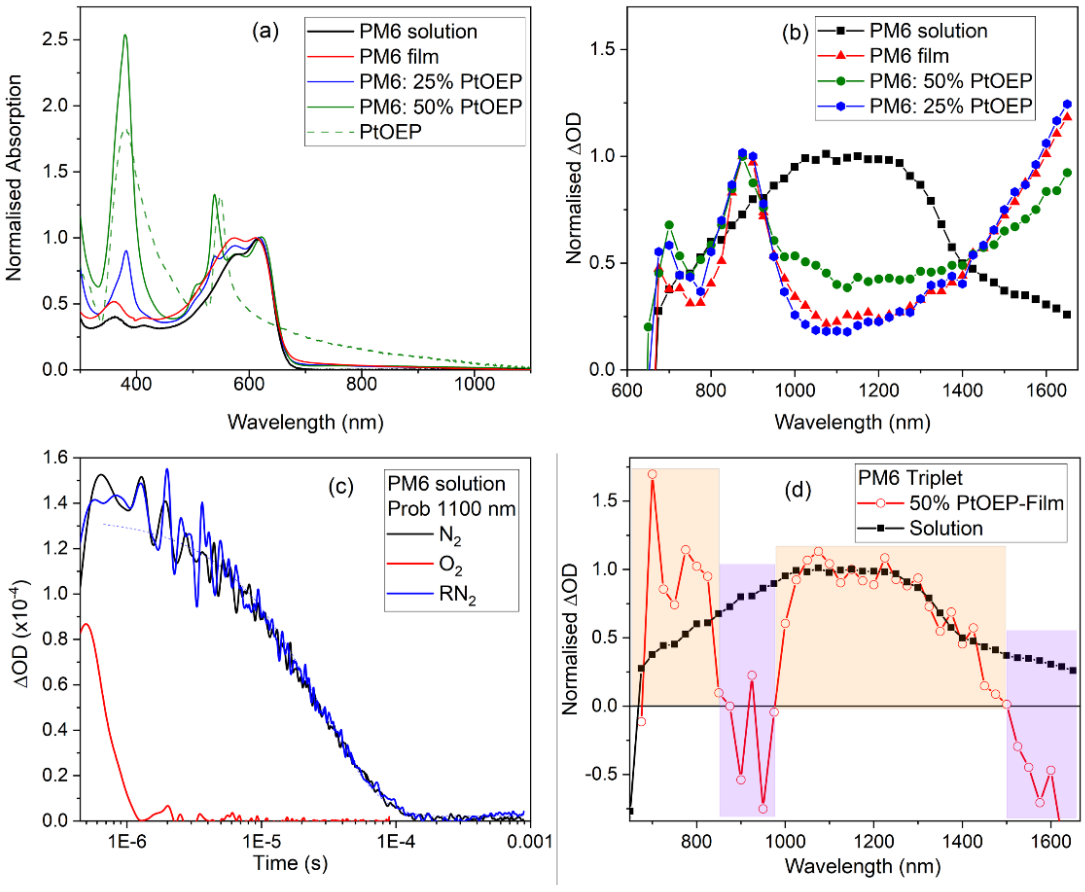

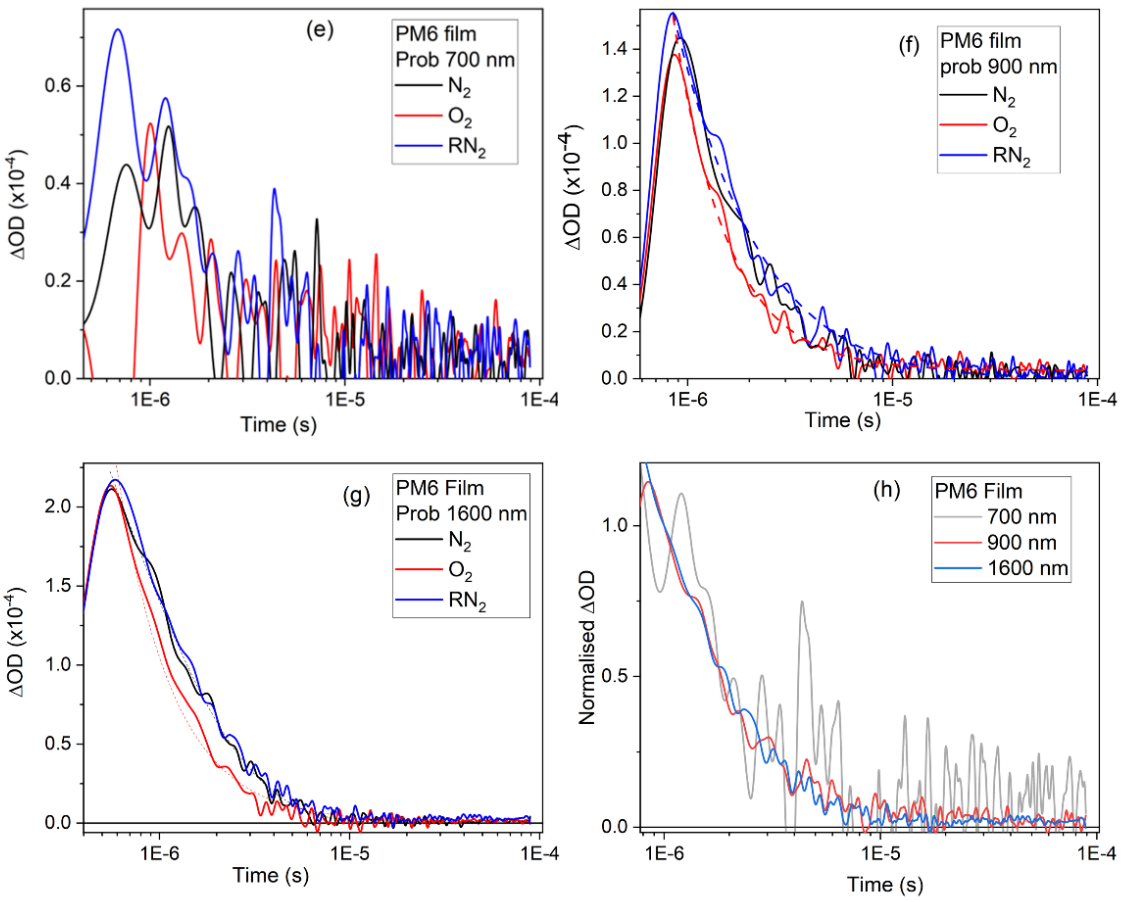

Figure 5.9 *(a) Normalised ground state absorption spectra and (b) µs-TA spectra for pristine PM6 solution, film, PM6:PtOEP (3:1), and PM6:PtOEP (1:1) films and the pristine PtOEP film. (c) Oxygen dependence decay dynamics of PM6 solution with probing wavelength at 1100 nm. (d) Normalised TA spectrum for PM6 solution and the spectrum with subtraction of PM6:50%PtOEP to pristine PM6 film. The negative TA intensity emphasised by purple rectangular represent PM6 charge formation while the positive TA intensity by orange rectangular is the PM6 triplet formation. Oxygen dependence decay dynamics of PM6 film with probing wavelength at (e) 700nm (f) 900 nm (g) 1600 nm under nitrogen (N_2), oxygen (O_2) and recovery nitrogen atmosphere (RN_2). (h) Normalised decay comparison for PM6 film with probe wavelength 700 nm, 900 nm and 1600 nm. An excitation wavelength of 610 nm was used for both pristine solution and film, with excitation densities 22 µJ cm^{-2} and 16 µJ cm^{-2}, respectively. An excitation wavelength of 538 nm (to excite mainly the porphyrin) is used for PM6 with 25% and 50% PtOEP film, with excitation density 20 and 12 µJ cm^{-2}, respectively.*

Further evidence for the triplet formation in pristine PM6 film was given by the triplet sensitisation experiment performed using 25% and 50% triplet sensitiser platinum octaethylporphyrin (PtOEP), as displayed in blue and green circle lines in Figure 5.9b. The excitation wavelength 545 nm was chosen to mainly excite the PtOEP. Therefore, along with the efficiently generated triplet PtOEP, the lower energy polymer triplet can be formed via energy transfer from the high energy triplet PtOEP in the PM6: PtOEP film. It is worth noting

that the 545 nm excitation wavelength was not selectively exciting PtOEP but also a small number of PM6, resulting in the formation of the PM6 polaron as well. The PM6: PtOEP (3:1) TA spectrum shows a similar TA spectra shape as the pristine PM6 film. When increase the percentage PtOEP to 50%, a new broad band ranged from 900 nm to 1400 nm was appeared. Since the PtOEP triplet was discovered in chapter 3 below 800 nm (Figure 3.8d), the estimated triplet spectrum in film can be obtained by subtracted the PM6 film spectrum from the PM6: 50%PtOEP blend spectrum as shown in Figure 5.9d, the positive TA intensity is attributed to the triplet and the negative TA signal ascribed as the polymer polarons.

5.3.4.2 Triplet formation in pure PDFC solution

Normalised (to 1) µs-TA spectra for pristine PDFC NFAs' solutions are shown in Figure 5.10a. The excitation wavelength 670 nm was used to excite anti-PDFC and syn-PDFC and 660 nm for PDFC-Ph. The TA spectrum for anti-PDFC solution shows a sharp peak at 900 nm and a broad band centred around 1300 nm, which are both assigned to the triplet state as evidenced by the oxygen-dependent mono-exponential decay (Figure 5.10c-d). A similar lifetime of the 900 nm and 1300 nm (1 µs) band was observed (shown in Figure 5.10b), indicating both bands belong to the triplet. The fast decay of the triplet state in the anti-PDFC solution might be because of the highly rigid structure of the anti-PDFC assisting with the strong intermolecular interaction.

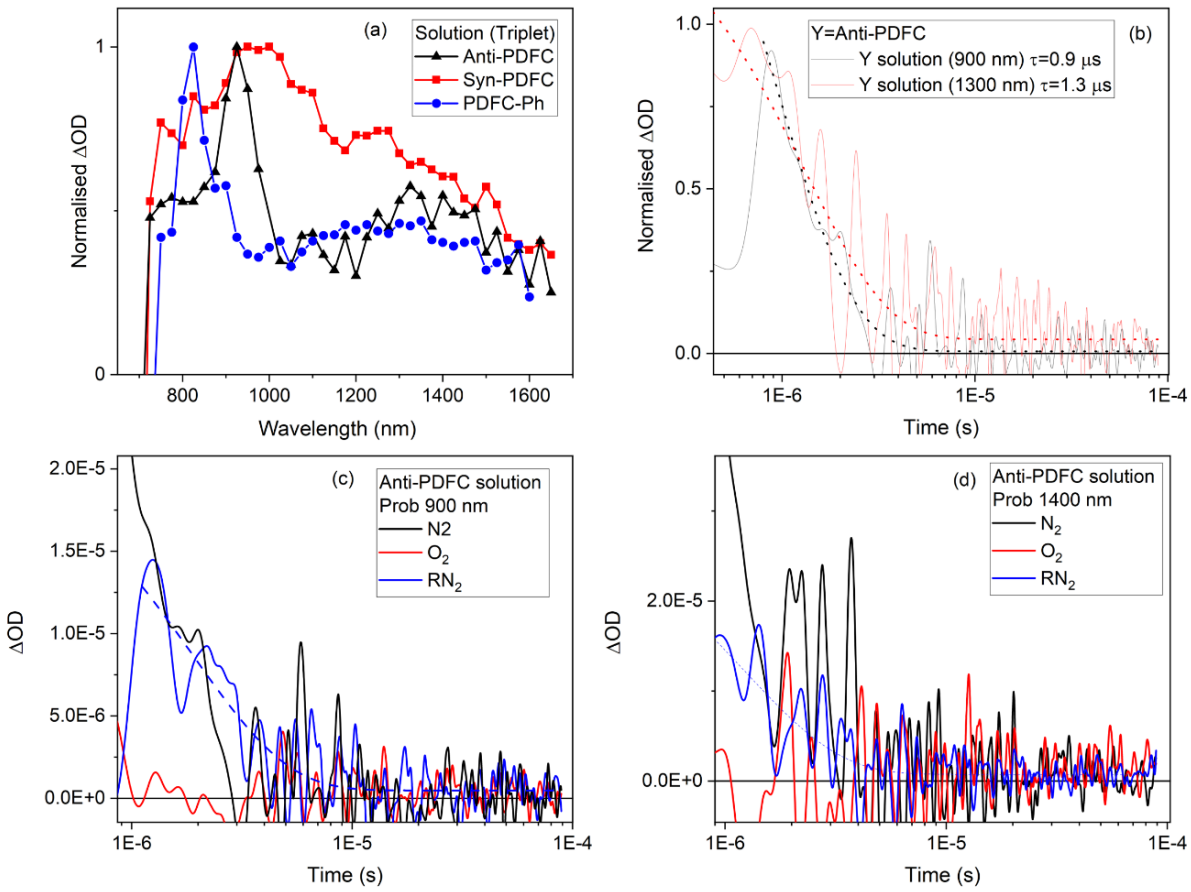

Figure 5.10 *(a) Normalised (to 1) TA spectra for anti-PDFC, syn-PDFC, and PDFC-Ph solutions (b) Normalised (to 1) decay dynamics for anti-PDFC solution, probing at 900 nm and 1300 nm. The dash lines represent the mono-exponential decay fitting. The excitation wavelength 660 nm for PDFC-Ph solution and 670 nm for Syn-PDFC and anti-PDFC solution, with excitation energies used for above solution is in a range of 27 to 33 μJ cm^{-2}. Oxygen dependence decay dynamics for anti-PDFC solution for (c) probing at 900 nm (d) 1400 nm in nitrogen, oxygen and recovery nitrogen atmosphere.*

Similarly to the spectral shape and FWHM of the anti-PDFC solution (0.14 eV), PDFC-Ph solution TA spectrum exhibits a blue shift with two bands formed at 825 nm and a broad band centred at 1300 nm with the FWHM of 0.13 eV. The blue shift of the PDFC-Ph solution is consistent with the shift observed in the ground state spectra. A similar lifetime of the 800 nm and 1300 nm (1.3 μs) bands were observed (shown in Figure 5.11a) and the oxygen dependence decay indicates both bands belong to the triplet.

Interestingly, the μs-TA spectrum for syn-PDFC solution shows a broader band centred around 1000 nm and a similar transient band at 1300 nm. The FWHM of 0.72 eV for the syn-PDFC solution is around 5 times higher than the other two PDFC solutions, potentially indicating aggregations in the syn-PDFC solution. As shown in Figure 5.11d, a similar mono-exponential

kinetics was fitted to the 1000 nm and 1300 nm band with a lifetime of 17 µs, which can be attributed to triplet as evidenced by the oxygen dependence decay dynamics (Figure 5.11d).

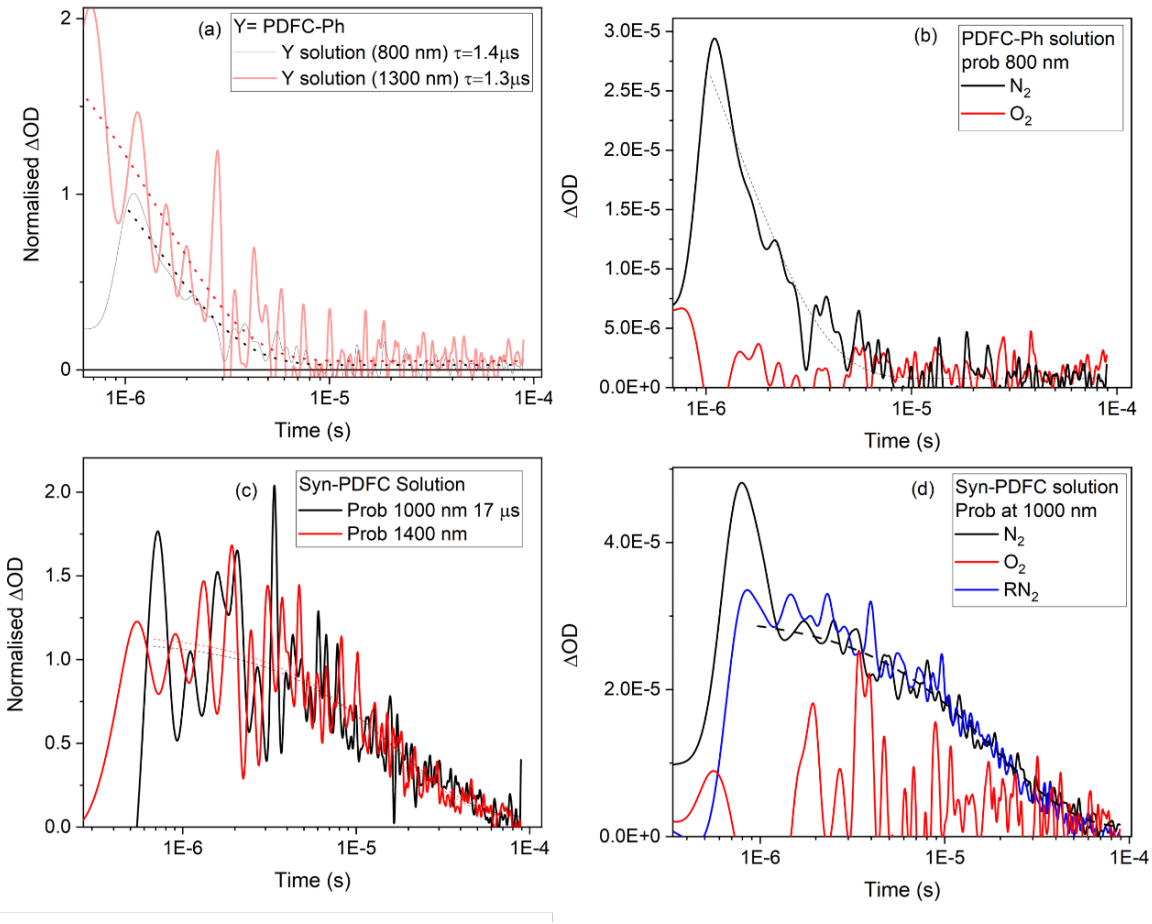

Figure 5.11 *Normalised decay dynamics for (a) PDFC-Ph solution with probing wavelength at 800 nm and 1300 nm (c) syn-PDFC solution with probing wavelength at 1000 and 1400 nm. Oxygen-dependent decay dynamics for (b) pristine PDFC-Ph solution probing at 800 nm and (d) pristine syn-PDFC solution probing at 1000 nm. All these decays fitted with mono-exponential decay (dash line). The oxygen dependence decay dynamics in solution for certain probing wavelength was measured in order under nitrogen, oxygen, and recovery in the nitrogen atmosphere.*

5.3.4.3 Triplet formation in pure PDFC films

To check the spectrum shift and transient species generated from the solution to the condensed phase (film), the TA spectra were measured in pristine PDFC NFA films. As shown in Figure 5.12, the normalised (to 1) TA spectrum for the pure anti-PDFC film shows a long tail to 1600 nm, which could be attributed to the anti-PDFC anions, consistent with the SEC spectrum. However, the absorption 800 to 1100 nm was positive in the µs-TA spectra but negative in the SEC spectra, this might be because of the difference in anion concentration

that was generated in the respective conditions. The noisy and low signal decay dynamics probing at 1550 nm of the anti-PDFC film suggested that the TA signal is largely gone prior to 1 µs.

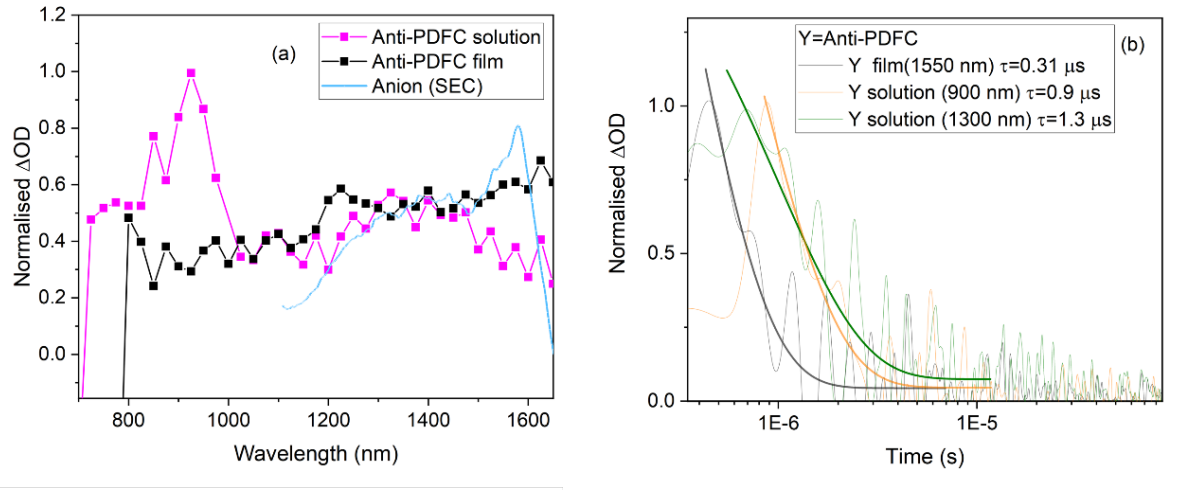

Figure 5.12 *(a) Normalised (to 1) at 1 µs TA spectra of pristine anti-PDFC film, solution and the SEC anion spectrum. (b) normalised (to 1) decay kinetics for anti-PDFC film probing at 1550 nm, and solution probing at 900 nm and 1300 nm, fitted with mono-exponential decay. Excitation wavelength 685 nm and energy 36 µJ cm^{-2} were used for pristine anti-PDFC films.*

Comparing to anti-PDFC, TA spectrum for PDFC-Ph film shows not only an intense band beyond 1500 nm but also a positive feature around 950 nm, as shown in Figure 5.13a. Both the 950 nm and 1500 nm bands in pristine films show a faster decay rate under the oxygen atmosphere and recovery to the original TA intensity under the nitrogen atmosphere, indicating the coexistence of triplet and charges. It should be noted that the magnitude of triplet quenching is greater at 950 nm compared to 1500 nm, suggesting that the contribution of triplet is around 950 nm but anions around 1500 nm. The faster decay dynamics at 950 nm compared to the 1500 nm give further evidence that two types of excited states were generated in pristine PDFC-Ph film.

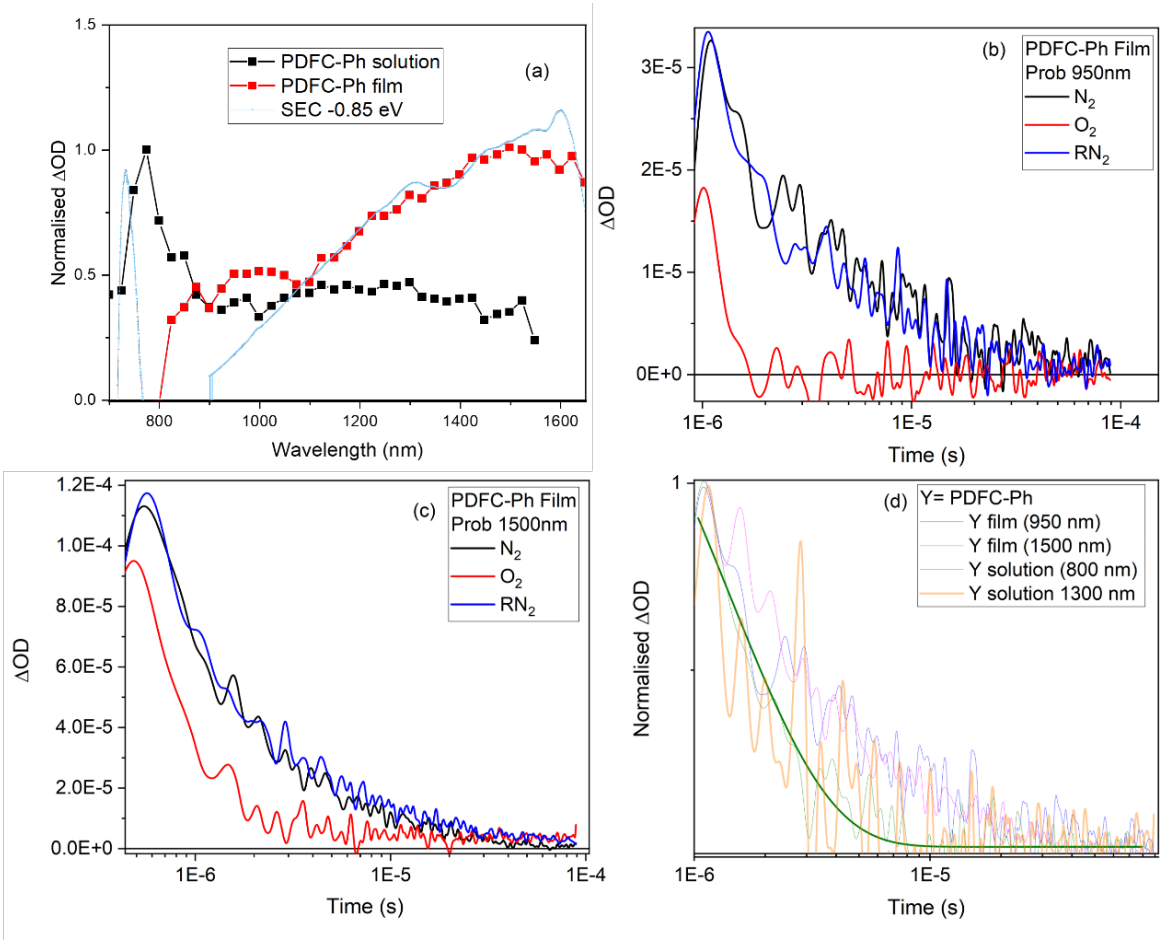

Figure 5.13 *(a) Normalised (to 1) at 1 µs TA spectra for pristine PDFC-Ph film, solution and the SEC spectrum of PDFC-Ph anions (pale blue). The excitation wavelength 660 nm and excitation energy 53 µJ cm^{-2} were used for PDFC-Ph film. Oxygen dependence decay dynamics for PDFC-Ph film with probing wavelength at (b) 950 nm and (c) 1500 nm under the nitrogen, oxygen and recovery nitrogen atmosphere. Normalised decay dynamics for (d) PDFC-Ph film and solution, probing at 950 and 1500 nm, 800 nm and 1300nm, respectively. The dash line is the mono-exponential fitting.*

Similar to PDFC-Ph, TA spectrum for syn-PDFC film shows both a tail beyond to 1600 nm and two positive features around 1050 nm and 1350 nm, as displayed in Figure 5.14a. The spectral overlap between the 1600 nm tail and the SEC spectrum of syn-PDFC film at -0.97 V shows the 1600 nm tail assigned to the syn-PDFC anion. The two positive features around 1050 nm and 1350 nm were attributed to the triplet as evidenced by the spectral overlap with the triplet in syn-PDFC solution. The negative intensity below 900 nm is because of the greater GSB of the pristine film obscures the triplet peak. It is worth noting that the triplet absorption peak at 1300 nm shows higher intensity than the 1050 nm in film while the solution is inverse. This is because the underlying anion spectrum simply creates a rising baseline.

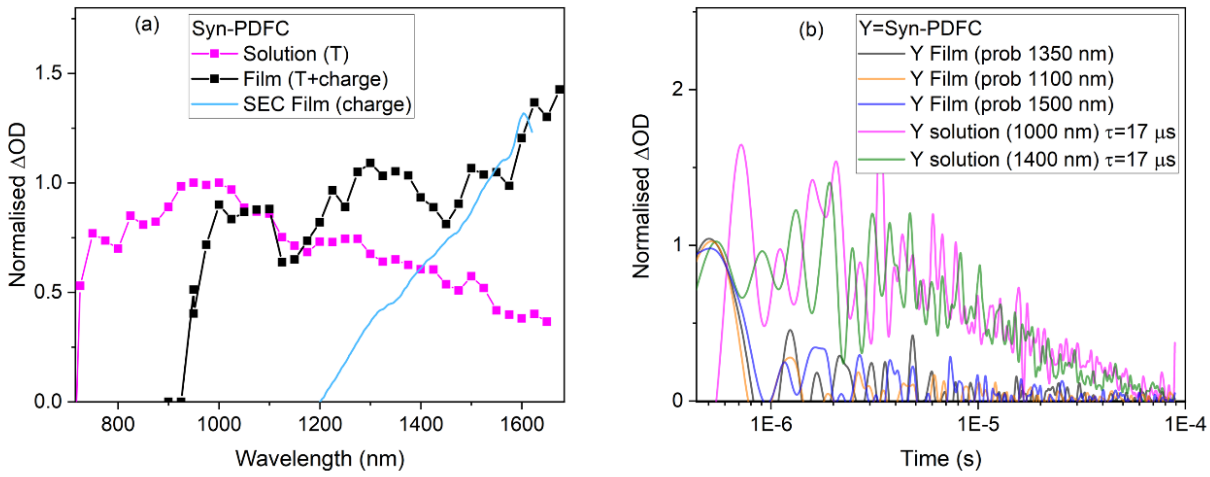

Figure 5.14 *Normalised (to 1) at 1 μs TA spectra for pristine syn-PDFC film, solution and the SEC spectrum of syn-PDFC film. Excitation wavelength 670 nm and energy 41 μJ cm^{-2} used for pristine syn-PDFC film. (b) Normalised decay dynamics for syn-PDFC film probing at 1350 nm, 1100 nm, and 1500 nm and for syn-PDFC solution probing at 1000 nm and 1400 nm.*

5.3.4.5 Annealed PM6: PDFC Films

Since the high device performance (12.56%) was found in the annealed PM6: anti-PDFC in comparison to the 10.49% in annealed PM6: syn-PDFC and 6.53% in the annealed PM6: PDFC-Ph organic photovoltaic devices (after annealing at 140 °C for 5 mins), it is crucial to understand the photophysics process behind it. As the PM6 and PDFC NFAs charge and triplet formation have been investigated in the solution and solid phases, it is the right time to characterise the photophysical process in annealed PM6 with PDFC series' blend systems on ns-μs timescales. At the end of the characterisation, a comparison study about the charge yield among three different annealed PM6:PDFC NFAS blends will be performed.

TA spectra of PM6 with each PDFC NFAs are characterised by two excitation wavelengths: 520 nm mainly excites the polymer (but still a small amount of PDFC could be excited) and 665 nm is used to selectively excite the PDFC NFAs. Three bands appearing at <700 nm, 900 nm and a long tail up to 1600 nm are shown in all three annealed PDFC blend with PM6 TA spectra. This indicates that same types of transient species were generated irrespective of the excitation wavelength, indicating that hole transfer could occur with the NFA excitation. To assign transient bands in each μs-TA spectra of the annealed PM6:NFAs blend film, the PDFC NFAs' anion and triplet reference spectra were used from their individual SEC spectrum of the film and μs-TA spectrum of the solution. Figure 5.15a shows the normalised TA spectra of annealed PM6: anti-PDFC film, the <750 nm, 900 nm and the 1600 nm tail shown with both

the 520 nm and 665 nm excitation wavelengths. Both the µs-TA spectra are very similar in spectral shape, exhibiting a close match with the SEC spectra of the pristine PM6 film and a control TA spectrum of PM6:PC60BM film. Thus, the <700 nm and 900 nm bands are attributed to the polymer polarons. Since both polymer cation and anti-PDFC anion show 1600 nm tail features in their pristine films, the 1600 nm band in the annealed blend ascribes as the coexistence of PM6 cations and anti-PDFC anions. Note that syn-PDFC and PDFC-Ph anion at 1600 nm is particularly apparent for the PDFC dominant 665 nm excitation, while this is not the case for anti-PDFC anion, as shown in Figure 5.15a-c. This might be because of the intrinsic charge photogeneration in the pristine PDFC-Ph and syn-PDFC domain and, thus, anion formation in the same spectral region. The lack of anti-PDFC anion with NFA dominant excitation might be due to the good miscibility of the PM6 with anti-PDFC, creating a smaller anti-PDFC pure domain but a relatively larger polymer domain.

Interestingly, as was observed in SEC spectra, the relative intensities of the two PM6 polaron bands at <700 nm and 900 nm band vary across the samples. Pristine PM6 is dominated by the more ordered polaron, same as the PM6:anti-PDFC and PM6:PDFC-Ph films, while the PM6:syn-PDFC film appears to be more dominated by the more amorphous polaron. However, for the PM6:syn-PDFC film, care must be taken as it is likely that syn-PDFC anion also absorbs in this region.

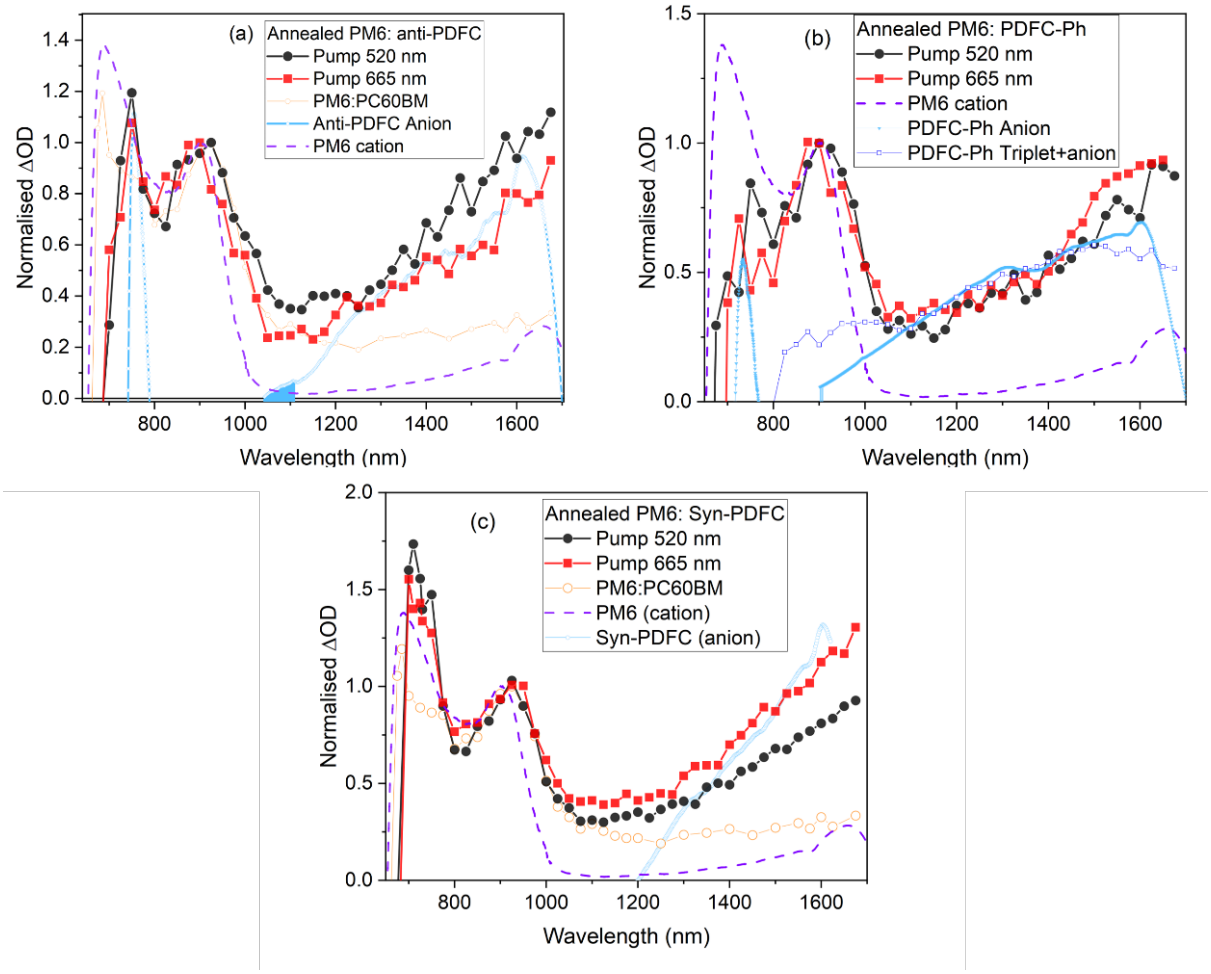

Figure 5.15 *Normalised (to 1) transient absorption spectra of annealed (a) PM6: Anti-PDFC film, (b) PM6: PDFC-Ph film (c) PM6:Syn-PDFC films, with excitation pump wavelengths of 520 and 665 nm. Excitation densities used were in the range 12 – 15 μJ cm^{-2}. Also, reference spectra, including polymer cation (SEC), NFA anion (SEC), and triplet (TA film), and polymer cation in PM6:PC$_{60}$BM blend film have been showing.*

As shown in Figure 5.16a, the kinetics for polymer cation (probed at 900 nm in all three blend films) shows nearly identical decay dynamics, which is similar to the polymer cation in pristine PM6 film. The kinetics can be fitted to a power law with a gradient α of 1, attributed to trap-free recombination. Furthermore, the energy-independent decay dynamics at 900 nm indicate a lack of bimolecular recombination (Figure 5.16b). As such, the 900 nm polymer cation recombination is likely dominated by that occurring within pure polymer domains and may suggest a migration of the PDFC anions into the PM6 domain such that recombination possibly occurs primarily via the PM6 interchain polaron pair.

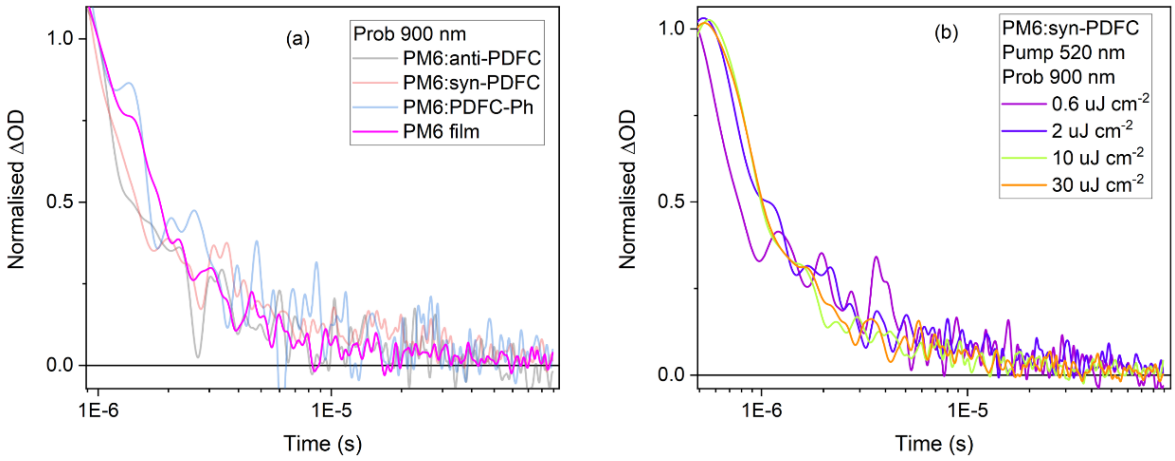

Figure 5.16 *Normalised decay dynamics for the transient species observed in the annealed PM6: anti-PDFC, PM6:syn-PDFC and PM6:PDFC-Ph blend films, together with the pristine PM6 film and PM6:PC60BM film, with probing wavelength at 900 nm. (b) Energy dependence decay dynamics for annealed PM6:syn-PDFC with excitation wavelength at 520 nm and excitation energy ranging from 0.2 to 30 μJ cm^{-2}.*

A particularly useful aspect of μs-TAS is that the TA amplitude signal is directly proportional to the population of the photogenerated species. The amplitude of the polaron TA signal at 1 μs is proportional to the photovoltaic device's J_{sc} and external quantum efficiency (EQE).[25,26] To evaluate the relative populations of the excited state in annealed PM6 with PDFC NFA blends, the TA spectra per photon absorbed were assessed for each pristine and blend film, as shown in Figure 5.17. The triplet and anion formation in pristine PDFC-Ph film shows eight times higher population than the anion only anti-PDFC and the coexistence of triplet and anion syn-PDFC film. This reveals that PDFC-Ph film shows a greater intrinsic charge generation.

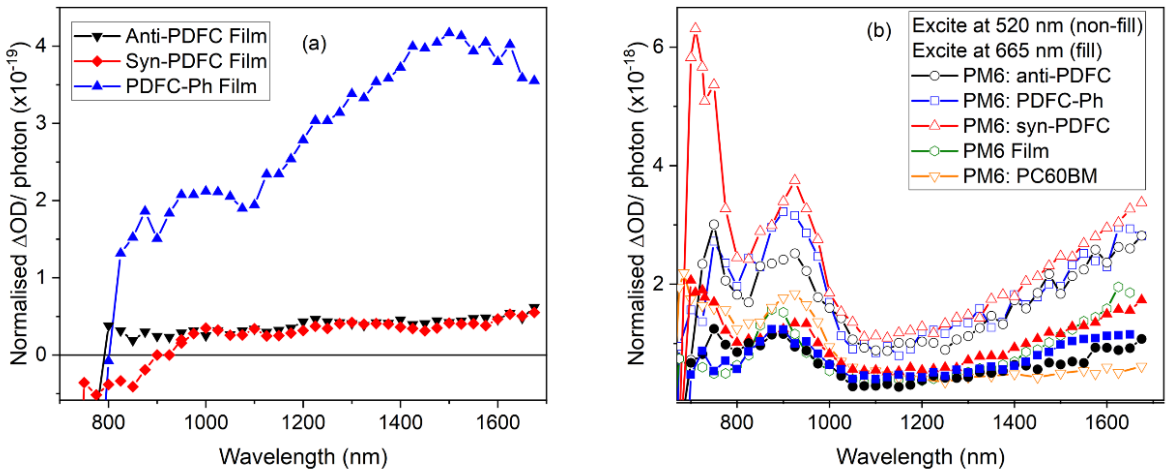

Figure 5.17 *Normalised (per photon) absorption spectra for (a) pristine anti-PDFC, syn-PDFC and PDFC-Ph films with excitation wavelength at 665 nm. (b) annealed PM6 with anti-PDFC, syn-PDFC and PDFC-Ph blend films with both the polymer (520 nm) and NFAs excitation (650 nm) wavelength in comparison to the yield of charge generation in pristine PM6, and PM6:$PC_{60}BM$ blends with excitation wavelength at 520 nm.*

As shown in Figure 5.17b, the annealed blend films were characterised under both polymer (520 nm) and NFA-dominated excitation (650 nm) wavelengths. When exciting the NFA, no additional polymer polarons are created relative to the polymer on its own. It is only when excited the polymer that the charge population started getting much greater polaron yields. In comparison to the fullerene based PM6 blend, the charge yield is two times lower than the PDFC based blend films. Interestingly, the greater intrinsic charge generation capability observed in pristine PDFC-Ph film was not shown in the annealed PM6:PDFC-Ph film with selectively excited PDFC-Ph. As such, polymer polaron formation in PM6:PDFC-Ph film under the NFA excitation was achieved by the energy transfer process that is faster than the intrinsic charge generation.

Annealed PM6:syn-PDFC blend shows the greatest charge yield and contains the largest proportion of the <700 nm polymer cation among the other two annealed blend films. This might be explained by the good miscibility of the polymer and NFAs, creating a well-mixed D/A domain for charge separation (consistent with the PL and AFM results). In addition, the enhanced polymer crystallinity in the annealed PM6:syn-PDFC blend facilitates the polymer cation generation via the interchain polaron pairs dissociation, which is consistent with the ground state absorption results.

5.3.5 Picosecond transient absorption spectroscopy (ps-TAS)

Since the long-lived PDFC NFAs triplet and anion spectrum have been investigated by the µs-TAS, ps-TAS was employed to study further the charge carriers with shorter lifetime dynamics in pristine PM6 and PDFC NFAs films. This serves as a good tool to investigate excited states and the mechanism for charge photogeneration and recombination in PM6 with PDFC NFAs blend systems.

5.3.5.1 Pristine PM6 film

The ps-TA spectrum for the pristine PM6 film is shown in Figure 5.18a-b as a function of pump-probe delay time, in colour intensity and linear scales, with an excitation wavelength at 520 nm. At early timescales (100fs - 1 ps), TA spectrum of pristine PM6 film shows the singlet state (S_1) as a broad photo-induced absorption (PIA) band centred at 1150 nm. A new band gradually appears at 900 nm along with the decay of the 1150 nm S_1 band. It should be aware that the PM6 S_1 state amplitude at early timescale was 10 times higher than the PM6 polarons at late timescale. Figure 5.18c displayed the kinetics for the pristine PM6 film, probing at 900, 1155 nm and 1400 nm with an excitation energy 30 µJ cm^{-2}. The decay dynamics for all three probing wavelengths were fitted with biexponential with varying decay lifetime. It has been shown that the decay lifetime with the probing wavelength at 1160 nm was similar to the 1400 nm (τ_1=0.5 ps, τ_2=12 ps) but varies to 900 nm, which confirms the existence of the two types of transient species generated in the pristine film. The biexponential decay of the 900 nm band showing the decay lifetime with τ_1=5 ps and τ_2=60 ps.

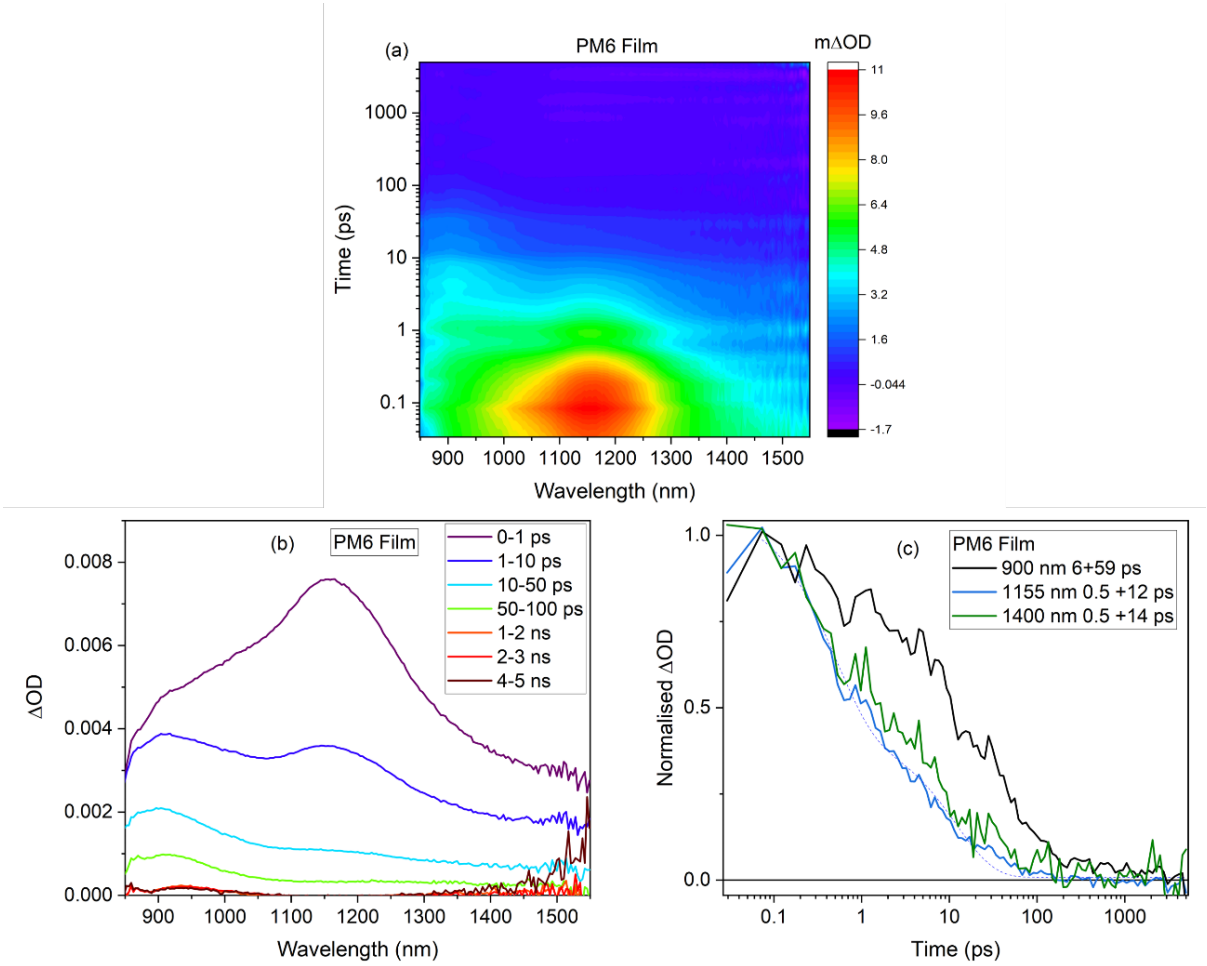

Figure 5.18 *Picosecond TA spectra of PM6 film in (a) colour intensity scales (b) linear scales, with excitation wavelength at 520 nm and 30 μJ cm^{-2}. (c) Normalised decay dynamics with probing wavelength at 900 nm, 1155 nm, and 1400nm (raw data). The dash line represented the bi-exponential fitting with the decay lifetime shown in the figure caption.*

To understand the ps-TA data with the existence of different excited states, global analysis (GA) was used to deconvolute the TA spectrum and kinetics for respective excited states from the raw ps-TA data. GA results for the PM6 film are displayed in Figure 5.19, with the broad 1150 nm PM6 singlet exciton as a reference to extract the other one transient species. The validity of the GA results was tested by inputting the later timescales ps-TA spectrum showing with 900 nm band as a reference and a similar exciton spectral shape was found. Figure 5.19a shows ps-TA spectra of the pristine PM6 film with GA. Despite the formation of PM6 exciton, the other excited state generated at 900 nm with a tail to 1400 nm was attributed to PM6 charge as the evidenced by the good spectral overlapping to the SEC spectrum of PM6 cation.[6,27]

The global analysis of kinetic decay for individual transient species was shown in Figure 5.19b. The good overlap of the exciton decay with GA to the raw data probing at 1155 nm gives a good indication that the decay of the exciton independently to PM6 charges. Figure 5.19c shows the decay dynamics of exciton in pristine PM6 film as a function of excitation energy. The energy-independent decay dynamics for 1150 nm band provide further evidence for the exciton assignment.

As shown in Figure 5.19d, the GA decay kinetics for the PM6 charge was fitted with mono-exponential decay. The energy-independent decay dynamics of the PM6 charge show likely the geminate recombination of an interchain polaron pair/ CT state as such early timescales.

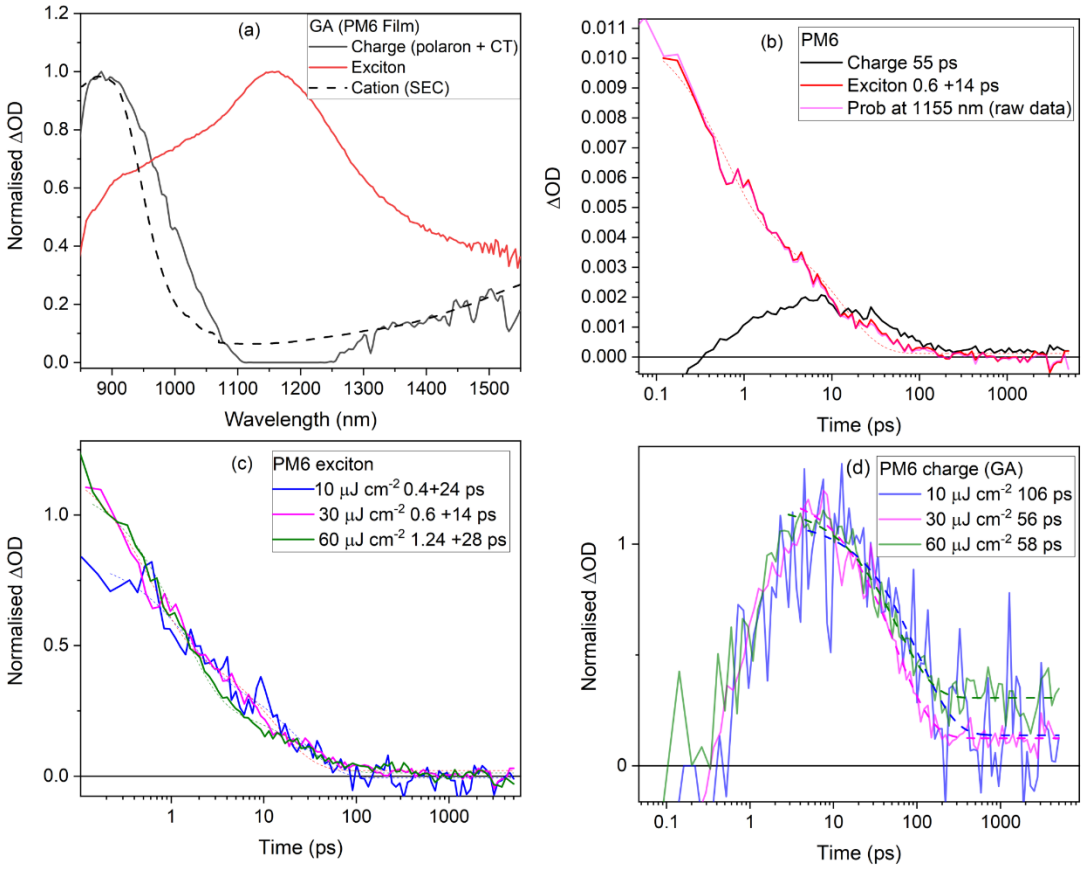

Figure 5.19 *(a) Global analysis (GA) of picosecond transient absorption spectra for PM6 film, the red solid line represented the PM6 exciton (0–1 ps) as a reference and the black solid line is the PM6 charge as the evidence by the matched black dash line for the SEC spectra of PM6 cation. It should be noted that the charge transfer (CT) state also be observed as the PM6 polaron position, and the PM6 charge will be used to represent the combination of the PM6 polaron and CT state. (b) Decay dynamics for PM6 exciton and charge with GA and the normalised decay dynamics probing at 1155 nm (raw data). Energy dependence decay dynamics of (c) PM6 exciton and (d) charge with excitation at 10, 30 and 60 μJ cm^{-2}, in the time range from 0.1 ps to 5 ns.*

5.3.5.2 ps-TA for pristine PDFC films

The ps-TA spectrum for the pristine anti-PDFC film is shown in Figure 5.20a-b as a function of pump-probe delay time, in colour intensity and linear scales, with an excitation wavelength at 665 nm. The anti-PDFC exciton observed at early timescale was shown as a band at 875 nm with a shoulder at 930 nm and a low absorption shoulder at 1050 nm with a tail to 1600 nm. Figure 5.20c shows the normalised kinetics for the anti-PDFC film with probing wavelength at 900 nm, 1200 nm and 1400 nm fitted with a bi-exponential decay. The varying lifetime in different probing wavelengths indicates more than one transient species present.

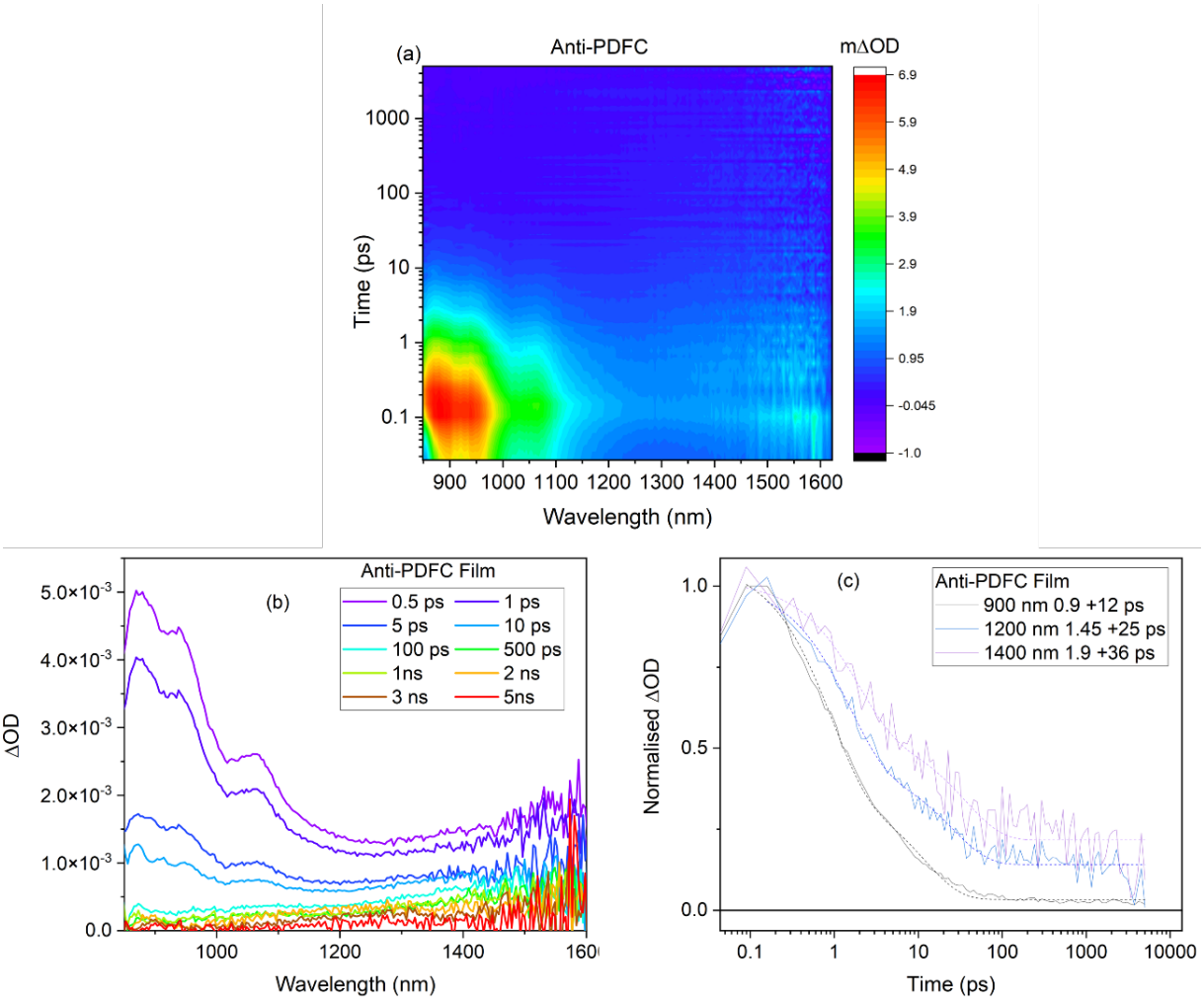

Figure 5.20 *(a) Picosecond TA spectra of anti-PDFC film in (a) colour intensity scales (b) linear scales, with excitation wavelength at 665 nm and 30 μJ cm^{-2}. (c) Normalised decay dynamics with probing wavelength at 900 nm, 1200 nm, and 1400nm (raw data). The dash line represented the bi-exponential fitting with the decay lifetime shown in the figure caption.*

GA was used to deconvolute the ps-TA spectrum of the pristine anti-PDFC as shown in Figure 5.21a, with the anti-PDFC exciton spectrum as the reference to extract another one

component. The second transient species after deconvolution displayed a wide absorption band from 1000 to 1600 nm, which shows a good overlapping with the 4.5 ns TA spectrum from the raw data. The good spectral overlapping of the second component with the anti-PDFC anion SEC spectra confirms the anti-PDFC charge formation. It should be noted that although anti-PDFC triplet was identified not only as a tail to 1600 nm but also a peak at 950 nm which was inconsistent with the spectral shape of the second component after GA. Therefore, this second component was surely attributed to the anti-PDFC charge. The good overlapping of the exciton decay with GA to the raw data probing at 900 nm gives a good indication that the decay of the exciton independently to the second component.

The kinetics probed for the anti-PDFC exciton was shown in Figure 5.21c as a function of excitation energy. The decay becomes faster as the excitation energy increase. Even at the lowest measured excitation energy (measured at 9.4 μJ cm^{-2}), the exciton decay still was fitted with a biexponential decay dynamics with a lifetime 4 ps and 46 ps. The shorter lifetime 4 ps could be the charge separation of the exciton, and the longer lifetime 46 ps could be attributed to the exciton relaxing back to the ground state.[28] Interestingly, it can be observed that the reduced exciton lifetime was proportional to the increased excitation energy. This indicate that the loss of the mono-exponential decay for the exciton at higher excitation energy was due to the exciton-exciton annihilation and the annihilation rate is proportional to the excitation energy.

The energy dependence decay dynamics of anti-PDFC charge is shown in Figure 5.21d, it could be clearly seen that the creation of polaron become faster under higher excitation energy (13 ps vs 1.2 ps vs 0.38 ps from high to low excitation energy), which implies that the formation of anions was influenced by exciton generated in the pristine film. Since the anions are hard to be generated in the pristine film, it either required an interface for CT state dissociation, or higher energy to provide more photons. For the anti-PDFC polaron formation, therefore, it could be explained by either the energy transfer process at higher excitation energy or the observation of the anti-PDFC aggregates (AFM). The energy transfer process could be achieved by the extra energy obtained by the exciton-exciton annihilation process, as there was a much faster decay rate at higher excitation energy. From the morphology view, a rougher surface morphology (R_q=7.35 nm) was observed for the pristine anti-PDFC film,

indicating the anti-PDFC aggregates formation, which could form grain boundaries to accelerate the CT state dissociation.

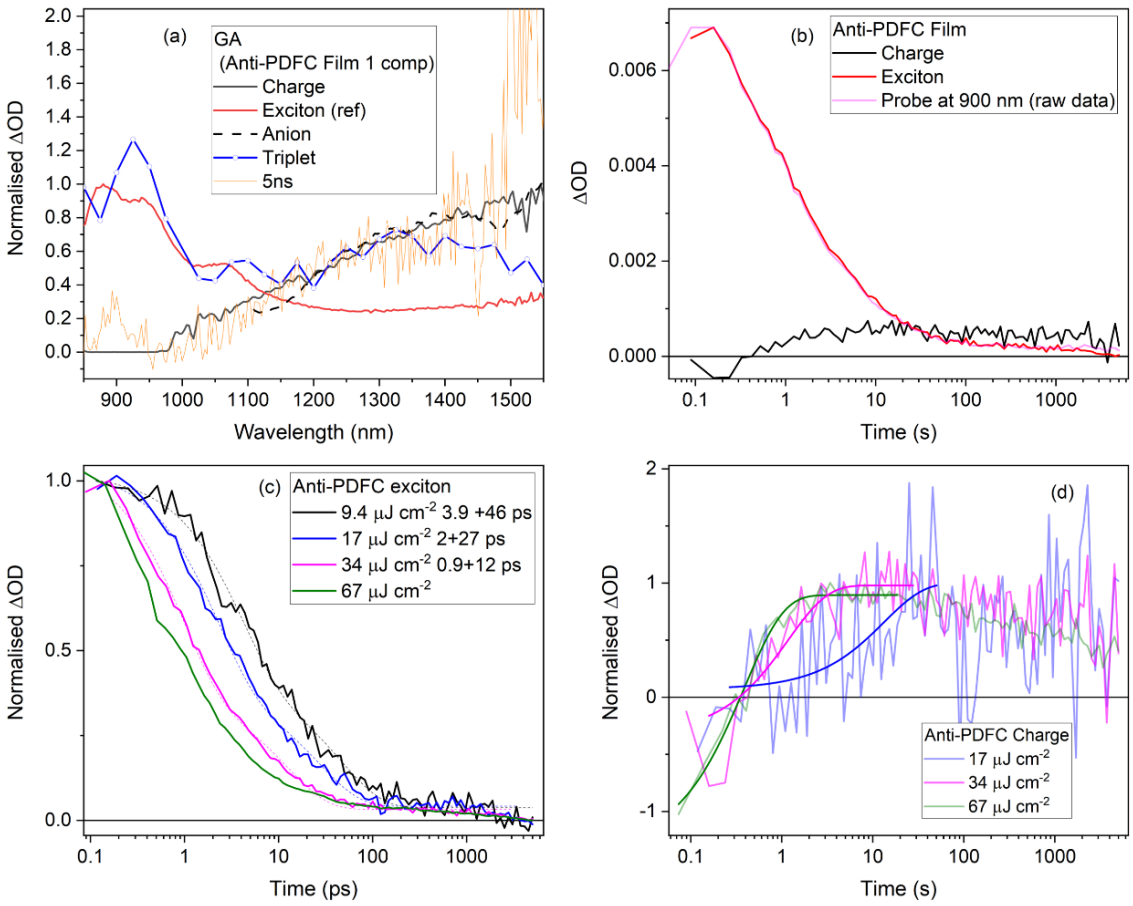

Figure 5.21 *(a) GA of ps-TA spectra for anti-PDFC film, the red solid line represented the Anti-PDFC exciton (0-1ps) as a reference and the black solid line is deconvoluted spectrum matched with the SEC spectra of Anti-PDFC anion (black dash line) and the 5 ns spectrum from the raw data. The solid blue circle line was the anti-PDFC triplet obtained from μs-TA spectrum of anti-PDFC solution at 1 μs. (b) Decay dynamics for exciton and anti-PDFC charge with GA and the normalised decay dynamics probing at 900 nm (raw data). (c) Normalised energy-dependent decay dynamics for Anti-PDFC exciton from GA results and (d) for Anti-PDFC charge with excitation at 10 – 60 μJ cm^{-2}, in the time range from 0.1 ps to 5 ns.*

The ps-TA spectrum for the pristine PDFC-Ph film is shown in Figure 5.22a-b as a function of pump-probe delay time, in colour intensity and linear scales, with an excitation wavelength at 665 nm. Being different to the distinctive bands formed in the anti-PDFC, the PDFC-Ph exciton was formed as a relatively broadband at 890 nm with a weak shoulder around 1050 nm. A new PIA feature with low intensity was observed at 1000 nm and 1300 nm at later timescales of 5 ns. The different decay dynamics with probing wavelength at 900 and 1300 nm indicate two types of transient species were observed by ps-TAS (Figure 5.22c).

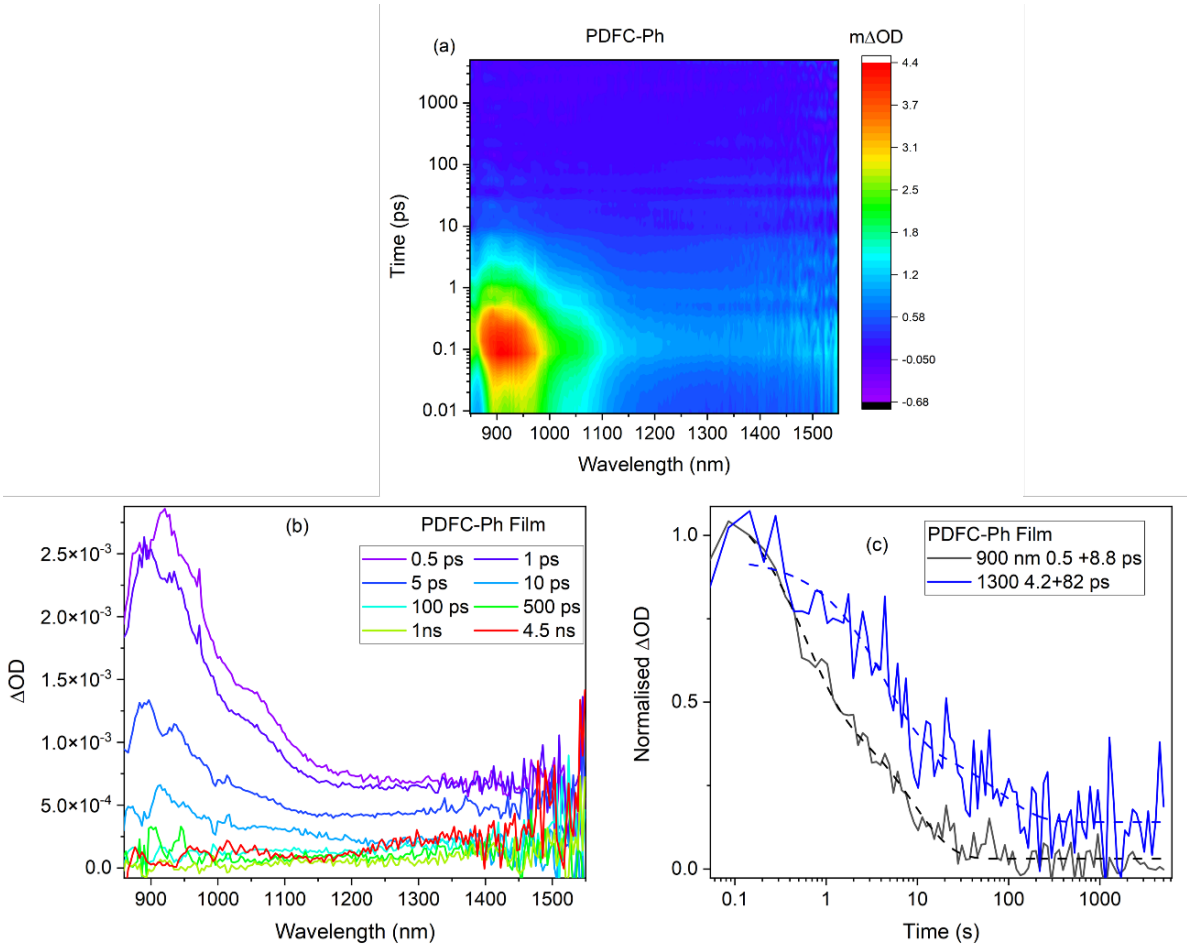

Figure 5.22 *(a) Picosecond TA spectra of PDFC-Ph film in (a) colour intensity scales (b) linear scales, with excitation wavelength at 665 nm and 30 μJ cm^{-2}. (c) Normalised decay dynamics with probing wavelength at 900 nm, and 1300 nm (raw data). The dashed line represented the bi-exponential fitting with the decay lifetime shown in the figure caption.*

Using the PDFC-Ph exciton as a reference for GA, the second component was extracted as a high-intensity tail from 1000 nm to 1500 nm, as shown in Figure 5.23a. It was assigned to the PDFC-Ph charge as evidenced by the spectra overlapping to the SEC spectra of the pristine PDFC-Ph film. Being different from the anti-PDFC film, the TA spectrum of 4.5 ns (raw data) not only shows the long tail to 1600 nm, but also a low-intensity pump at 900 nm, which shows a good spectral overlapping with the μs-TA spectrum of pristine PDFC-Ph film (triplet + anion). However, the good kinetic overlap between the exciton after GA and probing wavelength at 900 nm reveals that a small number of triplets is generated in the film, which is hard to be measured precisely in comparison to the large number of excitons. Similar to the anti-PDFC exciton decay, an energy-dependent decay dynamics was observed for the PDFC-Ph exciton as displayed in Figure 5.23c, fitted with biexponential decay, and the lifetime was 2.6 ps and 40 ps with the lowest 10 μJ cm^{-2} excitation energy. In comparison to the anti-PDFC

exciton, the exciton dissociation lifetime was similar to the PDFC-Ph film (2.6 ps vs 3.9 ps) and similar decay lifetime back to the ground state (46 ps vs 40 ps).

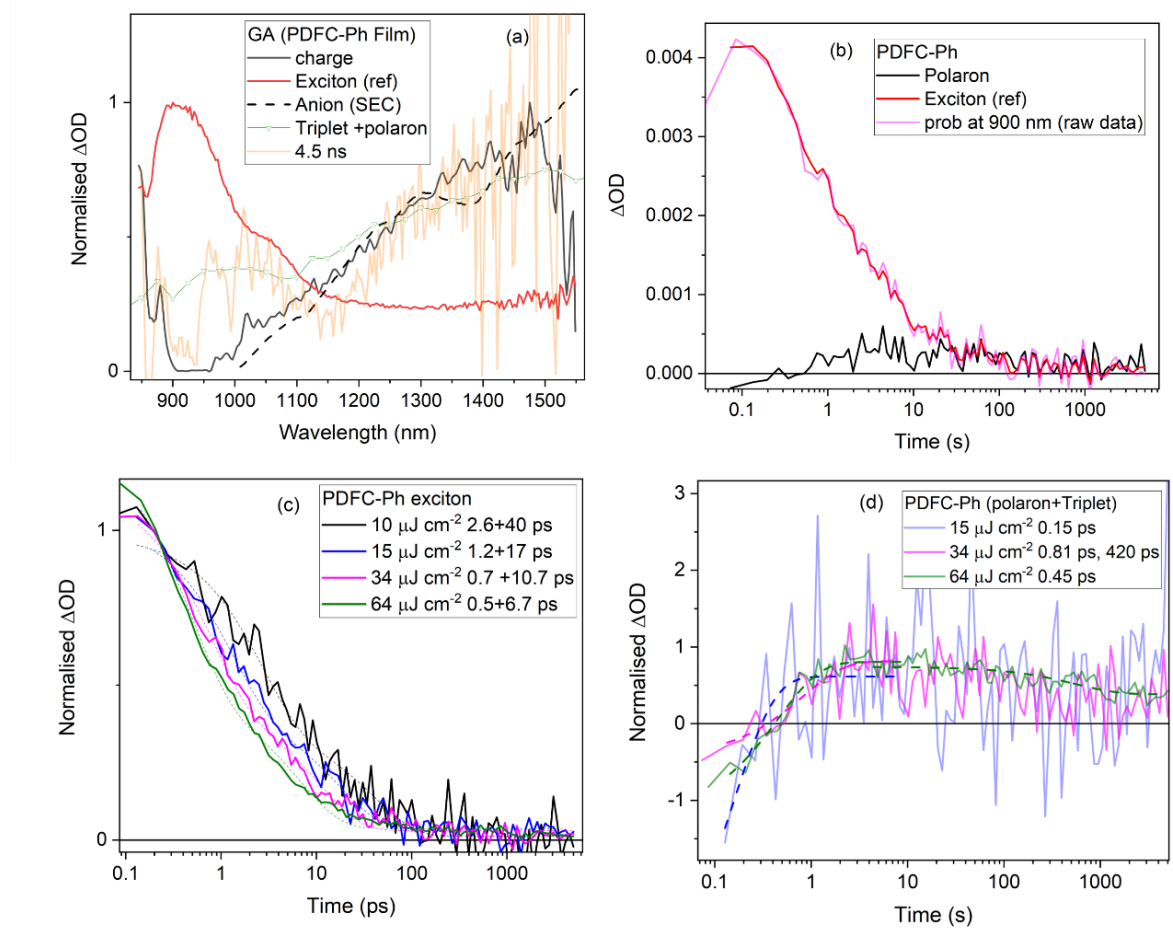

Figure 5.23 *(a) GA of ps-TA spectra of PDFC-Ph film, the red solid line represented the PDFC-Ph exciton (0-1ps) as a reference and the deconvoluted spectrum (black solid line) is the charge as the evidence matched with the black dash anion SEC spectra, orange solid line is the 4.5 ns spectrum from raw data. The green triangle line was the μs-TA spectrum of pristine PDFC-Ph film include both triplet and anion formation. (b) Decay dynamics after GA for PDFC-Ph exciton, charge and the decay dynamics at 900 nm from the raw data with an excitation energy at 30 μJ cm^{-2}. (c) Normalised decay dynamics for PDFC-Ph exciton from GA results and (d) for PDFC-Ph charge with excitation at 10 – 60 μJ cm^{-2}, in the time range from 0.1 ps to 5 ns.*

The ps-TA spectrum for the pristine syn-PDFC film is shown in Figure 5.24a-b as a function of pump-probe delay time, in colour intensity and linear scales, with an excitation wavelength at 665 nm. The syn-PDFC exciton is shown as a band at 875 nm with a long tail up to 1500 nm as the purple line at 0.5ps. At longer timescales (5 ns), a broad PIA band from 1500 nm is shown as the red line in Figure 5.24b. The similar decay trend (Figure 5.24c) between 900 nm

and 1500 nm /1050 nm and 1300 nm give an indication that there are two main transient species generated in the pristine syn-PDFC film.

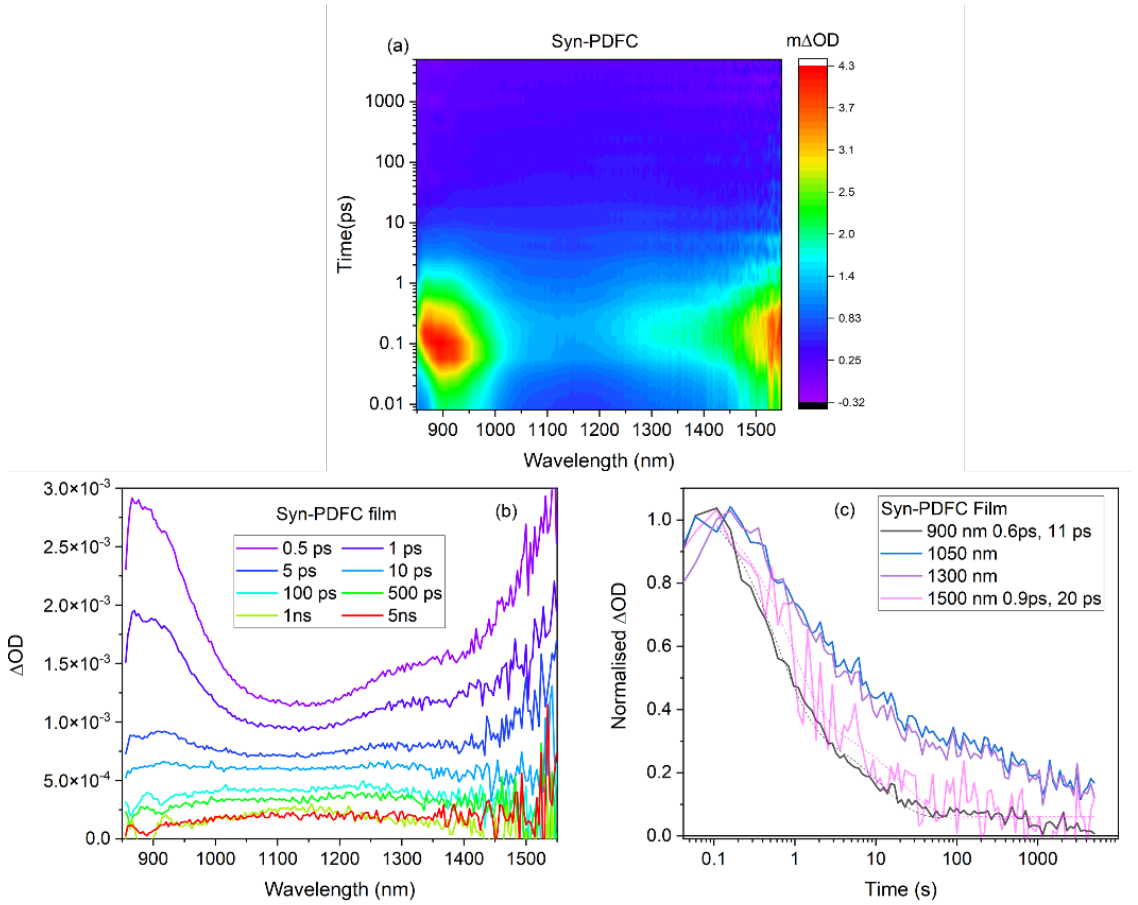

Figure 5.24 *(a) Picosecond TA spectra for Syn-PDFC film in (a) colour intensity scales (b) linear scales, with excitation wavelength at 665 nm and 30 μJ cm^{-2}. (c) Normalised decay dynamics with probing wavelength at 900 nm, 1050 nm, 1300 nm and 1500nm (raw data). The dash line represented the bi-exponential fitting with the decay lifetime shown in the figure caption.*

The ps-TA spectra after GA, using the syn-PDFC exciton as a reference and one component, shows the deconvoluted TA spectrum as a broad band range from 950 nm to 1500 nm and centred around 1150 nm (Figure 5.25a). This band allocated around 1150 nm was neither match the syn-PDFC anion SEC spectrum nor the syn-PDFC triplet. However, the 5 ns spectrum from the raw data shows a band around 1080 nm with a tail to 1400 nm which shows the spectral overlapping with the μs-TA spectrum of the syn-PDFC film. As such, the second component after GA and the 5ns spectrum can be attributed to the coexistence of triplet and anion. The validity of the GA can be demonstrated by the non-changed decay dynamics for exciton (reference spectrum) and the probing wavelength at 900 nm (Figure 5.25b). Similar

to the anti-PDFC and PDFC-Ph exciton, a biexponential decay dynamics was fitted to the syn-PDFC exciton kinetics (Figure 5.25c) with a lifetime 1.3 ps and 24 ps at 10 μJ cm^{-2}. In comparison to the anti-PDFC and PDFC-Ph exciton decay, an energy-independent decay dynamic was observed for syn-PDFC exciton, and the decay lifetime is half than anti-PDFC or PDFC-Ph exciton.

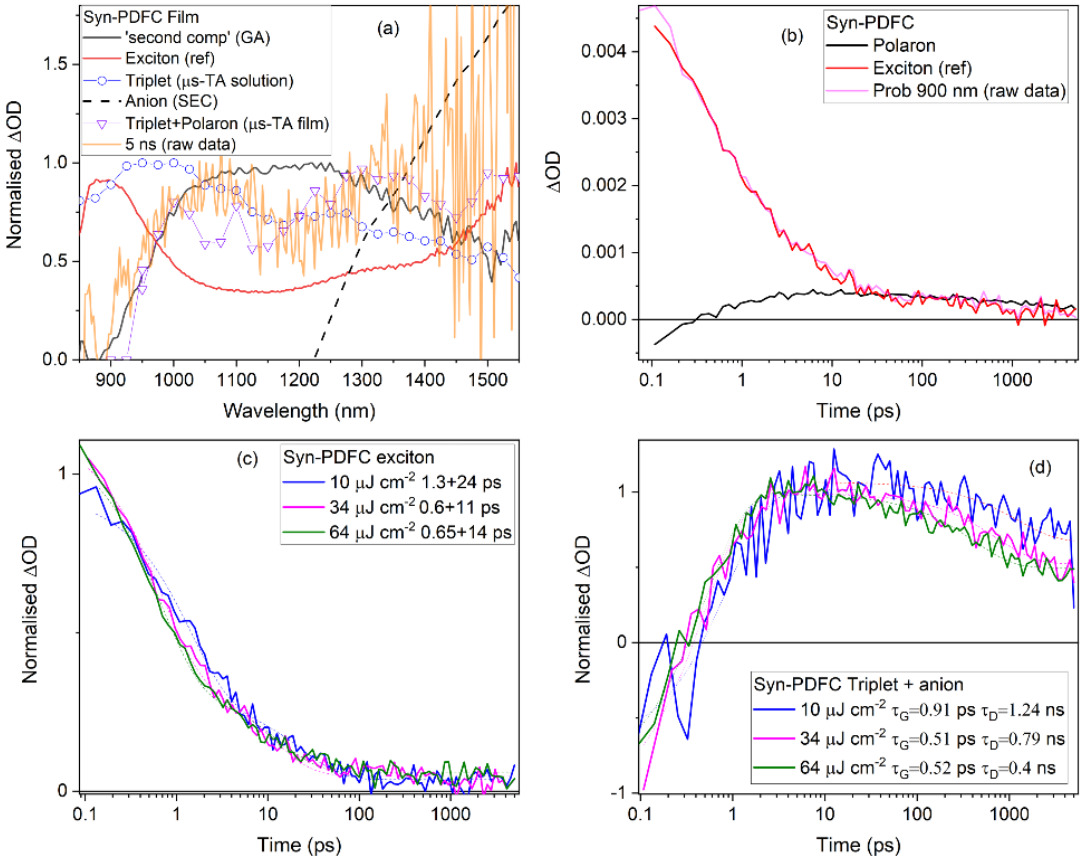

Figure 5.25 *(a) GA of ps-TA spectra of Syn-PDFC film, the red solid line represented the syn-PDFC exciton (0-1ps) as a reference and the deconvoluted spectrum (black solid line), orange solid line is the 5 ns spectrum from raw data, the black dash line is the SEC spectra for syn-PDFC anion. The purple triangle line was the μs-TA spectrum of the pristine syn-PDFC film, including both triplet and anion formation. (b) Decay dynamics for syn-PDFC exciton and the deconvoluted second component with excitation energy at 30 μJ cm^{-2}. Normalised decay dynamics (c) for Syn-PDFC exciton from GA results and (d) for Syn-PDFC triplet+anion with excitation at 10 – 60 μJ cm^{-2}, in the time range from 0.1 ps to 5 ns.*

5.3.5.3 ps-TAS for annealed PM6 with PDFC NFA blend films

As short-lived excited states: exciton, CT and triplet state for pristine donor PM6 and PDFC NFAs have been identified by ps-TAS as section 5.3.5.2, the ps-TA spectrum of them will be used as the reference for the following annealed blend analysis. As shown in Figure 5.26, the ps-TA spectra of annealed PM6 with three PDFC NFA blends are displayed in their contour

and linear scales. The excitation wavelength at 520 nm was used to excite predominately the polymer to maximise the charge photogeneration yield. From both the contour and linear ps-TA spectra, all three blends initially (0-1 ps) exhibit strong intensity bands at 900 nm and 1150 nm, and a band at 900 nm with a tail to 1500 nm is shown in later timescales (4-5 ns). According to the ps-TA results of the pristine NFA and PM6 films, the 900 nm band created at the early timescales ascribes as NFA exciton and 1150 nm is attributed to the PM6 exciton, and the 900 nm with 1600 nm tail at later timescales is assigned to PM6 charge.

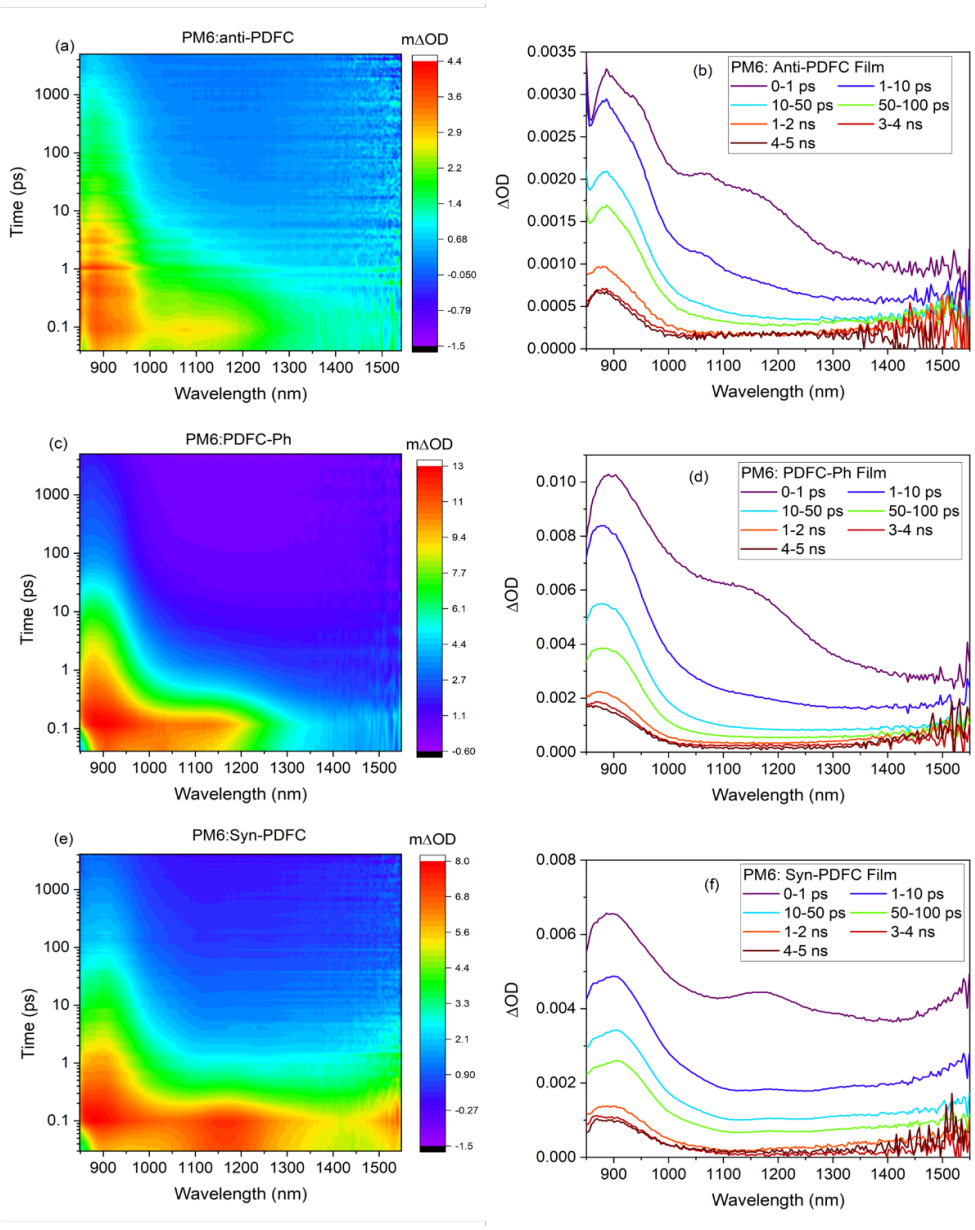

Figure 5.26 *Picosecond TA spectra in colour intensity scales and linear scales for annealed, (a) and (b) PM6:anti-PDFC film, (c) and (d) PM6:PDFC-Ph film, (e) and (f) PM6:syn-PDFC film, with excitation wavelength at 520 nm and excitation energy 30 μJ cm^{-2}.*

GA was used to deconvoluted the ps-TA spectrum and the decay dynamics for the annealed PM6:PDFC blends by using the NFA exciton as the reference spectrum (obtained from the ps-TA data of the pristine NFA film) and extract another two components. Since the similar types of excited states were observed in all three annealed PM6 with PDFC blends, the ps-TA results with GA for annealed PM6:syn-PDFC blend is shown as an example, as shown in Figure 5.27a. The validity of the ps-TA results with GA can be confirmed by the good spectral overlap of the deconvoluted spectra with both the PM6 exciton (pristine film) and PM6 cation (SEC spectrum), providing evidences for three types of excited states existed in the annealed PM6:syn-PDFC blends. This is consistent with the hypothesis made from the raw contour and linear scales ps-TA data.

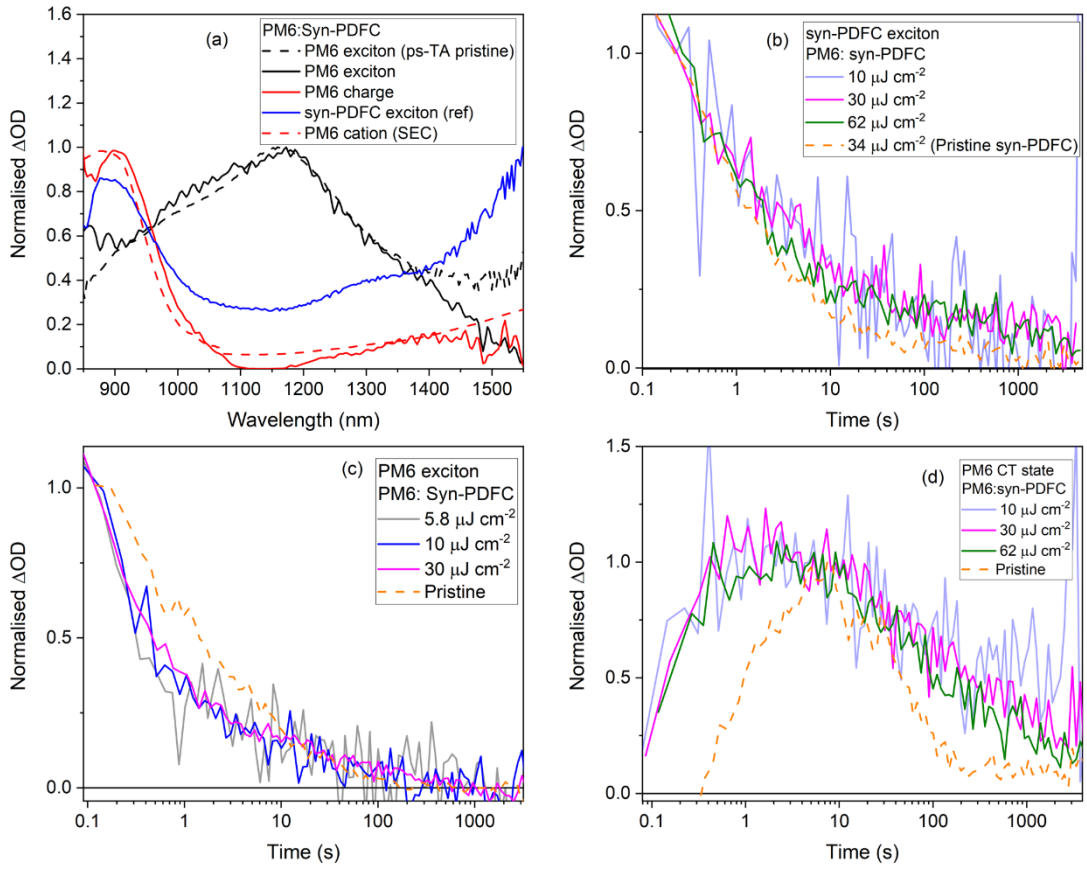

Figure 5.27 *(a) GA of ps-TA spectra for annealed PM6:syn-PDFC film, the blue solid line represented the syn-PDFC exciton (0-1ps) as a reference and the deconvoluted spectra(black and red solid line), black dash line is PM6 exciton in pristine film, the red dash line is the SEC spectra for PM6 cation. Energy dependence decay dynamics for (b) syn-PDFC exciton (c) PM6 exciton (d) PM6 charge in blend film in comparison with their decay in pristine film with excitation energy at 34 μJ cm^{-2}.*

It is surprising to find out that not only the syn-PDFC exciton was observed in the femtosecond timescales as the minor ground state absorption of syn-PDFC at 520 nm, but also the lifetime of the syn-PDFC exciton is longer in the annealed blend than the pristine film. There are two possible explanations for this observation. One can be explained by the energy transfer from the PM6 singlet state to the syn-PDFC, extending the lifetime of syn-PDFC exciton. This is consistent with the relatively higher S_1 energy of PM6 (1.92 eV) than that of 1.79 eV for syn-PDFC, providing 0.13 eV driving force for energy transfer from PM6 to syn-PDFC. In addition, this is also consistent with the PL spectrum of the annealed blend is similar to the pristine syn-PDFC film. Another explanation is due to hybridisation and dynamic equilibrium between the S_1 and CT state. This is due to the fact that the energy of CT state at the D/A interface of about 1.71 eV (estimated by the energy difference between the HOMO of donor and LUMO of the acceptor) is very close to the Syn-PDFC S_1 energy. It is of particular interest that the driving force for energy transfer and electron transfer (approximated as the D and A LUMO level offset) from the PM6 is identical at ~0.1 eV, suggesting that in the absence of other factors, both processes are likely to occur. The energy of polymer and NFA singlet excitons and CT states are summarized in Table 5.3.

Table 5.3 *Lifetime summary for PDFC NFA exciton, CT state in pristine and annealed PM6 with PDFC NFA blend films.*

	energy (eV)		PDFC NFA exciton (ps)		CT (ps) pristine		CT state (ps) blend		PM6 exciton (ps)	
	S_1	CT	blend	pristine	rising	decay	rising	decay	blend	pristine
Anti-PDFC	1.77	1.70	1.2+13+840	1+14	1.2	2500	0.8	1200	0.3+2	-
PDFC-Ph	1.80	1.61	1+12+870	0.7+11	0.9	130	0.35	1100	0.4+3	-
Syn-PDFC	1.79	1.71	0.2+4+60	0.6+12	0.6	800	0.2	150	0.2+2	-
PM6	1.92		-		0.7	60	-		-	0.5+12

The PM6 exciton in the annealed blend (Figure 5.27c), also displayed an energy-independent decay with a bi-exponential fitting, but the lifetime of the PM6 exciton in the blend is shorter than the pristine film. This is consistent with the formation of D/A mixed domain facilitating

PM6 exciton quenching in the blend. The PM6 charges in the annealed PM6:syn-PDFC blend show a rising time of 200 fs, peaking at ~2 -7 ps, followed by a monoexponential decay lifetime of ~150 ps, suggesting geminate recombination of the CT state. In comparison to the lifetime of PM6 charge in pristine film (60 ps), the CT states in the blend are longer-lived, suggesting that the formation of CT state at the D/A interface not the same as polymer polaron pairs in pristine film. The rapid decay of CT states in the blend gives an explanation for the lack of long-lived charges observed on μs timescales.

A comparison ps-TA study in annealed PM6 with PDFC blend films is shown in Figure 5.28, including PDFC exciton and the CT states, with an excitation wavelength at 520 nm and excitation energy around 30 μJ cm^{-2}. The lifetimes for exciton and CT state in the annealed blend and pristine NFAs are summarized in Table 5.3. Similar to the longer lifetime of syn-PDFC exciton in the annealed blend than the pristine syn-PDFC film, both anti-PDFC and PDFC-Ph exciton also show a longer lifetime in their blend films with PM6 than their pristine film (Figure 5.28a). This is consistent with the PL spectrum of PM6 overlapping with the ground state absorption spectrum of the PDFC NFAs (Figure 5.2), indicating an energy transfer process from the PM6 singlet to the anti-PDFC or PDFC-Ph singlet in their respective annealed PM6 blend films.

For the CT states, a similar rapid rise time of 300 fs was observed in the annealed PM6:PDFC-Ph film, peaking around 3 – 8 ps, both of which were quicker than the rise time in the pristine PM6 film. In contrast, a slower rise time of 13 ps was observed for CT state in annealed PM6:anti-PDFC, which is around similar rise time as the pristine PM6 film, potentially indicating that the large polymer domain in annealed PM6:anti-PDFC than the other two blend films, because increases the average length an exciton has to diffuse to the D/A interface before the CT state formation. An overlapping mono-exponential decay dynamics of the CT states were observed in the annealed PM6 with anti-PDFC and PDFC-Ph blends, indicating that the bulky side chain plays a negligible role to the geminate recombination rate of the CT state. However, the fast CT state decay rate observed in the syn-PDFC blend in comparison to the other two blends might be because of the good π-π stacking that could accelerate the electron transfer rate which is consistent with the GIXRD results.

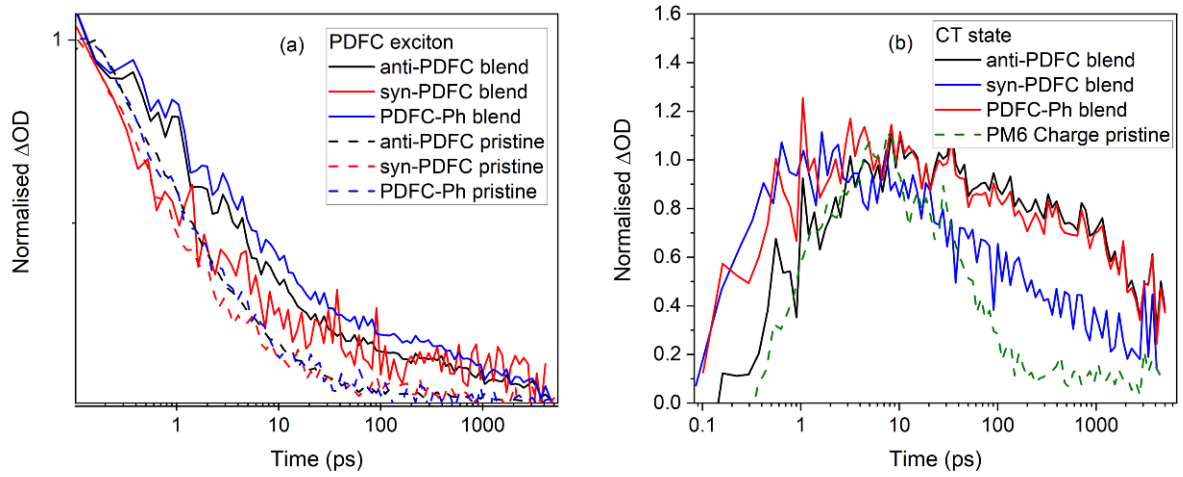

Figure 5.28 *Normalised decay dynamics for (a) PDFC exciton (b) CT state in annealed PM6 with PDFC blend films and pristine films, with an excitation wavelength 520 nm and excitation energy at 34 μJ cm^{-2}.*

Figure 5.29 shows normalised (per photon) TA spectra for CT state in all three annealed PM6 with PDFC NFA blend films. It is shown that the high FF (81 %) and high PCE (12.56 %) annealed PM6:anti-PDFC exhibit the least CT state population before 10 ps, which is 2 times lower than annealed PM6:syn-PDFC film with FF value of 77 % and PCE value of 10.49%. The CT state population is near equal in all three annealed blends after 300 ps. Therefore, although the low yield of CT state was observed in annealed PM6:anti-PDFC blend system, the high device performance in such a blend system is dominated by the longer lifetime (1250 ps) with a slower geminate recombination decay rate and Zhong et al. also reported a reasonably good electron and hole mobility in such blend system. Although the fast decay rate of the CT state was observed in annealed syn-PDFC blend, it can be compensated by the fast electron and hole mobility.[29] However, this is only the case in some situations where the high FF could be achieved by suppression of geminate recombination. For example, the CT state lifetime in annealed PM6:PDFC-Ph blend is as long as 880 ps, and the yield of CT state is around 20% higher in comparison with the annealed PM6:anti-PDFC blend. Nevertheless, the device performance of annealed PM6:PDFC-Ph film shows the FF value as low as 66 % and PCE of 6.5%. This is likely due to the unbalanced electron and hole mobility as evidenced by the observation of efficient intrinsic charge photogeneration in the pristine PDFC-Ph film.

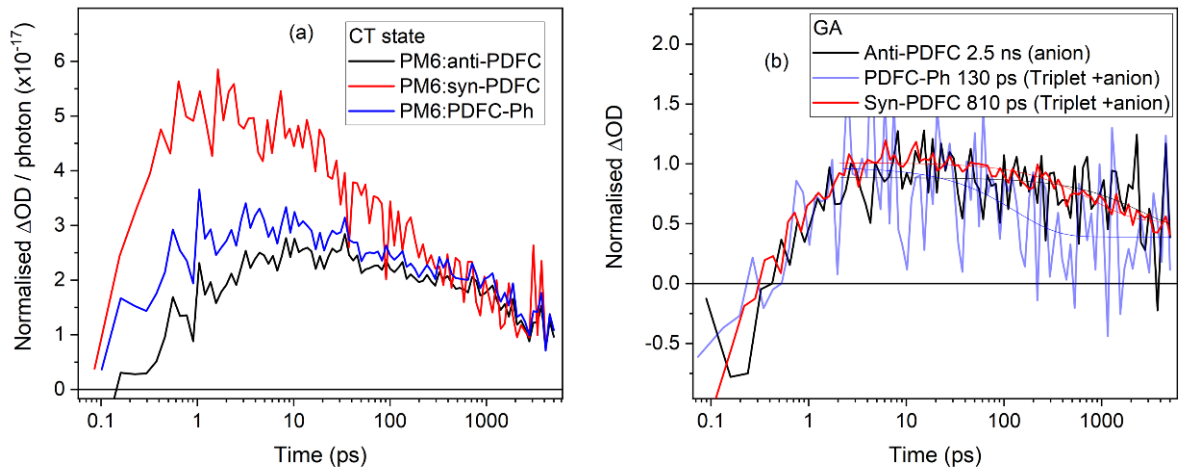

Figure 5.29 *(a) Normalised (per photon) decay dynamics of the CT state in annealed PM6:anti-PDFC, PM6:syn-PDFC, PM6:PDFC-Ph blend films, with an excitation wavelength 520 nm and excitation energy 30 μJ cm^{-2}. (b) Normalised (to 1) decay dynamics of the second component after GA in pristine anti-PDFC, syn-PDFC, PDFC-Ph films, with an excitation wavelength 665 nm and excitation energy 30 μJ cm^{-2}.*

Finally, the ps-TA results for pristine polymer film confirmed the formation of polymer exciton and polaron pairs (CT state) with an energy-independent decay dynamic. A substantially longer anti-PDFC charge lifetime of 2.5 ns was observed in its pristine film, followed by the coexistence anion and triplet lifetime 800 ps in pristine syn-PDFC film and the least 180 ps coexistence anion and triplet lifetime was observed in pristine PDFC-Ph film. For annealed PM6:PDFC blends, the ps-TA results show an energy transfer process from the polymer singlet to the NFA exciton in all three annealed blends, resulting in not only the PM6 exciton, CT state but also the NFA exciton were observed with the polymer dominant excitation. The difference in CT state rising and decay lifetime correlates well with the PM6 with NFA blend device performance. As the prolonged CT state lifetime (1.25 ns) was observed in the annealed PM6:anti-PDFC, despite the low yield of CT state, the high device performance in such blend system is due to the suppressed geminate recombination decay rate. In contrast, the 2 times higher CT population observed in annealed PM6:syn-PDFC and the longer triplet and anion lifetime in pristine syn-PDFC film, both give evidence for the high FF and PCE although the geminate decay rate of CT state is high in such blend system. Combined the short-lived anion and triplet state generated in the pristine PDFC film and the relatively low CT state yield, the low device performance of annealed PM6:PDFC-Ph film is attributed to the additional energy loss process.

5.4 Conclusions

This chapter contains a morphology and spectroscopic study of polymer PM6, three PDFC NFAs and their blends after annealing at 140° for 5 mins. A strong aggregation was observed in both annealed PM6:anti-PDFC and PM6:PDFC-Ph film with an enhanced crystallinity of the D/A interface while a little interacted D/A domain that could also be illustrated by the unchanged ground state absorption spectrum of the annealed PM6:syn-PDFC film.

On microsecond timescales, both polaron cations and NFA anions are observed in annealed PM6:PDFC blends, with the later species showing high intensity with the NFA dominant excitation in syn-PDFC and PDFC-Ph blends. The higher polymer polaron population with polymer dominant rather than NFA dominant excitation indicates the intrinsic charge photogeneration within the pure polymer domain in the annealed blend. The similar decay dynamics for the polymer polarons in annealed blend to the pristine polymer show that the polaron recombination is occurring within the PM6 domains along with a NFA anion migration.

On picosecond timescales, polymer exciton and CT state have been shown in the annealed PM6 with PDFC blends, and the NFA exciton was observed in femtosecond timescales, with the polymer dominant excitation. The observation of NFA exciton resulted from the energy transfer process from singlet polymer exciton to the NFAs or the hybridisation and dynamic equilibrium between the NFA S_1 and CT states at the D/A interface. Despite the low yield of CT state, a suppressed geminate recombination decay rate is used to explain the high FF and PCE in annealed PM6:anti-PDFC film. In contrast, the high FF and PCE in the annealed PM6:syn-PDFC blend is highly likely because of the generation of CT states and high electron and hole mobility compensate for the rapid geminate recombination of the CT states. The low device performance in annealed PM6:PDFC-Ph blend system could be due to the unbalanced electron and hole mobility as the strong intrinsic charge photogeneration in the pristine PDFC-Ph film. Both the morphology and spectroscopic results highlight the importance of polymer miscibility and the NFA crystallinity contributing to the OSCs device performance.

5.5 References

1 K. Vandewal, K. Tvingstedt, A. Gadisa, O. Inganäs and J. V. Manca, *Nat Mater*, 2009, **8**, 904–909.

2 S. Li, L. Zhan, N. Yao, X. Xia, Z. Chen, W. Yang, C. He, L. Zuo, M. Shi, H. Zhu, X. Lu, F. Zhang and H. Chen, *Nat Commun*, 2021, **12**, 4027.

3 M. Ghasemi, N. Balar, Z. Peng, H. Hu, Y. Qin, T. Kim, J. J. Rech, M. Bidwell, W. Mask, I. McCulloch, W. You, A. Amassian, C. Risko, B. T. O'Connor and H. Ade, *Nat Mater*, 2021, **20**, 525–532.

4 S. Li, L. Zhan, W. Zhao, S. Zhang, B. Ali, Z. Fu, T. K. Lau, X. Lu, M. Shi, C. Z. Li, J. Hou and H. Chen, *J Mater Chem A Mater*, 2018, **6**, 12132–12141.

5 K. Vandewal, *Annu Rev Phys Chem*, 2016, **67**, 113–133.

6 R. Wang, C. Zhang, Q. Li, Z. Zhang, X. Wang and M. Xiao, *J Am Chem Soc*, 2020, **142**, 12751–12759.

7 A. Classen, C. L. Chochos, L. Lüer, V. G. Gregoriou, J. Wortmann, A. Osvet, K. Forberich, I. McCulloch, T. Heumüller and C. J. Brabec, *Nat Energy*, 2020, **5**, 711–719.

8 S. Li, L. Zhan, C. Sun, H. Zhu, G. Zhou, W. Yang, M. Shi, C. Z. Li, J. Hou, Y. Li and H. Chen, *J Am Chem Soc*, 2019, **141**, 3073–3082.

9 J. Liu, S. Chen, D. Qian, B. Gautam, G. Yang, J. Zhao, J. Bergqvist, F. Zhang, W. Ma, H. Ade, O. Inganäs, K. Gundogdu, F. Gao and H. Yan, *Nat Energy*, 2016, **1**, 16089.

10 K. Nakano, Y. Chen, B. Xiao, W. Han, J. Huang, H. Yoshida, E. Zhou and K. Tajima, *Nat Commun*, 2019, **10**, 2520.

11 J. M. Hodgkiss, A. R. Campbell, R. A. Marsh, A. Rao, S. Albert-Seifried and R. H. Friend, *Phys Rev Lett*, 2010, **104**, 177701.

12 Y. Liang, Z. Xu, J. Xia, S. T. Tsai, Y. Wu, G. Li, C. Ray and L. Yu, *Advanced Materials*, 2010, **22**, E135.

13 F. D. Eisner, M. Azzouzi, Z. Fei, X. Hou, T. D. Anthopoulos, T. J. S. Dennis, M. Heeney and J. Nelson, *J Am Chem Soc*, 2019, **141**, 6362–6374.

14 K. Ding, T. Shan, J. Xu, M. Li, Y. Wang, Y. Zhang, Z. Xie, Z. Ma, F. Liu and H. Zhong, *Chemical Communications*, 2020, **56**, 11433–11436.

15 C. B. Nielsen, S. Holliday, H. Y. Chen, S. J. Cryer and I. McCulloch, *Acc Chem Res*, 2015, **48**, 2803–2812.

16 P. E. Hartnett, H. S. S. Ramakrishna Matte, N. D. Eastham, N. E. Jackson, Y. Wu, L. X. Chen, M. A. Ratner, R. P. H. Chang, M. C. Hersam, M. R. Wasielewski and T. J. Marks, *Chem Sci*, 2016, **7**, 3543–3555.

17 T. Shan, K. Ding, L. Yu, X. Wang, Y. Zhang, X. Zheng, C. C. Chen, Q. Peng and H. Zhong, *Adv Funct Mater*, 2021, **31**, 2100750.

18 A. D. Shaller, W. Wang, H. Gan and A. D. Q. Li, *Angewandte Chemie - International Edition*, 2008, **47**, 7705–7709.

19 D. Xia, X. Y. Wang, X. Guo, M. Baumgarten, M. Li and K. Müllen, *Cryst Growth Des*, 2016, **16**, 7124–7129.

20 F. C. Spano, *Acc Chem Res*, 2010, **43**, 429–439.

21 R. Ma, T. Liu, Z. Luo, Q. Guo, Y. Xiao, Y. Chen, X. Li, S. Luo, X. Lu, M. Zhang, Y. Li and H. Yan, *Sci China Chem*, 2020, **63**, 325–330.

22 T. Shan, K. Ding, L. Yu, X. Wang, Y. Zhang, X. Zheng, C. C. Chen, Q. Peng and H. Zhong, *Adv Funct Mater*, 2021, **31**, 2100750

23 F. Lin, K. Jiang, W. Kaminsky, Z. Zhu and A. K. Y. Jen, *J Am Chem Soc*, 2020, **142**, 15246–15251.

24 G. Zhang, X. K. Chen, J. Xiao, P. C. Y. Chow, M. Ren, G. Kupgan, X. Jiao, C. C. S. Chan, X. Du, R. Xia, Z. Chen, J. Yuan, Y. Zhang, S. Zhang, Y. Liu, Y. Zou, H. Yan, K. S. Wong, V. Coropceanu, N. Li, C. J. Brabec, J. L. Bredas, H. L. Yip and Y. Cao, *Nat Commun*, 2020, **11**, 3943

25 H. Cha, C.-H. Tan, J. Wu, Y. Dong, W. Zhang, H. Chen, S. Rajaram, K. S. Narayan, I. McCulloch and J. R. Durrant, *Adv Energy Mater*, 2018, **8**, 1801537.

26 T. M. Clarke, A. Ballantyne, S. Shoaee, Y. W. Soon, W. Duffy, M. Heeney, I. McCulloch, J. Nelson and J. R. Durrant, *Advanced Materials*, 2010, **22**, 5287–5291.

27 J. Kosco, S. Gonzalez-Carrero, C. T. Howells, T. Fei, Y. Dong, R. Sougrat, G. T. Harrison, Y. Firdaus, R. Sheelamanthula, B. Purushothaman, F. Moruzzi, W. Xu, L. Zhao, A. Basu, S. De Wolf, T. D. Anthopoulos, J. R. Durrant and I. McCulloch, *Nat Energy*, 2022, **7**, 340–351.

28 J. Marin-Beloqui, G. Zhang, J. Guo, J. Shaikh, T. Wohrer, S. M. Hosseini, B. Sun, J. Shipp, A. J. Auty, D. Chekulaev, J. Ye, Y. C. Chin, M. B. Sullivan, A. J. Mozer, J. S. Kim, S. Shoaee and T. M. Clarke, *Journal of Physical Chemistry C*, 2022, **126**, 2708–2719.

29 U. Würfel, D. Neher, A. Spies and S. Albrecht, *Nat Commun*, 2015, **6**, 6951.

Chapter 6 Conclusions and Future Work

6.1 Conclusions

This thesis explores the parameters that affect the photophysical mechanisms in both fullerene and non-fullerene based OSCs. In particular, the role of morphology and chemical structure affects the charge and triplet photogeneration and recombination processes in D/A blends. Chapter 3 and 4 investigate the photophysics of PffBT4T-based TDA polymers blended with fullerene or NFA on ns-μs timescales. Chapter 5 investigates the photophysics over a broad timescale from ps to μs in the blend films of polymer PM6 with novel PDI-based NFAs.

Chapter 3 shows the understanding of the relationship between morphology and charge photogeneration in PffBT4T-based polymer with fullerene blend systems. The changing morphology of D/A blends is achieved through the alkyl chain length of the polymer and the D/A blend films under thermal annealing conditions. For amorphous polymer (PffBT4T-C9C13), not only polymer triplet was observed in the polymer:fullerene blend (first time to be identified in such high performance fullerene blend system), but also two types of polymer polarons were generated in different morphological environments named as bimodal polarons. Compared to charge photogeneration in pristine polymer film and the inert polymer matrix with polystyrene, one polymer polaron is determined in polymer-dominated domains and the other types of polaron with a narrower bandwidth are investigated in the fullerene induced ordering mixed domains. However, PffBT4T-2OD with one shorter alkyl chain length shows solely a polymer polaron peak that is generated in polymer-dominated domain. The lack of fullerene induced ordering in PffBT4T-2OD:$PC_{70}BM$ is attributed to the good miscibility between polymer and fullerene. Despite the large differences in photophysics, a comparison to the literature shows that PffBT4T-C9C13 and PffBT4T-2OD based solar cells exhibit similar device performances. We attribute this to the more amorphous PffBT4T-C9C13 blend possessing both slower charge carrier recombination kinetics and lower charge carrier mobility. This highlights how crystallinity and polymer miscibility lead to large changes in charge generation, recombination, and mobility for two very similar materials in terms of chemical structure, demonstrating how morphology control is key for OSC device efficiency.

Chapter 4 focussed on the well-studied polymer PffBT4T-C9C13 as an electron donor to study charge photogeneration with four different NFAs (ITIC, ITIC-2F, ITIC-Th and Y6) blend films. NFA anions were investigated from SEC spectra of the pristine NFA films, and NFA triplet states were determined in their inert polystyrene matrix. Triplet sensitisation experiment is used to quantify NFA triplet population in both solution and films, with the calculated triplet extinction coefficient. In the polymer:NFA blend films, triplets are extremely prevalent, and there is no consistent pattern regarding triplet behaviour. Polymer triplet states are detected in both the ITIC and ITIC-2F blend systems under the polymer dominant excitation, and the long-lived triplet formation is attributed to the non-geminate recombination. In contrast, ITIC-Th blend film shows only the NFA triplet decay under either the polymer or NFA dominant excitation, due to the triplet energy transfer process from polymer triplet to ITIC-Th. There is only charge detected in the polymer:Y6 blend with large phase segregation. There are ramifications of these results for OPV device performance. Firstly, the variation in photophysical mechanisms across the different NFA blends suggests a complex interplay between intrinsic behaviour, energetics, and morphology that dictates that new OPV materials must be considered on their own merits. The morphology study of the PffBT4T-C9C13:ITIC-2F blend with varying blend ratios indicates that the charge recombination to form triplets is significantly enhanced when intermixed, well-dispersed domains are present. However, the clear observation that triplet populations also scale with charge carrier populations implies that future research directions must attempt to decouple the two or employ strategies to harness triplet states to benefit device performance.

Chapter 5 investigates the charge photogeneration and recombination process in high-performing (high PCE and high FF) pristine and blend films of polymer PM6 with anti-PDFC and syn-PDFC NFAs and the relatively low-performing PM6:PDFC-Ph blends. The polymer cation and PDFC NFA anions are determined from their SEC spectra, and μs-TAS characterised the triplet spectral shape in their pristine solution. Different types of excited states are observed in the μs-TA spectrum of pristine film, which could be related to the morphology of the films. A rougher film surface was observed for anti-PDFC that the decay dynamics only show anti-PDFC anion in pristine film whereas the smoother film of PM6, syn-PDFC and PDFC-Ph films shows both the triplet and cation/anion features, with a speedy decay rate. The solely anti-PDFC anions observed in the rougher pristine film may be due to the charge

photogeneration at the grain boundaries. For all three PM6:PDFC NFA blend films, μs-TA spectra results exhibit that both the PM6 and NFA polarons are observed with polymer or NFA dominant excitation with a fast decay rate as the polymer polarons in pristine polymer film.

Finally, the characterisation of the short-lived excited state (exciton, CT states) in the pristine and annealed PM6 with PDFC NFA blend films were explored. The main finding here is a longer-lived NFA exciton was observed under the polymer dominant excitation, which is attributed to the energy transfer process from the polymer singlet to NFA singlet state. For the anti-PDFC and syn-PDFC blend systems with a small driving force (~0.1 eV) for energy and electron transfer, there is another explanation for the observation of longer-lived NFA exciton under polymer excitation due to the hybridisation and dynamic equilibrium between the NFA S_1 state and the CT states at the D/A interface. In combination with the morphology and spectroscopic study, high FF and PCE of the annealed PM6:anti-PDFC blend system could be explained by the suppressed geminate recombination decay rate and good electron and hole mobility. In contrast, the high FF and PCE in annealed PM6:syn-PDFC blend are highly likely attributed to the rapid geminate recombination decay rate could be compensated by the high electron and hole mobility and the rapid CT states generation. The low device performance in annealed PM6:PDFC-Ph film is likely due to the unbalanced electron and hole mobility as the strong intrinsic charge photogeneration in the pristine PDFC-Ph film. The morphology and spectroscopic results for the annealed blend PM6 with three PDFC acceptors highlight the importance of polymer miscibility and the NFA crystallinity to the OSCs device performance.

6.2 Future work

This thesis has identified the triplet formation in TDA polymer:fullerene or non-fullerene blend films could be formed via charge back recombination. Using a series of non-fullerene acceptors, the fluorination of the acceptor shows the potential to suppress the triplet yield with an increasing in charge population. After studying the mechanism of such TDA polymer with different NFAs and they present different conclusions, further studies are required to suppress the energy loss pathways by either manipulating the energy level of molecules inside the OSCs to increase the energy of triplet states and minimise the possibilities for charge back recombination. More studies need to explore the optical and electric properties of the new emerging sets of NFAs and the photophysical mechanisms behind different combinations of

polymer:NFAs blend systems. For example, how to link the molecular structure (rigidity, delocalisation) to the formation of charge carriers and triplet states, how to vary molecular structure to suppress the triplet formation but increasing the yield of free charge carriers. Although in this thesis, the yield of triplet states on different polymer:NFA blend films have been studied, the estimated triplet extinction coefficient of NFA solutions and the correction factor from solution to film can be estimated. However, because the yield of triplet states on thin film is obtained indirectly, there are some deviations and discrepancies. Further research can deduce the triplet extinction coefficient and the yield of triplet states on thin films from direct and more precise methods. For an instant, the triplet extinction coefficient of films can be determined via triplet sensitisation experiments of pristine films by selecting an appropriate triplet sensitiser (the way to choose sensitiser in section 2.8.1.1), excitation wavelength and molecular ratios of the sensitiser and NFAs. Once a more reliable triplet quantification method is identified in the polymer:NFA blend films, it can be applied to quantify triplet states in the organic photovoltaic devices under operational conditions to investigate the actual role of triplet states.

It has proved that the essential role of blend nanomorphology is to suppress the triplet formation and prolong the charge lifetime in TDA PffBT4T-based polymer OSCs. More studies are required to control the blend morphology to improve the molecular percolation pathways, thereby reducing the recombination and enhancing charge dissociation. Some more advanced techniques combine the advantages of transient spectroscopy and microscopy to minor the correlation between excited states formation, decay and the morphology of films as a function of time, such as transient absorption microscopy. By using such techniques, it is more obvious to understand nanomorphology's key role in charge photogeneration.

Since geminate recombination of CT states has been identified as a loss mechanism that limits the film charge formation in all three PM6 with PDFC acceptors blend films, there are less obvious differences in photophysical mechanisms among them. It is essential to understand more in-depth the device's physics. For example, how the electron mobility affects the charge yield? Do the unbalanced electron and hole mobility create any internal field? In addition, as the unique advantages provided by the novel PDFC NFAs and the electronic properties of organic semiconductors are largely affected by vibronic coupling, further studies can be done to understand the correlation between the simultaneous dynamic and their structural

information. One approach is applying vibrational spectroscopy, like time-resolved transient infrared spectroscopy, which is extremely sensitive and small changes in the geometry of hundredths of angstroms are detectable. This will potentially make us know more deeply about the structure-property relation for NFAs and guide future research direction for synthesising new materials to improve the device performance further.